STRUCTURAL PERFORMANCE OF A FULL-DEPTH PRECAST BRIDGE DECK SYSTEM PRESTRESSED AND REINFORCED WITH AFRP BARS

A Thesis

by

SHOBEIR PIRAYEH GAR

Submitted to the Office of Graduate Studies
Texas A&M University
in partial fulfillment of the requirements for the degree of

DOCTOR OF PHILOSOPHY

Approved by:

Co-Chairs of the Committee,	Monique Hite Head
	Stefan Hurlebaus
Committee Members,	John B. Mander
	Mary Beth Hueste
	Anastasia Muliana
Head of Department	John Niedzwecki

December 2012

Major Subject: Civil Engineering

ABSTRACT

During the last 70 years, corrosion-induced deterioration of bridge concrete decks has resulted in replacement and repair of the deck and a serious need for finding alternative design strategies that would substantially reduce susceptibility of the concrete deck to corrosive environments and the subsequent maintenance cost as well. One alternative is to replace the reinforcing or prestressing steel in concrete with fiber-reinforced polymer (FRP) composite bars, which are corrosion-resistant, and have a very high strength-to-weight ratio. FRP bars can be used as either non-prestressed or prestressed reinforcement. Despite ongoing research mostly focused on prestressed and non-prestressed FRP reinforced concrete beams, less attention has been focused on the structural performance of bridge deck slabs with actual dimensions, boundary conditions, and structural details. Clear understanding of the structural performance and failure mechanism of the bridge deck slab as well as constructability issues are not achievable unless full-scale tests are conducted.

The main objective of this research is to establish a design methodology that can be applied to designing a bridge deck system prestressed and reinforced with aramid fiber reinforced polymer (AFRP) bars under service and ultimate loads. The research approach of this investigation consists of conducting an experimental study on a full-scale bridge deck slab including two precast concrete panels prestressed and reinforced with AFRP bars perpendicular to, and parallel to the traffic direction, respectively. The precast panels are connected via a cast-in-place seam (wet joint). In order to gain clearer insight and valid interpretation of the structural performance, the components of the bridge deck are separately tested as well. This includes flexural and shear tests of the cast-in-place panel-to-panel seam, flexural tests of an 1830 mm long strip prestressed with AFRP bars representing the bridge deck section *perpendicular* to the traffic direction, and flexural tests of an 1830 mm long strip reinforced with AFRP bars representing the bridge deck section *parallel* to the traffic direction. Once the flexural capacity of the strips and panel-

to-panel seam is known, the load capacity of the bridge deck and the corresponding failure mechanism can be better analyzed. Yield line theory, commonly used for analysis and design of steel reinforced concrete slabs, is employed and modified to perform the failure load analysis of the deck slab in spite of the linear and brittle behavior of AFRP bars.

Tensile characteristics of AFRP bars are experimentally investigated in the first phase of the project to provide a reliable data set for analytical and experimental studies of the bridge deck system in subsequent steps. Other than the bridge deck slab, this research presents development of a comprehensive computational model for analysis and design of a bridge girder in composite action with the deck slab. To compute the maximum deflection, rational equations based on studying the curvature distribution are derived herein for both prestressed and non-prestressed FRP reinforced concrete beams. The existing deflection equations are typically empirically-derived formulae, which were originally calibrated for steel reinforced concrete beams and hence not suitable for FRP case as the FRP bars have lower modulus of elasticity compared to conventional steel.

Consequently, from this research, the structural performance of an AFRP concrete bridge deck slab with full-depth precast prestressed panels is studied and an applicable method for design and failure load analysis is established. Moreover, for FRP reinforced and prestressed concrete beams, two rational deflection equations are developed for suitable design office implementation.

DEDICATION

To my wife, Marta Taghavi.

ACKNOWLEDGEMENTS

I would like to extend my warm appreciation to Dr. Monique Head, my PhD dissertation advisor, for her valuable guidance, technical advice, and financial support during my PhD studies. I would also like to express my gratitude to Dr. Stefan Hurlebaus, my PhD dissertation co-advisor, who taught me how to conduct experimental research in laboratory and financially supported me during this period. My deep gratitude is given to Dr. John Mander, my committee member, who taught me how I should look at a physical phenomenon and extract an engineering application out of it. The technical comments provided by Dr. Mary Beth Hueste, Construction, Geotechnical and Structures Division Head within the Zachry Department of Civil Engineering, and Dr. Anastasia Muliana from Mechanical Engineering Department are greatly appreciated.

The achievements gained through this research project are undoubtedly the result of contributions and help provided by my colleagues. I would like to thank my research partner Jose C. Medina, graduate student, for his endless help and support during the experimental phase of the project. I would also like to thank my colleagues Kyle Wieghaus, Joshua White, and Jae Baik who kindly supported me whenever I needed help in the lab. The effective assistance provided by Kosieme A. Okafor, and Wes Cummings, undergraduate students, is sincerely acknowledged. The technical comments regarding the test procedure provided by Matt Potter, Technical Lab Manager, and Dr. P. Keating, Director of the High-Bay Structural and Materials Testing Laboratory at Texas A&M University are also greatly appreciated.

This research was supported by a grant from the National Science Foundation (NSF 0927333) for which Dr. Monique Head was the Research Supervisor. I am very honored and grateful to have been involved in this research project.

TABLE OF CONTENTS

Page

LIST OF FIGURES

Page

LIST OF TABLES

Page

1. INTRODUCTION

1.1 Research Motivation

Critical infrastructure of the United States, particularly roadways and bridges, are deteriorating and facing a nationwide problem due to corrosion of the reinforcing steel as a result of aging and aggressive environments. This is a major concern as the economy of the U.S. is greatly tied to its transportation system, where bridges are an integral part of the transportation network that connects people and businesses. Steel corrosion leads to member degradation, endangers structural integrity, and may even cause catastrophic failures. The corrosion decay in concrete structures has continued to be a challenge in the scientific and engineering communities. In 1997, the Intermodal Surface Transportation Efficiency Act (ISTEA) spent $2.5 billion for the Highway Bridge Replacement Program, where a majority of the funds went towards replacement or rehabilitation of bridge decks that were damaged by corrosion deterioration. This problem has led to a serious need for finding alternative design strategies that can reduce the likelihood of corrosion decay in concrete structures and the subsequent maintenance cost.

The main idea is to use high performance materials that have inherent properties to provide durable corrosion protection and prevent the premature spalling or corrosion-induced cracking. Recent advancements in the field of material science have resulted in the development of new products that can be used in many areas of civil engineering, where conventional materials have failed to provide satisfactory service life. In particular, fiber reinforced polymer (FRP) materials, which present unique properties such as very high strength-to-weight ratio, and corrosion-resistivity, have received significant attention and have been considered as an ideal alternative for steel.

AFRP bars can be manufactured as reinforcing bars for RC (reinforced concrete) and PRC (prestressed reinforced concrete) structures, sheets and laminates for external strengthening of beams, slabs and masonry walls, wraps and shells for confinement of columns, etc. A bridge deck system that consists of concrete beams and slabs prestressed

and reinforced with FRP bars seems to be a feasible alternative to prevent premature spalling or corrosion-induced cracking and enhances the durability of the concrete bridge deck slabs.

Considerable research has been conducted on the behavior of prestressed and non-prestressed FRP concrete beams; however, less attention has been paid to the performance of FRP RC or PRC bridge deck systems including concrete slabs and girders in a full scale. Hence, there are knowledge gaps in the performance of FRP concrete bridge deck systems due to lack of theoretical and experimental data and design specifications. This research is intended to establish a design methodology that can be applied to design a bridge deck system prestressed and reinforced with aramid fiber reinforced polymer (AFRP) bars under service and ultimate loads. Experimental investigation is conducted on a full-scale bridge deck including two precast concrete panels prestressed and reinforced with AFRP bars perpendicular to and parallel with the traffic direction, respectively. The structural performance and failure mechanism are carefully studied and compared to a similar full scale specimen reinforced with conventional steel (Mander et al. 2009). Failure load analysis is subsequently performed to find the load capacity of the bridge deck slab compared to the experimental results. The experimental and analytical results reveal whether a satisfactory structural performance has been achieved.

1.2 Research Need

As stated, most of the investigations on FRP reinforced concrete members have been focused on individual beams or one-way slabs, and the structural performance of a full-scale bridge deck as a two-way slab where dimensions, boundary conditions, and structural details realistically represent a bridge deck system, seems to be less noticed. Furthermore, analysis and design process of FRP reinforced concrete bridge deck as a two-way slab is not as clear as steel RC slabs, since FRP bars, in contrast to conventional steel rebar, do not have a yielding point and behave linearly up to rupture. Therefore, the classical methods of plastic analysis such as yield line theory may not be

applicable. Hence, there is a crucial need to experimentally study the structural performance of a full-scale bridge deck system with a close view on the failure mechanisms and load capacity of the interior spans and overhangs. Establishing a theoretical as well as practical method of analysis capable of accurately predicting the failure load that can be employed by design engineers and suitable for the design office implementation is one of the major needs in this field of study. Load-deflection response, deformability of the deck, and sufficiency of the panel-to-panel seam are the other knowledge gaps that need to be addressed in order to establish a design methodology.

1.3 Research Objectives

The main objectives of the proposed research project are to:

1- experimentally evaluate the structural performance of a full-scale concrete bridge deck slab with precast panels reinforced with prestressed and non-prestressed AFRP bars compared to its conventional steel counterpart.

2- experimentally and analytically investigate the flexural behavior of AFRP RC and PRC strips representing the bridge deck section in *x* and *y* directions. This helps to better analyze the bridge deck as a two-way slab.

3- measure the flexural and shear strength of the cast-in-place seam connecting the precast panels of the bridge deck.

4- establish a theoretical as well as practical method capable of accurately predicting the failure load of the interior spans and overhangs of the bridge deck. Such a method can be appealing for design office implementation.

5- derive rational based equations to evaluate the maximum deflection of AFRP RC and PRC beams, as the deflection and not strength commonly governs the design due to low modulus of elasticity of FRP bars compared to reinforcing steel.

6- summarize the constructability issues faced when constructing the precast prestressed panels. Construction in the laboratory environment can resemble the off-site precast plant conditions.

1.4 Research Approach

Experimental investigation is the main approach taken herein to study the structural performance of a full-scale bridge deck slab reinforced and prestressed with AFRP bars. In the first phase of the project, the uniaxial characteristics of the AFRP bras are studied. Then a full-scale bridge deck specimen, measuring 5490 × 4880 mm, including two precast panels resting on three supporting beams is tested for truck wheel load mimicked by a monotonically increased concentrated load to determine the load capacity and failure mechanism of the interior spans and overhangs. The full-depth precast panels are reinforced with AFRP bars parallel to the traffic direction (*y*-direction) and prestressed perpendicular to the traffic direction (*x*-direction). String pots are used to record the deflection of the deck in both directions beneath the truck wheel load. Therefore, the curvature distribution can be subsequently determined which helps to better interpret the flexural performance of the deck. In order to find out the governing failure mechanism, crack pattern on top and beneath the deck is carefully mapped and studied.

Since the bridge deck is a more complex system than a beam or a one-way slab, one AFRP reinforced strip representing the bridge deck section in *x*-direction and one AFRP prestressed strip for *y*-direction are separately tested under four-point loading to investigate their flexural behavior and to better analyze the experimental results of the bridge deck tests. Additionally, an extensive computational model is developed to perform numerical analyses for strip specimens, which will be verified by the experimental data. The experimental and numerical results help to characterize the flexural behavior of strip elements.

To specify the structural capacity of the panel to panel seam, two AFRP RC strip specimens resembling the panel to panel seam will be separately tested to measure the flexural and shear capacity of the joint. Having all the experimental and numerical results known, the concept of plastic method of analysis, such as yield line theory, is employed and modified to perform the failure load analysis of the bridge deck slab.

Comparison between the analytical and experimental load capacity of the bridge deck slab verifies the fidelity of the method developed.

To analyze the AFRP concrete bridge deck girder in composite action with deck slab, a comprehensive computational model is developed capable of performing refined non-linear analysis. The results, which will be verified by experimental data, can show whether the girder meets the serviceability and ultimate limit states. Since the deflection limit, as a serviceability criterion, commonly governs the design of FRP concrete beams, rational deflection equations, based on studying the curvature distribution, are developed for either FRP reinforced or prestressed concrete beams. The deflection equations are verified with experimental data, and presented in a convenient-to-use form suitable for design office implementation. Fig. 1 shows the bridge girder and deck specimens along with the bridge prototype.

1.5 Organization of Thesis

This thesis consists of eleven core chapters. The literature survey and research background is covered in Chapter 2. Chapter 3 presents the uniaxial characteristics of AFRP bars for prestressing application. The results of this chapter are essential for analysis, design, and implementation of the bridge deck slab specimen. The experimental investigation on the full-scale bridge deck slab with full-depth precast prestressed panels is presented in Chapter 4 to study the structural performance of the proposed bridge deck system. Chapter 5 illustrates the experimental behavior of the AFRP concrete strip elements representing the bridge deck section in x and y directions as well as the panel-to-panel seam. The results of this chapter aid to characterize the structural behavior of the strip elements which is critical for failure load analysis of the bridge deck slab.

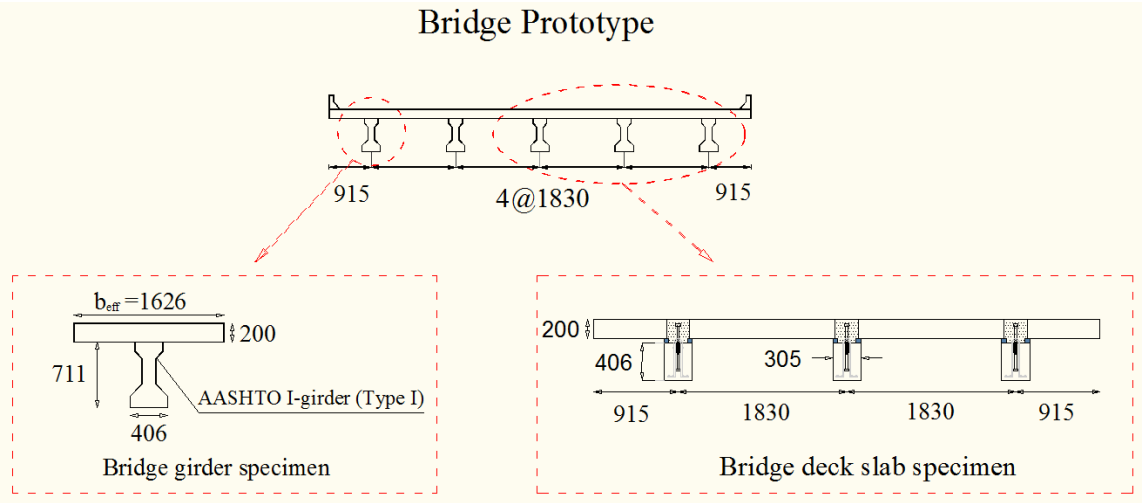

Fig. 1. Bridge girder and deck specimens for this study (Dimensions: mm)

Chapter 6 utilizes the results of Chapters four and five, and based on the yield line concept, a rational method for failure load analysis of the bridge deck slab is developed. Chapter 7 comprehensively presents the analysis and design procedure of an AFRP prestressed bridge deck girder in composite action with bridge deck slab. A full computational model developed for numerical analysis of the girder is illustrated in this chapter. Chapter 8 focuses on developing a rational model for effective moment of inertia to find the maximum deflection of FRP prestressed concrete beams. Likewise, Chapter 9 discusses about the deflection equations for FRP reinforced concrete beams where two applicable and convenient-to-use equations are derived and verified with experimental data. Chapter 10 fully discusses about the tension stiffening phenomenon in prestressed concrete beams through developing a closed-form equation for moment-curvature relationship. Chapter 11 summarizes the major results and draws the conclusions of this research.

2. LITERATURE SURVEY AND RESEARCH BACKGROUND

The application of FRP materials in bridge applications initiated from the first pedestrian FRP bridge built by Israelis in 1975 (Hastak et al. 2004) and continued to other pedestrian bridges with pultruded shapes consisting of hybrid glass and carbon FRP composites that have an increase in stiffness with relatively little additional cost. Bride deck systems were constructed and tested in the early 1990s, where the first U.S. all-composite vehicular public bridge was opened to serve on December 4, 1996 in Russell, Kansas. The construction process for this bridge consisted of FRP decks being shop-fabricated with composite honeycomb cells sandwiched between two face sheets (Tang and Podolny 1998). The bridge was installed in one day, which is definitely accelerated construction that helped in minimizing the impact of construction on commuters and commerce that bridges serve within the transportation network. The cost savings of the accelerated construction offset higher initial costs for the FRP materials.

Flexural testing of FRP prestressed concrete beams began in Japan in the mid 1980's under a nationally coordinated program to develop design guidelines for concrete reinforced or prestressed with FRP bars. Similar research began in Europe and United States in the late eighties (Dolan 1990, 1991; and Gerritse and Werner 1991). Since this work was completed, a large amount of research has been documented and published. Several attempts have been made to develop design guidelines for FRP reinforcement, but these are in various states of completion (ACI 440.4R 2004). The lack of uniformity in testing procedures, material definitions, and reporting the results have caused great difficulty in developing guidelines. Several of the guidelines in development have been evaluated and compared in a published article by Gilstrap et al. (1997). The literature survey in this chapter is divided into three major parts: transfer and development length, FRP concrete beams and FRP concrete slabs.

2.1 Transfer and Development Length

Nanni et al. (1992) used concrete strain measurements and static flexural tests to determine transfer lengths of braided FIBRA AFRP bars of nominal 8, 12 and 16 mm diameters. The reported transfer length for the bars is approximately 400, 450, and 550 mm. Some increase in transfer length for increased prestressing force and some decrease for multiple strand applications can be noted. Nanni and Tanigaki (1992) reported development lengths of < 850 mm, >1000 mm, and 1040 mm for the same material.

Taerwe et al. (1995) used 7.5 and 5.3 mm diameter ARAPREE aramid fiber rods in their transfer length study. They suggested a transfer length of 16 times the nominal diameter of the rods for all of these ARAPREE rods.

Ehsani et al. (1997) conducted tests on three kinds of aramid FRP bars: ARAPREE 10 mm, FIBRA 10.4 mm and TECHNORA 7.4 mm. The transfer and development lengths were found to be 33 times bar diameters and 83 times bar diameters for FIBRA, 43 times bar diameters and 117 bar diameters for TECHNORA, and 50 bar diameters and 102 bar diameters for ARAPREE. Since the AFRP bars for this project are of ARAPREE type with 10 mm diameter, the transfer and development length reported by Ehsani et al. (1997) is selected as the reference.

2.2 FRP Concrete Beams

Most of the research on the application of FRP bars in reinforced and prestressed concrete is focused on beams. McKay et al. (1993) investigated the flexural behavior of concrete beams prestressed with AFRP bars. One of the major findings of this research was that FRP prestressed beams should only be designed as fully prestressed members, otherwise fretting of the rod surface decreases the bond strength between the rods and the concrete leading to concrete horizontal splitting failures at the level of the rods.

Naaman et al. (1993) tested two T-beams partially prestressed with CFRP strands. The beams had conventional steel reinforcing bars in addition to CFRP. An accidental CFRP strand failure during stressing and anchoring was experienced, which suggested

that extreme care should be taken for prestressing operation. A comparison with similar beams using steel strands showed that for the same global reinforcing index, the cracking load is lower and the crack width is larger, while the beam stiffness is smaller when CFRP strands are used. The load-deflection responses of the beams prestressed or partially prestressed with FRP bars can be predicted with reasonable accuracy using conventional methods of equilibrium, strain compatibility and material stress-strain relationships.

Abdelrahman et al. (1995) tested four prestressed concrete T-beams pretensioned with FRP cables, as girders of the first smart highway bridge built in Canada. They concluded that behavior of the beams with CFCC and leadline cables were bi-linearly elastic up to failure. Unloading of the beams showed an elastic response and negligible residual deformations. Beams pretensioned by FRP normally exhibited considerable warning before failure due to the presence of large, extensively distributed cracks and large deflection before failure. They found out that in beams with a wide flange in the compression zone, such as T-sections, failure normally occurs by rupture of the FRP bars. They also proposed ductility method providing an adequate model to measure ductility of the beams prestressed by FRP bars.

Shahawy et al. (1995) studied the static flexural response of members pretensioned with multiple layered AFRP. They concluded that ARAPREE bars can be successfully employed as prestressing strands; however, durability and long-term performance should be investigated. The double-tee beam that they tested exhibited excessively large deformations in the post-cracking stage and had excellent deformation recovery of about 95% upon removal of the applied load, which corresponds to about 80% of theoretical ultimate load. Methods for evaluating the flexural strength of an FRP prestressed beam were published in 1996 (Dolan 1996). This paper covered the derivation of the flexural strength equations and provided a calibration against test beams taken from the available published literature.

Abdelrahman (1997) tested prestressed and partially prestressed concrete beams with CFRP bars to study their flexural behavior. Eight beams were prestressed with CFRP bars and two with conventional steel bars. The beams were tested using quasi-static monotonic concentrated loads. The research studied the serviceability limit states in terms of crack width, crack spacing and deflection prior to and after cracking. The modes of failure and the ultimate carrying capacity of the beams were also investigated. The tested beams were analyzed using a strain compatibility approach to predict the moment-curvature relationship. The deflection was calculated using two different techniques, integration of the curvature at many sections along the beam span, and a simplified method where the deflection was calculated using an equivalent moment of inertia for the entire beam. The proposed models had less than 20% margin of error compared to the experimental results. The tested beams pretensioned by CFRP exhibited considerable warning before failure due to the presence of extensively distributed cracks and large deflection prior to failure. Change of the reinforcement ratio resulted in a change in failure mode and deformability. Partial prestressing increased the deformability of the beams. New parameters were proposed based on experimental and analytical results to accurately predict the deflection, prior to and after cracking, and crack width. Recommendations for flexural design, and deflection and crack width computation of beams partially prestressed with CFRP bar were introduced.

Lu (1998) performed flexural tests on beams prestressed with three types of FRP bars including two kinds of CFRP and one AFRP type bar. The primary variable in the study was the type of FRP materials. The flexural test was a four-point bending test to evaluate moment-curvature and load-deflection behavior of the specimens. Two methods were used to determine curvature. The first method was to attach LVDTs on one side of the beam to directly measure concrete strains. The second method was to measure beam deflection at five different locations along the beam within the constant moment zone by potentiometers. The deflection curve formed by the five points should be a part of the circle, and the radius of the circle equal to the inverse of the curvature in the constant moment zone. Both bond slip failure and flexural failure occurred. Beams with AFRP

bars exhibited larger deflection, curvature and more cracks at failure than the beams with CFRP bars, but the CFRP prestressed beams had larger moment capacity. The FRP prestressed beams had smaller incremental crack width openings than those reinforced with steel strand, indicating a stronger bond mechanism between concrete and the FRP bars.

Performance of concrete beams prestressed with aramid fiber-reinforced polymer bars have been investigated by Toutanji and Saafi (2000). The results of their experiments show that ductility can be significantly enhanced by using a combination of bonded and unbonded bars or by the addition of non-tensioned rebar. Dolan et al. (2001) proposed detailed equations to determine the capacity of vertically aligned bars which is also valid for harped prestressing. They found the difference in estimating capacity using both the proposed formula and the simplified equation for bars in a single layer within 1%. For the application of aramid bars in high strength concrete, Rashid et al. (2005) have conducted some experimental tests and investigated the behavior of ten aramid fiber-reinforced polymer reinforced high strength concrete beams under three-point loading. Their test results have shown that a concrete beam, when reinforced with AFRP bars, becomes more flexible in the post-cracking range than an equivalent steel-reinforced beam and may fail in an unusual flexure-shear mode.

The background of the research clearly confirms the applicability of FRP bars as reinforcement or prestressing tendons for concrete beams in place of conventional steel. The experimental results show that the ultimate strength can be estimated with an acceptable accuracy using the conventional method of stress block and writing equilibrium and compatibility equations. However, there is still lack of rational equations that can be conveniently utilized by engineers to evaluate the maximum deflection as a governing limit state for FRP concrete beams. The existing equations are typically empirically derived formulae that have been originally calibrated for conventional steel. Furthermore, the experimental beam specimens are commonly tested without the effect of composite action induced by the topping deck.

2.3 FRP Concrete Slabs

Matthys et al. (1996) performed research on concrete slabs prestressed with AFRP and steel bars, respectively. Higher ultimate deflections and higher ratios of ultimate to cracking load are obtained for the slabs pretensioned with AFRP. This ensured a higher safety margin between design load and ultimate load. This favorable aspect partly compensates for the sudden fracture of the slabs pretensioned with FRP.

Salakawy and Benmokrane (2004a) investigated the construction of a new highway bridge using FRP bars which was located on highway 55 North over the Magog River Quebec, Canada (Fig. 2). The bridge deck was 22 mm thick and 83.7 m long supported by five steel girders over three spans. One full end span was entirely reinforced with FRP bars and the other two spans were reinforced with galvanized steel. The concrete deck slab was designed based on Canadian Highway Bridge Design Code (CHBDC). The bridge was tested for service performance under standard truck loads. As they reported, no problems to construction with FRP bars were faced. Light weight of FRP bars helped to carry and place them with less effort. During the serviceability test, deflection of the steel girders and bridge deck slab did not exceed 6 and 2 mm, respectively. The results confirmed that the flexural design method of CHBDC is very conservative.

Salakawy and Benmokrane (2004b) studied the flexural performance and serviceability of concrete bridge deck slabs reinforced with FRP bras. 10 full-size one-way slabs measuring 3100 × 1000 × 200 mm were tested under four-point loading where the simply supported span was 2500 mm long with a shear span of 1000 mm. Five slabs were reinforced with GFRP, three slabs with CFRP, and two with conventional steel. The results showed that all slabs reinforced with FRP bars failed in shear while the steel-reinforced slabs failed by steel yielding and crushing of concrete, subsequently. Only two of the FRP reinforced slabs failed in combined tension-shear in the vicinity of the support resulting in increase of the load capacity of 26 and 55%. These two slabs had reinforcement ratio equal to balanced reinforcement ratio. It was found that the load

carrying capacity of the slabs reinforced with FRP bars was much higher than steel reinforced slabs. However, FRP reinforced slabs showed larger deflection and crack width indicating that serviceability and not strength governs the design.

Fig. 2. Magog bridge deck reinforced with FRP bars (Canada 2002)

Gamal et al. (2005) investigated the structural performance of edge restrained concrete bridge deck reinforced with GFRP and CFRP bars under concentrated loads. They studied six full-scale deck slabs 3000 × 2500 mm wide and 200 mm thick. Three slabs were reinforced with GFRP, two with CFRP, and the remaining one with conventional steel as a control specimen. The deck slabs were supported on two steel girders spaced at 2000 mm center-to-center and were subjected to a monotonic single concentrated load acting on the center of each slab. Punching shear was reported as the governing failure mode for all of the specimens. Load capacity of the deck was found to be larger than three times the design factor load stipulated by CHBDC. The maximum measured deflection was reported less than 1.5 mm which is well below the allowable

code limit. A new empirical equation for punching shear capacity was proposed and proved to be in good agreement with experimental test data.

Dulude et al. (2010) conducted experimental tests on five large-scale two-way slabs four of which were reinforced with GFRP bars and the remaining one with conventional steel as a control specimen. The slabs were 2500 × 2500 mm wide and 200 or 350 mm thick along with a column stub 300 × 300 or 450 × 450 mm which was extended 300 mm above and below the slab. The edges of the slab were free to rotate and restrained against displacement. They generally concluded that there was no significant difference between the test specimens in terms of overall behavior and mode of failure. However, replacing the steel bars with GFRP bars reduced the punching strength with about 32%. It was also concluded that ACI 440.1R 2006 provides a very conservative prediction of punching shear resistance, about 54% of the experimental result, but JSCE (1997) resulted in good predictions about 93% of the actual value.

Rahman et al (2000) tested a full-scale two-way bridge deck slab measuring 6000 × 6000 × 185 mm, reinforced with carbon fiber reinforced polymer (CFRP) mesh. The slab specimen rested on three support steel beams and was connected through the shear studs, and formed two continuous spans, each 2000 mm long, and two overhangs on both sides, each 1000 mm long. The slab was tested under two wheel loads simultaneously applied on the adjacent interior spans which typically. The failure mode was found as punching shear at a load level of larger than five times the maximum design wheel load. The deflection under service load level was small and the overall behavior of the slab was reported satisfactory. The double-wheel load was the only load case under which the failure of the slab was investigated. Single concentrated load or axle load on the interior span as well as the overhang was not considered in this study. Hassan et al. (2000) similarly investigated the behavior of two full-scale two-way FRP RC slabs representative of a portion of a highway bridge deck slab. The specimens were tested under only single concentrated loads and punching shear was observed as the governing failure mode. The load capacity was reported much higher than the ultimate design code.

Mander et al. (2009, 2010, 2011) conducted experimental tests on full-depth precast concrete overhang panels, for bridge deck application, to investigate the load capacity, failure modes, cracking pattern, and load-deformation behavior. Two full-scale bridge decks were constructed of 100 mm SIP (stay-in-place) bottom panels and 100 mm CIP (cast-in-place) topping deck prestressed and reinforced with conventional steel, respectively. The bridge deck was tested under different concentrated load cases and it was observed that the full-depth precast overhang failed in a different mode compared to conventional CIP deck overhang. The load capacity was also reduced by about 13%. This reduction was reported to be attributed to the partial depth panel-to-panel connection. Yield line theory was modified to account for the development length of the mild steel reinforcing at overhang. Failure of the full-depth panels was found to be influenced by the partial-depth transverse panel-to-panel seam. Hence, the modified yield line theory was coupled with panel-to-panel shear interaction. The analytical results were reported within 1-6% of experimental results for critical cases showing the high accuracy of the modified yield line theory. They concluded that flexure is the governing mode of failure in concrete bridge deck overhangs. For interior spans, a compound shear-flexural failure was recognized as the governing failure mode where the CIP panel failed in punching shear and the SIP panel failed in flexure. The results of failure load analysis were reported to be within 2% accuracy of the experimental results. It was also shown that AASHTO LRFD (2007) punching-shear formula underestimates the load capacity by 20-25% for critical load cases. Although the full-scale experimental specimens were reinforced and prestressed with conventional steel, they are selected as the control specimens of the current research project.

The research background shows the lack of experimental and analytical studies on full-scale FRP concrete bridge deck slabs where the dimensions, boundary conditions, structural details, and load configuration are all realistically taken into consideration. Under such circumstances, the experimental outcomes can be reliably used to establish a design methodology, which is one of the major objectives of this research project.

3. UNIAXIAL CHARACTERISTICS OF ARAPEE BARS FOR PRESTRESSING APPLICATION

3.1 Introduction

As already discussed, corrosion-induced deterioration of reinforced concrete is degrading the serviceability of the infrastructure in the United States, particularly bridges. This is a serious concern as the economy of the US is greatly tied to its transportation system. Of the total 587,964 bridges in the US, 14% are in serious need for rehabilitation due to corrosion issues (NCHRP 2006) which requires a huge budget spent yearly. Fiber reinforced polymer (FRP) composite bars which are inherently corrosion resistant have been employed in place of conventional steel since the past couple of decades to overcome corrosion problems and to obviate the need for costly repair and replacement programs. FRP bars have a large tensile strength-to-weight ratio and are typically manufactured in three types named AFRP, CFRP, and GFRP where the fibers used in matrix are aramid, carbon, and glass, respectively. Compared to other two types of FRPs, AFRP bars have good fatigue and creep-rupture characteristics, considerable tensile strain capacity, and reasonable price which make them an appealing substitute for conventional prestressing steel (Trejo et al. 2000). However, further experimental research on uniaxial characteristics of AFRP bars needs to be conducted by virtue of which analysis and design can be more reliably carried out. Such experimental research should include the tensile test where the ultimate stress and strain as well as modulus of elasticity can be found, testing the load capacity of the anchorage system, tension stiffening test to find the post-cracking tensile strength of the reinforced concrete, creep test to reveal the reliable level of prestressing during the lifetime of the structure, and relaxation test to determine the relaxation loss during the time.

Experimental research on creep-rupture characteristics of AFRP bars have shown a linear relationship between the creep-rupture strength and logarithm of time where the 50-year creep-rupture strength can be readily extrapolated. The creep-rupture strength is

typically defined as the ratio of stress at failure to the ultimate stress, which has been reported for AFRP bars equal to 0.5 (Taerwe 1995), 0.47 (Yamaguchi et al. 1997), 0.66 (Ando et al. 1997), and 0.6 (Dolan et al. 2001) for a 50-year duration. Based on these experimental results, a range of 0.45-0.65 for creep-rupture strength of AFRP bars seems to be a reasonable assumption. ACI 440.1R (2006) applies a safety factor of 1/0.6 to the existing experimental data and recommends an allowable sustained stress level equal to 0.3. Similar creep-rupture studies on AFRP bars with 6 mm diameter was conducted by Mukae et al. (1993) at different stress levels where the creep-rupture strength for 100-year lifetime was reported 61%, approximately.

McKay and Erki (1993) studied the relaxation of AFRP tendons and reported 10-12% prestressing loss due to relaxation for a 50-year duration. Ando et al. (1997) conducted similar tests and found the relaxation of AFRP bars between 5-8% after 1000 hours, and between 11-25% for 50-year duration depending on the initial prestressing. Increasing the temperature was reported as an influential factor that increases the relaxation loss. Saadatmanesh and Tannous (1999) tested the relaxation of AFRP bars, ARAPREE type, and found that the relaxation loss in a 50-year duration, when the specimen is exposed to air, is between 8-11% and 9-14% for 40% and 60% initial prestressing, respectively. Similarly, the raise in temperature resulted in increase of relaxation loss.

In spite of ongoing research on mechanical characteristics of AFRP bars, there is still limited experimental data available where the existing inconsistencies in test procedures and results raise the need for further research. Variations in the FRP manufacturer's products add more difficulties given seemingly in consistency of results since the behavior of FRP bars can readily change depending upon the type of fiber or resin. In this research, the AFRP bar, named ARAPREE, with 10 mm diameter is selected and comprehensive experimental tests including uniaxial tensile test of bare bar, load capacity test of the anchorage system, tensile test of bar embedded in concrete so called tension stiffening test, creep test, and relaxation test are conducted. For creep and

relaxation tests, the ARAPREE bar is embedded in concrete to mimic the actual surrounding environment and the test runs during 1000 hours for 50 and 60% initial prestressing, which is basically considered as a long-term test. The experimental outcomes of this study are aimed to provide a reliable data for prestressing application of ARAPREE bars as an alternative for conventional prestressing steel.

3.2 Tensile Tests of Bare Bars

Six ARAPREE bar specimens with 10 mm diameter and 1420 mm length were tested under uniaxial tensile load. The anchorage system consisted of steel pipes with 457 mm length, 48 mm diameter, and 5 mm wall thickness, which were filled with an expansive and quick setting grout named Shep Rock. The anchorage steel pipes were gripped by the jaws of a 250 kN MTS machine where the load was monotonically applied with the rate of 22 kN per minute, according to ASTM D638 (2008). The applied load was recorded via a load cell connected to the MTS machine and the elongation of the specimen was measured through strain gages mounted at the middle of the bar. For all the specimens a quasi linear stress-strain relationship was achieved and the bar ruptured in a brittle and sudden fashion (Fig. 3). No local failure was observed at the anchorage system indicating a full grip of the bar inside the pipe. The experimental results are summarized in Table 1 in terms of ultimate stress, strain capacity, and elastic modulus where the mean and standard deviation are presented. The standard deviation is calculated using the unbiased estimator where the degree of freedom is deemed equal to the number of samples minus one. The mean of elastic modulus and strain capacity are equal to 69 GPa and 0.02 mm/mm, respectively, with small standard deviations. Given a linear stress-strain relationship, the dependable value for ultimate stress can be calculated as $69000 \times 0.02=1380$ MPa, which is very close to the lower bound of 95 percent confidence interval equal to 1457-63.4=1393.6 MPa. According to ACI 440.4R (2004), the longitudinal tensile strength of ARAPREE, is expected to be between 1200 and 1500 MPa, the modulus of elasticity between 62 and 64 GPa, and the maximum longitudinal strain about 0.024. It is seen that, the tensile strength and strain capacity are

in the expectable range, however the elastic modulus is larger than what has been suggested, 62-64 GPa. According to ASTM A416, the stress-relieved 7-wire strands (Grade 270) have the ultimate strength 1860 MPa, elastic modulus 186 GPa, and strain capacity 0.04. The strands are typically prestressed up to 70-75% of the ultimate strength where the yielding is at 85% of ultimate strength corresponding to the strain 0.01. Comparison shows that the ultimate strength, strain capacity, and elastic modulus of ARAPREE bar with 10 mm diameter are about 75%, 50%, and 37% of that of prestressing steel strands, respectively.

Table 1- Tensile test results

Specimen	Ultimate stress (MPa)	Strain capacity (mm/mm)	Elastic modulus (GPa)
1	1549.9	0.022	70.4
2	1448.2	0.021	68.9
3	1431.3	0.021	68.2
4	1358.8	0.021	64.7
5	1464.2	0.021	69.7
6	1489.1	0.020	74.4
Mean	**1457**	**0.021**	**69.38**
Standard deviation (unbiased estimator)	**63.4**	**0.0006**	**3.16**

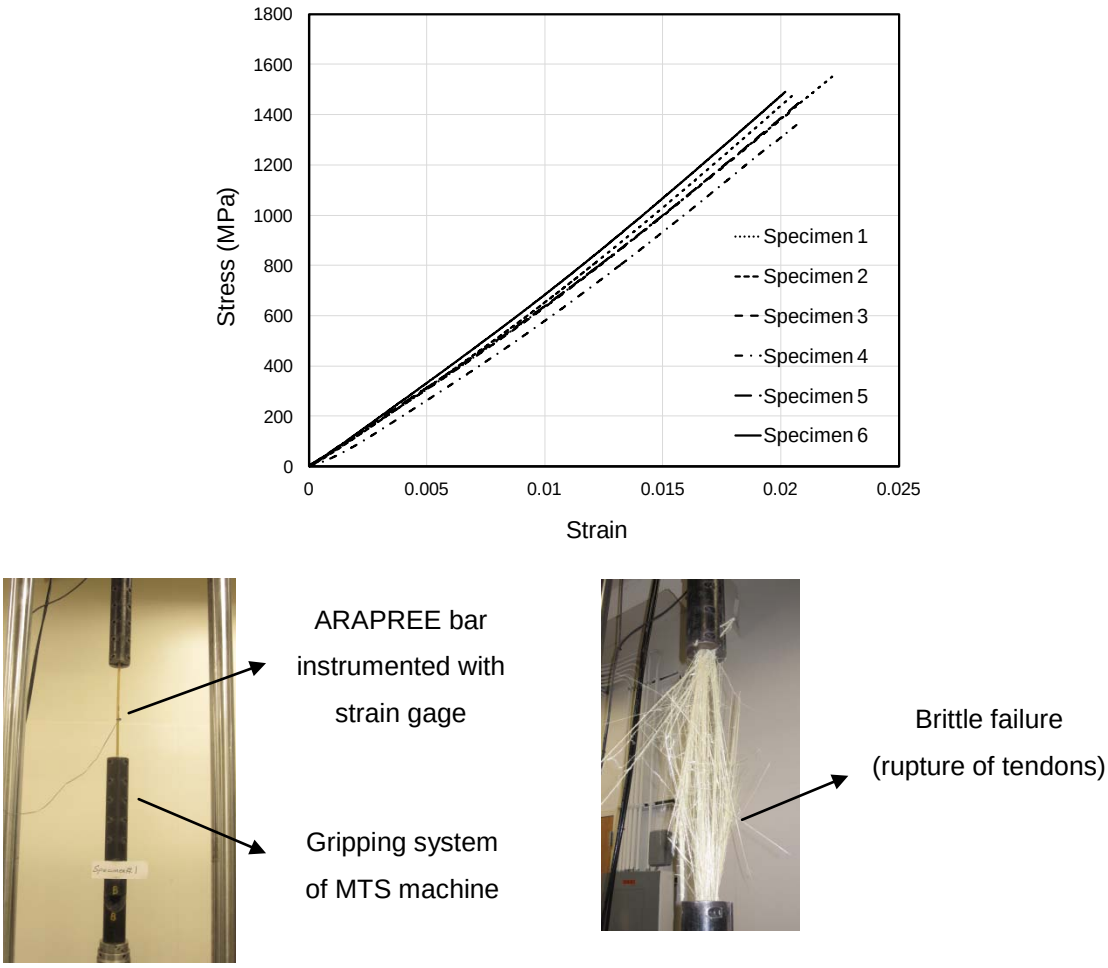

Fig. 3. Tensile test of ARAPREE bars (Medina 2011)

3.3 Load Bearing Capacity of the Conventional Anchorage System

The conventional anchorage system fabricated by the manufacturer was tested with the same procedure as employed for the tensile test to find the load capacity and failure mode. An applicable and reliable prestressing anchorage system should be capable of sustaining the prestressing load for a long period of time without causing a major loss or premature failure. The conventional anchorage system consisted of hard plastic wedges and steel casing. Five specimens were tested and it was observed that all the ARAPREE bars locally failed at the anchorage location in a very sudden and brittle fashion. As

presented in Table 2, the mean failure stress is equal to 1024 MPa which is about 70% of the mean tensile strength. The reason for such a premature and local failure was further investigated and it was found that the plastic wedge causes a stress concentration due to applying transverse stresses when gripping the bars. These transverse stresses tend to crush the bar and cause a premature failure since the AFRP bars are not strong in the transverse direction. This is the reason why the potted anchorage systems with materials like resin, non-shrink cement, expansive cement, or epoxy, where the tensile force can be transferred through a uniformly distributed longitudinal stresses, are commonly preferred over the conventional anchorages (ACI440.4R 2004). Fig. 4 shows the failure of the ARAPREE bar close to the anchorage. Although the load capacity of the conventional anchorage system seems to be above the typical prestressing range, say between 50-60% of the tensile strength, the margin of safety is not large enough to represent a reliable system. Furthermore, the anchorage system should be capable of sustaining the prestressing load for a long period required to conduct the creep and relaxation tests. To investigate the sustainability, the anchorage system was subsequently tested under a sustained load equal to 55% of the tensile strength. The experimental results showed that after about 20 hours a local failure occurred at the anchorage indicating the incapability in sustaining the prestressing load. Comprehensive experimental tests on conventional anchorage system can be found in Medina (2011). The results confirm the need for another anchorage system to prestress the AFRP bars for creep and relaxation tests.

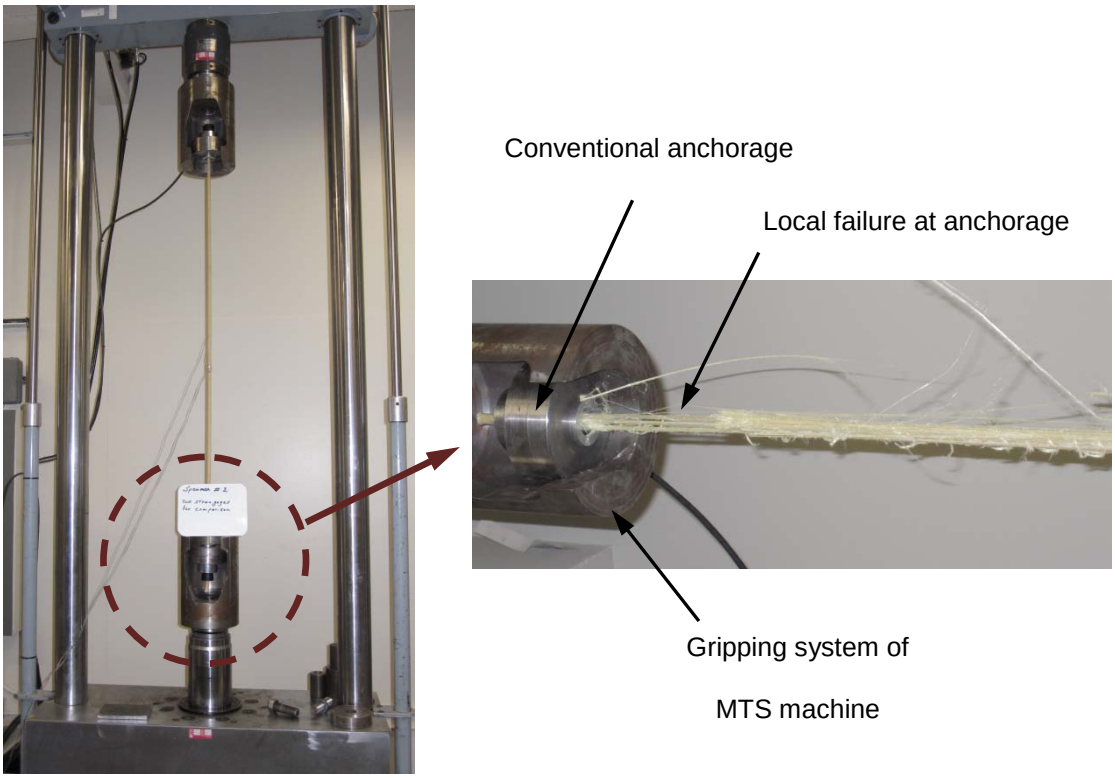

Fig. 4. Load bearing capacity test of conventional anchorage (Medina 2011)

Table 2- Results of the tensile tests using the conventional anchorage system

Specimen	Failure stress (MPa)
1	1030
2	1010
3	1006
4	1058
5	1015
Mean	**1024**
Standard deviation (unbiased estimator)	**21**

3.4 Prestressing Operation

The challenging step in prestressing the AFRP bars is designing a reliable anchorage system that can reach to the desirable load level and sustain the load for a long period of time without causing a major loss or premature failure. As discussed, the conventional anchorage system failed to provide an applicable and reliable prestressing system. In this research, an anchorage system is designed for the relaxation and creep tests in place of the conventional anchorage system. As shown in Fig. 5, the anchorage is basically composed of a steel pipe with 457 mm length, 48 mm outer diameter, and 5 mm wall thickness filled with an expansive and quick setting grout called Shep Rock. This grout is mainly used for demolishing purposes by injecting to the cracks of massive rocks. The final set of Shep Rock grout takes 45 min at 75°F degree and it can reach to a compressive strength over 69 MPa in one day. The bar is passed through the center of the pipe and held by plastic stoppers, which have a central hole, at both ends of the pipe. There are two holes on the pipe's surface which allow for injecting the grout. The grout is poured through the first hole until it comes out from the second one to ensure that there is no air bubble entrapped inside the pipe. The plastic stoppers close the both ends of the pipe and prevent leakage of the grout. The walls of a concrete block are used as the dead and live ends of the prestressing frame. The anchorage at the dead end is first casted and left to be set. The live end includes two pipes in front and back of the hydraulic jack that has a central hole allowing the bar to pass through it. The front pipe is first filled with grout and then after three hours, based on the preliminary tests, the hydraulic jack can be pumped to push the front pipe, while seating on the rear pipe. This action pulls the AFRP bar until reaching to the desirable level of prestressing where the rear pipe is injected with grout to lock the bar. After three hours, when the bar is fully gripped inside the pipe, the hydraulic jack is released and the rest of the bar in front of the jack is cut in order to be able to move the jack. The instrumentation includes a load cell placed between the pipe and concrete block to measure the load, an LVDT (linear variable differential transformer) attached to the end of the bar extended out from the grouted pipe to measure the slippage of the bar, and the strain gages mounted on

ARAPREE bar to record the change in strain. The preliminary tests showed a successful prestressing up to 60% of the bar capacity where the anchorage was capable of sustaining the load for a long time without a significant prestressing loss or a local failure. The prestressing loss was recorded with a high frequency and it was observed that the total loss during a 100 hours period is less than 5%. The rate of prestressing loss during the first 20 hours is more pronounced and then a slighter rate is seen, Fig. 6. Considering the large load capacity of the 450 mm long grouted pips, observed in the tensile test, and the sustainability of the prestressing load confirmed by this test, the prestressing system and test setup shown in Fig. 5 is selected to conduct the creep and relaxation tests.

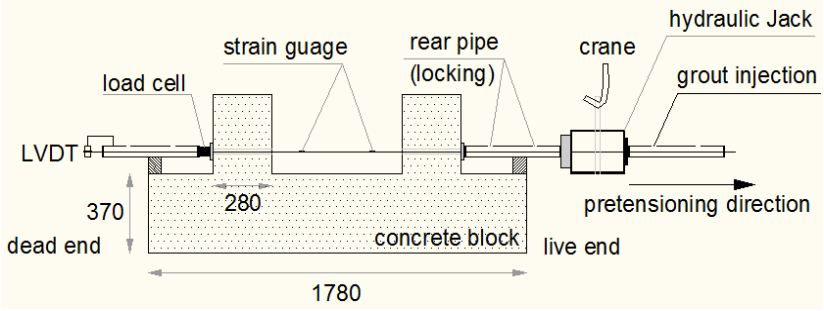

Fig. 5. Preliminary test of prestressing system

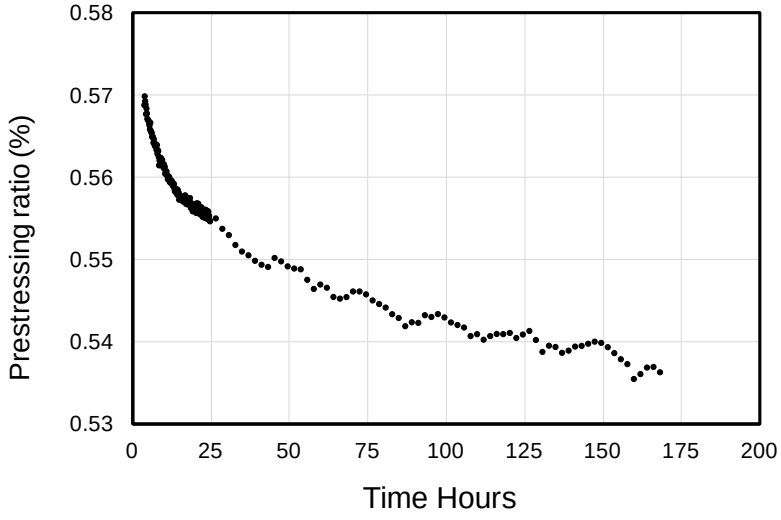

Fig. 6. Prestressing loss (initial prestressing 60%)

3.5 Tension Stiffening Test

Tension stiffening is the ability of the concrete to carry tension between the cracks, which increases the post-cracking stiffness of the cracked member. The modulus of elasticity of the reinforcement affects the tension stiffening characteristics of the reinforced concrete beams. Pirayeh Gar et al. (2012) have shown that the tension stiffening effect in fully prestressed concrete beams is negligible. However, in order to study the tension stiffening effect in non-prestressed concrete sections reinforced with ARAPREE bars, six concrete specimens measuring 1000×76×76 mm reinforced with one ARAPREE bar at the center were selected to test under uniaxial load. The same anchorage system as for the tensile test was used at both ends of the specimen and connected to the 500 kN MTS machine. The load was applied in a displacement control mode with a rate of 0.25 mm per minute, and measured with a load cell attached to the top jaw of the MTS machine. The total elongation of the concrete specimen was measured using two LVDTs with 800 mm gage length on both sides of the specimen which helped to remove the possible bending effects on data recorded. The experimental test setup and cracking pattern of the specimens are shown in Fig. 7.

Fig. 7. Test setup and cracking pattern in tension stiffening test

The total uniaxial tensile force applied to the specimen is indeed resisted by the concrete section and the ARAPREE bar as well. Given the elastic modulus of the bar and the elongation of the specimen, the axial force developed in the bar is calculated, and if deducted from the total load, the axial load resisted by the concrete section can be subsequently determined. The tensile stress carried by the concrete section versus the elongation of the specimen, for specimen 1, has been shown in Fig. 9(a). In this figure, the vertical axis represents the tensile stress normalized to the cracking stress and the horizontal axis indicates the member strain. The following equation is proposed by Bischoff and Paixao (2004) to predict the tension bearing capacity of FRP reinforced concrete, f_t, in terms of the tensile strain demand, ε_c, which is used to compare with the experimental results

$$f_t = f_{cr} \exp[-1100(\varepsilon_c - \varepsilon_{cr})(E_f / E_s)] \quad (1)$$

where ε_{cr} is the strain corresponding to the tensile strength of the concrete f_{cr}, and E_f and E_s are the modulus of elasticity of FRP bars and steel rebar, respectively. Based on the

tensile test results, the assumption of $E_f / E_s = 1/3$ is made. As shown, a good agreement is seen between Eq. (1) and experimental results. For some of the specimens, longitudinal cracks at both ends were observed which indicates the debonding of the reinforcing bar and concrete. For all the specimens, there is a distinct change in slope of the tension stiffening diagram representing a strain at which the cracks stabilizes. The results of tension stiffening test is summarized in Table 3. As presented, the average crack spacing s=114 mm, the strain when cracks are stabilized ε_{st}=0.003, and the strain when the tension bearing capacity of the concrete reaches to zero ε_0=0.007. Therefore, the tension stiffening behavior can be characterized as shown in Fig. 8(a). According to Bischoff and Paixao (2004), ε_{st} and ε_0 for steel reinforced sections are about 0.0008 and 0.002, respectively, which are considerably smaller than that of ARAPREE reinforced specimens, as illustrated in Fig. 8(b). The reason is ARAPREE bar with a lower modulus of elasticity over the conventional steel, acts as a softer spring between the cracks and hence requires a larger deformation to transfer the same amount of force to the concrete section as compared to the steel reinforced concrete section.

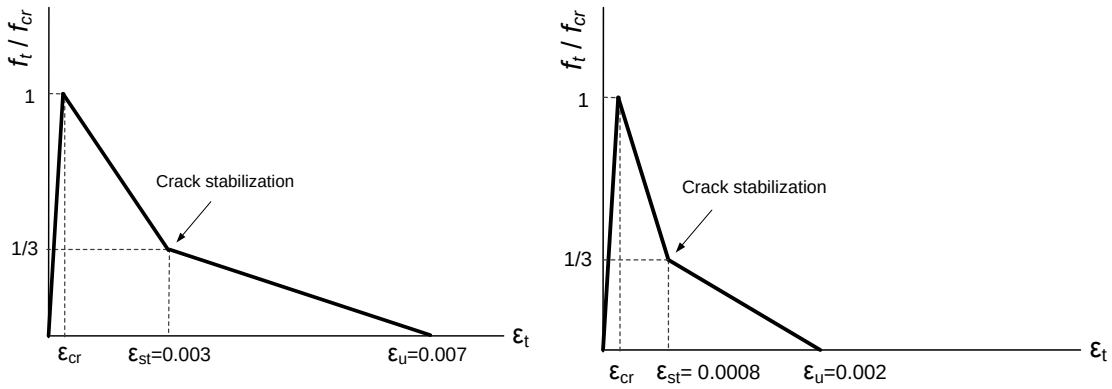

a) ARAPREE bars *b) conventional steel*

Fig. 8. Characterized tesnsion stiffening behavior

Table 3- Results of tension stiffening test

Specimen	ε_{st}	ε_0	s (mm)
1	0.0025	0.008	124
2	0.0040	0.006	107
3	0.0035	0.007	90
4	0.0027	0.007	102
5	0.003	0.007	114
6	0.0027	0.008	144
Mean	**0.003**	**0.007**	**114**

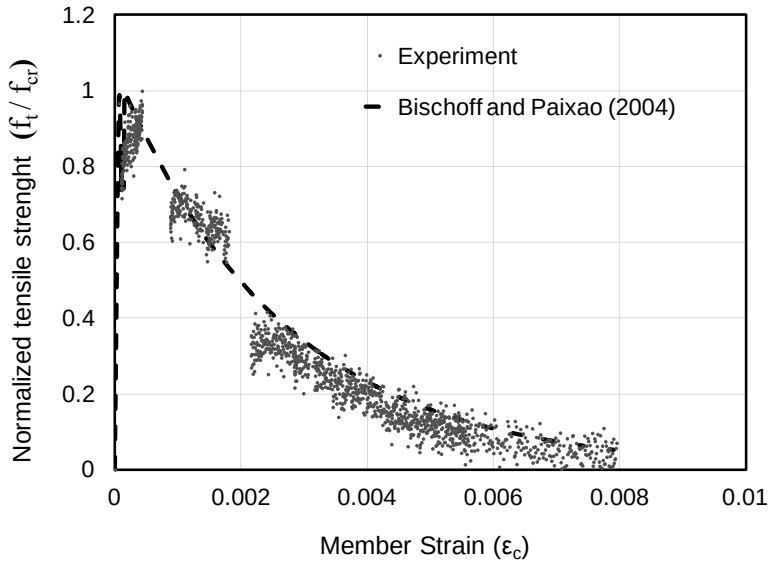

a) tensile strength of the reinforced concrete

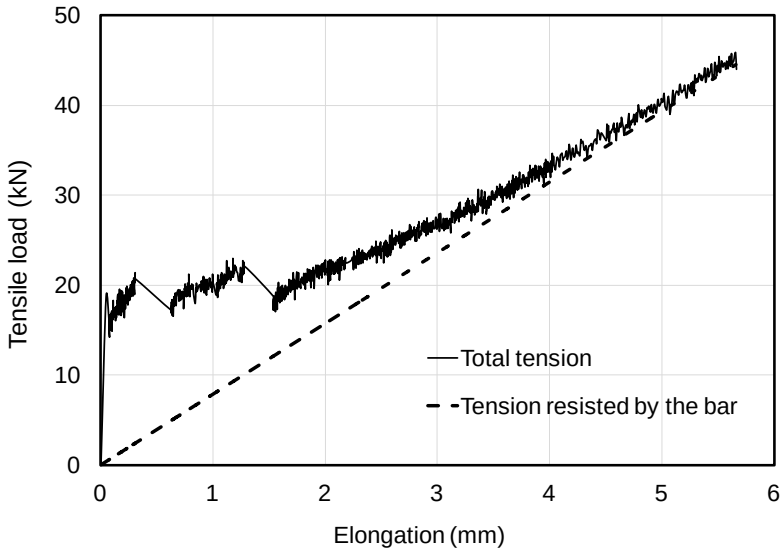

b) tensile strength of the whole specimen

Fig. 9. Tesnsion stiffening behavior (Specimen 1)

3.6 Long-Term Relaxation Test

Six ARAPREE bars each 2210 mm long were tested to study the relaxation during a 1000 hours period where the loss in stress at constant strain was supposed to be measured. Three specimens were prestressed up to 50% of the tensile strength and the other three were prestressed up to 60%. As explained, the grouted steel pipes were used as the anchorage system for prestressing. After 70 hours, the concrete was poured and the prestressed bar was embedded in concrete to mimic the actual surrounding environment (Fig. 10). To measure the total prestressing loss, load cells were installed at the dead end between the concrete block and anchorage system. The total loss was indeed composed of relaxation of the bar, slippage of the bar inside the grouted pipe, and increase in strain due to creep. Therefore, the loss due to slippage and creep need to be deducted from the total loss to find the net relaxation loss. To measure the loss due to slippage, an LVDT was installed at the live end, where the bar was extended out from the anchorage pipe. The LVDT recorded the slippage of the bar inside the grouted pipe, thereby the strain released could be measured and converted to the stress lost. To find the creep strain, the prestressed bar was instrumented at the middle with a strain gage protected from the rough concrete environment by a special coating material consisting of a microcrystalline wax, Butyl rubber tape, and epoxy resin. In fact, the slippage of the tendon is also reflected in the value that the strain gage shows and should not be doubly accounted for. LVDTs, load cells, and the strain gage were all connected to a DAQ (data acquisition system) that recorded the data every 30 minutes.

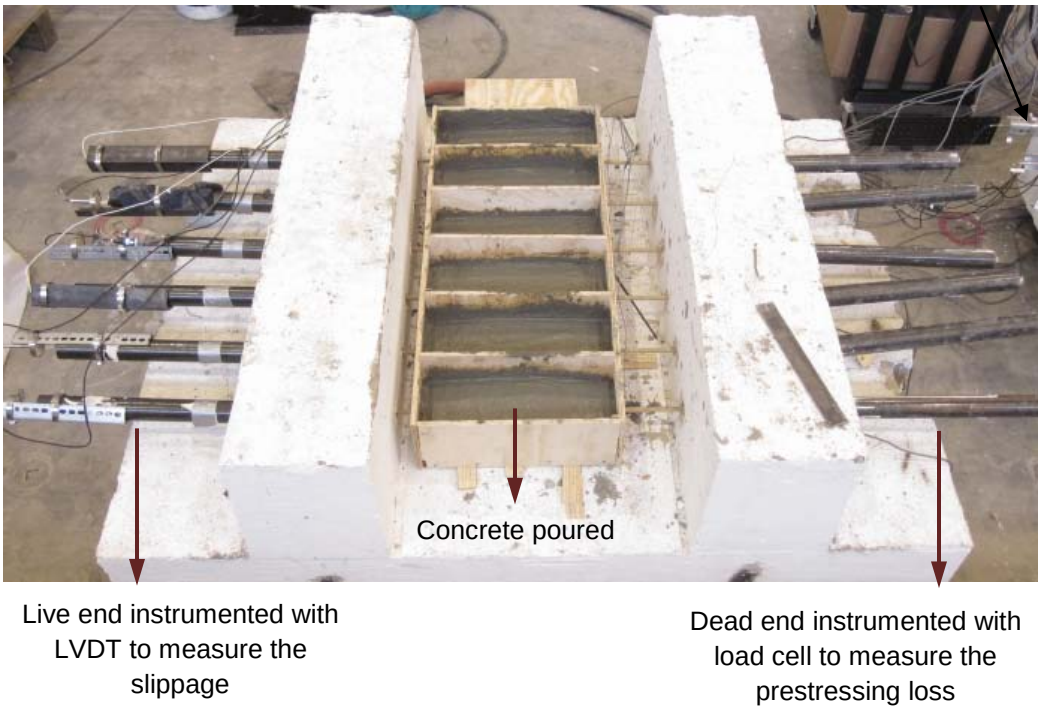

Fig. 10. Relaxation test setup

The relaxation loss diagrams have been shown in Figs. 11(a) and 11(b) in a log scale for initial prestressing level of 50% and 60%, respectively. The graphs imply an approximate bilinear trend between the relaxation loss and logarithm of time. For both groups of specimens, the relaxation rate increases after 20 hours. The average of relaxation loss for 50% initial prestressing is about 7.5%. For Specimen 5, at the zone between the concrete specimen and anchorage system, some surface cracks on the fibers of the ARAPREE bar was observed which caused a larger loss compared to Specimens 4 and 6. This might be due to rubbing the bar against the concrete block when prestressing operation. The average of relaxation loss for Specimens 4 and 6, where the initial prestressing is 60%, is equal to 9.7%. The experimental results show that the increase in initial prestressing raises the relaxation loss. For example, comparison between Specimens 1 and 4 at 100 hours reveals the change in relaxation loss from 47.7% to 56%. If the test was extended beyond 1000 hours, the relaxation would be expected to

converge to a constant value. Based on the experimental results, it can be concluded that for 1000 hours period, the relaxation loss varies between 6-10% depending upon the initial prestressing ratio. The summary of the long-term relaxation test is presented in Table 4. Pouring the concrete after 70 hours seems not to have any effect on the rate of relaxation loss. The data recorded confirmed that more than 90% of the whole prestressing loss is induced by the relaxation and the share of creep and slippage is very small. The typical relaxation of stress-relieved steel strands at 1000 hours is between 8-12% depending on the initial stress ratio ranged from 70-80% (Naaman 2004), which shows that the ARAPREE bars and prestressing steel strands are very similar from relaxation view point.

Table 4- Results of long-term relaxation test (1000 hours)

Specimen	Initial prestressing (%)	Relaxation loss (%)	Average relaxation loss (%)
1	49.4	5.5	7.5
2	47.5	9.2	
3	49.7	8	
4	57.5	10.2	9.7
5	57.8	14.6	
6	55	9.3	

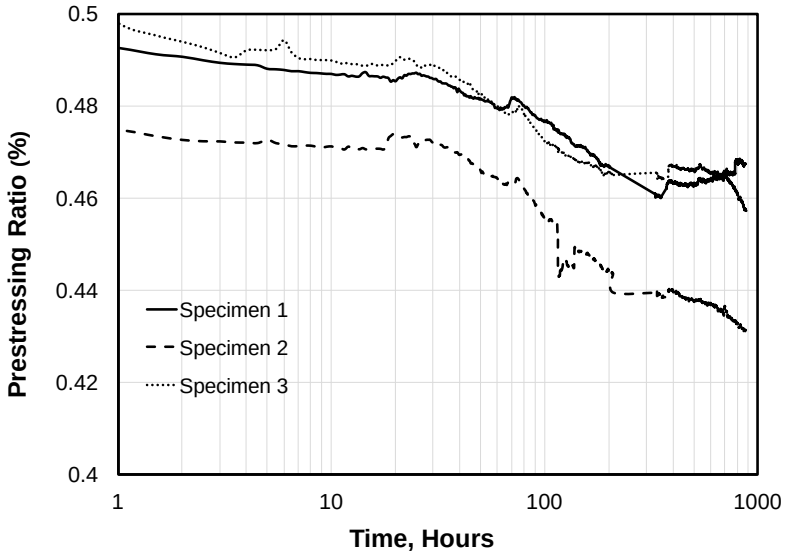

a) 50% initial prestresing

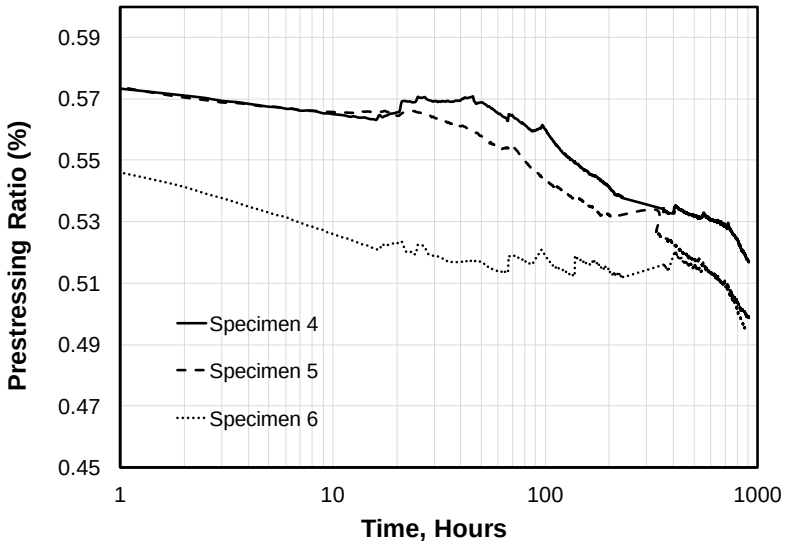

b) 60% initial prestressing

Fig. 11. Prestressing loss due to relaxation for different levels of initial prestressing

3.7 Long-Term Creep Test

Similar to the relaxation test, six ARAPREE bars each 2388 mm long were selected for creep test to measure the increase in strain at constant stress. The major difference between the test setup of the relaxation and creep test was using disc springs (Belleville washer) for each bar at the dead end between the pipe anchorage and concrete block, as shown in Fig. 12, which helped to keep the load constant. A flat steel plate was used between the spring and load cell to allow for a better seat of the anchorage pipe. LVDTs were connected to the end of the bars extended out from the anchorage at the live end to measure the possible slippage of the bar inside the pipe. Each bar was instrumented at the middle with a strain gage to measure the change in strain after prestressing. All the instrumentations were connected to DAQ where the data were recorded every 30 minutes. Three specimens were prestressed up to 50% of the tensile capacity and the other three were prestressed up to 60%. The concrete was poured about 70 hours after prestressing and the creep deformation was measured during a 1000 hours period. The initial prestressing ratio was limited and not expected to lead to rupture and the test was basically considered as a long-term creep test. Creep deformation was basically composed of three phases: primary, secondary, and tertiary, as shown in Fig. 13. The primary phase starts with high strain rate and quickly converges to a constant strain rate, so called secondary phase, which is typically the longest phase. If the prestressing is very high, the secondary phase is followed by the tertiary phase where the strain rate starts to considerably raise resulting in rupture of the bar. As shown in Fig. 14(a), for the first three specimens with 50% initial prestressing, the primary phase almost lasts 200 hours with about 1.5% increase in strain. At the end of 1000 hours almost 4% increase in strain is observed, however the secondary phase is not fully developed during this time as no sign of considerable increase in strain rate implying the tertiary phase is seen. For Specimen 1, the data is only available for 700 hours due to sudden slippage of the bar inside the grouted pipe. For specimens prestressed to 60%, the primary phase is about 150 hours. For Specimens 5 and 6, sudden slippage of the bar inside the grouted pipe happened after 150 and 350 hours, respectively, and hence the secondary phase could

not be well captured. Similarly, the Specimen 4 failed due to slippage of the bar after 550 hours resulting in 6.5% increase in strain. The summary of the long-term creep test is presented in Table 5. As the spring holds the load almost constant and prevents the drop in load, the slippage of the prestressed bar inside the potted anchorage is more critical compared to the relaxation test where the drop in the load is allowed. Therefore, a longer pipe is recommended for creep test. Comparison between Specimen 1 and 4 after 500 hours shows that changing the initial prestressing from 50% to 60% raises the change in strain from 3.5% to 6.5%. The experimental results confirm that within 50-60% range of initial prestressing, the tertiary phase is very unlikely to be achieved during 1000 hours. However, ACI 440.1R (2006) considers a safety factor of 1.67 and limits the allowable sustained stress to 30% which is very low compared to existing experimental results.

Fig. 12. Creep test setup (dead end)

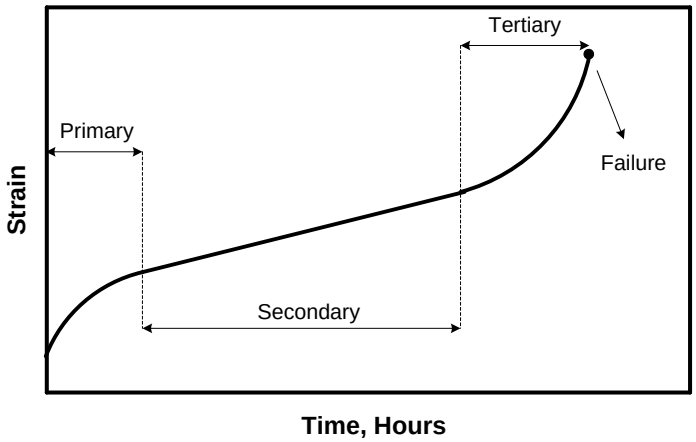

Fig. 13. Three stages of creep deformation

Table 5- Results of long-term creep test

Specimen	Initial prestressing (%)	Duration (hours)	Raise in strain (%)
1	50	700	4
2	50	1000	4
3	50	1000	3.5
4	60	550	6.5
5	60	100	1.4
6	60	200	4.5

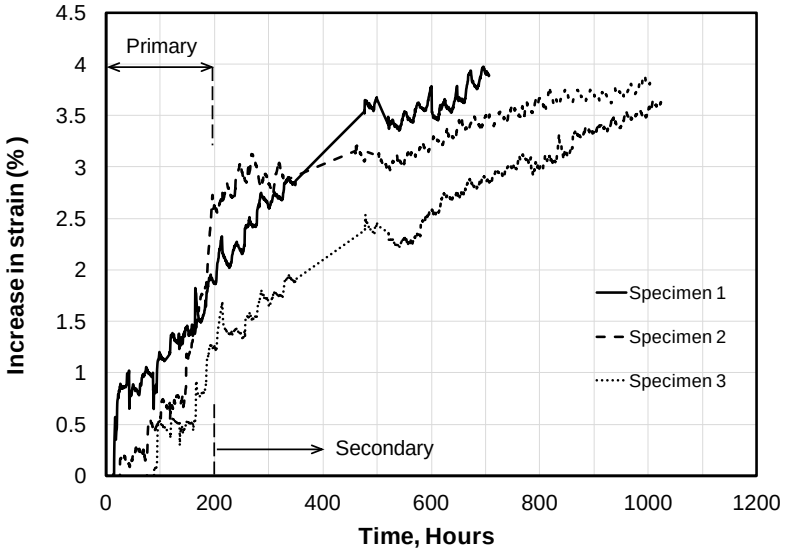

a) 50% initial prestresing

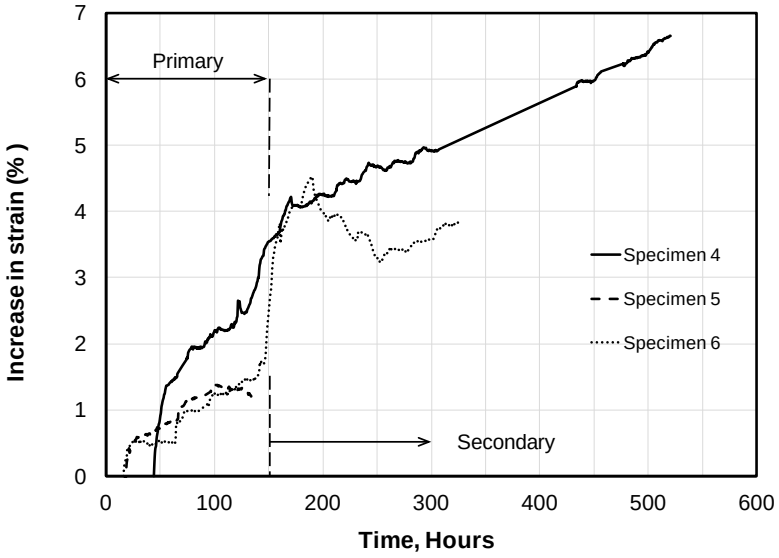

60% initial prestresing

Fig. 14. Increase in strain due to creep

It should be noted that between 300 and 450 hours the data was not recorded by DAQ which has been shown with a straight line in Fig. 14.

3.8 Short-Term Creep Test

To study the short-term creep response, creep test was repeated with higher levels of initial prestressing load. The test setup and instrumentation was exactly the same as the tensile test. Five specimens were tested with 80 and 85% initial prestressing, however the slippage problem occurred for two of the specimens and terminated the test. As illustrated in Fig. 15, for the specimen with 80% initial prestressing, the primary phase of creep deformation lasted around 2.5 hours and the tendon ruptured after about 11 hours. For the first specimen with 85% initial prestressing, the primary phase of creep deformation lasted about 1 hour and the specimen failed around 3 hours. For the second specimen prestressed up to 85%, step wise rupture of the fibers was observed and the tendon suddenly failed after 2 hours. The experimental results show that the initial prestressing significantly affects the creep-rupture strength of the ARAPREE bars.

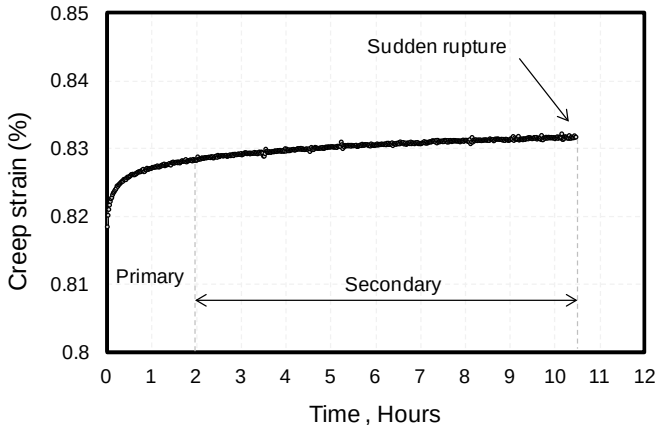

a) 80% initial prestressing

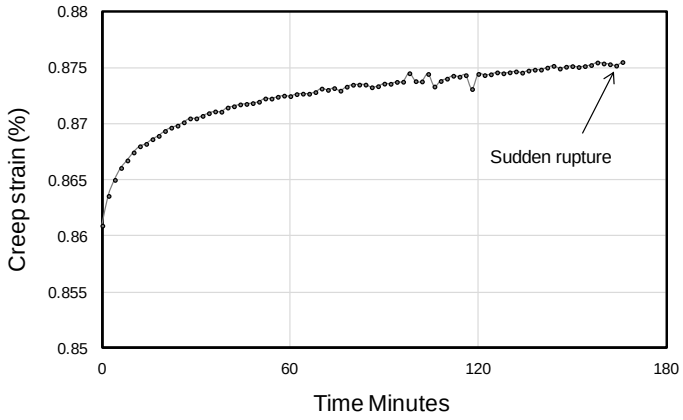

b) 85% initial prestressing

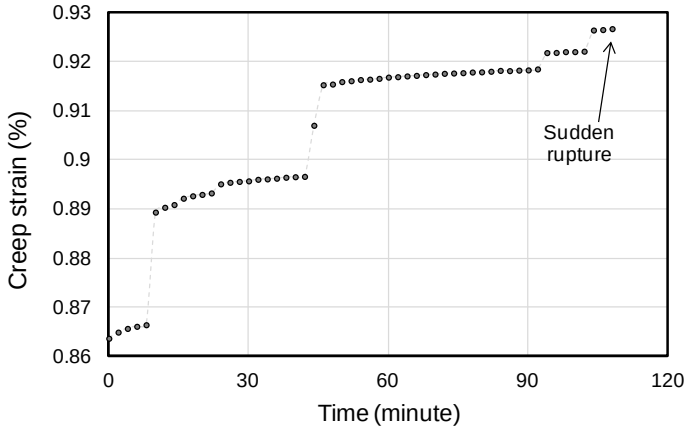

c) 85% initial prestressing

Fig. 15. Short-term creep test

3.9 Conclusions

Uniaxial characteristics of ARAPREE bar, as a type of AFRP, with 10 mm diameter was experimentally evaluated. The experimental tests included uniaxial tensile test, performance test of anchorage system, tension stiffening test, long-term relaxation test, long-term creep test, and short-term creep test. The following conclusions are drawn from this study:

1- The uniaxial tensile test on six ARAPREE bars showed the following dependable values which can be used for analysis and design purposes: modulus of elasticity E=69 GPa, strain capacity ε_u=0.02, and the tensile strength f_u=1380 MPa. The modulus of elasticity found is somewhat larger than the range suggested by ACI 440.4R (2004), 62-64 GPa. The ends of each bar were anchored through steel pipes filled with expansive grout. During the test no local failure was observed at the anchorage location and the bar eventually failed in a sudden and brittle fashion due to rupture of the tendons.

2- The conventional anchorage system was used for another set of uniaxial tensile test. The mean failure stress was found 990 MPa, about 67% of the tensile strength of the bar, which is larger than the typical range of 50-60% for prestressing, but with a very low safety margin. Further tests on specimens with 50% prestressing to study the sustainability of the anchorage showed that the anchorage system is not capable of sustaining the load for a short or long period of time and the specimen locally failed at anchorage after about 20 hours.

3- An anchorage system was designed for prestressing operation which consisted of steel pipes filled with an expansive and quick setting grout. The anchorage included two pipes at the live end: in front and behind the hydraulic jack. The front pipe was basically used to pretension the bar and the rear pipe was used to lock the prestressing load upon reaching to the desirable level. The preliminary

tests showed a successful prestressing up to 60% where the total prestressing loss during 100 hours was less than 5%.

4- Tension stiffening test was conducted on six specimens to study the post-cracking tensile strength of the concrete reinforced with ARAPREE bars. Tension stiffening behavior is highly dependent on the elastic modulus of reinforcement. The experimental results showed a considerable tensile strength after cracking where the average member strain at crack stabilization point was found about 0.003. The average member strain corresponding to zero tensile strength was found equal to 0.007, and the average crack spacing was equal to 114 mm. The equation proposed by Bischoff and Paixao (2004) showed a good agreement with experimental data.

5- Long-term relaxation test was conducted on six specimens prestressed to 50% and 60% for a period of 1000 hours. The average relaxation loss was found equal to 7.5% and 9.7% for 50% and 60% initial prestressing, respectively. The increase in relaxation loss as a result of higher initial prestressing was evident. In a more general conclusion, the relaxation loss for 50-60% initial prestressing was ranged between 6-10% during 1000 hours. Taking a comparative look, the relaxation loss of prestressing steel strand for 70-80% initial prestressing is typically ranged between 8-12%.

6- Long-term creep test was conducted on six specimens prestressed to 50% and 60% of the tensile capacity. The primary phase of creep strain was found almost within the first 200 and 150 hours for 50% and 60% initial prestressing, respectively. The secondary phase could not fully develop as the test was terminated at 1000 hours and the initial prestressing was not very high. For specimens with 50% initial prestressing, the average increase in strain after 1000 hours was found equal to 4%. For specimens with 60% initial prestressing, the slippage of the bar inside the anchorage pipes was found as a problem that

terminated the test before reaching to 1000 hours. Specimen 4 showed 6.5% increase in strain after 550 hours. Comparison showed that the increase in initial prestressing significantly raises the creep strain. Although ACI 440.1R (2006) uses a high safety factor and recommends the sustained stress level equal to 30%, the experimental results implies that within the initial prestressing range of 50-60%, the tertiary phase of creep strain which leads to rupture is very unlikely to occur.

7- Short-term creep test was also conducted on five specimens with 80% and 85% initial prestressing. Two specimens failed due to slippage and did not end up with desirable results. The results gained from the other three specimens revealed a sudden rupture after couple of hours.

8- Based on the experimental results, initial prestressing higher than 60% is not recommended.

4. EXPERIMENTAL INVESTIGATION ON AFRP CONCRETE BRIDGE DECK SLAB WITH FULL-DEPTH PRECAST PRESTRESSED PANELS

4.1 Introduction

Critical infrastructure of the United States, particularly bridge decks, is deteriorating due to corrosion of reinforcing steel. Studies ascertained that 14% of the total of 587,964 bridges is structurally deficient due to corrosion issues. The cost to maintain the nation's bridges during the 20-year period from 1999 to 2019 is estimated to be $5.8 billion per year, and the cost to improve and eliminate deficiencies over the same period is evaluated to be $10.6 billion (NCHRP 2006). To put this budget into perspective, a comparison can be made with the US president's budget request, $7.4 billion, to *strengthen the nation's health & human service infrastructure & workforce* for year 2013 (NIH 2012).

In order to overcome the corrosion-related issues, FRP bars which are inherently corrosion resistant have been growingly used as an alternative for either conventional reinforcing or prestressing steel over the past couple of decades. Noticeable number of experimental laboratory research on application of FRP bars for bridge deck slabs has been conducted to this end (Gamal et al. 2005 and 2007, Rahman et al. 2000, Hassan et al. 2000, Salakawy and Benmokrane 2004a), where obtained experimental results confirm that the satisfactory structural behavior can be achieved by employing FRP bars in place of conventional steel. However, the test specimens typically do not reflect an actual bridge deck in a full-scale with realistic boundary conditions and structural details capable of revealing the real failure mode, cracking pattern, and load capacity as well as addressing the constructability issues. As a result of such experimental studies, application of FRP bars has been recently transferred from laboratory to the field. Headingley Bridge in Manitoba (Rizkalla and Tadros 1994), Joffre Bridge in Sherbrooke, Quebec (Benmokrane et al. 2004), and Magog Bridge in Quebec (Salakawy

and Benmokrane 2004b) are the examples of the cast-in-place bridge deck slabs reinforced with FRP bars. Long-term monitoring of these bridge deck slabs in terms of deflection, strain in FRP reinforcement, and cracking are typically carried out using fiber optic sensors (Benmokrane et al. 2001).

Although FRP bars seem to be successfully employed in cast-in-place bridge deck slabs, less attention has been paid to the application of FRP bars for bridge deck slabs with full-depth precast prestressed panels. In this system the precast prestressed panels are longitudinally connected through the shear keys which are typically female-to-female connections (Issa et al. 1995). The shear transfer between the panels and support girders is achieved via composite shear pockets where a mechanical connector like high strength bolts or threaded rods is embedded in the pocket. The precast panels are reinforced longitudinally, in parallel with traffic direction, and prestressed transversely, perpendicular to the traffic direction. Construction of a bridge deck slab with full-depth FRP concrete precast prestressed panels can offer a structural system with the following advantages: (1) accelerated construction, reduced on-site labor, ease in construction, and increased safety (Issa et al. 2000); (2) obviating the need for formwork and falsework to cast the overhang which is a costly, time-consuming, and at some points dangerous process (Mander et al. 2010); (3) requiring low tolerance of error in construction and placement of the panels; (4) no risk of corrosion-induced deterioration as a result of replacing the conventional steel with FRP bars, and hence increased durability and serviceability of the panels; (5) minimum need to overlap the FRP bars, thereby less material used and no concern as to flexural strength of the overlap part; (6) no need to step on the FRP grid when placement of the bars or casting the concrete and hence very low risk of damaging the bars which is a potential concern since FRP bars are not as strong as steel in transverse direction; (7) high quality control in construction stages particularly the prestressing operation; (8) mitigating the potential for cracking at negative moment regions like around the shear pockets as a result of transverse prestressing, and hence minimizing the ingress of moisture and chloride; (9) very

efficient system for possible rehabilitation program in future as it shortens the induced down time and minimizes the traffic disturbances.

On the other hand, there might be some concerns in design and construction of the bridge deck slab with full-depth FRP concrete precast prestressed panels that need to be considered: (1) shear transfer between the adjacent panels is critical to achieve a desirable level of serviceability, therefore improper design of shear key or incorrect placement of the grout resulting in voids can significantly affect the serviceability; (2) reliable and cost-effective anchorage system to prestress the FRP bars is required capable of sustaining the prestressing force for a short period of time, say 72 hours, without causing a significant prestressing loss; (3) FRP bars are brittle material so it may not be possible to bend them at precast plant, and in case of need, they should be fabricated in a bent shape; (4) long-term behavior of FRP bars such as fatigue and creep-rupture characteristics needs to be fully studied as it affects the serviceability of the deck slab.

This chapter presents the state-of-practice on AFRP concrete bridge deck slab with full-depth precast prestressed panels as an ideal structural system that can be used not only to provide an efficient construction but also to enhance the durability and long-term performance of the precast panels; thereby the serviceability of the bridge deck slab is raised. The precast panels are reinforced and prestressed with AFRP bas parallel with and perpendicular to the traffic direction, respectively. Compared to carbon or glass fiber reinforced polymer (CFRP or GFRP) bars, AFRP bars have an acceptable fatigue and creep-rupture characteristics as well as a reasonable price (Trejo et al. 2000), and hence were selected as reinforcement. All the construction stages are implemented in the laboratory environment to resemble the off-site precast plant conditions. Dimensions, boundary conditions, structural detail, and loading configurations are all realistically modeled to reflect an actual bridge deck slab where the constructability issues and structural performance can be truly evaluated. The structural performance of the bridge deck slab is investigated in terms of load capacity of the interior span and overhang,

induced deformability, deflection, cracking pattern, and failure modes. Sufficiency of the structural details such as panel-to-panel seam, and slab-to-beam connections are also evaluated. Subsequently, the results are checked according to AASHTO to see if the design code requirements are met. At the end, comparative study is subsequently conducted with the control specimen reinforced with conventional steel tested by Mander et al. (2010).

4.2 Full-Depth Precast Prestressed Panels

A full-scale bridge deck slab investigated in this research consisted of AFRP concrete precast prestressed panels (1) which were connected in the longitudinal direction through a female-to-female shear key (2). The precast panels achieve the shear transfer via composite pockets (3) where a mechanical connector, such as high strength bolts or threaded rods, is typically used inside the pocket as a shear connector (4). This connection provided a full composite action between the bridge deck slab and the support girders. As shown in Fig. 16, the AFRP bars were used to prestress (5) the precast panels in the transverse direction, and to reinforce (6) them in the longitudinal direction. The longitudinal non-prestressed bars were bent at the panel-to-panel seam, as will be discussed, in order to enhance the bond between the panels and provide adequate shear transfer which affects the overall serviceability of the bridge deck slab. To grade the bridge deck slab to the appropriate level, a haunch (7) or gap with a typical thickness ranged from 15 to 100 mm was considered between the topside of the support girder and underside of the precast panel. To implement this, compressible foam (8) was attached to the perimeter of the girder's topside with adhesive and then the precast panel was placed on this foam. The precast panel was subsequently leveled taking the advantage of leveling bolts (9) already embedded in the panel. Once the panels were leveled, the haunch was filled using a high performance grout with enough flowability, appropriate consistency, and desirable compressive strength upon hardening. To prevent grout leakage when casting the haunch, adhesive was used to attach the foam. The composite pockets can be filled with either high performance grout or structural concrete with an appropriate mixture. At the last step, the panel-to-panel seam was casted with structural

concrete. Surface finishing may be required at the location of pockets and panel-to-panel seam in case of having unacceptable riding surface. Four lifting bolts were embedded in each panel to lift the precast prestressed panel with a minimum possible deflection.

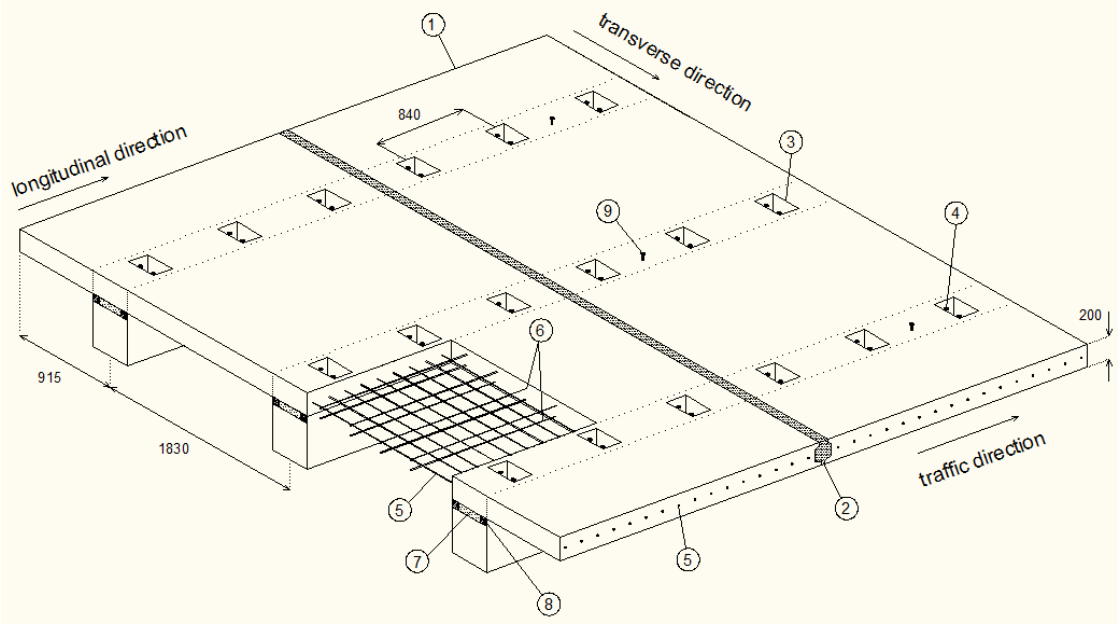

Fig. 16. AFRP concrete bridge deck slab with full-depth precast prestressed panels

4.3 Test Specimen Construction

4.3.1 Dimensions and reinforcing detail

Two full-depth precast prestressed panels, measuring 5490 × 2440 × 200 mm, were constructed. The precast panels were supported by three steel reinforced concrete beams spaced at 1830 mm on center, which rested on the strong-floor of the laboratory. As shown in Fig. 17, the bridge deck slab has two interior spans and two overhangs on both sides. Each precast panel was connected to the support beams via nine shear composite pockets each measuring 254 × 178 mm, where two high strength bolts with 25 mm diameter were coupled with their conjugate through a coupler already embedded in the support beams. The precast panels were concentrically prestressed with AFRP bars in the transverse direction, 125 mm on center, and reinforced with AFRP bars at top and bottom layers in the longitudinal direction, 150 mm on center. The longitudinal bar at the top and bottom layers of the section was actually one continuous bar fully bent in a U shape where the legs formed the top and bottom bars and the bent portion was placed at the panel-to-panel seam to provide a better bond between the panels and increase the shear transfer capacity. The AFRP bars were continuous through the pockets without crossing the shear bolts. Compressible foam, 63 mm thick, was attached to the topside edge of the beams with adhesive to provide a haunch between the soffit of the precast panels and support beams. Three leveling bolts composed of nuts and threaded rods with plastic housing were embedded in the precast panels, one on top of each support beam to level the precast panels upon placing on the foam. Since the panels were prestressed, four lifting points were conservatively implemented to reduce the deflection of the panel when lifted, and to be well safe from buckling. The panels were connected in the longitudinal direction through a female-to-female shear key with 150 mm width. When precast panels were placed on the support beams and leveled, the high performance SikaGrout 212 was used to fill the entire haunch and half of the shear pocket. The other half of the shear pocket along with the panel-to-panel seam was casted using the structural concrete. Fig. 18 shows the placement of support beams and precast panels.

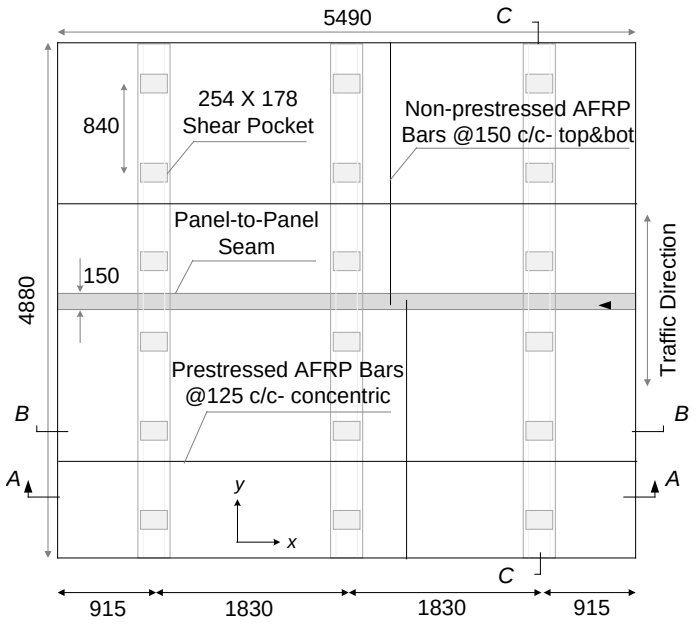

a) plan view of the bridge deck slab

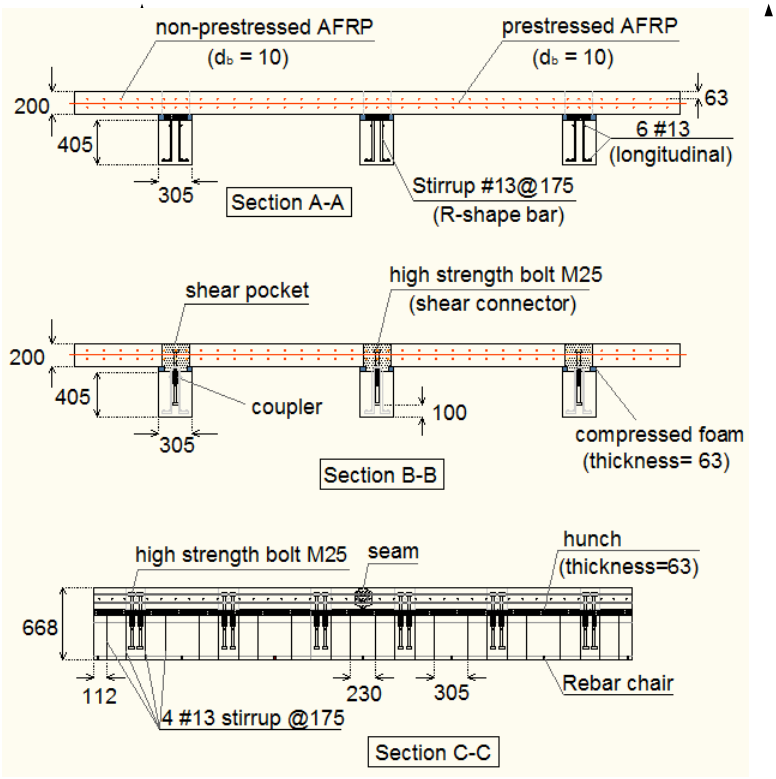

b) longitudinal and transverse sections

Fig. 17. Test specimen layout (Dimension: mm)

a) support beams placed in their position

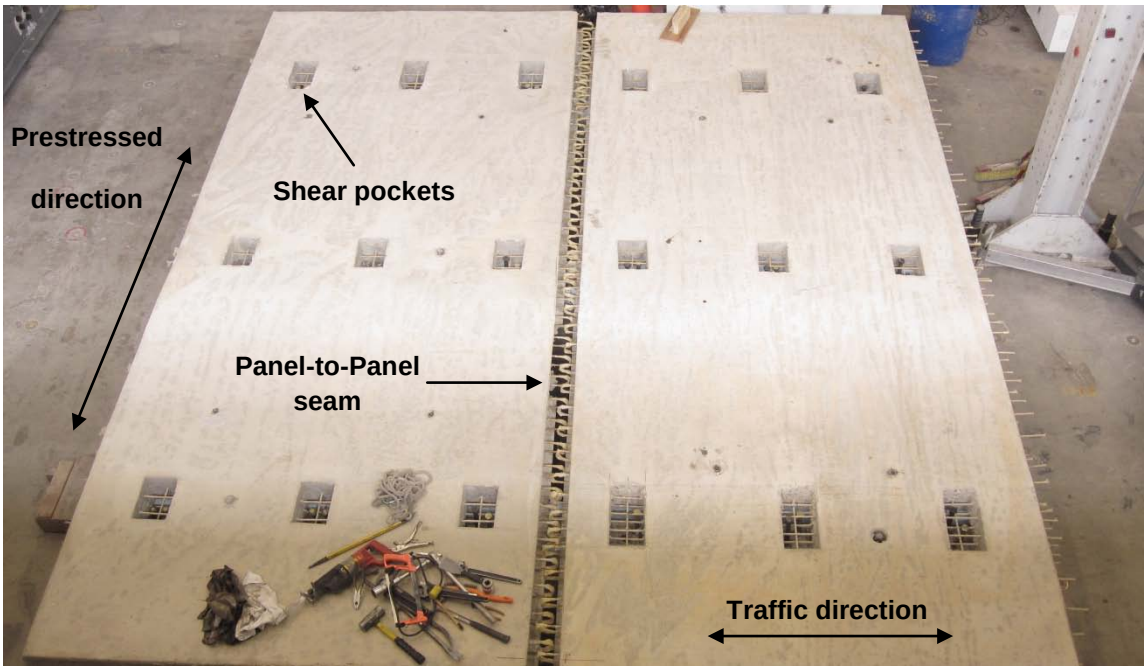

a) precast prestressed panels placed on support beams

Fig. 18. Construction of the bridge deck slab

4.3.2 Material properties

AFRP bars, ARAPREE type, with 10 mm diameter were used to reinforce and prestress the precast panels. The uniaxial tensile test showed the ultimate stress 1380 MPa, the strain capacity 0.02, and the modulus of elasticity 69 GPa (Medina 2011). The AFRP bars were prestressed up to 60% of their capacity, where the preliminary tests confirmed 5% loss due to relaxation of the bars and creep of the anchorage system during 72 hours gap between pretensioning and casting the panel. Therefore the effective prestressing force was assumed to be 55% of the capacity. The concrete mixture of the precast panels was designed for 41.5 MPa target compressive strength with 31.5 mm maximum aggregate size and 100 mm slump. The standard cylinder test showed the concrete compressive strength of the first panel 41 MPa, second panel 35 MPa, and panel-to-panel seam 38 MPa. The support beams were casted with a higher strength concrete, 48 MPa, to prevent any possible crushing or premature failure at the support when loading the bridge deck slab. Concrete compressive strength for different parts of the bridge deck is presented in Table 6, where a minimum of three specimens was used per component.

Table 6- Concrete compressive strength, day of test

Component	Strength (MPa)
First deck slab panel	41.4
Second deck slab panel	35
Support beams	48.3
Panel-to-panel seam	38
Haunch (grout)	35

4.3.3 Prestressing operation

One of the challenging steps in construction of the precast prestressed panels was pretensioning the AFRP bars. As discussed in Chapter 3, the conventional anchorage system composed of hard plastic wedges and stainless steel casing fabricated by the manufacturer failed to provide a reliable anchorage capable of sustaining the prestressing load. The prestressing method used for creep and relaxation tests with the same steel pipes, grouting material, and hydraulic jack was employed herein to prestress the panels. As illustrated in Fig. 19, the designed system included: (1) steel pipes already filled with an expansive and quick setting grout at the dead end to anchor the bars, (2) two holes on the pipes' surface to inject the grout, (3) plastic stoppers at both end of the pipes to prevent leakage of the grout and to hold the ARAPREE bar at the center of the pipe, (4) thick steel plates with a central hole as support of the dead anchorage, (5) steel double header beams as a part of prestressing frame and support of the thick steel plates, (6) steel longitudinal beams as a part of prestressing frame to connect the header beams, (7) wood formwork of the panel inside the prestressing system, (8) ARAPREE bars, (9) steel pipes at the live end and behind the hydraulic jack to lock the system upon reaching to desirable level of prestressing, (10) steel pipe in front of the hydraulic jack to pretension the bar, (11) hydraulic jack with central hole, (12) steel plate between the hydraulic jack and rear steel pipe for a better seat of hydraulic jack on the rear pipe. The concrete panels were successfully prestressed using this system. Only one failure was observed as a result of poor grouting and weak gripping in anchorage which was subsequently fixed. Fig. 20 shows the prestressing setup and operation implemented in laboratory.

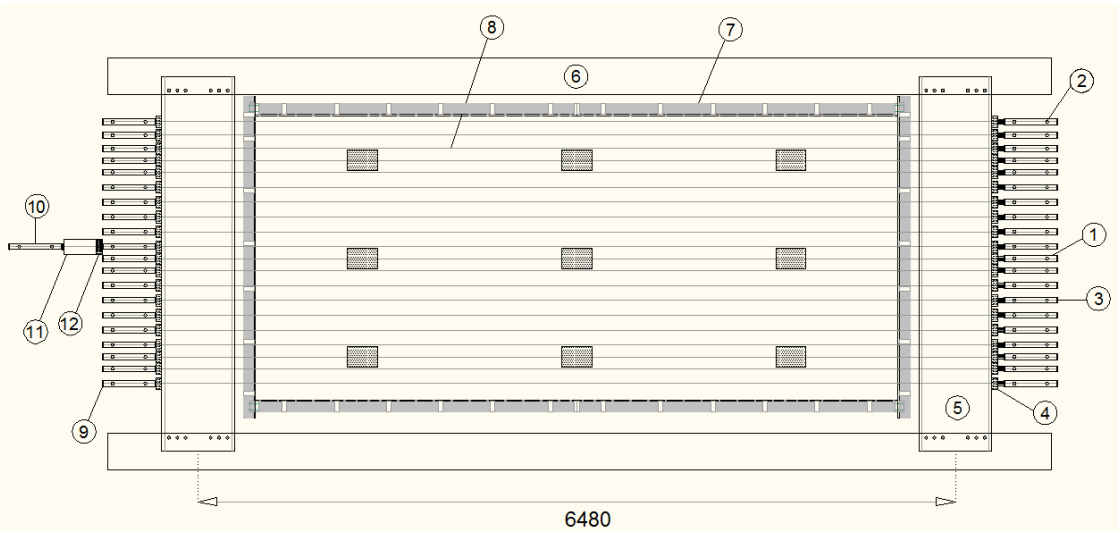

Fig. 19. Prestressing system

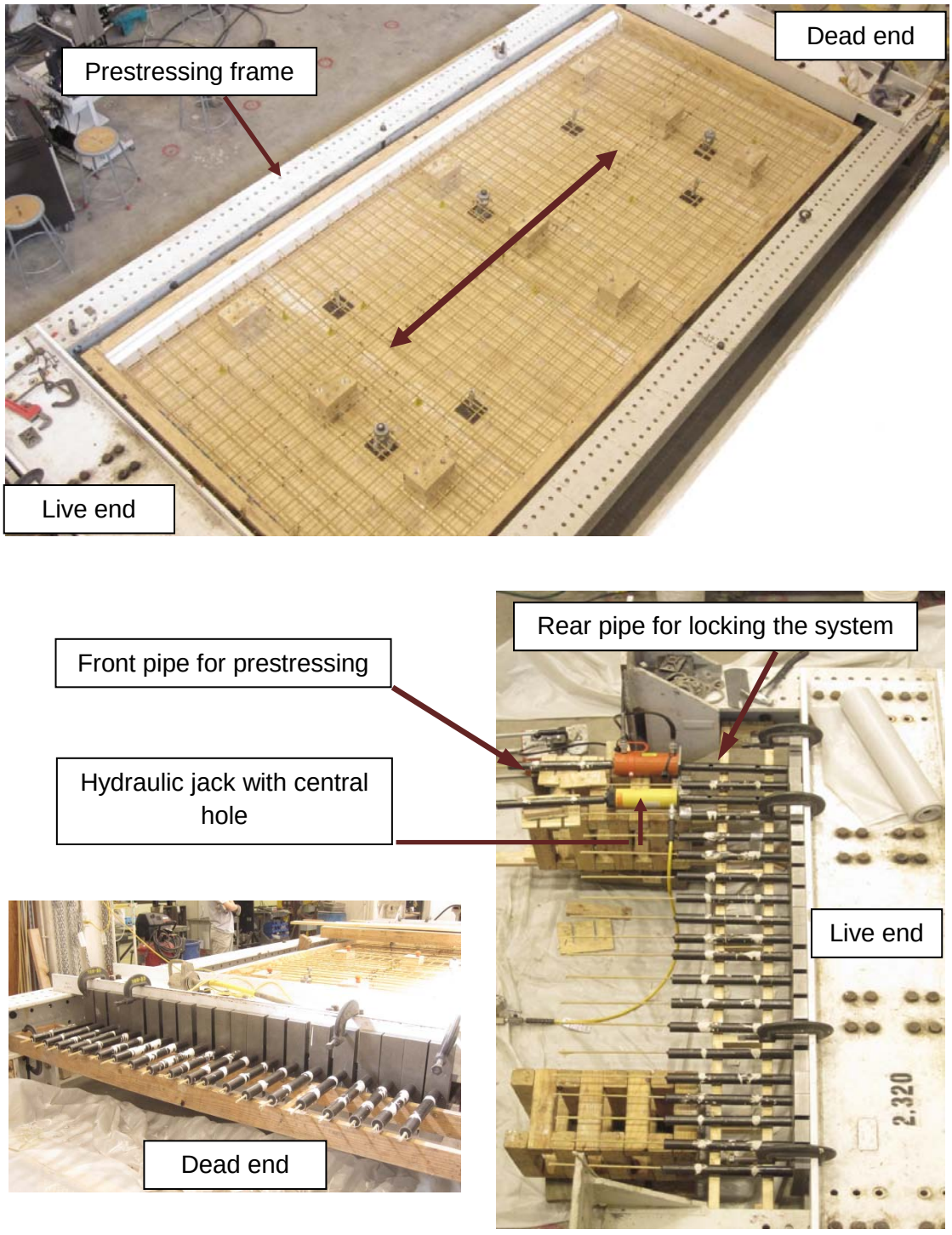

Fig. 20. Prestressing operation

4.3.4 Panel-to-panel seam detail

To increase the bond and shear transfer capacity of the panel-to-panel seam, the longitudinal reinforcing bars were at the joint. Since FRP bars are brittle material, they cannot be easily bent like conventional steel, and in fact, they should be fabricated in a bent shape. However, preliminary tests showed that the AFRP bars, ARAPREE type, can be bent taking the advantage of their thermoplastic characteristics. The bending method of the AFRP bars included heating the corresponding zone to somewhat melt the resin of the surface, hammering the heated zone to widen the surface, and then twisting the bar around a fixed pipe with an appropriate diameter to form the bent zone. When hammering, a sheet of hard plastic was used on AFRP bars to avoid the direct contact of hammer and bar and damaging the fibers. Implementing this method, AFRP bars were successfully bent in a U shape where the legs formed the top and bottom reinforcement in the longitudinal direction and the bent portion was placed right at the panel-to-panel seam. Fig. 21 shows the bent bars, and the detail of reinforcement at the panel-to-panel seam.

4.3.5 Closure pour

Closure pour was the last step in construction of the bridge deck slab. A non-shrink cementitious grout, SikaGrout 212 was used to fill the entire haunch and half of each composite pocket. Low bleed, low heat build-up, multiple fluidity, and ease in use are the advantages of this grout. To mix the grout, the optimum water-to-powder ratio of w/p=0.19 was selected based on the research done by Mander (2009). To control the performance of the grout, the flowability and consistency tests were conducted according to ASTM C939 and C230/C230M, respectively. In flowability test, the efflux time was found equal to 20, and in consistency test through the flow cone the diameter of the spread grout was measured equal to 216 mm. The specified cube test showed the compressive strength of the grout equal to 35 MPa. The results of the grout tests confirm a suitable structural grout.

a) top view

b) front view

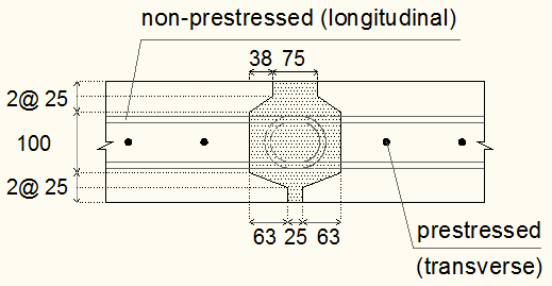

c) reinforcement detail

Fig. 21. Panel-to-panel seam detail

Fig. 22 shows the consistency and flowability tests of the grout as well as the composite pocket filled to the half. The other half of the composite pocket and the panel-to-panel seam are subsequently filled with structural concrete.

4.4 Control Specimen

Similar bridge deck slab specimen; however, reinforced with conventional steel, with the same structural geometry, dimensions, and loading configuration was tested by Mander et al. (2010), which is selected as the control specimen of the current research to compare the structural behavior under corresponding load cases. The control specimen's slab consists of 100 mm thick stay-in-place (SIP) panels at bottom and 100 mm thick cast-in-place (CIP) panels at top. The bottom SIP panels were transversely prestressed using 9.5 mm diameter tendons and longitudinally reinforced with welded wire mesh at 465 mm^2/m.

a) flowability test

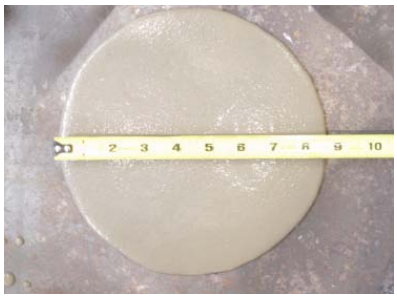

d) consistency test

b) composite pocket

Fig. 22. Closure pour with SikaGrout 212

The top CIP panels were transversely and longitudinally reinforced with D16 and D12 at 150 mm on center, respectively. The bottom SIP panels span between the support beams and act as a formwork for the top CIP panels. Two full-scale specimens were constructed in that research with different overhangs on both sides; precast, lab cast and conventional CIP overhang. To compare the amount of reinforcement used in AFRP and control specimens, the reinforcement ratio ρ_{it} is defined as the total area of reinforcement to the entire cross sectional area of the concrete slab in *i* direction. As shown in Table 7, the reinforcement ratios in *y* direction are close, however, in *x* direction the reinforcement ratio in control specimen is three times that of the AFRP specimen. The moment capacities for bridge deck slab section per unit width are also presented in Table 7. Compared to the control specimen, the AFRP concrete slab is almost isotropically reinforced in the sense that the moment capacities in both *x* and *y* directions are very close.

Table 7- Moment capacities per unit width (kNm/m) and reinforcement ratios

Section	M_x	M_x'	M_y	M_y'	ρ_{xt}	ρ_{yt}
Control specimen-interior span	106.97	100.26	53.02	58.85	0.009	0.006
Control specimen-precast overhang	124.5	96.5	31.0	66.6		
AFRP specimen	70	70	76	76	0.003	0.005

4.5 Loading Plan and Test Setup

According to AASHTO LRFD Bridge Design Specification (2010), the wheel load of HS20 truck is equal to 71 kN. If the lane factor of 1.2, impact factor of 1.33, and live factor of 1.75 are applied, the maximum factored load will be estimated about 200 kN. The bridge deck slab was tested under monotonically increased concentrated loads until failure. Seven different load cases were considered through which the interior spans and overhangs could be tested for wheel and axle loads. The load was applied through a 250 × 500 mm steel plate which represents the tire footprint per AASHTO LRFD (2010). The steel plate was 75 mm thick and seated on a 12.5 mm thick neoprene pad. A 2200 kN actuator was used for loading where the magnitude of the applied load was measured through an in-series load cell connected to the tip of the actuator.

As shown in Fig. 23, load cases 1, and 4 represent the axle load, and load case 7 indicates the wheel load on the interior span. Also, load cases 2 and 5 indicate the wheel load and axle load on the overhangs, respectively. Load cases 3 and 6 don't represent an actual load case on a bridge deck slab and were tested just to check the capacity of the corners. All the load cases, except for load case 4, were applied close to the seam, to cause the critical case of loading and evaluate the structural sufficiency of the joint. AASHTO LRFD (2010) stipulates the center of the load on overhang to be 300 mm from the barrier face; however, in this test the load was applied on the edge of the overhang to induce a larger moment and to measure the flexural capacity of the overhang. String pots were used underneath the bridge deck spaced at 150 mm center-to-center to record the deflection profile in both *x* and *y* directions which will be used to find out the curvature distribution. In order to map the cracking pattern, the top and bottom surface of the slab were meshed with a 200 × 200 mm grid labeled from A to Z in *x* direction and 1 to 23 in *y* direction. The location and arrangement of the string pots for each load case is shown in Fig. 24, and the test setup for load case 1, as an instance, is presented in Fig. 25.

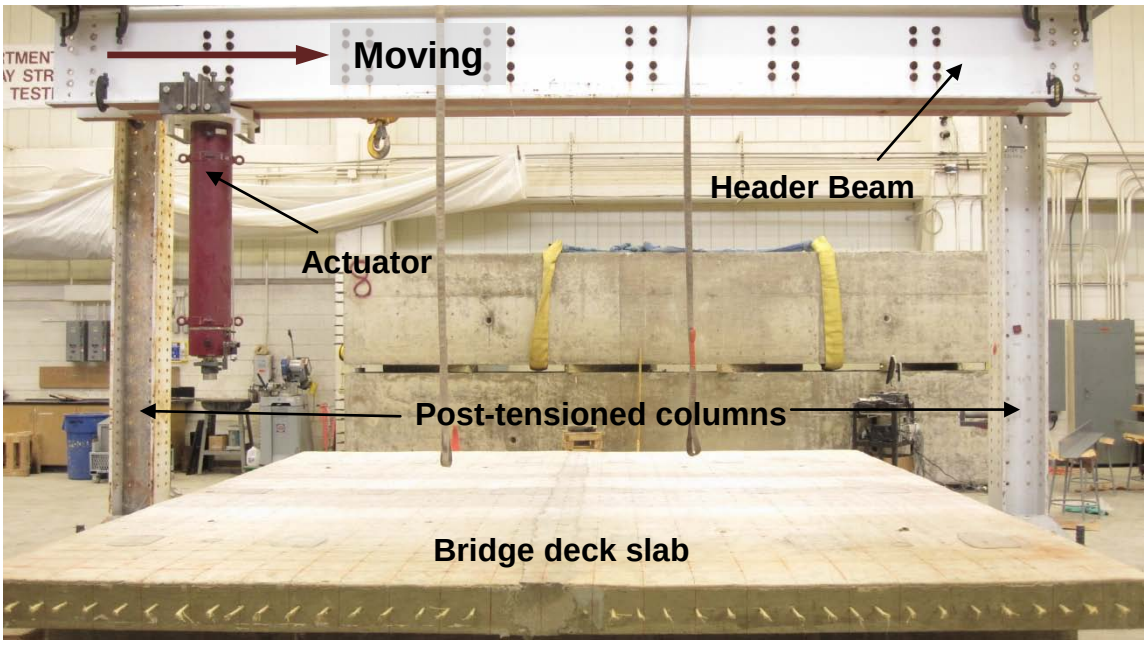

a) Loading frame

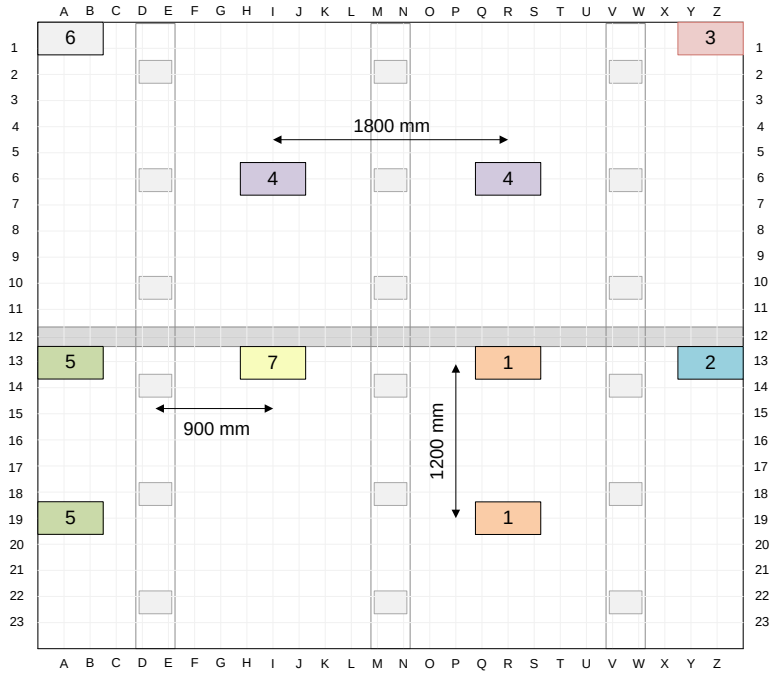

b) Loading plan

Fig. 23. Testing Plan

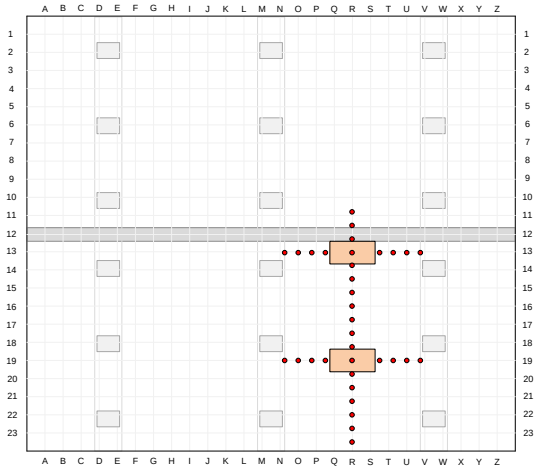

a) load case 1

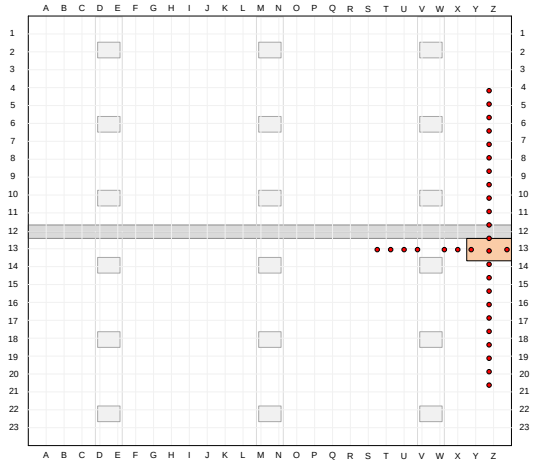

b) load case2

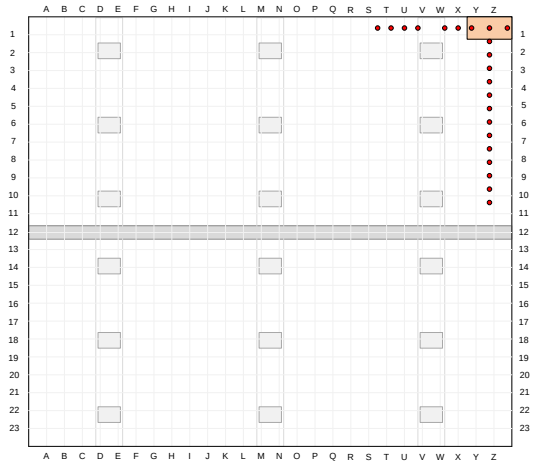

c) load case 3 (same as 6)

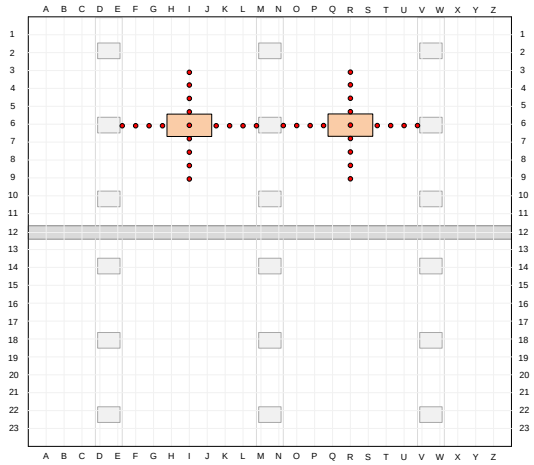

d) load case 4

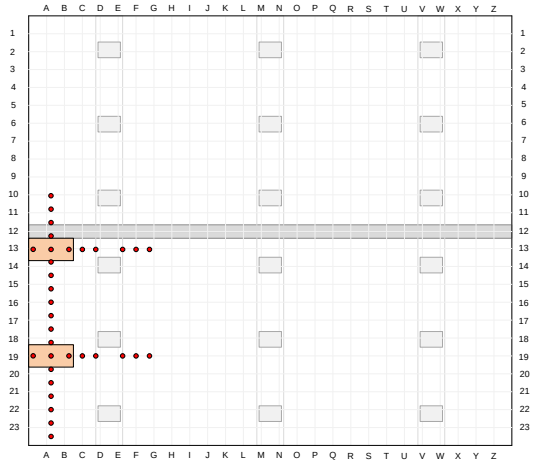

e) load case 5

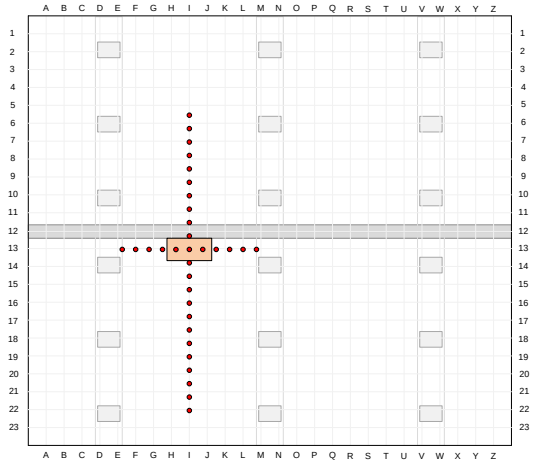

f) load case 7

Fig. 24. Location of string pots for each load case

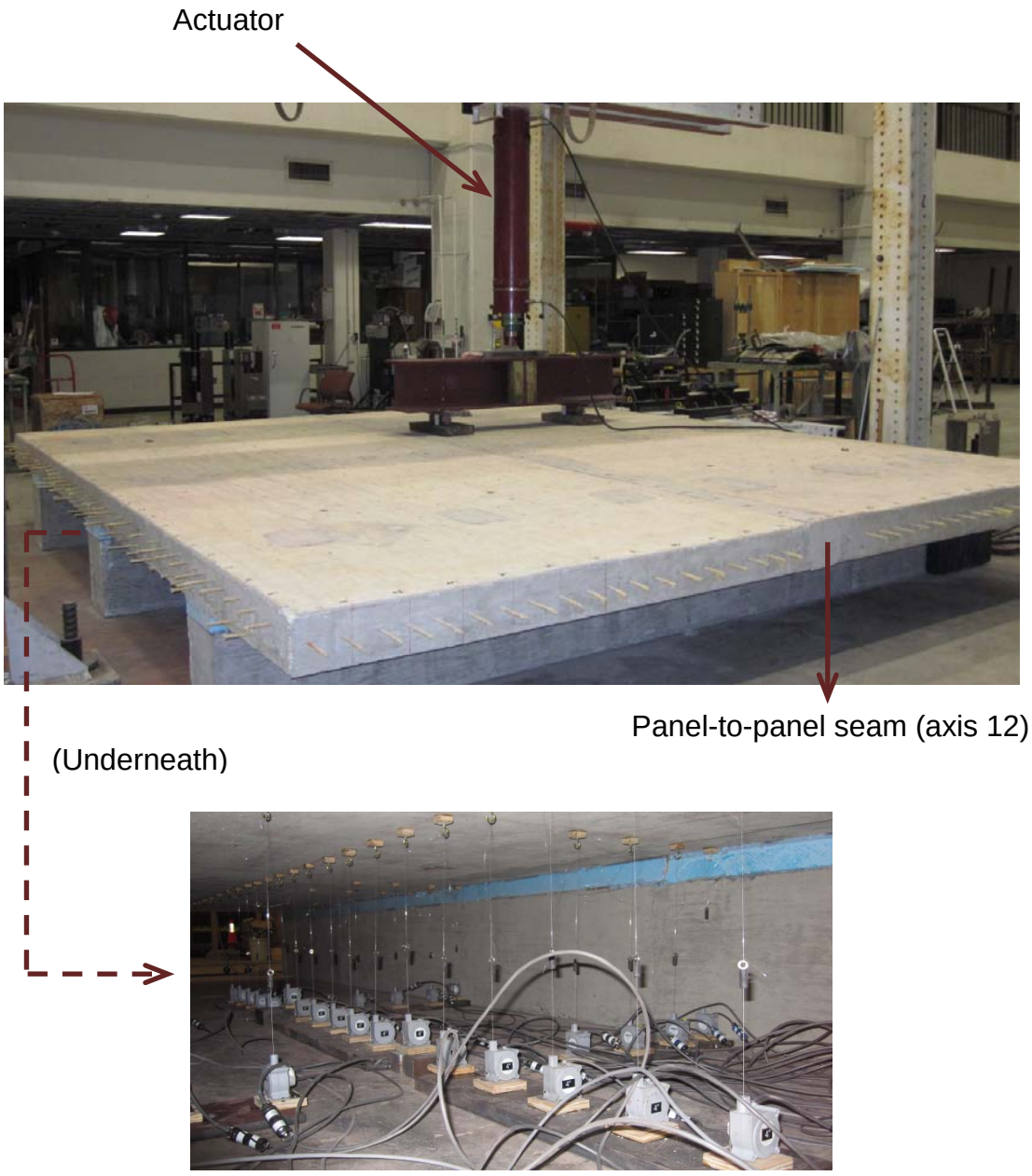

Fig. 25. Test setup for load case 1 (axle load on interior span)

4.6 Experimental Results

4.6.1 Overhang

Flexural cracks were first observed close to the exterior support beam and propagated in parallel with it due to the large negative moments that developed at the support. As shown in Fig. 26(a), the wheel load and deflection at cracking was found about 180 kN and 5 mm for load case 2, and 120 kN and 2 mm for load case 5, respectively. With increasing the load, the flexural cracks propagated around the loading plate and reached to the edge of the slab in an approximate triangle shape. Under load case 5, complete flexural mechanism developed at both panels and very large deformability was achieved. However, under load case 2 compound shear-flexural failure was observed including flexural mechanism of the deck panel subjected to the wheel load and shear failure at the seam. The cracking patterns are presented in Fig. 27, where the black lines indicate the cracks on top and the gray lines represent the cracks beneath the bridge deck.

The ultimate wheel load and deflection was observed equal to 320 kN and 25 mm for load case 2, and 225 kN and 35 mm for load case 5, respectively. The load capacity of the slab is seen to be well above the maximum factored load, 200 kN. For load case 5, the average deflection underneath the loading plates was used to depict the diagram as the deflection of the loading plates was very similar. Table 8 shows the summary of the test results. As seen, the ultimate to cracking load ratio is equal to 18 for either load cases 2 or 5. Also, the maximum to cracking deflection is about 4.9 and 17.5 for load cases 2 and 5, respectively, which demonstrates considerable deformability, particularly for load case 5. Unloading of the load case 5 showed a significant energy absorption which resulted in 16 mm residual plastic deflection, say almost half of the total deflection. Comparison between the two load cases confirms a larger deformability in load case 5 as the load is applied through the axle in a less concentrated manner compared to the single wheel load. Complete transfer of the flexural cracks between the panels is indeed a sign of sufficient structural connectivity at panel-to-panel seam and integrity of the bridge deck panels. This can also be inferred by studying the deflection

profile and curvature distribution along the traffic direction (y axis). The ratio of the flexural stiffness at failure (K_u) to that of the uncracked section (K_g) can be indicative of flexure contribution at failure. This can be inferred by measuring the slope of the load-deflection diagram. As shown in Table 8, this ratio is almost zero for load cases 2 and 5 which demonstrates that the failure mechanism of the overhang is mainly governed by flexure. Although load cases 3 and 6 do not represent an actual loading case, the deformability observed is considerable.

4.6.2 Interior span

At interior spans, similar to the overhangs, flexural cracks were first observed on top of the slab and close to the support beams and beneath the slab right below the loading plate. For all load cases 1, 4, and 7 the load and deflection at cracking was found approximately 250 kN and 1.5 mm, respectively. Increase in load resulted in propagation of the top cracks around the loading plates and the bottom cracks toward the edge of the supports in a diagonal manner, and the slab eventually failed in a punching fashion; however, flexural cracks were evident and sufficient warning was achieved before the failure. The load deflection diagram and cracking patterns at failure are shown in Fig. 26(b) and 27, respectively. The ultimate strength for load cases 1, 4, and 7 were observed equal to 700 kN, 770 kN, and 880 kN, respectively. The behavior of load cases 4 and 7 are very similar as they both have one wheel load on the interior span. But, load case 1 with two wheel loads (axle load) on the same interior span results in a larger deformability due to transferring the load in a more distributed manner.

The maximum deflection observed is equal to 19 mm, 12.5 mm, and 13.5 mm for load cases 1, 4, and 7, respectively. No evidence of local failure at the panel-to-panel seam was observed in load cases 1 and 7, which indicates a sufficient connectivity between the panels. The maximum-to-cracking load and deflection ratios are summarized in Table 8. The ratio of the flexural stiffness at failure to that of uncracked section implies that the failure was mostly governed by flexure; however, shear also contributed in the failure mechanism due to the restrained edges. The deflection limit of

span/800 has been stipulated in AASHTO LRFD (2010) for vehicular loads. This deflection limit is to control the vibration, which is a serviceability-related issue and not a safety-related issue. The deflection of the interior span at service load is about 1 mm for all load cases, which is less than the allowable amount *span/800*= 2.25 mm.

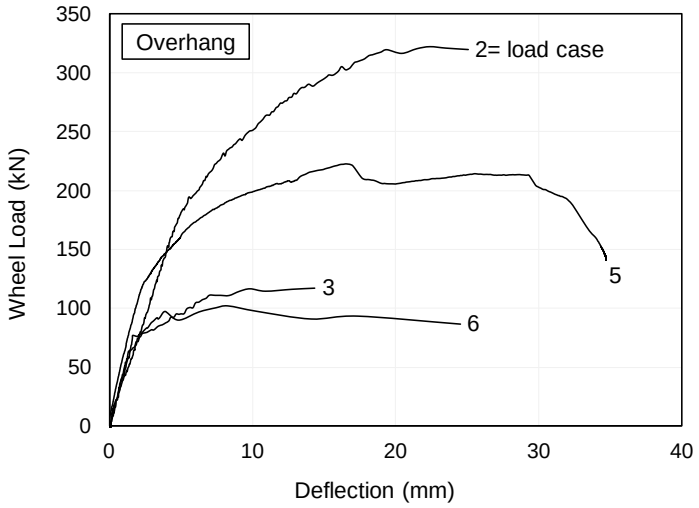

a) load-deflection response (overhang)

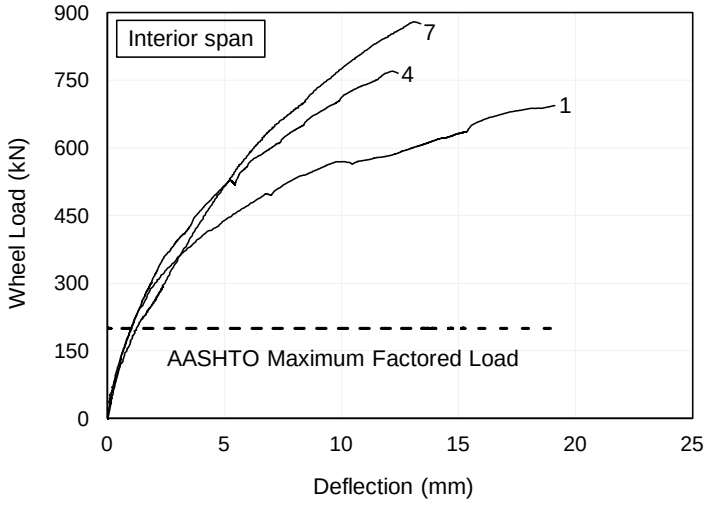

b) load deflection response (interior span)

Fig. 26. Experimental results: load-deflection diagrams

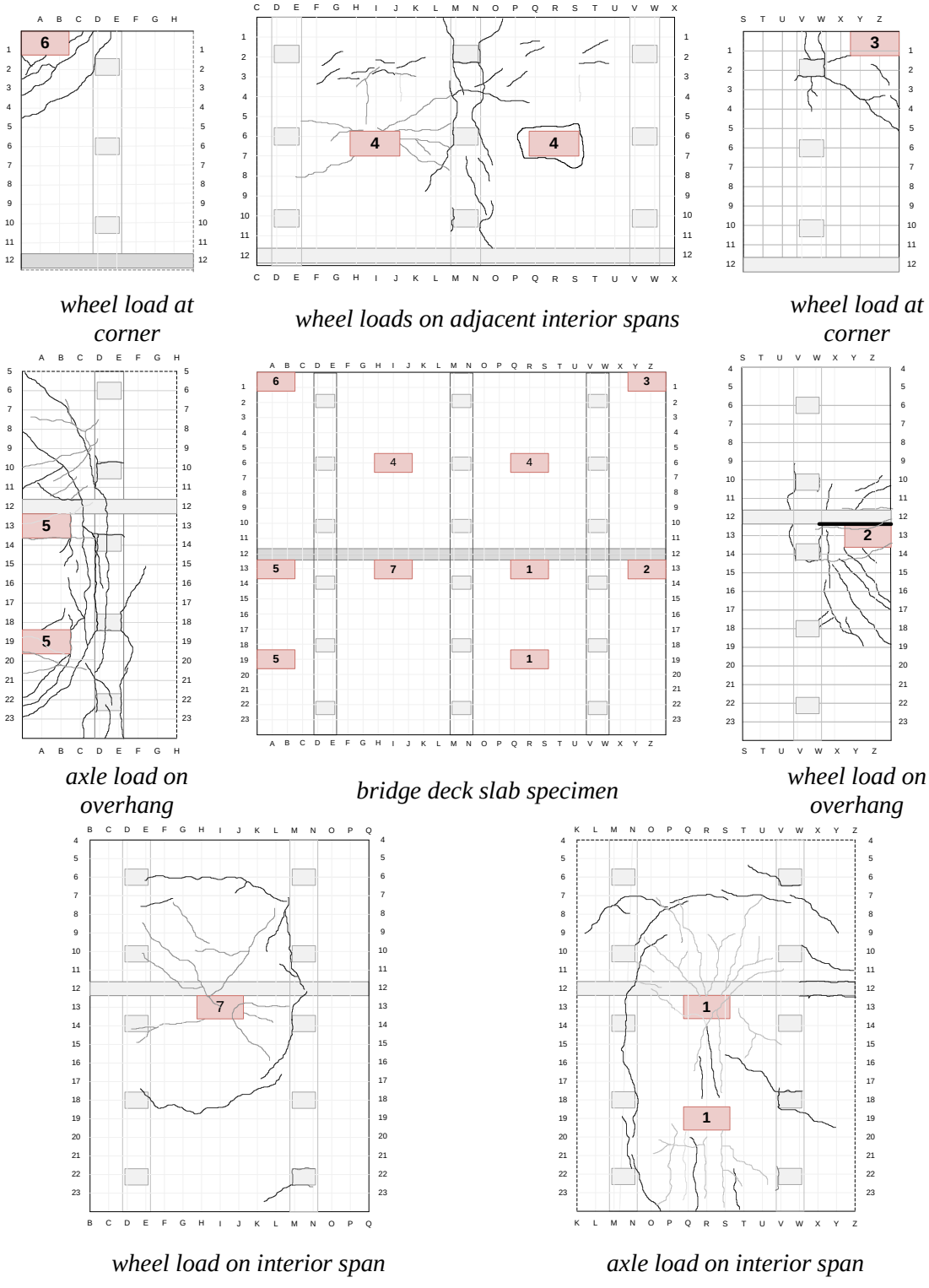

Fig. 27. Experimental results: cracking pattern at failure

Table 8- Summary of the test results

Load case	P_u (kN)	P_{cr} (kN)	Δ_u (mm)	Δ_{cr} (mm)	P_u / P_{cr}	Δ_u / Δ_{cr}	K_u / K_g
1	700	250	19	1.5	2.8	12.7	0.028
2	320	180	24.5	5	1.8	4.9	0
3	117	75	-	1.5	1.6	-	0
4	770	250	12.5	1.5	3.1	8.3	0.085
5	225	125	35	2	1.8	17.5	0
6	100	75	25	1.5	1.3	16.7	0
7	880	250	13.5	1.5	3.5	9	0.112

4.7 Evaluation of the Test Results

4.7.1 Flexural behavior

The cracking pattern and the deformability observed in the load-deflection diagram implied the governing flexural behavior of the bridge deck slab, particularly at overhang. At interior spans, after flexural cracks were developed, the bridge deck slab eventually failed in a punching manner as a result of the restrained edges. The extent of flexural mechanism can be further investigated by studying the deflection profile and curvature distribution close to failure. Curvature distribution is computed as the second derivative of the deflection profile gained from the data recorded by the string pots. Both *x* and *y* directions perpendicular to and parallel with the traffic direction are studied herein; however, *x* direction as the stiffer direction of the two-way slab undergoes most of the flexural demand and develop larger curvature. The normalized curvature is defined herein as the actual curvature multiplied by the height of the section (h=200 mm). The deflection profiles and curvature distributions are presented in Fig. 28-34 along with the string pots that were installed underneath the deck (referring to Fig. 24).

For load case 1, as an instance of loading on interior span, the maximum deflection underneath the load is equal to 19 mm. The observed deflection at the support is not zero firstly because the closest string pot to the support is at 2.5 mm away from the beam face, and secondly due to the extensive cracking and small rotation of the support beams. Since only the middle beam is tightened to the strong floor, the rotation of the exterior beam is larger which causes larger deflection at the location of the closest string pot to the support. However, once small rotations took place, the beams act as a fixed support. This is confirmed by the considerable negative moments developed at the support showing its rotational rigidity. The maximum curvature at both midspan and supports is seen to be equal to 0.0075, which is about 38% of the curvature capacity of the corresponding strip in *x* direction, 0.02, and 19 times the cracking curvature (see Chapter 5). The large curvature developed at the support and beneath the load indicates the considerable moment redistribution and deformability upon cracking until failure of the slab. Contribution of the flexural behavior seems to be larger for load case 5 at the overhang compared to load case 1 due to less constraint at the edge. The maximum deflection at the free edge of the slab is 35 mm and the maximum curvature close to the support is about 0.01 which is 50% of the curvature capacity of the corresponding strip in *x* direction and 25 times the cracking curvature. The governing flexural mechanism is evident from the curvature distribution.

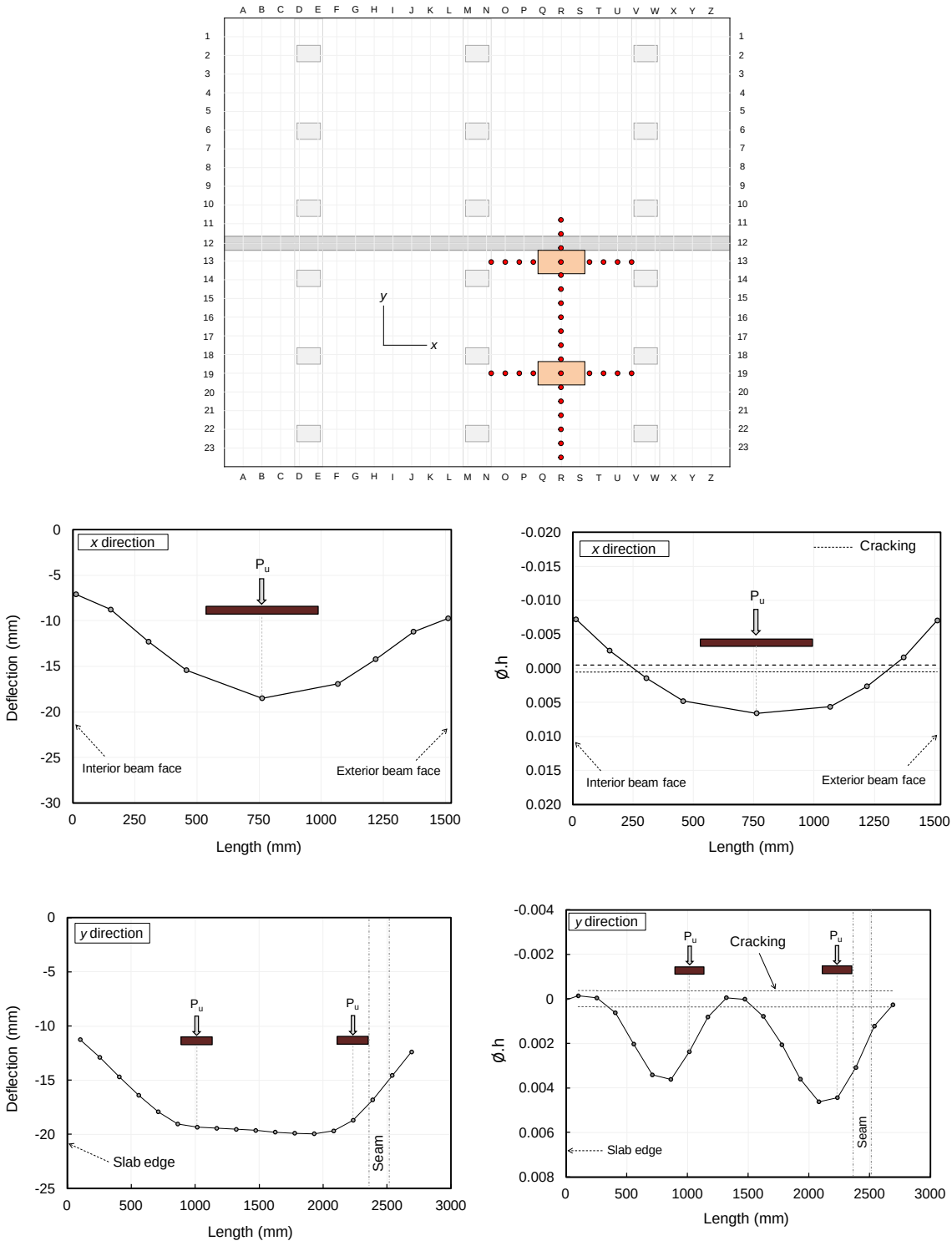

Fig. 28. Deflection profile and curvature distributions (load case 1)

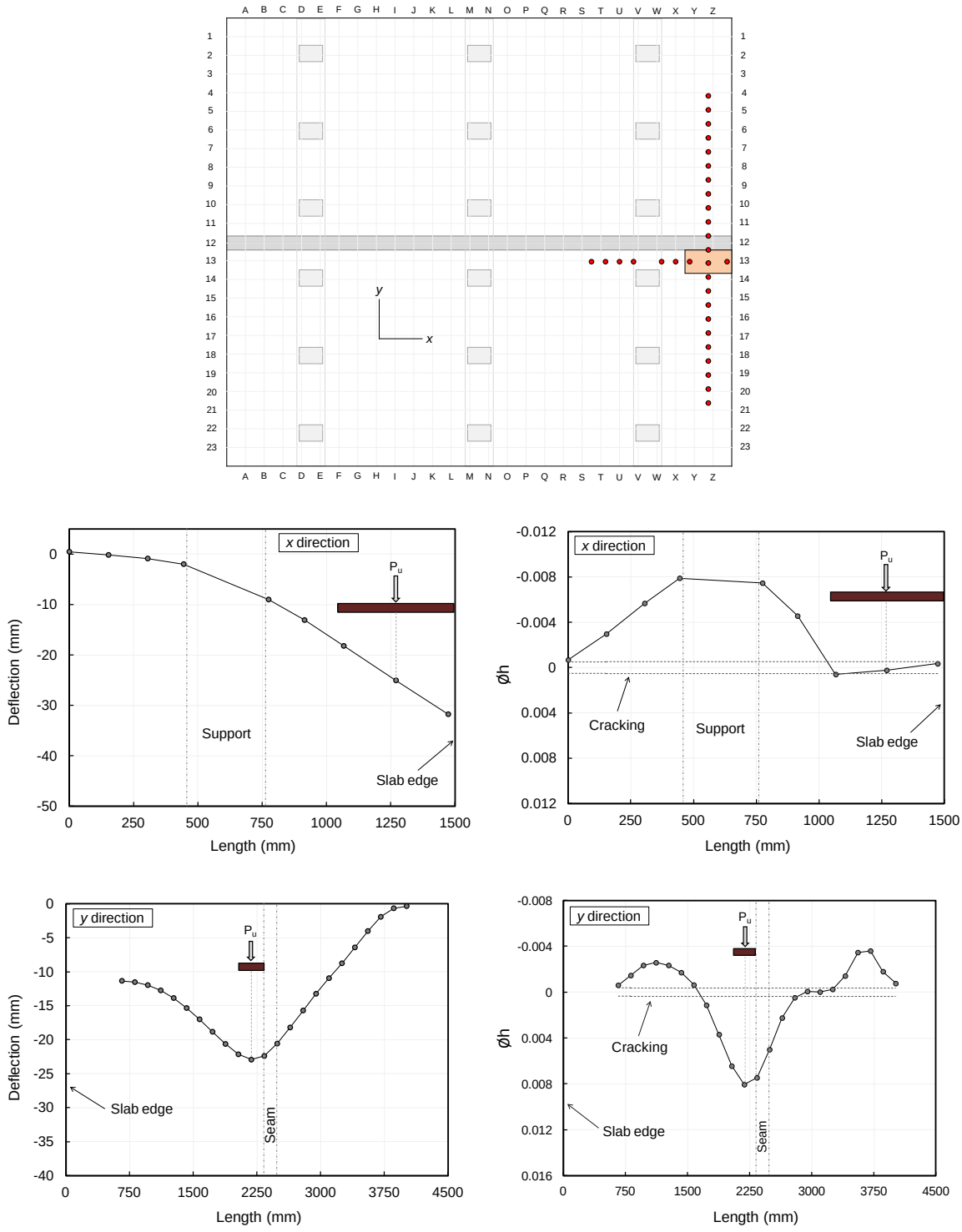

Fig. 29. Deflection profile and curvature distributions (load case 2)

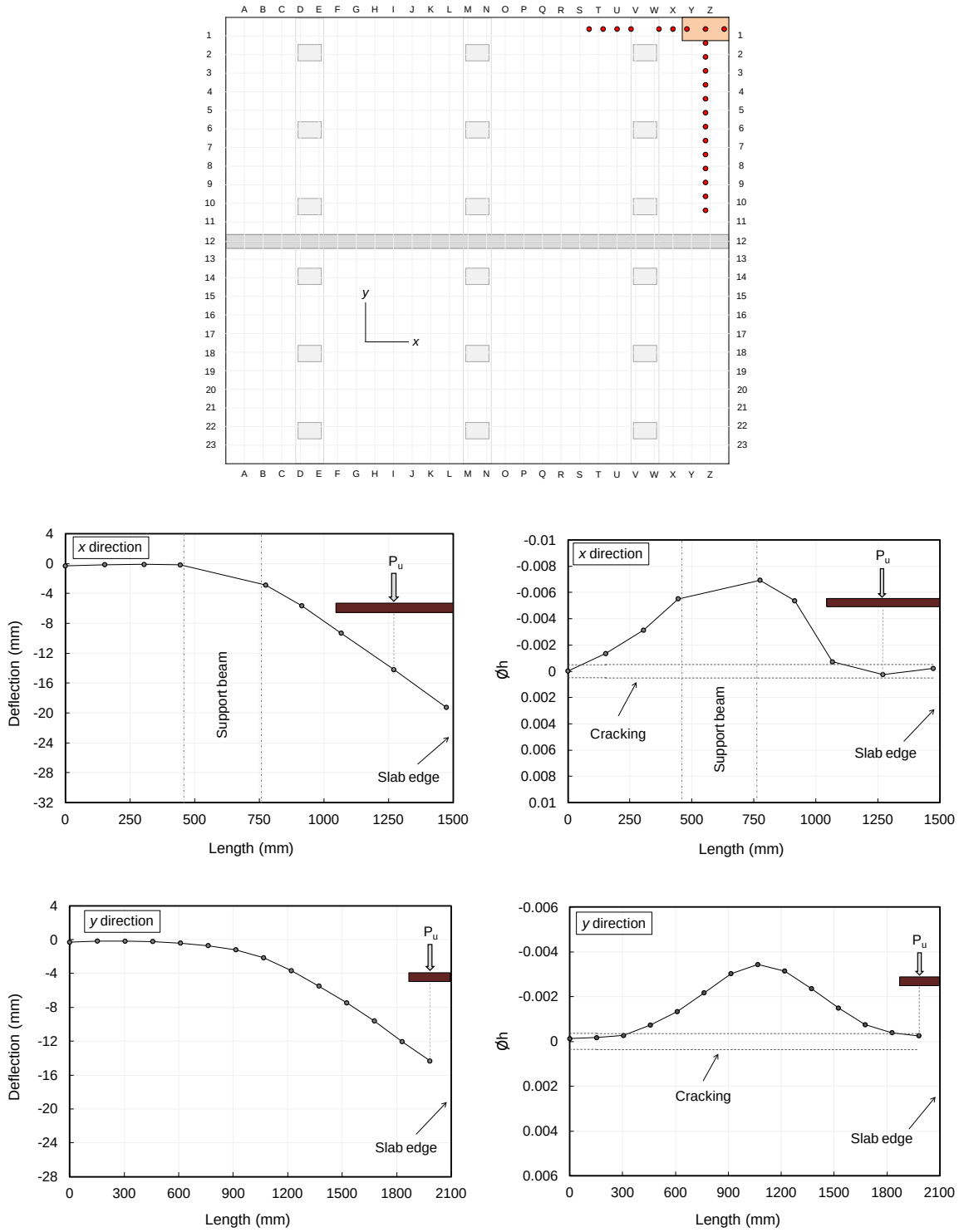

Fig. 30. Deflection profile and curvature distributions (load case 3)

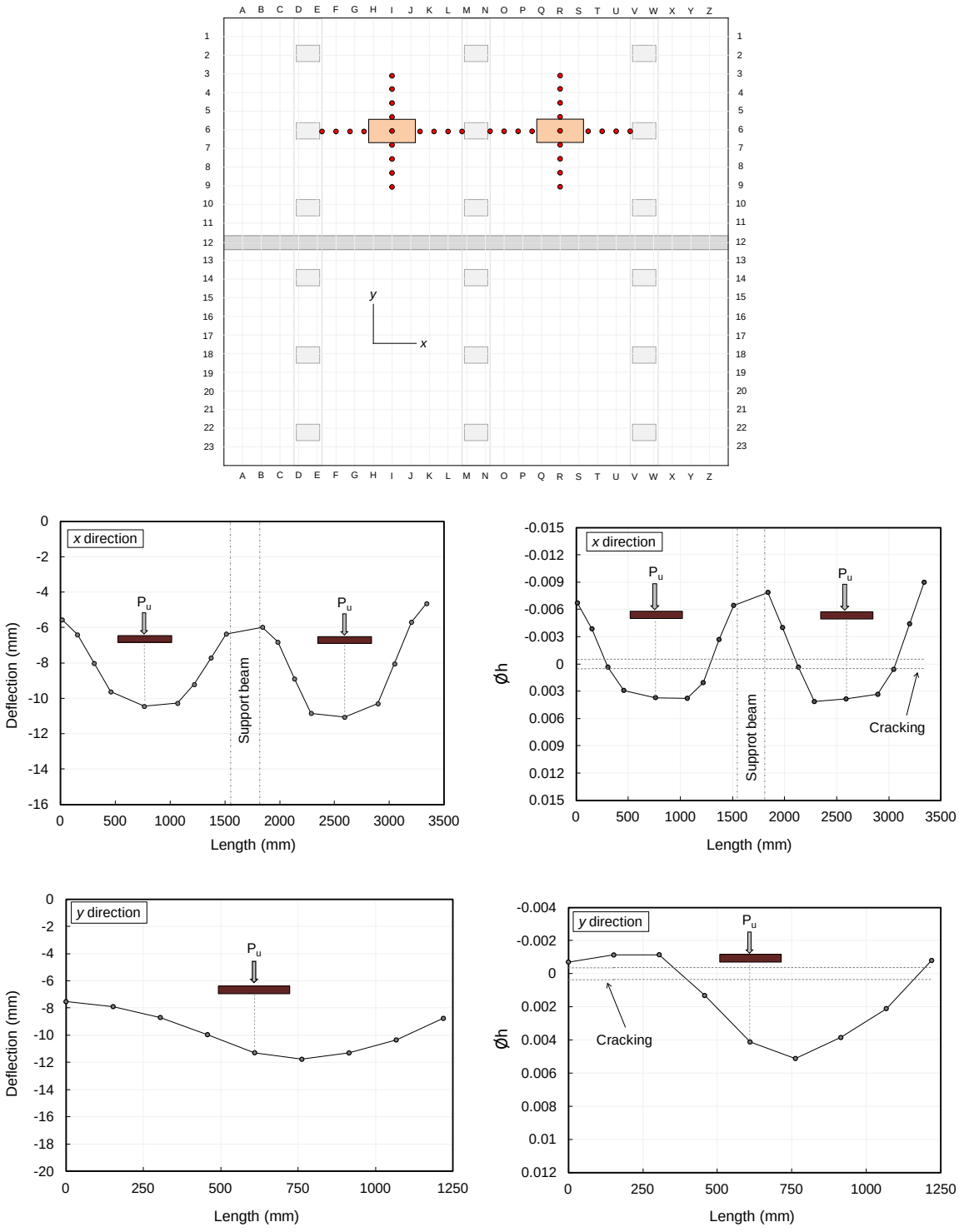

Fig. 31. Deflection profile and curvature distributions (load case 4)

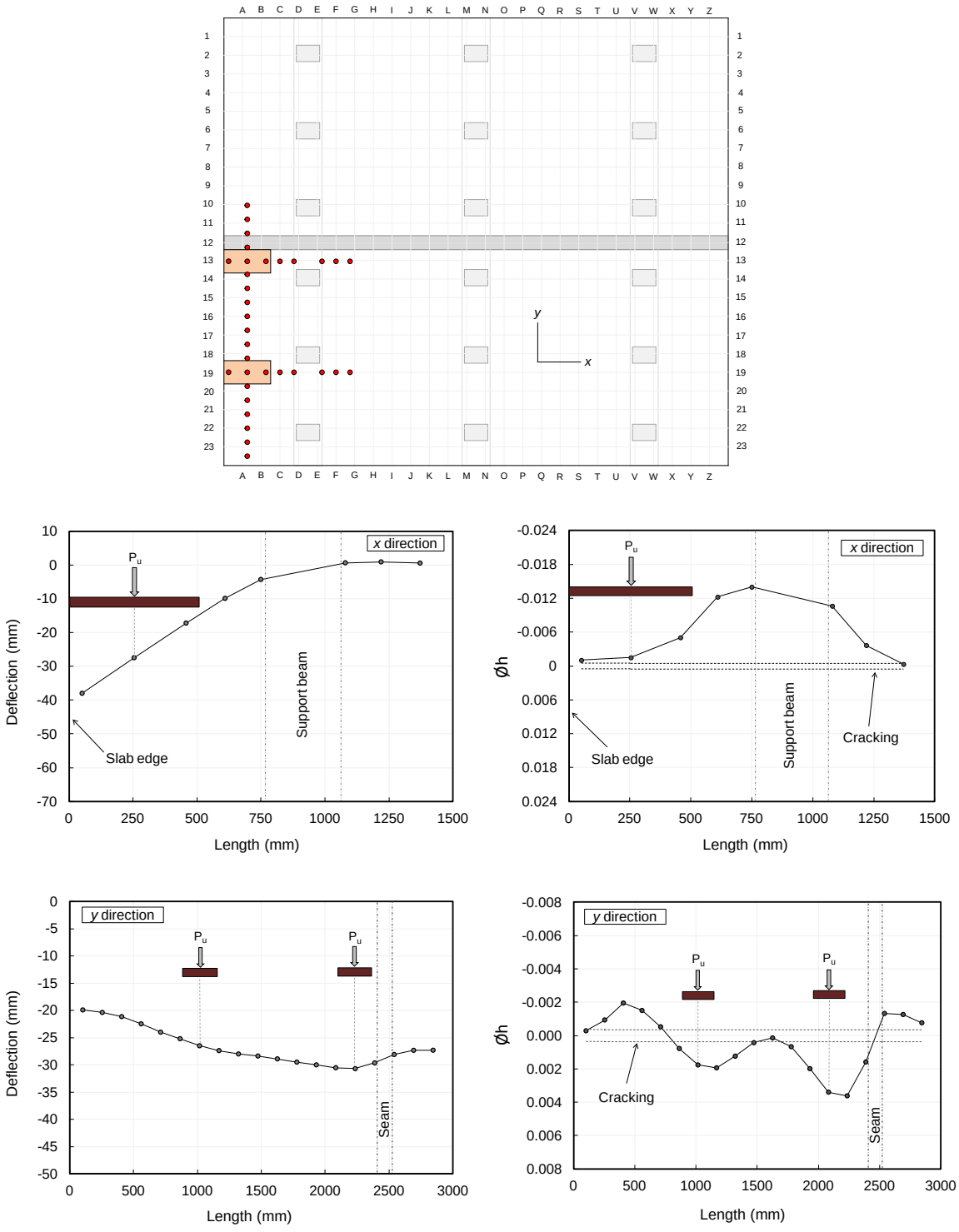

Fig. 32. Deflection profile and curvature distributions (load case 5)

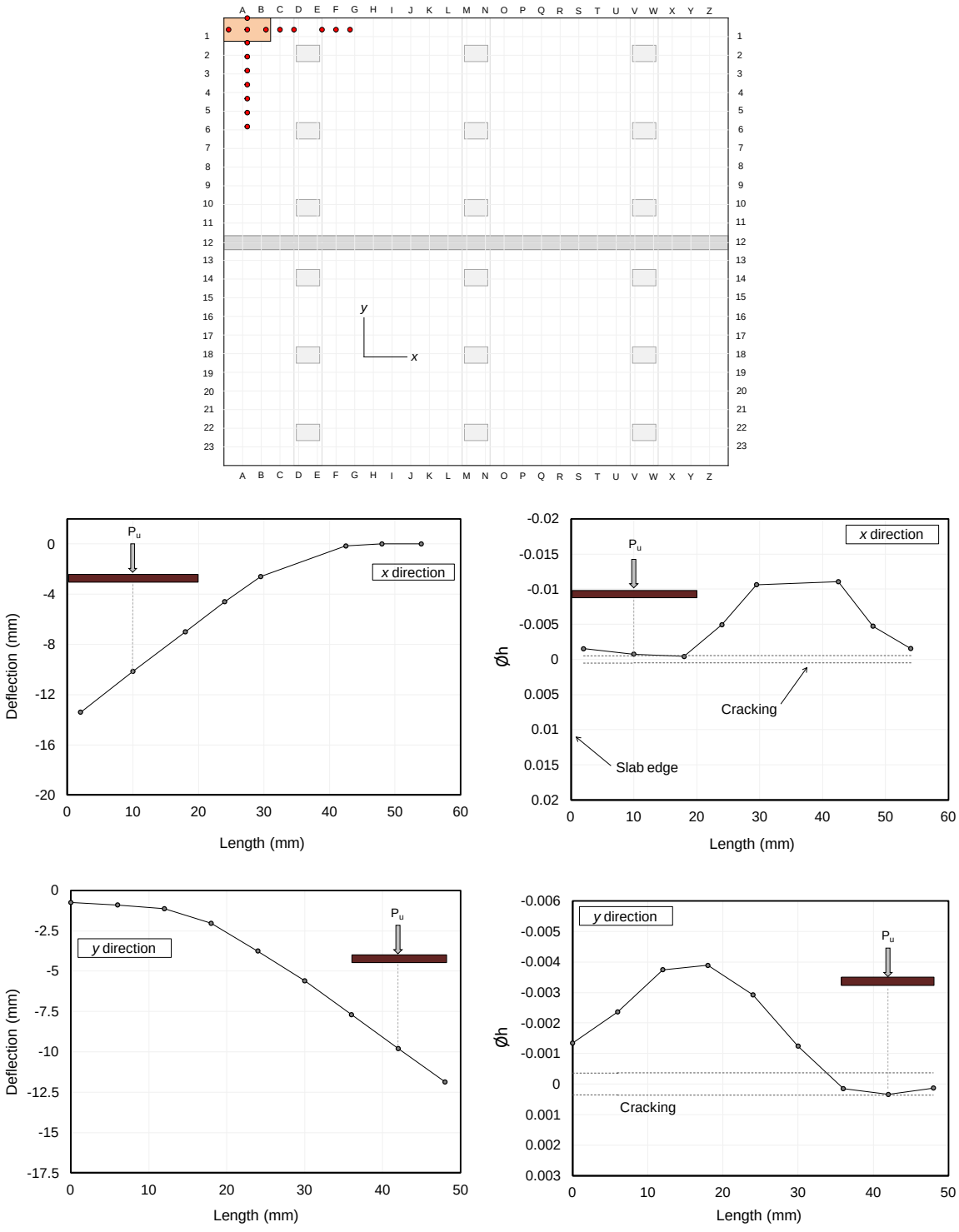

Fig. 33. Deflection profile and curvature distributions (load case 6)

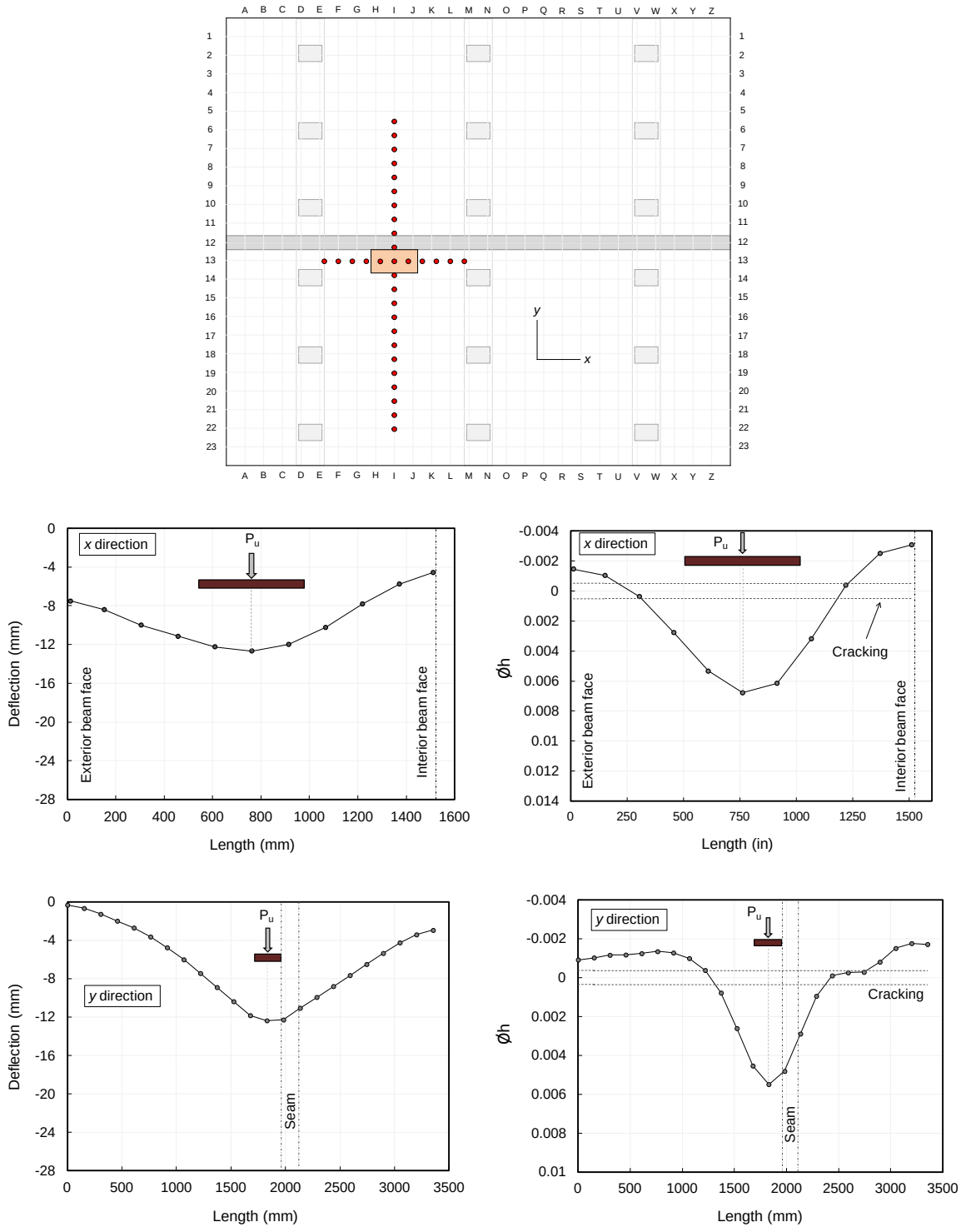

Fig. 34. Deflection profile and curvature distributions (load case 7)

4.7.2 Punching shear strength

While flexural behavior seems to govern the overall behavior of the bridge deck slab in both interior spans and overhangs, the failure mechanism of the interior span takes place in a punching manner due to restrained edges. Load deflection diagram and K_u/K_g ratio for the interior span confirms that shear somewhat contributes to the failure mechanism. Therefore, it is interesting to evaluate the punching shear strength of the bridge deck slab at interior span based on different existing equations.

Current equations in design codes were empirically derived for two-way slabs reinforced with conventional steel rebar. Researchers have recently modified the code equations to apply them to FRP reinforced slabs based on their experimental studies. These equations are presented in Table 9. The definition of the parameters can be found in the references. In non-prestressed direction (y direction), the shear strength predicted by existing equations is directly used in calculations; however, in x direction the shear strength is added up by $0.3f_{pc}b_0d$ to account for the effect of prestressing. This increase is inferred from AASHTO LRFD (2010), where f_{pc} is the prestressing stress acting on the section. Some of the main punching shear equations and the ratio of the predictions to the experimental results are summarized in Table 10.

It is seen that, all the proposed equations for FRP reinforced slab predict the punching shear strength approximately from 50% to 70% less than the actual load capacity observed in the experiment. Such a significant underestimation cannot be attributed to the conservative characteristic of these equations. It is, indeed, implying that the failure mechanism of the bridge deck slab is mostly governed by flexure rather than shear, as already discussed. In fact, flexural cracks first form around the loading plate in a larger area compared to critical perimeter of the punching failure because of the geometry of the slab, and boundary conditions. Then, due to low modulus of elasticity of AFRP bars the flexural stiffness of the slab section drops significantly which leads to larger deflection and less depth of the neutral axis. Increase in load, raises the flexural demand and reduces the neutral axis depth until the shear demand becomes higher than the shear

resistance of the concrete slab section. At this point, the load tends to punch through the slab as the slab edges are restrained. However, this cannot be considered as punching shear failure since the slab exhibited a considerable flexural behavior.

Table 9- Punching shear equations (f_c' in MPa)

Razaqpur (2009)	$V_c = 0.3\left[\left(f_c'\right)^{1/3} + 0.184\sqrt{f_c'}(E_f \rho_f)^{0.42}\right]\left(\frac{d}{b_o}\right)^{0.55} b_o d$
ACI 440.1R-06	$V_c = 0.8\sqrt{f_c'}u_{0.5d}c$
JSCE	$V_c = \beta_d \beta_p \beta_r \frac{f_{pcd}}{\gamma_b} u_{0.5d} d$
Matthys and Taerwe (2000)	$V_c = 1.36\frac{\left(100\rho_f \frac{E_f}{E_s} f_{cm}\right)^{1/3}}{d^{1/4}} b_o d$
El-Ghandour et al. (2003)	$V_c = 0.33\sqrt{f_c'}\left(\frac{E_f}{E_s}\right)^{1/3} b_o d$
Ospina et al. (2003)	$V_c = 2.77(\rho_f f_c')^{1/3}\sqrt{\frac{E_f}{E_s}} b_o d$

Table 10- Predictions of punching shear equations

Load case	$V_{u,exp}$ (kN)	predicted-to-test ratios					
		ACI 440.1R-06	JSCE (1997)	Razaqpur (2009)	Matthys and Taerwe (2000)	El-Ghandour et al. (2003)	Ospina et al. (2003)
1	700	0.36	0.38	0.41	0.48	0.53	0.59
4	770	0.32	0.32	0.37	0.44	0.49	0.53
7	880	0.28	0.28	0.32	0.39	0.42	0.47
Ave.	-	**0.32**	**0.33**	**0.36**	**0.44**	**0.48**	**0.53**

4.7.3 Deformability

In design of steel reinforced concrete, ductility concept is used to assure enough deformation will take place after yielding of steel until failure, and hence enough warning is going to be achieved. For FRP reinforced concrete; however, there is no yielding point, and so deformability is used as a more appropriate concept to evaluate the adequacy of the deformation after cracking and before failure. Different deformability indices have been proposed by researchers that can be found in Zou (2003). Three main indices are used in this paper to evaluate the deformability of the bridge deck slab at both interior span and overhang. The following equation is *Naaman and Jeong model,* which is an energy based equation

$$\mu = 0.5\left(\frac{E_{tot}}{E_{ela}} + 1\right) \tag{2}$$

where E_{tot} and E_{ela} represent the total energy and elastic energy under the load-deflection diagram, respectively. The elastic portion of the total energy can be found by unloading. *Abdelrahman model* is a deflection based equation defined as

$$\mu = \frac{\Delta_u}{\Delta_l} \tag{3}$$

where Δ_u is the deflection at failure and Δ_l is the equivalent deflection of an uncracked specimen under the same failure load. *Zou model* utilizes both deflection and load to define the deformability index

$$\mu = \frac{\Delta_u}{\Delta_{cr}} \times \frac{P_u}{P_{cr}} \tag{4}$$

where *u* and *cr* subscripts refer to ultimate and cracking stages, respectively. Load cases 1 and 5 as representatives of loading at the interior span and overhang are considered herein to measure the deformability. Table 11 shows the computed deformability index based on the above equations. It is seen that, both *Naaman and Jeong*, and *Abdelrahman* models predicts a larger deformability for load cases 5 over the load case 1, as opposed to the model proposed by Zou (2003). As confirmed by experimental observations, the deformability of the interior span is smaller than the interior span. This was also clarified by looking at the curvature distribution in the main direction of the flexure. The result of such a study showed that in load case 5, the maximum curvature of the slab in *x* direction is 50% of the ultimate curvature of the corresponding strip with unit width, while for load case 1 this value is equal to 38% which implies that the deformability of the overhang is approximately 1.32 times that of the interior span. The deformability index ratio of overhang to interior span shows that *Abdelrahman model* provides a more reasonable result compared to the other two models.

Table 11- Deformability indices

load case	*Naaman and Jeong model*	*Abdelrahman model*	*Zou model*
1	2.91	7.04	35.47
5	3.17	8.75	31.5
$(\mu_5 / \mu_1)^*$	1.09	1.24	0.88

* The deformability index ratio of load case 5 (overhang) to load case1 (interior span)

4.8 Comparison with Control Specimen

As discussed, at interior span, flexural cracks due to negative moment were first observed on top surface of the slab close to the support beams and then propagated around the loading plates. The flexural cracks due to positive moment initiated beneath the loading plate and propagated toward the support beams in a diagonal fashion. Since the deck slab at interior span is restrained by the support beams, the slab eventually failed in a punching manner. The failure mode of the interior span was realized as the compound shear-flexural failure. The contribution of the flexure was evident from the extension of the flexural cracks and also the deformability observed in the load-deflection diagram. Similar cracking pattern was reported for the control specimen and the failure mode was recognized as the punching shear at the top CIP panel and flexural failure at the bottom SIP panel (Mander et al. 2010). Corresponding load cases between AFRP and control specimens are presented in Table 12.

Table 12- Corresponding load cases

Description	AFRP specimen	control specimen
Axle load on interior span	1	2.4
Wheel load on overhang	2	1.6
Double-wheel load on adjacent interior spans	4	1.7
Axle load on overhang	5	2.3

Fig. 35 shows the load deflection diagram and cracking pattern at failure of the interior span for both AFRP and control specimen. For load case 1 representing the truck axle load on the interior span, the load capacity was found equal to 700 kN which is about 1.2 times that of the control specimen under load case 2.4. The maximum deflections are similar and equal to 19 and 21 mm for the AFRP and control specimen,

respectively. As already illustrated, the cracking pattern of the AFRP specimen was recorded on both top and bottom surfaces of the deck shown by black and gray lines, respectively. However, for the control specimen only the top cracks were reported. For load case 4 resembling the double-wheel load on the interior span, the load capacity and maximum deflection were found equal to 770 kN and 12.5 mm, respectively. It can be inferred that the axle load induces the critical case of loading, however with larger deformability as a result of applying the load in a amore distributed manner. The corresponding load case at control specimen, 1.7, was not continued until failure and hence the cracking pattern is not available in the reference for comparison.

At overhang, flexural cracks were first observed on top surface of the slab due to negative moment close to the exterior beam and then propagated around the loading plates and reached to the free edge of the slab in a triangle shape. The failure mechanism for load case 5 was mostly governed by flexure as the flexural cracks extensively propagated around the loading area and became widened conspicuously before failure. However for load case 2 the flexural failure of the loaded panel was accompanied by the shear failure of the panel-to-panel seam which indeed prevented the adjacent panel from flexural failure. Likewise, the failure mechanism of the control specimen under both load cases 1.6 and 2.3 was reported to be governed by flexure of the loaded panel and shear failure of the transverse seam (Mander et al. 2010).

Fig. 36 shows the load deflection diagram and cracking pattern at failure of the overhang for both AFRP and control specimen. For load case 5 representing the axle load on the overhang, the load capacity and maximum deflection were found equal to 225 kN and 35 mm. A larger load capacity, 350 kN, and a less deflection, 20 mm, was reported for the control specimen under the corresponding load case 2.3. For load case 2 representing the wheel load on the overhang, the load capacity and maximum deflection were found equal to 320 kN and 25 mm, respectively. The corresponding load case at control specimen, 1.6, resulted in maximum load and deflection equal to 370 kN and 12 mm. The experimental results are summarized in Table 13. Cracking pattern is indeed a function of geometry of the specimen, boundary condition, reinforcement detail, and loading configuration. Experimental results show that the cracking pattern at interior span resembles an elliptical shape, but at overhang it appears like a trapezoid. Although AFRP bars, as opposed to conventional steel, behave linearly up to rupture, so called brittle failure, the shape of failure mechanism of the AFRP and control specimen seems to be similar.

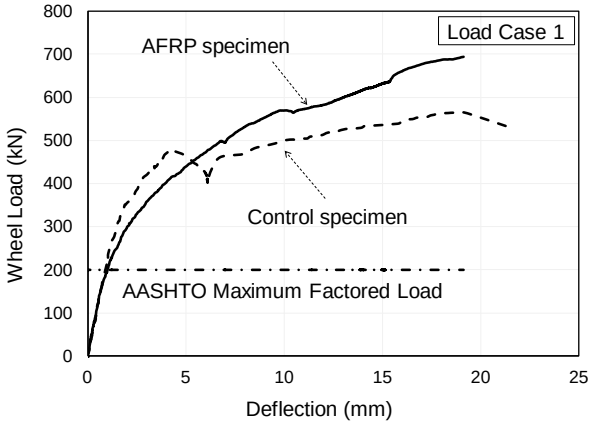

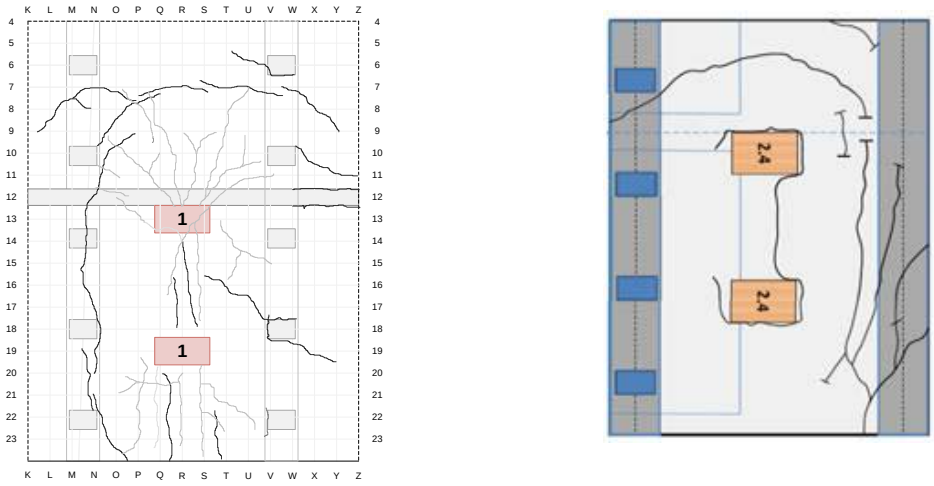

a) axle load on interior span

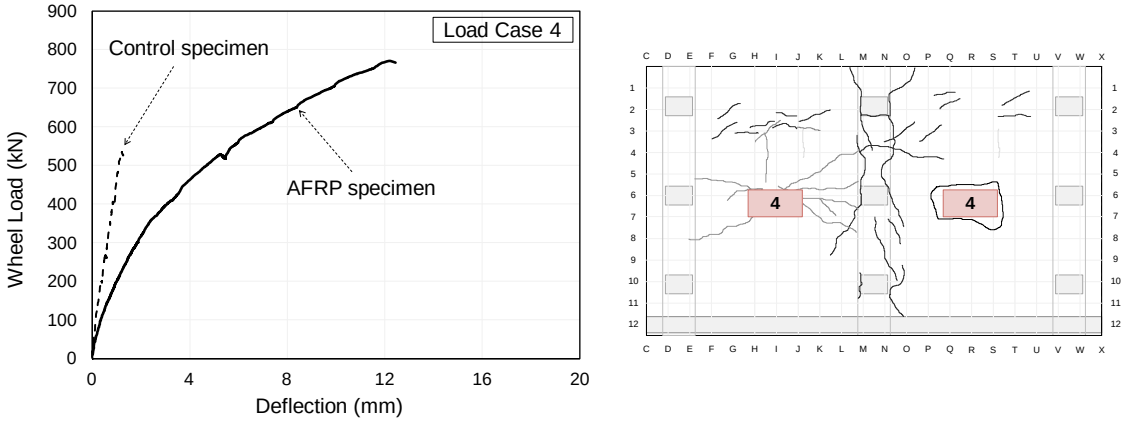

b) double-wheel load on interior span

Fig. 35. Comparison at interior span

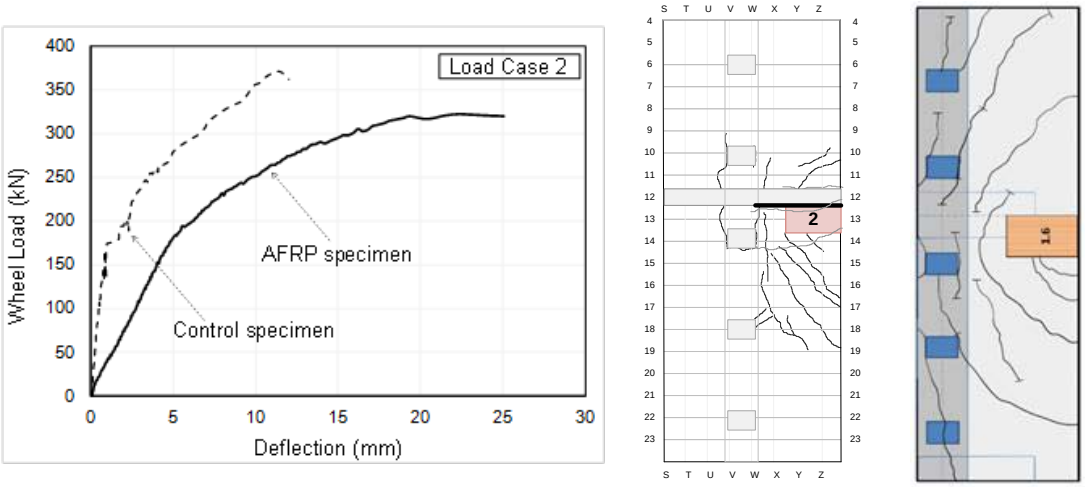

a) single wheel load on overhang

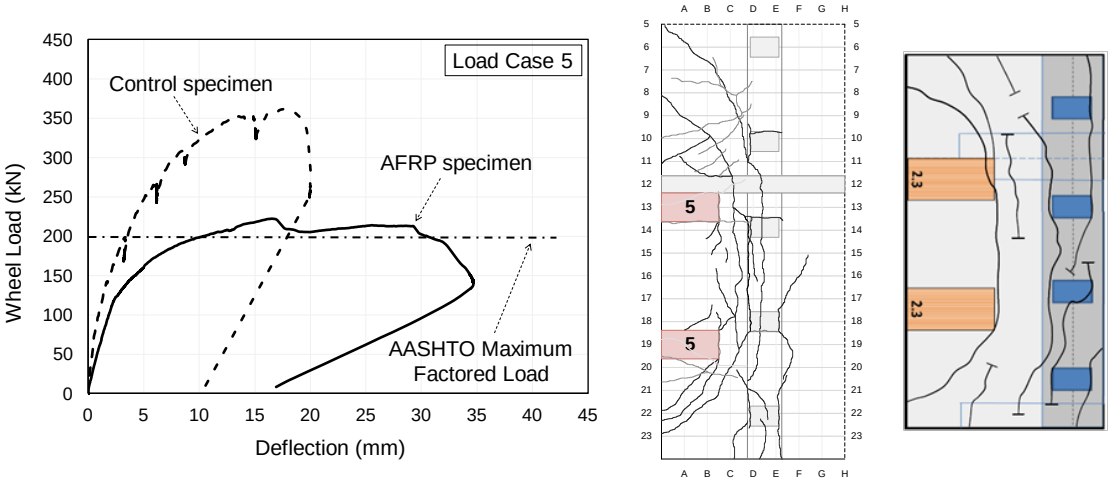

b) axle load on overhang

Fig. 36. Comparison at overhang

Table 13- Summary of the experimental results, AFRP specimen (control specimen)

	Interior span		Overhang	
Load case	1 (2.4)	4 (1.7)	2 (1.6)	5 (2.3)
Deformability (ductility)	7.04 (5.4)	2.5 (NA)	3 (7.2)	8.75 (6)
Load capacity, kN	700 (565)	770 (NA)	320 (374)	225 (360)
Load capacity / maximum factored load	3.5 (2.8)	3.85 (NA)	1.6 (1.87)	1.12 (1.8)
Maximum deflection, mm	19 (21)	12.5 (NA)	25 (12)	35 (20)

4.9 Conclusions

A full-scale bridge deck slab consisting of two full-depth precast panels was tested under concentrated load and the concept of using AFRP bars as reinforcement as well as prestressing tendon instead of conventional steel was verified. The panels were prestressed and reinforced with AFRP bars perpendicular to and parallel with the traffic direction, respectively. Load cases 2 and 5 represented the wheel load and axle load on the overhang and load cases 1, 4, and 7 indicated the axle load, double-wheel load, and single wheel load on the interior spans, respectively. The following conclusions are drawn from this experimental investigation

1- Experimental results showed a satisfactory structural performance of the bridge deck slab where the strength and serviceability criteria were met. The average failure load of the interior spans and overhangs was found 3.8 and 1.3 times the maximum factored load specified by AASHTO LRFD (2010), respectively. The deflection of the interior span at service load level was found about 1 mm which is 40% of the allowable amount specified by AASHTO LRFD (2010).

2- Flexural mechanism governed the failure mode of the bridge deck slab, particularly at the overhang. This was evident from the cracking pattern and the curvature distribution along the strong direction of the slab. The bridge deck

overhang failed due to a complete flexural mechanism under load case 5 (axle load) and a compound shear-flexural mechanism under load case 2 (wheel load). In fact, under the axle load the slab failed in a more deformable manner compared to wheel load since the load is applied in a more distributed fashion. Calculations for the overhang (load case 5) showed the maximum negative curvature close to the support is equal to 0.01 which is 25 times the cracking curvature. Similar flexural mechanism was observed for the interior span; however, shear also contributed to the failure mechanism and the slab eventually failed in a punching manner due to restrained edges. Studying the curvature distribution close to failure confirmed a considerable deformability induced by flexure of the slab as the maximum curvature was found equal to 0.0075 which is about 19 times the cracking curvature. More research is still required to study the compound shear-flexural mechanism.

3- Studying the punching shear strength of the interior span based on the existing equations resulted in predictions from 30% to 50% of the actual failure load. This implies that the failure mechanism of the interior span is a compound shear-flexural failure, but mostly governed by flexure. Furthermore, these equations do not take into account the effect of reduced boundary condition.

4- In reality, truck tire pressure rarely exceeds 820 kPa and thus achieving a wheel load similar to the failure load observed in this experiment is unrealistic. Hence, it is very unlikely to have punching failure in the interior span as the failure mode. However, from theoretical point of view it is crucial to investigate the load capacity of the bridge deck slab.

5- Deformability of the slab was measured by three different indices. *Abdelrahman model* which is a deflection based equation resulted in more reasonable predictions. The authors believe that studying the curvature distribution is a more rational way to measure the deformability as it is directly related to flexure. The

deformability ratio of the overhang to the interior span was found about 1.32 which is close to what *Abdelrahman model* predicts $\mu = 1.24$.

6- Panel-to-panel seam showed a satisfactory performance and sufficient structural connectivity as the flexural cracks were completely transferred from the panel under the load to the adjacent panel. This could also be inferred from the deflection profile along the axis *y*.

7- Using nine shear pockets per panel, each reinforced with two high strength bolts as shear connector, was found sufficient to provide a complete composite action between the deck and support beams since no failure was observed at the connection, and also flexural cracks on top of the deck and close to the shear pockets showed the developed negative moment at the slab support.

5. EXPERIMENTAL STUDY OF AFRP CONCRETE STRIP ELEMENTS OF THE BRIDGE DECK SLAB

5.1 Introduction

The linear behavior of FRP bars up to rupture, so called brittle failure, can be a design concern that substantially reduces the desirable ductility typically observed in steel reinforced concrete members. Therefore, the plastic methods such as yield line theory commonly used for failure load analysis of steel reinforced concrete slabs seems not to be applicable in this case. In fact, application of FRP bars in bridge deck slabs lacks a rational method of analysis that can evaluate the load capacity of the slab. Although FRP bars are non-ductile materials, their low modulus of elasticity enhances the deformability of the concrete section in the post-cracking region that offsets the lack of ductility to some extent. This was well observed in the experimental results of the bridge deck slab presented in Chapter 4. In fact, this is a promising point that holds the potential for application of failure load analysis methods analogous to plastic methods typically employed for steel reinforced concrete slabs. However, the first step to explore such a potential, is to experimentally study the structural performance of the strip elements of the bridge deck slab in terms of strength, deformation capacity, and the failure mode. This is the main objective of this chapter which helps to characterize the structural capacity of the bridge deck slab section.

In this Chapter, the experimental plan for testing the strip specimens is put into perspective. Two strip specimens, one reinforced and one prestressed with AFRP bars representing the bridge deck slab section with unit width in parallel and perpendicular to the traffic direction, respectively, are tested under flexure. Subsequently, two strip specimens as samples of panel-to-panel seam are tested under both flexure and shear. The experimental results are reported in terms of ultimate strength, deformation capacity, and failure mode. In studying the experimental results, other than maximum curvature at midspan, a close view will be on curvature distribution along the strip specimen as it clarifies the extent of cracking and contribution of the flexure in failure.

5.2 Experimental Strip Specimens

Experimental strip specimens studied in this research belong to the full-scale bridge deck slab specimen discussed in Chapter 4. In order to find out the structural behavior of the slab section in both *x* (prestressed) and *y* (non-prestressed) directions as well as at the panel-to-panel seam, four strip specimens were constructed and tested. Each strip was 300 mm wide, 1800 mm long, and has the same thickness, reinforcement ratio, and concrete material as the bridge deck slab (Fig. 37). The experimental program included flexure tests of non-prestressed and prestressed strips as well as flexure and shear tests of seam strips. It should be noted that the non-prestressed bar in *y* direction that has been shown in two layers at Section C-C, is indeed a one continuous bar bent at the location of seam taking the advantage of thermoplastic characteristics of the AFRP bars (Section B-B). When casting the seam specimen, the joint was first left hollow and once the rest of the strip hardened the seam was casted. This is for the sake of consistency with construction procedure of the full-scale bridge deck slab. The compressive strength of concrete is shown in Table 14 for each strip specimen.

Table 14- Compressive strength of concrete, day of test

Specimen	Strength (MPa)
Non-prestressed strip	41.4
Prestressed strip (rebuilt)	48.3
Seam strip (non-joint)	48.3
Seam strip (joint)	32.4

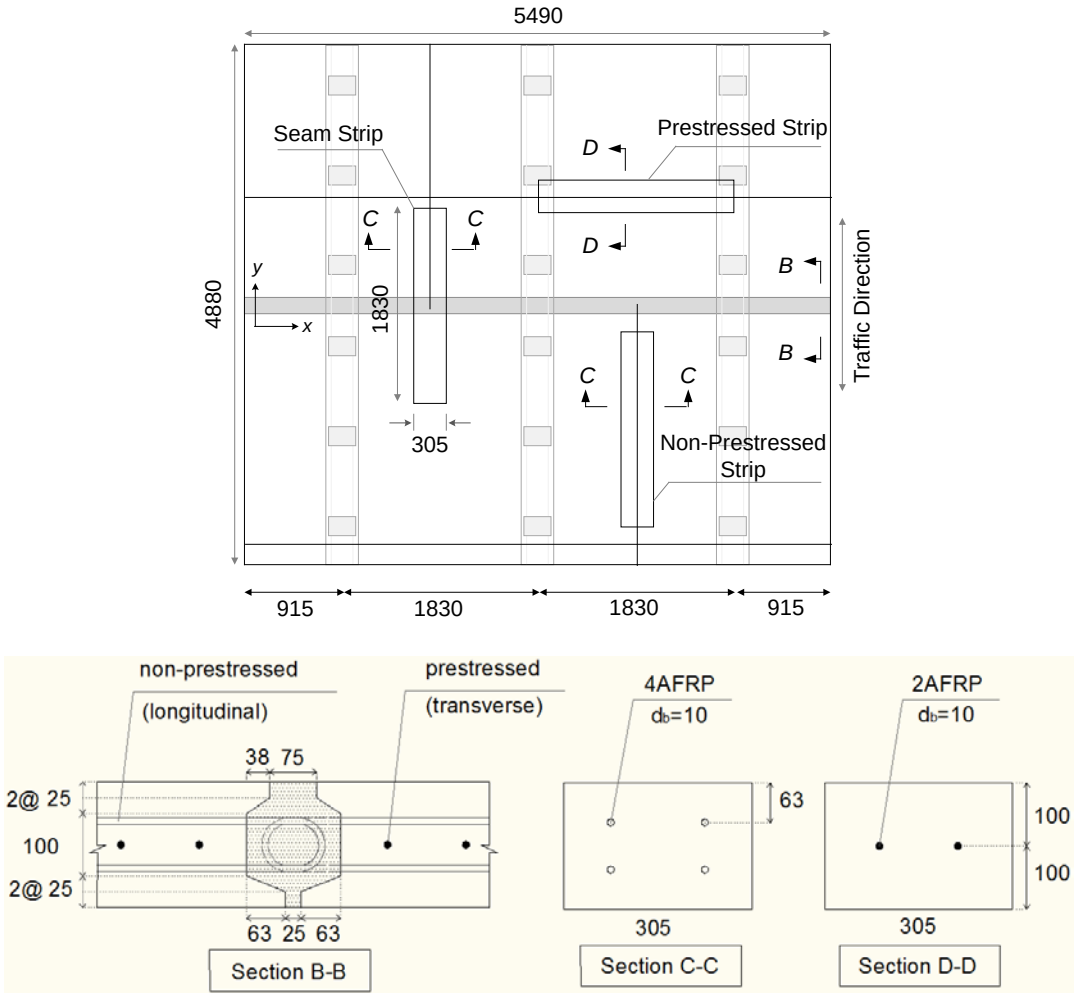

Fig. 37. Experimental strip specimens layout

5.3 Test Setup and Instrumentation

Non-prestressed and prestressed strip specimens as well as one of the seam strip specimens were tested under flexure using four-point loading configuration, and the other seam strip specimen was tested under shear. A 450 kN actuator was used to monotonically apply the load until failure, where the load was measured through an in-series load cell attached to the tip of the actuator. All strip specimens were simply supported beams where the deflection of the strip was measured at every 150 mm via

STP (String Pot). This helps to obtain the deflection profile and compute the curvature distribution along the beam, accordingly. Figs. 38 and 39 show the flexure and shear test setup, instrumentation, and the corresponding shear and moment diagrams. In flexure test, the effective length of the specimens between the simple supports was 1800 mm and the shear span length was equal to 675 mm. The maximum curvature at mid-span can be computed through two horizontal LVDTs (Linear Variable Differential Transformer) mounted on the side face of the beam at top and bottom fibers given the plain section remains plain after bending. The numbers shown under each STP represent the *x* coordinate assigned to compute the curvature distribution from deflection profile.

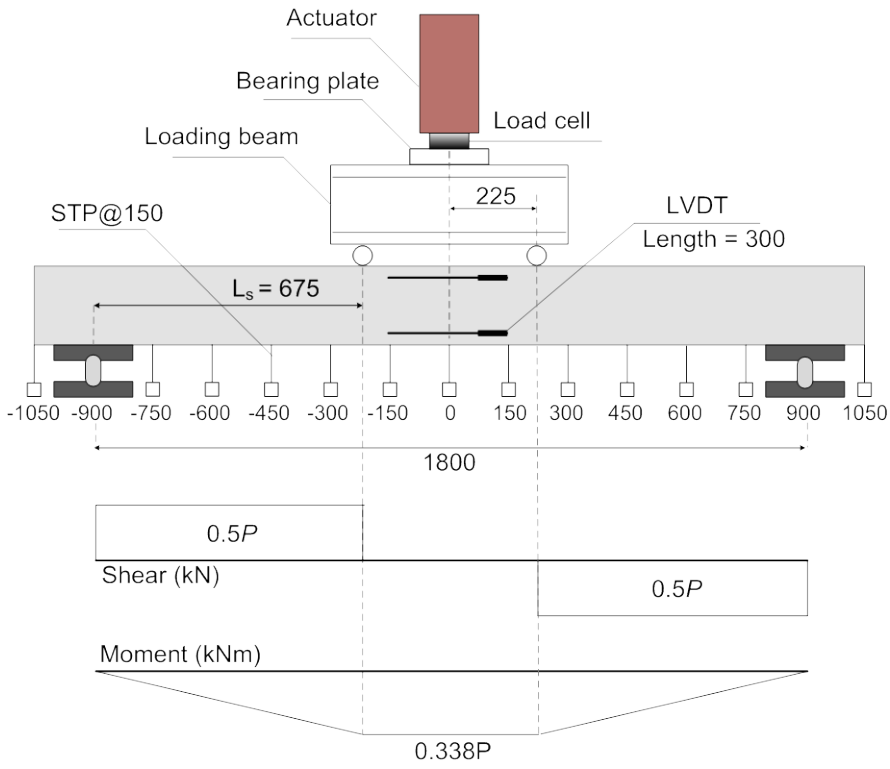

Fig. 38. Flexure test setup

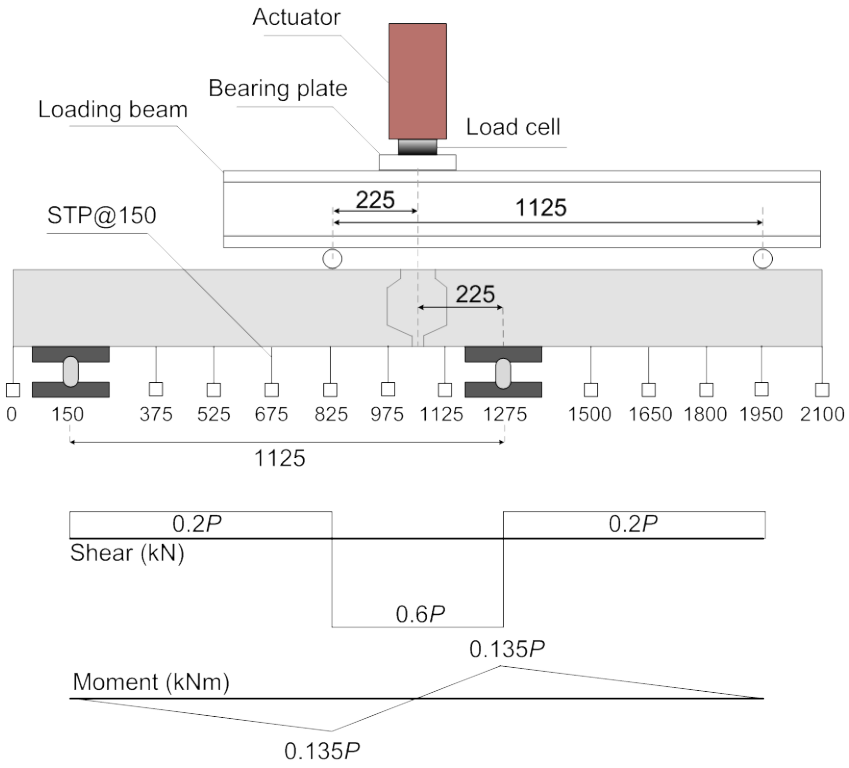

Fig. 39. Shear test setup

5.4 Prestressed and Non-Prestressed Strip Specimens

5.4.1 Experimental results

Non-prestressed strip failed due to concrete crushing as a result of compound shear-flexural mechanism at the shear span. This type of failure was expected as the shear span to depth ratio is $3<L_s/d=4.9<7$ and the strip is categorized as a slender beam according to Park and Paulay (1975). Flexural cracks were first observed within the constant moment span at P=23 kN which resulted in a considerable reduction in flexural stiffness. With increasing the load to P=36 kN, the inclined shear cracks initiated at a distance of 113 mm from the constant moment span, and propagated toward the loading points. The shear diagonal cracks widened and became clearly observable at P=53 kN and the strip eventually failed due to crushing of the concrete at P=70 kN with no evidence of tendon

rupture (Fig. 40). The maximum deflection at mid-span was found about 38 mm and significant deformability as well as enough warning before failure was achieved. The flexural strength and curvature capacity were reported equal to 23.5 kNm and 0.024, respectively. The curvature, herein, is expressed in a normalized format equal to curvature multiplied by the height of the section.

Prestressed strip failed due to rupture of the tendons while limited crushing of the concrete was observable. Flexural cracks were first observed within the constant moment span at P=40 kN and propagated vertically toward the top fibers of the section. The post-cracking flexural behavior of the prestressed strip was found nonlinear as a result of decompression of the prestressed section. No evidence of shear diagonal cracks was found in the shear span which seems to be reasonable as the shear span to depth ratio L_s/d=6.75 is close to 7 and the strip can be considered as a very slender beam. With increasing the load to P=60 kN concrete crushing commenced, however the strip suddenly failed at P=63 kN due to rupture of the tendons before concrete crushing can dominate the failure mechanism (Fig. 41). As will be discussed, based on the moment-curvature analysis, tendon rupture was expected as the failure mode, since due to prestressing; only 45% of the ultimate strain of the AFRP bars was left for flexure. The maximum deflection was found equal to 30 mm and considerable deformability was gained. The flexural strength and curvature capacity was reported 21 kNm and 0.02, respectively. Experimental moment-curvature and load-deflection response of non-prestressed and prestressed strips are shown in Fig. 42.

Fig. 40. Concrete crushing due to shear-flexural failure (non-prestressed strip)

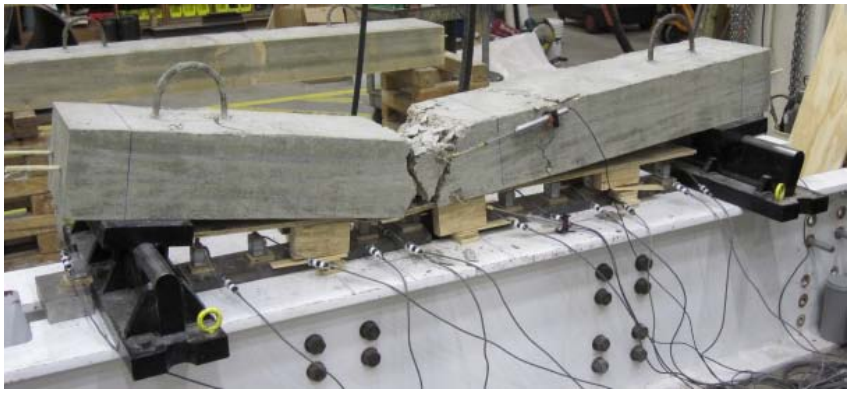

Fig. 41. Failure due to tendon rupture (prestressed strip)

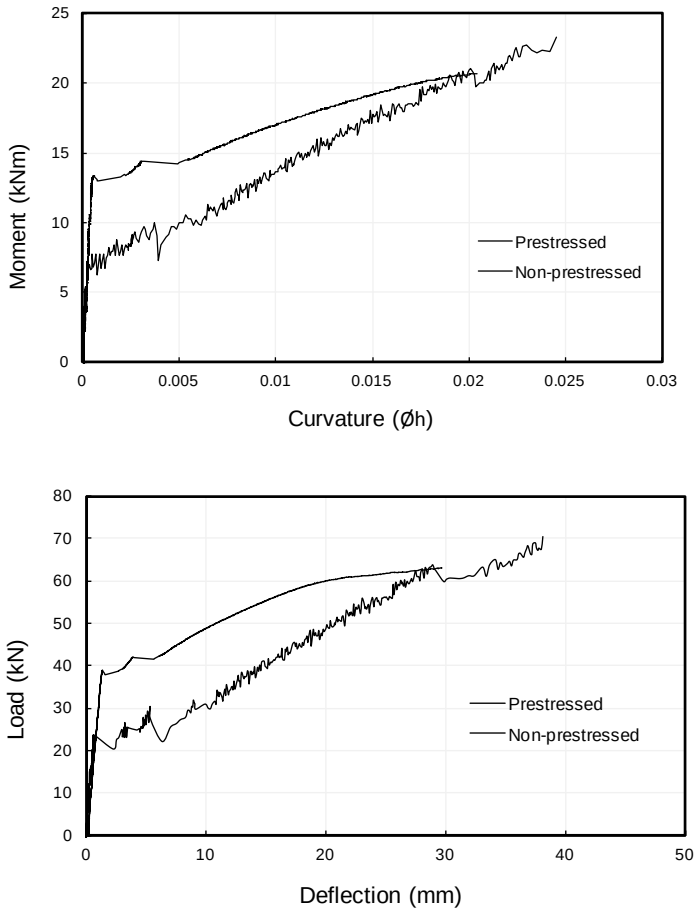

Fig. 42. Experimental results for prestressed and non-prestressed strip specimens

5.4.2 Moment-curvature analysis

An extensive computational model was developed to study the moment-curvature behavior of the strip specimens through the fiber element analysis. Material properties and effective prestressing force were modeled according to the experiment, and a refined iterative solution was employed to capture the cracking and failure. Popovic's equation (1973) was used to model the stress-strain behavior of the concrete in compression as follows

$$f_c = \frac{n(\varepsilon_c / \varepsilon'_c)}{n - 1 + (\varepsilon_c / \varepsilon'_c)^{nk}} f'_c \tag{5}$$

where ε'_c is the strain corresponding to the compressive strength of the concrete f'_c, n is a curve-fitting factor, and k is a factor that controls the slopes of the ascending and descending parts of the stress-strain curve. Formulas for the factors n and k can be found in the reference. To model the stress-strain behavior of the concrete in tension the following equation proposed by Bischoff and Paixao (2004) was used where the effect of tension stiffening, the ability of the concrete to bear tension between cracks, is taken into account

$$f_t = f_{cr} \exp[-1100(\varepsilon_c - \varepsilon_{cr})(E_f / E_s)] \tag{6}$$

where ε_{cr} is the strain corresponding to the tensile strength of the concrete f_{cr}, and E_f and E_s are the modulus of elasticity of FRP bars and steel rebar, respectively. As shown in Fig. 43, the result of moment-curvature analysis is in good agreement with the experimental data in terms of cracking and failure load as well as the post-cracking flexural stiffness. Bilinear model of moment-curvature response is computed for both non-prestressed and prestressed strips to compare with experimental and analytical results. As a result of prestressing, the moment-curvature response of the prestressed strip is very close to the bilinear model showing the negligible effect of tension stiffening (Pirayeh Gar et al. 2012). However, for non-prestressed strip the experimental curvatures are larger than bilinear model, and the effect of tension stiffening is evident from the difference between the experimental and cracked response. The summary of analytical and experimental results is presented in Table 15.

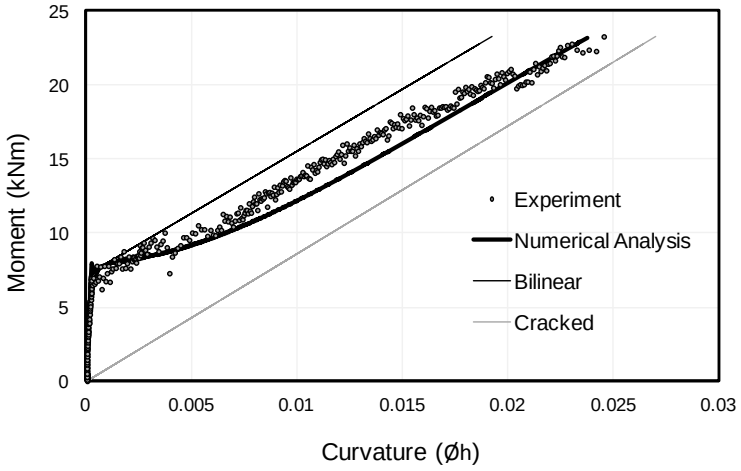

a) non-prestressed strip

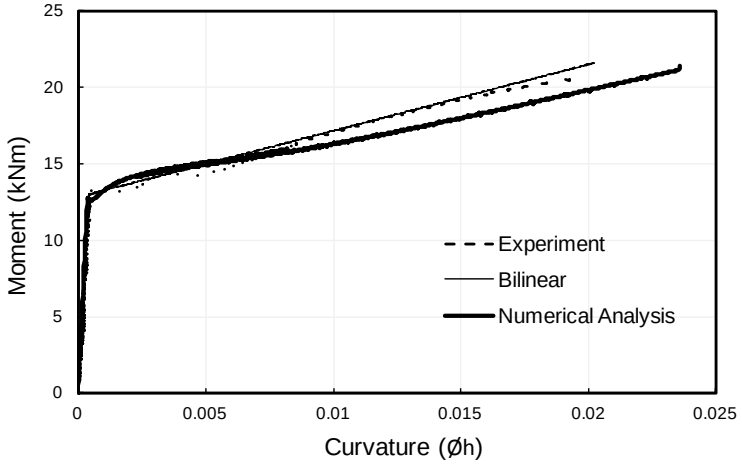

b) prestressed strip

Fig. 43. Moment-curvature analysis

5.4.3 Curvature distribution analysis

In experimental research, the maximum curvature is typically studied at the constant moment span, while distribution of the curvature along the specimen, particularly at the shear span, is not noticed. This is significant as it shows the extent of cracking and contribution of the flexure in failure mechanism.

Table 15- Summary of experimental and analytical results (moment: kNm)

Specimen	M_{cr}	M_u	$(\emptyset h)_{cr}$	$(\emptyset h)_u$	I_{cr}/I_g	ε_f^{u*}	ε_c^{u*}	failure mode
Non-prestressed (Experiment)	7	23.5	0.00025	0.024	—	—	—	1*
Non-prestressed (Analysis)	7.5	23.15	0.00022	0.023	0.03	0.013	< -0.003	1
Prestressed (Experiment)	13.15	21	0.0005	0.02	—	—	—	2*
Prestressed (Analysis)	12.8	21.3	0.0004	0.023	0.015	> 0.02	-0.0027	2

1= concrete crushing 2= tendon rupture ε_f^u = maximum tensile strain at AFRP bar when specimen fails ε_c^u = maximum compressive stress at concrete when specimen fails

Given the deflection profile recorded by STPs, curvature distribution is computed using the finite difference method. Experimental deflection and curvature along the strip are then compared with the analytical results based on the bilinear moment-curvature response of the section which is a simple model that can be used for engineering calculations. The first step of such analysis is to determine the moment diagram along the specimen. For non-prestressed strip, experimental results showed a tiny negative curvature at the simple supports. Further investigation revealed that due to bending of the specimen a frictional force was developed between the steel support and concrete strip and resulted in a small negative moment at the support. Therefore, the moment diagram is modified to account for the effect of such a frictional force given the friction coefficient μ=0.5. This problem, however, was fixed before testing the prestressed strip by releasing the displacement of the support in *x* direction. The inclined shear diagonal cracks induce a tensile force in AFRP reinforcing bars in addition to the tension caused by flexure. This additional tension increases the moment at the shear span, and hence the moment diagram needs to be modified, accordingly (Park and Paulay 1995). The detail of such calculations to modify the moment diagram is presented as follows.

5.4.3.1 The effect of friction at support

As discussed about the non-prestressed strip, small amount of negative curvature was found close to the support indicating the presence of a negative moment. Further investigation revealed that the simple support is restrained against displacement in *x* direction; thereby a friction force was developed between the steel support and concrete strip as a result of bending. As shown in Fig. 44, assuming a friction coefficient factor of $\mu=0.5$ gives the horizontal friction force equal to *P/4* which induces a negative moment $M'=Ph/8$, where *h* is the height of the section. Although accounting for the effect of friction force does not cause a considerable negative moment, it results in a more accurate evaluation of the curvature distribution.

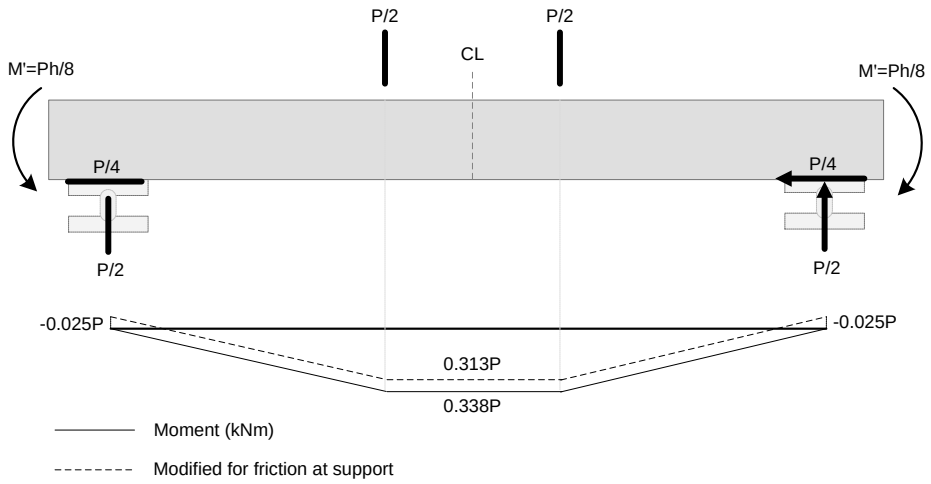

Fig. 44. Modification of moment diagram due to friction at support

5.4.3.2 The effect of shear diagonal cracks

Shear diagonal cracks increase the tension in the bottom reinforcement depending upon the magnitude of the shear and the angle of the diagonal crack. As a result of such an additional tension induced in the bottom reinforcement, the moment at the shear span increases, thereby the constant moment span becomes somewhat

larger and the moment at support is no longer zero. As shown in Fig. 45, x indicates the extension of the constant moment span and ΔM represents the increase in moment. The additional tension induced by the shear diagonal crack in the bottom reinforcement, ΔT, can be found from (Park and Paulay 1990)

$$\Delta T = \frac{V}{2tg\theta} = \frac{P}{4tg\theta} \tag{7}$$

where V is the shear force equal to $P/2$, and θ represents the slope of the crack. This additional tension induces an increase in moment equal to

$$\Delta M = \Delta T(jd) = \left(\frac{V}{2tg\theta}\right) jd \tag{8}$$

the extension of the constant moment span now can be found using the following equation

$$tg\alpha = V = \left(\frac{\Delta M}{x}\right) = \frac{Vjd / 2tg\theta}{x} \rightarrow x = \frac{jd}{2tg\theta} \tag{9}$$

where α is the slope of the moment diagram.

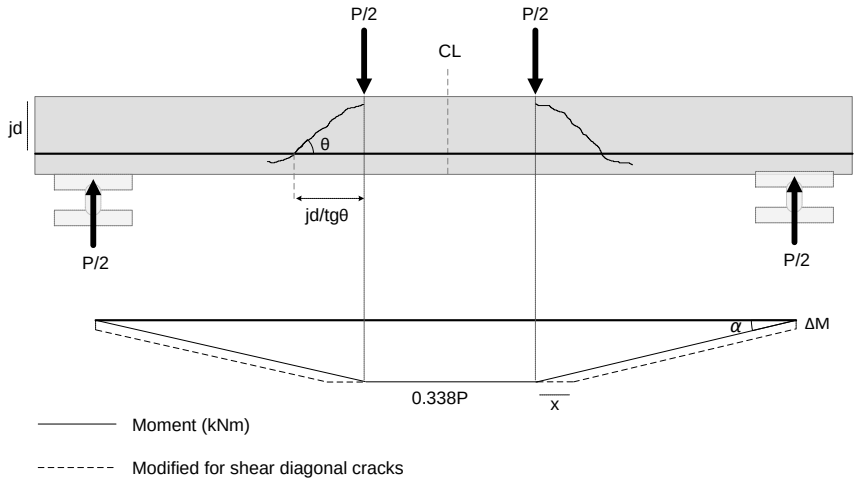

Fig. 45. Modification of moment diagram due to shear diagonal cracks

Having the moment diagram known, the theoretical curvature distribution based on the bilinear model is computed, and the deflection profile is subsequently found using the conjugate beam theory. Figs. 46 and 47 illustrate the curvature distribution for non-prestressed and prestressed strips close to failure. The results of analysis for non-prestressed strip shows that the bilinear model underestimates the maximum curvature and deflection at constant moment span, but gives nearly accurate values at the shear span. The curvature distribution shows that about 85% of the strip length is cracked before the specimen fails. Excessive cracking and low modulus of elasticity of AFRP bars results in a considerable deformability and desirable warning before failure which can offset the non-ductile behavior of AFRP reinforcing bars to some extent. For prestressed strip, the bilinear model seems to give conservative results particularly at the shear span. However, the maximum curvature at mid-span is in good agreement with the experimental result. The curvature distribution demonstrates that about 50% of the strip length is cracked before failure which indicates a more localized failure compared to the non-prestressed strip. The prestressing force increases the cracking strength and stiffness of the strip, but rather less capacity is left for flexure as there is an initial tensile and compressive strain in AFRP bars and concrete, respectively. As shown in Figs. 40 and 41, this was well inferred from the experiment as the prestressed specimen failed with a much localized cracking pattern at midspan.

5.5 Seam Strip Specimen

5.5.1 Flexural test

Similar flexural test procedure used for non-prestressed and prestressed strip specimen is employed to find out the flexural resistance of the seam strip specimen. Experiment showed that at a very low level of load P=10 kN, the specimen completely cracked from the seam and failed while the cracking load was estimated about P=21 kN. This was found due to the fact that the reinforcing bars in the left and right part of the seam are 180^{o} bent at the joint but not continuous to transfer the tension to the concrete and hence the joint acts as a hinge.

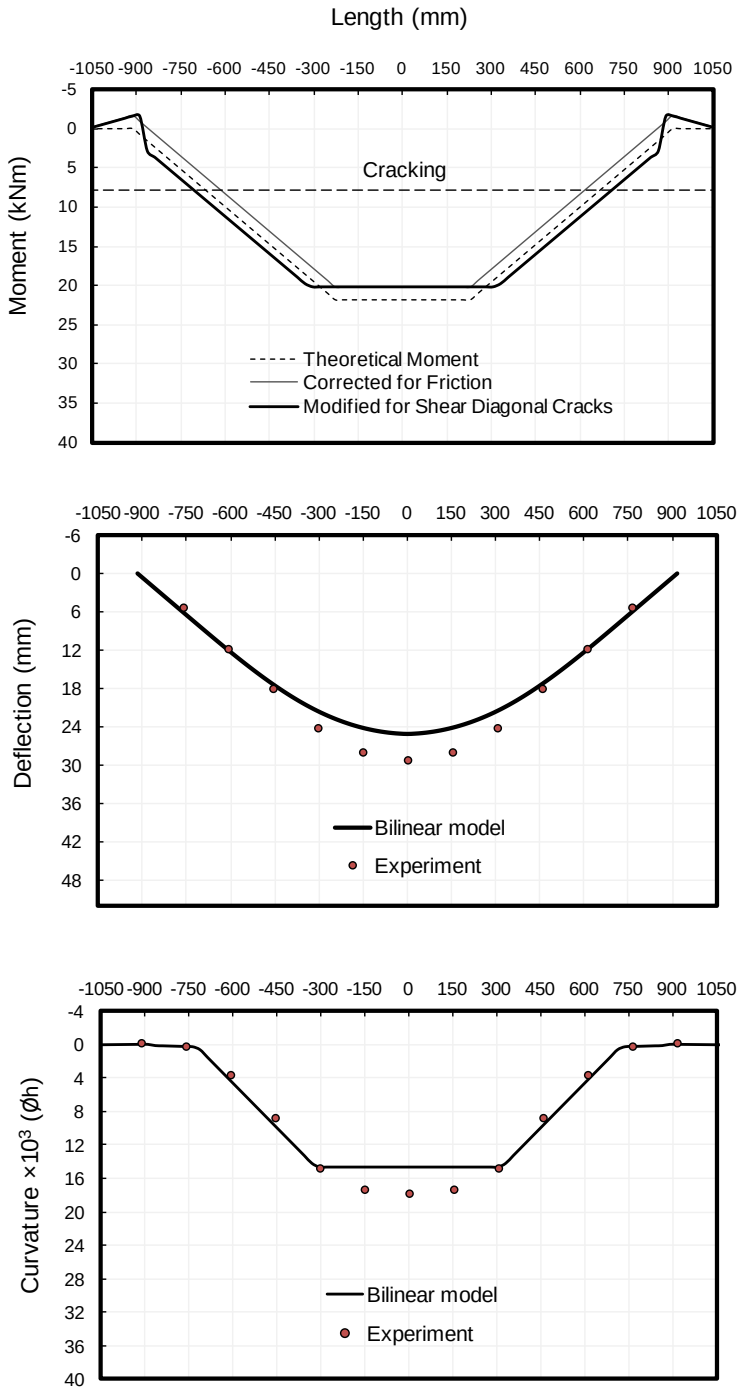

Fig. 46. Curvature distribution and deflection profile close to failure (non-prestressed strip P=63.4 kN)

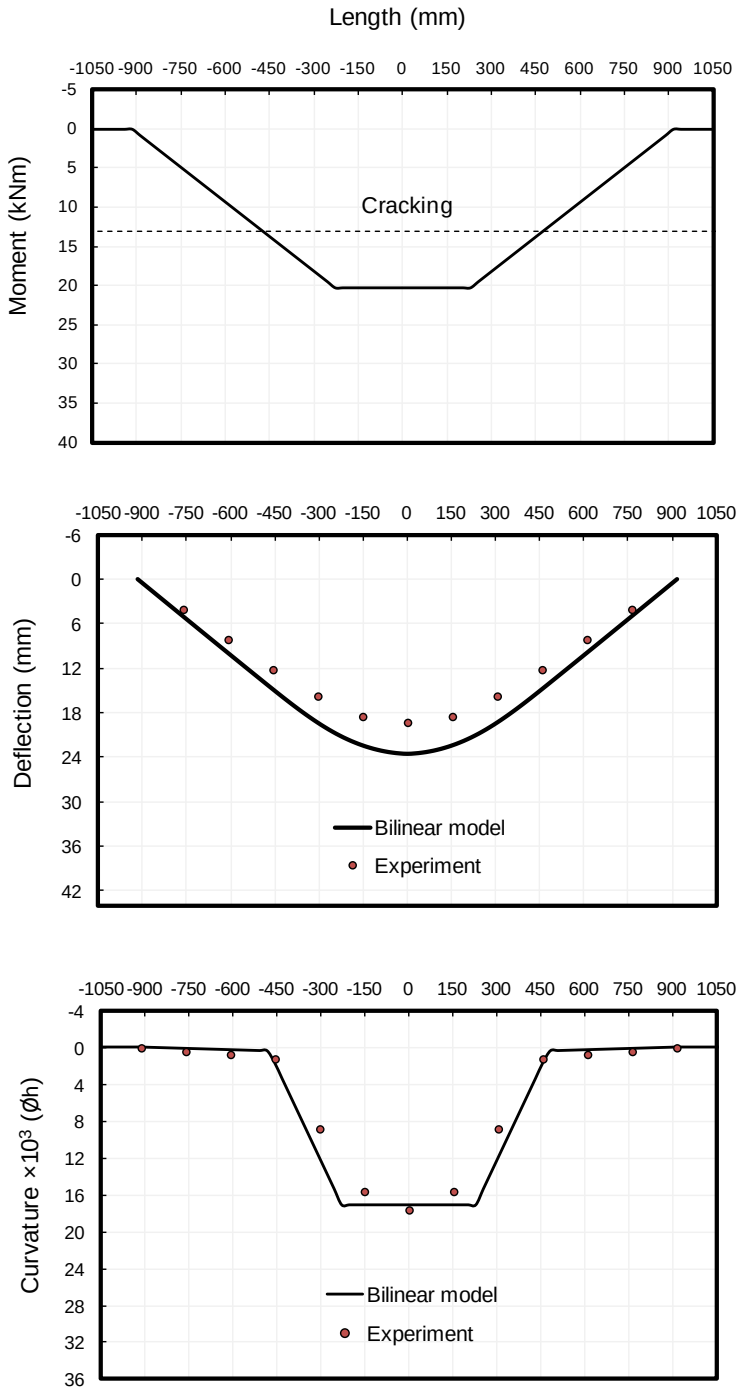

Fig. 47. Curvature distribution and deflection profile close to failure (Prestressed strip P=60 kN)

The negligible flexural strength observed in the experiment is because of very limited transfer of tension by the bent portion of the AFRP bars at the joint. Failure mode and load-deflection diagram are shown in Fig. 48. Based on the test results, the flexural capacity of the seam with the detail shown in Fig. 37 is recognized as negligible.

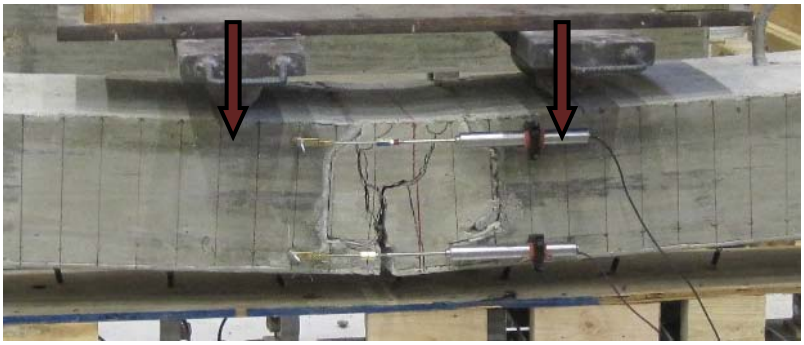

a) flexural failure of the seam specimen

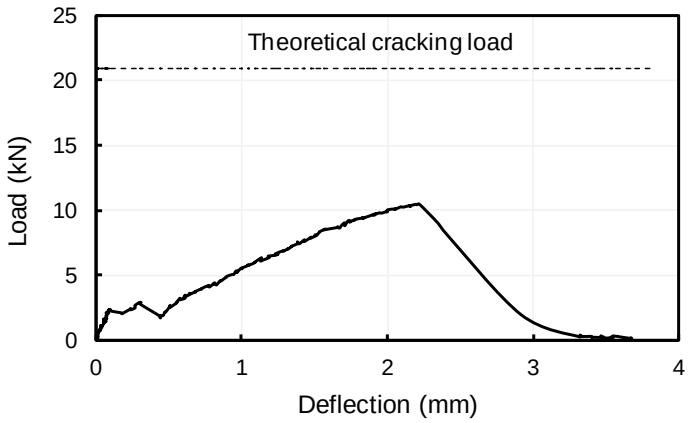

b) load-deflection response

Fig. 48. Flexural test of seam strip specimen

5.5.2 Shear test

Shear test of the seam strip specimen showed an acceptable resistance of the joint. Fig. 49 shows the load deflection graph where the applied load at the shear span is 80% of the actuator force, and the shear force at the shear span is 60% of the actuator force referring to the shear diagram. The deflection is recorded by the STP whose coordinate is x=825 mm recalling Fig. 39. When the applied load at the shear span reached to P=39 kN, the top left and the bottom right corner of the seam was crushed and resulted in a significant reduction in shear stiffness of the joint. With increasing the load, shear diagonal crack at the seam started to widen and became more evident and the joint eventually failed at load P=54 kN due to crushing of the concrete in the diagonal direction (Fig. 49). The maximum deflection was equal to 22 mm which shows a significant deformability achieved through the shear deformation of the joint. The shear capacity of the joint can be evaluated as

$$V_u = 0.6P_u = 0.6\times 68 \approx 41 \text{ kN} \rightarrow v_u = V_u/(bd) = 41000/(300\times 137) = 1 \text{ MPa} \quad (10)$$

$$f'_c = 32.4 \text{ MPa} \rightarrow \beta = v_u / \sqrt{f'_c} = 0.175 > 0.17$$

Calculations show the shear capacity of the seam equal to 41 kN (1 MPa) corresponding to β =0.175. According to ACI 318, $\beta > 0.17$ indicates an acceptable shear resistance of the joint. In order to theoretically find the failure load of the seam under shear, Compatibility Strut and Tie Analysis (CSTA) is employed. In this method, the shear induced compressive force is transferred through the combination of truss and arch struts while the tension force is carried by the longitudinal rebar. A 2D truss including concrete struts and AFRP ties is adopted to model the shear failure mechanism where the boundary condition is applied based on the existing shear and moment at both ends of the truss. Fig. 50 shows the strut and tie model and the distribution of a unit shear force between truss members. Since the arch is not very steep, it undergoes a significant compression force to keep the shear span in equilibrium. The width of the arch depends upon the ratio of the transverse bars to longitudinal bars as well as the shear span-to-depth ration of the section. According to Mander et al. (2011), the width of each arch

between AFRP ties is found about 80% of their spacing, ηb= 0.8×75=60 mm. The depth of the arch can be calculated referring to Holden et al. (2003)

$$W_a = 0.375\,jd / \cos\beta = 0.375\times 137.5 \text{ (mm)}/\cos 18^{o} = 54 \text{ mm} \quad (11)$$

The compressive strength of the arch is indeed less than f_c' due to the effect of the tensile strain perpendicular to the arch direction, ε_1 .

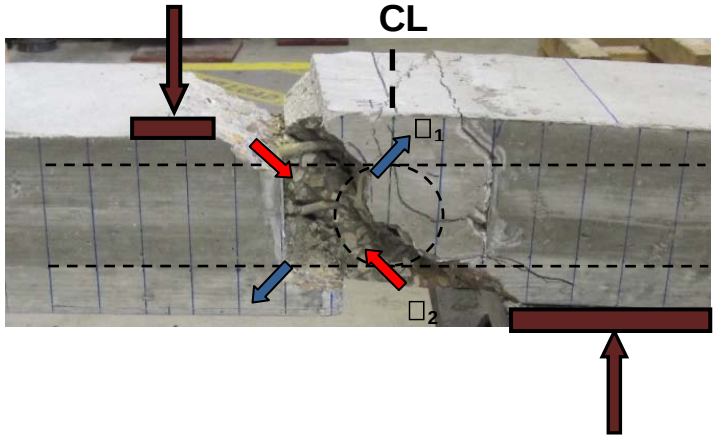

a) shear failure of the seam specimen

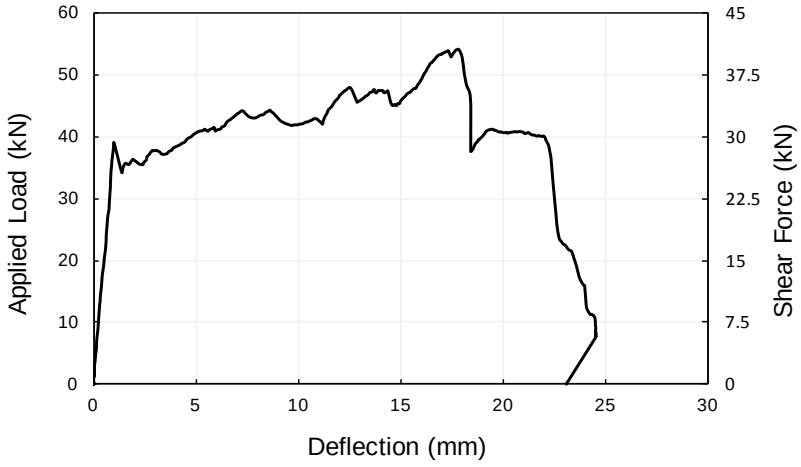

b) load-deflection response

Fig. 49. Shear test of seam strip specimen

The reduction factor, ξ, can be computed as (Mander et al. 2011)

$$\xi = \frac{1}{1+0.25\left(\varepsilon_1 / \varepsilon_2\right)} \tag{12}$$

where ε_2 is the compressive strain of the arch which is typically assumed 0.002 at failure. To find the ε_1, the dummy points A and B are defined, as shown in Fig. 50, so that the line AB be perpendicular to the arch direction. If the truss is analyzed for the ultimate load, the change in length of line AB can approximately represent ε_1.

Taking the advantage of computer modeling, the tensile strain ε_1 was found about 0.01 which results in the reduction factor equal to $\xi = 0.44$. Therefore, the compressive capacity of the arch can be computed as

$$P_a = (\xi f_c') \times (\eta b) \times W_a = 0.44 \times 32.4 \times 60 \times 54 = 46.19 \text{ kN} \tag{13}$$

given three arches between the AFRP bars, the shear capacity of the seam is equal to

$$V_u = 3 \times 46.19 \text{ (kN)} \times \sin 18^o = 42.82 \text{ kN} \tag{14}$$

which is close to the experimental result V_u= 41 kN. As the compatibility strut and tie model shows, there is a biaxial state of compressive forces at the center of the shear span which increases the strength of the arch and lead the failure out of this region where the tensile stresses can be developed perpendicular to the arch direction. This is well confirmed by the experiment, Fig. 49(a), where the failure is seen to be shifted to the left of the center.

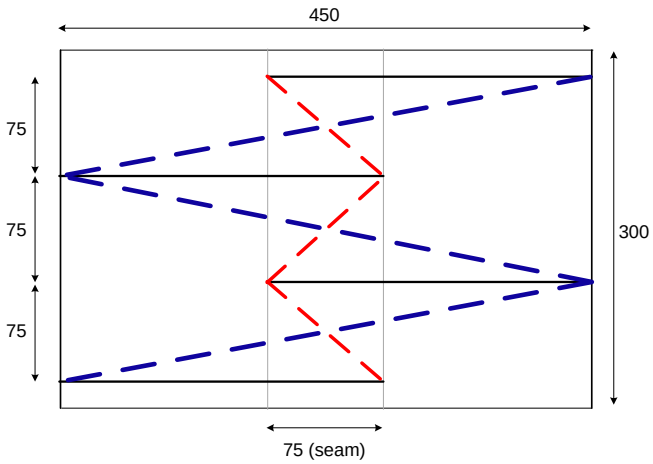

a) plan view

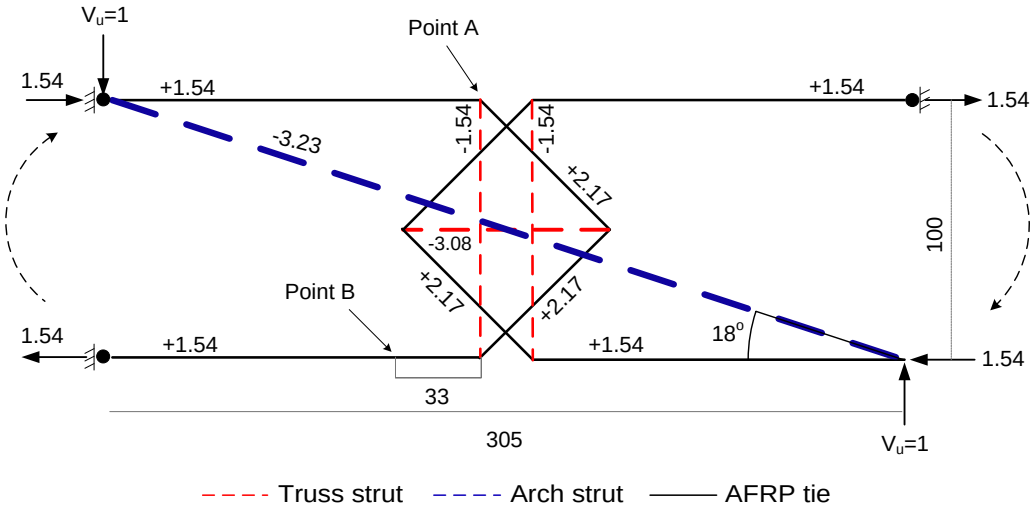

b) side view

Fig. 50. Compatibility strut and tie model

5.6 Discussion

Failure load analysis of steel reinforced concrete slabs can be done using the plastic methods of analysis such as yield line theory. This is applicable because of the ductility of the steel reinforced concrete section, which is the ability of sustaining inelastic deformations once the reinforcing steel yields. In contrast, FRP reinforced concrete

sections do not exhibit ductility due to linear and brittle behavior of FRP bars, and hence plastic methods of analysis may not be viable for failure load analysis of the bridge deck slab. However, the experimental and analytical results of testing the strip elements of a full-scale AFRP concrete bridge deck slab showed a significant post-cracking deformation, so called deformability. This mainly originates from the low modulus of elasticity of AFRP bars resulting in low post-cracking flexural stiffness and larger deformations, consequently. For instance, the post-cracking curvature capacity was found 95 and 40 times the cracking curvature for non-prestressed and prestressed strips, respectively. When a two-way FRP slab cracks in the maximum moment direction, the moment is substantially redistributed to the other directions due to considerable drop in flexural stiffness of the slab section in the crack direction as a result of low modulus of elasticity of FRP reinforcement. This, in fact, has a similar impact on response of the slab as yielding of the reinforcing steel has. This considerable deformability offsets the lack of ductility to some extent and enhances the possibility for application of plastic analysis concept for failure load analysis of FRP reinforced concrete slabs. Although the interaction between strip elements in x and y directions should be considered when analyzing a two-way slab, the bilinear response of the strip elements with low post-cracking flexural stiffness brings the thought that the plastic methods of analysis may be applicable if the response is approximated with an equivalent elasto-plastic graph.

5.7 Conclusions

Four AFRP concrete strip specimens were selected from a full-scale AFRP concrete bridge deck slab and tested in an intent to characterize the behavior of the slab section in terms of strength, curvature capacity, and failure mode. The experimental program included the flexural test of non-prestressed and prestressed AFRP concrete strips representing the bridge deck section in parallel and perpendicular to the traffic direction, respectively. Also, two strip specimens representing the slab section at panel-to-panel seam were considered for shear and flexure test. The following conclusions are drawn from this study:

1- Non-prestressed strip specimen failed due to concrete crushing in a shear-flexural manner with no evidence of tendon rupture. The ultimate strength M_u=23.5 kNm and the curvature capacity $(\emptyset h)_u$=0.024 were found at failure. Significant deformability was achieved as a result of excessive cracking and low modulus of elasticity of AFRP bars that can offset the non-ductile behavior induced by AFRP reinforcing bars.

2- Prestressed strip specimen failed due to rupture of the AFRP bars while crushing the concrete was already commenced. The ultimate strength M_u=21 kNm and the curvature capacity $(\emptyset h)_u$=0.02 were found at failure. The deformability was considerable; however, the strip failed with a localized cracking pattern as opposed to non-prestressed strip.

3- The result of moment-curvature analysis was in very good agreement with the experimental results in predicting the cracking and failure values. Modeling the tension stiffening via a rational equation is an influential factor affecting the accuracy of numerical analysis in post-cracking stages.

4- Studying the curvature distribution for the non-prestressed strip showed that the bilinear model underestimates the maximum curvature and deflection at midspan; however, it gives acceptable results in the shear span. For prestressed strip, the bilinear model seems to be a proper assumption, somewhat conservative though. The results confirmed the larger extent of cracking at failure in non-prestressed strip compared to the prestressed one due to the effect of prestressing force.

5- Flexure test of the seam strip specimen revealed a negligible flexural strength, and the joint basically behaved like a hinge. This makes sense as the bars are bent at the joint and not continuous to transfer the tension to the concrete and connect the left and right parts of the seam.

6- Shear test of the seam strip showed acceptable shear strength per ACI 318. The joint failed due to crushing of the diagonal concrete strut and the shear capacity was found equal to 41 kN (1 MPa). A compatibility strut and tie model was adopted to analyze the shear resistance of the joint which gave rise to shear capacity equal to 46 kN.

7- The observed bilinear response of the strip elements with low post-cracking flexural stiffness and considerable deformability that can be approximated with an equivalent elasto-plastic model raises the likelihood of applicability of the plastic analysis concept for failure load analysis of FRP concrete bridge deck slabs. Further investigation is still required to clarify this matter, though.

6. MODIFIED YIELD LINE THEORY FOR FAILURE ANALYSIS OF AFRP CONCRETE BRIDGE DECK SLAB

6.1 Introduction

For steel reinforced bridge decks, yield line theory has demonstrated to be a suitable method of strength analysis. Yield line theory offers an upper bound solution whose accuracy depends upon the pattern of the yield lines; however, it may underestimate the failure load when analyzing the slabs with fully restrained edges due to the effect of membrane forces. Nielsen (1999) presented accurate solutions for cantilevers subjected to point loads at the tips which can be utilized in failure load analysis of the overhangs in bridge decks. Yield line theory has been recently adapted and modified by Mander et al. (2011a, b) for full-depth precast concrete bridge deck slabs consisting of bottom stay-in-place (SIP) panels and top cast-in-place (CIP) panels prestressed and reinforced with steel, respectively. Experimental tests at a full-scale were conducted and load capacity of the overhangs as well as the interior spans was investigated. For overhangs, the yield line theory was modified to account for the development length of the steel rebar as well as the shear interaction of the partial-depth transverse panel-to-panel seam. The analytical results were acceptably accurate within 1-6% of experimental results for critical cases. For the interior spans, yield line theory was modified based on experimental observations to account for flexural failure in the lower SIP precast prestressed panels and punching shear failure in the upper CIP reinforced concrete panels. The proposed compound shear-flexure failure mechanism resulted in predictions within 2% accuracy of the actual failure load.

In contrast to steel reinforced concrete slabs where the plastic methods of analysis like yield line theory have been well established, for FRP reinforced bridge deck slabs it is difficult to find an analogous method of strength analysis because: 1) there is not enough experimental studies on FRP concrete bridge deck slabs with actual dimensions; boundary conditions; and structural details, 2) FRP bars behave linearly up to rupture and hence there is no distinct yield-point to induce a tension-based plastic behavior when

flexural strength of the section is reached. That is why the deformability concept, the ability of developing post-cracking deformations before failure, is used instead of ductility to evaluate the flexural performance of FRP concrete sections. Considerable deformability of the FRP RC and PRC slabs observed in existing experimental data as a result of low modulus of elasticity of FRP bars raised the question whether yield line concept can be modified and extended for FRP concrete slabs.

In this Chapter, the concept of effective plastic moment capacity for FRP systems is first proposed and the corresponding theoretical equations are developed for either FRP RC or PSC sections. Then, the experimental results of the full-scale AFRP concrete bridge deck slab are used to verify the proposed strength analysis method based on the modified yield line theory.

6.2 Effective Plastic Moment Capacity for FRP Systems

In spite of non-ductile characteristics of AFRP bars, considerable deformability observed in the experimental results of the AFRP concrete bridge deck slab, presents the possibility of adapting yield line concepts to enable prediction of failure loads. To achieve this aim, the moment-curvature response of FRP concrete sections is first characterized and then simplified with an energy-equivalent elasto-perfectly-plastic (EPP) idealized behavior, where the conventional yielding moment is replaced with an effective plastic moment (M_p) to reflect the deformable response of the section.

6.2.1 FRP reinforced concrete sections (FRP-RC)

As depicted in Fig. 51(a), the flexural behavior of FRP RC sections is linear up to cracking and then followed by a curve that coincides with the line whose slope represents the cracked stiffness of the section. This curve reflects the tension-stiffening effect of the reinforced concrete due to the well-known ability of the concrete section to carry tension between cracks. If the section is “over-reinforced”, the flexural failure will be governed by concrete crushing with some nonlinearity close to the failure as a result of inelastic compressive stresses in the concrete. The flexural behavior of FRP RC

sections can be theoretically expressed as trilinear, where EI_g and EI_{cr} denotes the flexural stiffness of the concrete section before and after cracking, Fig. 51(a). Herein, it is proposed to simplify this trilinear behavior with an energy-equivalent elasto-perfectly-plastic (EPP) idealized behavior, where the area beneath the trilinear (U_{RC}) and the idealized (U_{EPP}) responses are equalized

$$\frac{M_u{}^2}{2EI_{cr}}+\frac{M_{cr}{}^2}{2EI_{cr}}-\frac{M_{cr}{}^2}{2EI_g}=\frac{M_p}{E}\left(\frac{M_u}{I_{cr}}-\frac{M_p}{2I_g}\right) \tag{15}$$

which has an exact solution of

$$M_p=\frac{M_u}{(I_{cr}/I_g)}\left[1-\left(\sqrt{1-\frac{I_{cr}}{I_g}}\right)\left(\sqrt{1-\frac{I_{cr}}{I_g}\left(\frac{M_{cr}}{M_u}\right)^2}\right)\right] \tag{16}$$

I_{cr}/I_g typically ranges from 0.05 to 0.15 for lightly to heavily reinforced FRP RC sections. Substituting the typical design values, I_{cr}/I_g=0.1 and M_{cr}/M_u=0.33, and simplifying using a binomial expansion of $\sqrt{1+X}\approx 1+\frac{X}{2}$ (for X<1) results in a satisfactory approximation of M_p in terms of M_{cr} and M_u

$$M_p=0.5M_u+0.15M_{cr} \tag{17}$$

6.2.2 FRP prestressed concrete sections (FRP-PSC)

As depicted in Fig. 51(b), the flexural behavior of FRP PSC sections is typically bilinear, where the first and second lines represent the pre-cracking and post-cracking behavior, respectively. Pirayeh Gar et al. (2012) have shown that in prestressed concrete sections, tension stiffening is negligible and barely affects the flexural behavior. Again it is proposed to model the behavior of FRP PSC as an equivalent-energy EPP system of the more realistic bilinear behavior, where the area beneath the bilinear response (U_{PSC}) and the idealized behavior (U_{EPP}) are equalized

$$\frac{M_{cr}{}^2}{2EI_g}+\frac{\left(M_u{}^2-M_{cr}{}^2\right)}{2EI_{cr}}=\frac{M_p}{E}\left(\frac{M_{cr}}{I_g}+\frac{M_u-M_{cr}}{I_{cr}}\right)-\frac{M_p{}^2}{2EI_g} \tag{18}$$

which has an exact solution of

$$M_p = \frac{M_u}{I_{cr}/I_g}\left(1-\sqrt{1-\frac{I_{cr}}{I_g}}\right)+\frac{M_{cr}}{I_{cr}/I_g}\left(\frac{I_{cr}}{I_g}-1+\sqrt{1-\frac{I_{cr}}{I_g}}\right) \quad (19)$$

Similar simplification using the binomial expansion results in

$$M_p = 0.5M_u + 0.5M_{cr} \quad (20)$$

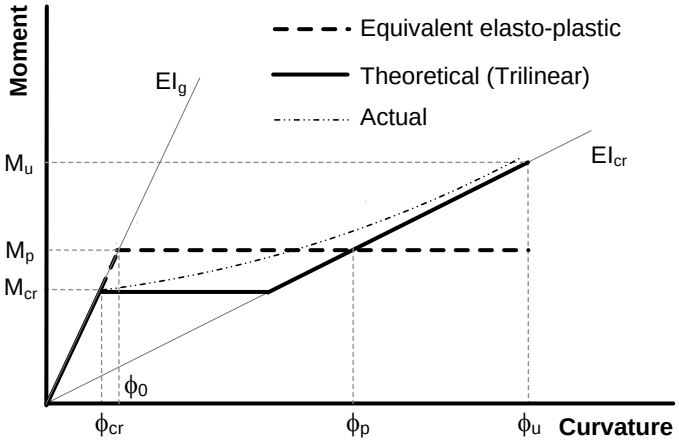

a) FRP RC section

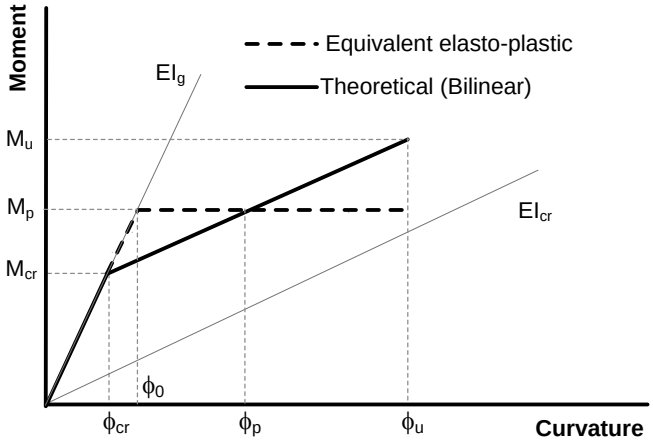

b) FRP PRC section

Fig. 51. Moment-curvature response of FRP concrete section

Section analysis of the bridge deck slab confirmed by experimental testing of the strip specimens, as discussed in Chapter 5, showed the cracking and ultimate moment of the unit width of the slab equal to 42 kNm/m and 70 kNm/m for *x* (prestressed direction),

and 25 kNm/m and 76 kNm/m for *y* (non-prestressed) direction, respectively. Due to symmetry in the section, these values are identical for positive and negative moments. Substituting the cracking and ultimate moments in Eqs. (17) and (20) gives the equivalent plastic moment for both directions equal to M_{px} = 56 kNm/m and M_{py} = 41 kNm/m. It should be noted that M_{px} and M_{py} denote the equivalent plastic moments inducing normal stresses in *x* and *y* directions, respectively. Table 16 shows the summary of section analysis of the bridge deck in *x* and *y* directions for unit width.

Table 16- Results of section analysis of the bridge deck slab (moment: kNm/m)

Bridge deck section	M_{cr}	M_u	M_p	$\phi_{cr}h$	$\phi_u h$	$\phi_0 h$	$\phi_p h$
prestressed (*x* direction)	42	70	56	0.0004	0.023	0.00051	0.01
non-prestressed (*y* direction)	25	76	41	0.00022	0.023	0.00036	0.012

6.3 Yield Line Pattern

The first step in failure analysis using modified yield line theory is identifying the yield line pattern based on the observed cracking pattern and the inferred curvature distribution. For interior spans, flexural cracks due to negative moments were first observed on top of the deck and in parallel with support beams and then propagated around the loading plate. The flexural cracks due to positive moments initiated beneath the bridge deck and propagated from the loading spot toward the support beams in a diagonal manner. The cracking pattern resembled an elliptical yield line pattern on the interior span. Compared to load cases 4 and 7, under load case 1, where both wheel loads were applied on the same interior span, larger deformability and failure surface is achieved due to transferring the load in a more distributed manner.

For overhangs, flexural cracks due to negative moments were first observed close to the exterior beam and propagated toward the slab edge. For load case 2, flexural failure of the panel subjected to the wheel load along with the shear failure of the panel-to-panel seam was recognized as the failure mechanism. In fact, shear failure of the joint prevented the adjacent panel from flexural failure. However, for load case 5 where the axle load was applied instead of single wheel load, flexural failure on both panels was evident without any sign of shear failure at the seam. The cracking pattern generally resembled an trapezoidal yield line pattern. Similar to the interior span, it is seen that using axle load causes a more extensive flexural mechanism and larger failure surface. For load cases 3 and 6, the cracking pattern implied a triangle yield line pattern.

Based on the observed cracking pattern and the curvature distribution, several failure mechanisms were assumed for each load case and failure load analysis was performed, as will be discussed. The failure mechanism with minimum failure load was chosen as the governing one. Cracking pattern and the governing failure mechanism are presented in Fig. 52 for each load case which shows an in-scale drawing, where the length and angle of the crack line can be measured taking advantage of the 200 × 200 mm grid. For cracking pattern, the black and gray lines represent the cracks on top and beneath the deck due to negative and positive moments, respectively. For yield line pattern, the dashed line shows the negative curvature, the solid line represents the positive yield line, the dotted line indicates no flexural resistance and the very thick line for load case 2 shows the shear failure.

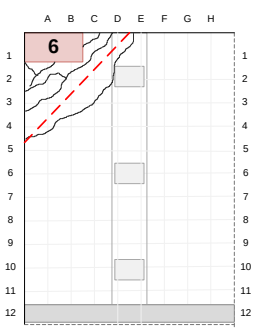

wheel load at corner

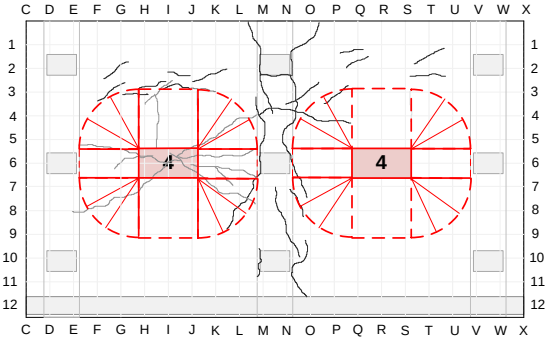

double-wheel load on interior spans

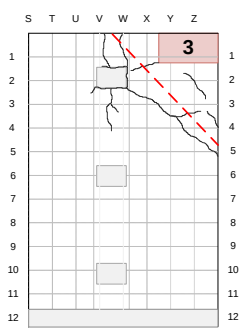

wheel load at corner

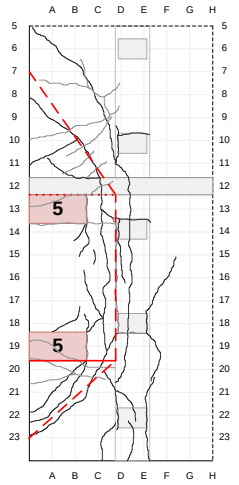

axle load on overhang

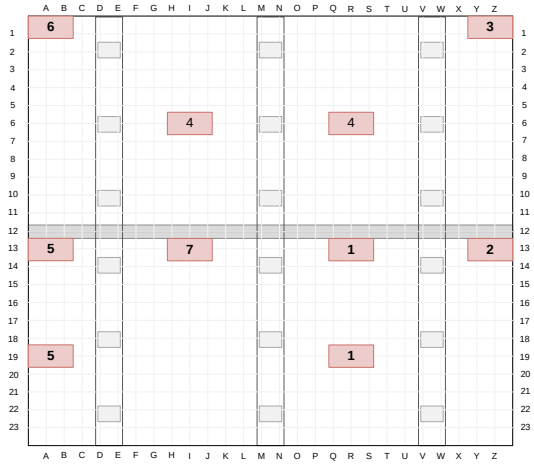

bridge deck slab specimen

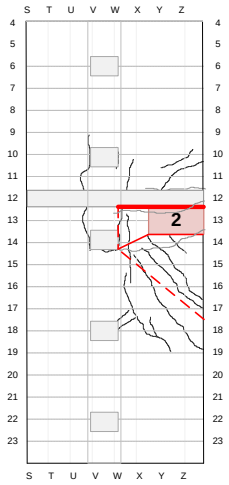

wheel load on verhang

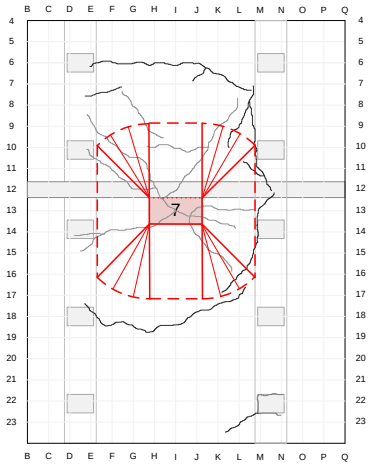

wheel load on interior span

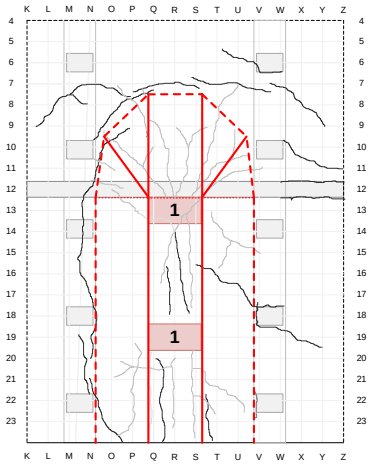

axle load on interior span

Fig. 52. Cracking pattern and adapted failure mechanism

6.4 Ultimate Load Capacity

As discussed, the equivalent plastic moment for unit width of the slab in *x* (prestressed) and *y* (non-prestressed) directions were found M_{px} = 56 kN.m/m and M_{py} = 41 kN.m/m, which represents an orthotropically reinforced slab from analysis point of view. Therefore, the equivalent plastic moment for any crack line with an angle θ in *x*-*y* plane can be found from (Park and Gamble 2000)

$$M_{p\theta} = M_{px}\sin^2\theta + M_{py}\cos^2\theta = 56\sin^2\theta + 40\cos^2\theta \tag{21}$$

The external work done (*EWD*) and internal work done (*IWD*) can be computed from Eq. (22) where P = failure load; δ = vertical displacement below the center of the load; w_d = self-weight of the slab; A_d = area of the failure mechanism; δ_c = vertical displacement at area center of the failure mechanism; α_θ = rotation of the crack line; and l = length of the crack line.

$$EWD = P\delta + \sum w_d A_d \delta_c \quad \text{and} \quad IWD = \sum\left(M_{p\theta}\right)\left(\alpha_\theta\right)(l) \tag{22}$$

Since the failure mechanism of load cases 1, 2, 5, and 7 might be influenced by the panel-to-panel seam, the shear and flexural capacity of the joint was taken into account in failure load analysis. As discussed in Chapter 5, the experimental results showed that the flexural strength of the joint is negligible; however, the plastic shear capacity is considerable and equal to 110 kN/m. Therefore, the internal work done by flexure of the panel-to-panel seam is deemed zero and will be shown by a dotted line. However, in case of shear failure at the joint, like what was observed at load case 2, the internal work done by shear is taken into account. Additionally, for failure load analysis of the overhang, the transfer length of the prestressed bars needs to be considered since the plastic moment capacity of the slab section in *x* direction can only be reached if the prestressing force is fully developed through the bond between the bar and concrete.

Ehsani et al. (1997) reported the transfer length of the ARAPREE bar, with 10 mm diameter, about 50 times of the bar diameter which is equal to 500 mm. Supposing a

linear increase in prestressing force through the transfer length, 250 mm is deemed as the effective length from the free edge of the slab where the plastic capacity of the section can be reached. Therefore, the internal work done can be expressed in a general form accounting for the effect of panel-to-panel seam as well as the transfer length of the prestressed bars at the overhang

$$IWD = \Sigma\left(M_{p\theta}\right)\left(\alpha_{\theta}\right)\left(l^{*}\right) + \Sigma\left(V_{p}\right)\left(\delta_{v}\right)\left(l_{v}\right) \tag{23}$$

where, l^{*} is the length of the flexural crack reduced to account for the transfer length of the prestressed bars at overhang, l_v is the length of the shear crack along the panel-to-panel seam, V_p is the plastic shear capacity for the unit width of the slab section at the seam, and δ_v is the differential shear deformation at the seam.

Fig. 53 illustrates the application of the modified yield line theory for failure load analysis under load case 2, as an example. The results of the failure load analysis are also summarized in Table 17. It is seen that the proposed modified yield line theory predicted the ultimate load capacity precisely and within 2% accuracy of the experimentally observed results. The fidelity of the modified yield line theory is indeed dependent upon the value of the equivalent plastic capacity of the bridge deck section and shape of the failure mechanism as well. It should be noted that, the accuracy of the yield line theory can be affected when punching shear considerably contributes to the failure mechanism of the slab and results in a brittle failure like short spans with fully-restrained edges or when there is a significant axial load due to membrane action. However, the considerable deformability and excessive flexural cracks observed in the test implied that the failure mechanism is mainly governed by flexure. The results of failure load analysis are conclusive in showing that the concept of yield line theory can be modified and employed for FRP RC of PRC bridge deck slabs where the flexure mostly governs the failure, although the FRP bars are inherently non-ductile materials.

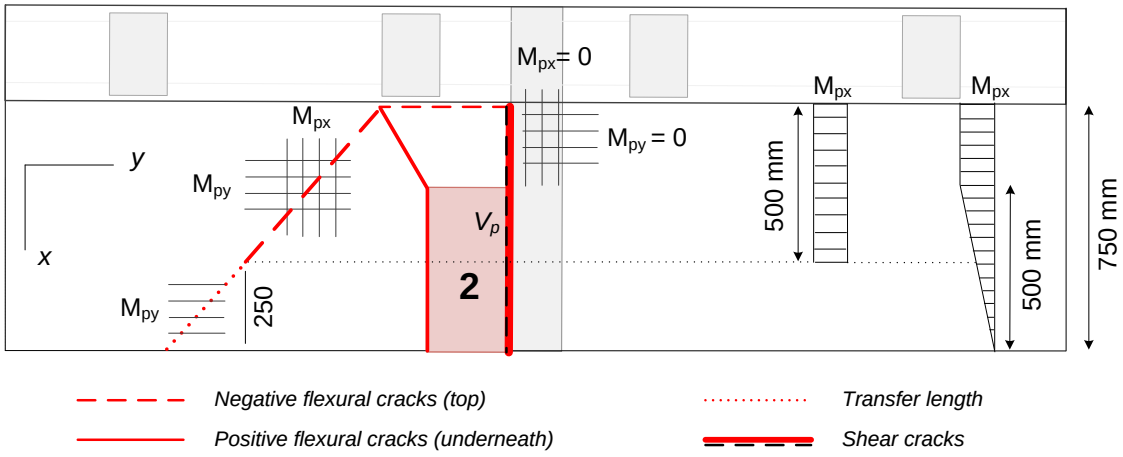

a) modified yield line theory

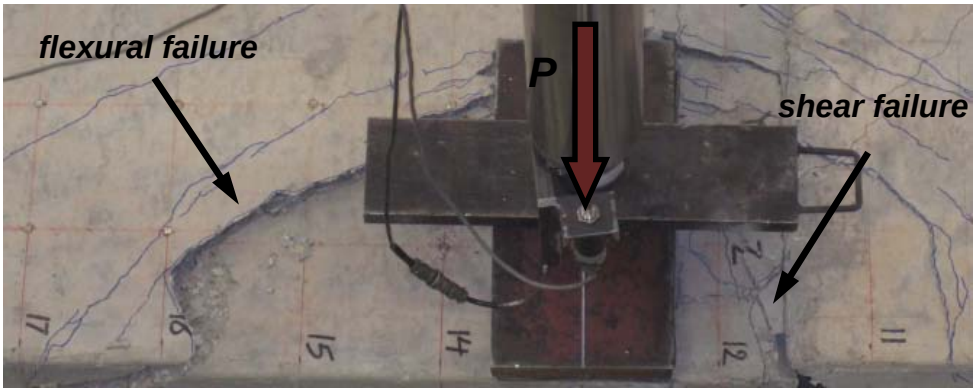

b) compound shear-flexural mechanism (top view)

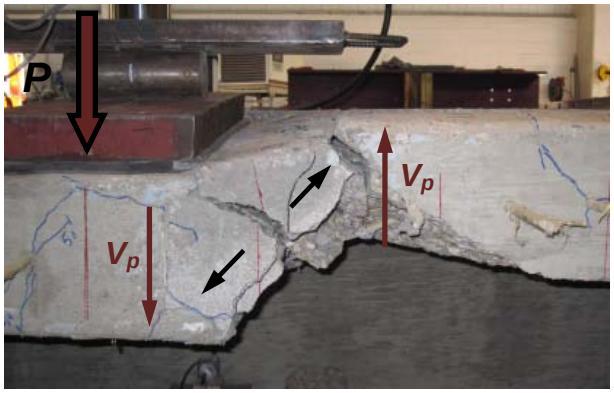

c) shear failure of the seam (front view)

Fig. 53 Failure load analysis of load case 2

Table 17- Results of failure load analysis (P = whell load: kN)

Load case	1	2	3	4	5	6	7	
$(P_u)_{theo.}$	700	329	110	845	226	110	896	
$(P_u)_{exp.}$	694	323	120	765	223	102	890	
$(P_u)_{theo.}/ (P_u)_{exp.}$	1.008	1.028	0.916	1.104	1.013	1.078	1.007	**Ave. = 1.02**

6.5 Discussion

The idea of using the yield line concept for failure load analysis was based on the considerable deformability that bridge deck slab exhibited in spite of linear and brittle behavior of AFRP bars. But, the main question herein is where this deformability originates from. The observed deformability mainly originates from the low modulus of elasticity of AFRP bars, say about one third of that of steel (Medina 2011). In other words, a large moment is first developed in the *x* direction of the slab, the stiffer direction, which results in initiation and propagation of flexural cracks. Consequently, the flexural stiffness of the bridge deck slab section in the *x* direction substantially decreases because of the low modulus of elasticity of AFRP bars. This causes the moment to be highly redistributed and hence the slab section in the *y* direction undergoes larger moment, subsequently. Propagation and widening of the cracks in both directions gives rise to considerable deformability until the complete failure mechanism of the slab is reached. This makes the failure mechanism of the slab to be more governed by flexure than shear.

Interestingly, the results of previous experimental studies on punching shear behavior of two-way FRP RC slabs clearly showed the significant deformability prior to failure (Gamal et al. 2005, Ospina et al. 2003, Lee et al. 2009, dulude et al. 2010). Ahmad et al. 1993 and Matthys and Taerwe 2000b reported considerable flexural cracks and strong interaction between flexure and shear before punching failure. However, it was reported that the control specimen, which was reinforced with conventional steel,

failed in a more shear manner due to high modulus of elasticity of steel rebar. Research on steel RC two-way slabs has shown that the reinforcement ratio determines whether flexure or shear failure governs (ASCE-ACI Committee 426 1974). In fact, the higher the reinforcement ratio, the higher the post-cracking flexural stiffness and the less likelihood of flexural failure. In a more general statement, the flexural stiffness of the cracked section that is mainly a function of the reinforcement ratio and modular ratio determines whether the failure mechanism will be governed by flexure or shear. Therefore, replacing steel with FRP, with a similar reinforcement ratio, tends to increase the likelihood of flexural failure because of the lower modular ratio. This enhances the potential for application of the yield line concept for failure load analysis of FRP concrete bridge deck slabs.

6.6 Conclusions

The yield line theory was modified by substituting the yield moment with the equivalent plastic moment proposed based on an equivalent energy-based elasto-perfectly-plastic (EPP) system, and the corresponding theoretical equations were developed for either FRP RC or PSC sections. A full-scale bridge deck slab with precast panels reinforced and prestressed with AFRP bars was subsequently tested to verify the proposed modified yield line theory. The following conclusions are drawn from this study

1- The proposed modified yield line theory predicted the ultimate load capacity precisely and within 2% accuracy of the experimentally observed results. The results are conclusive in showing the applicability of the modified yield line analysis for both FRP RC and FRP PSC bridge deck slabs.

2- The fidelity of the modified yield line theory depends on the reasonable assessment of the equivalent plastic moment. For instance, transfer length of the prestressed bars at the slab overhang was accounted when calculating the equivalent plastic moment as the flexural capacity of the slab section in the *x* direction cannot be achieved unless the full prestressing force is fully developed

through the bar-concrete bound. The panel-to-panel seam shear and flexural strength were also considered in the analysis.

3- Physical modeling of the realistic boundary conditions was found critical as the slab overhang failure was fully governed by flexure; however, the flexural failure of the interior span happened in a punching manner as a result of the slab restrained edges. Moreover, loading configuration proved to govern the failure mode. For instance, the slab overhang under load case 5 (axle load close to the seam) failed due to flexural mechanism of the both precast panels, but under load case 2 (wheel load close to the seam) failed due to flexural mechanism of the panel subjected to the load and shear failure of the seam.

4- The observed deformability in the bridge deck slab tested in this research as well as previous experimental studies on punching shear behavior of FRP RC two-way slabs clearly show that replacing steel with FRP enhances the deformability due to low modulus of elasticity of FRP bars and hence increases the likelihood of flexural failure versus punching shear failure. This holds the potential for application of the modified yield line theory. However, further experimental and analytical research is still required to study the load capacity and failure mechanism of FRP concrete bridge deck slabs, particularly for the cases where the shear-flexure interaction governs the mechanism.

7. COMPUTATIONAL MODELING OF AN AFRP PRESTRESSED GIRDER IN COMPOSITE ACTION WITH BRIDGE DECK

7.1 Introduction

In the 1970s, corrosion-induced deterioration of concrete structures, particularly in bridge decks, led to a need to find alternative design strategies that would reduce the likelihood of corrosion decay in concrete structures. One alternative was to replace prestressed steel strands with prestressed fiber-reinforced polymer (FRP) bars. Since FRPs have high-strength and are corrosion resistant, non-magnetic, as well as light-weight, their application in construction, retrofitting, and rehabilitation of structures has grown considerably (Trejo et al. 2000). FRP tendons are typically made from one of these three basic fibers: glass (GFRP), carbon (CFRP), and aramid (AFRP). The latter is the subject of the present study. In spite of superior durability, the modulus of elasticity of AFRP is approximately three times lower than that of steel, leading to a substantial reduction in flexural stiffness of AFRP prestressed girder after cracking, and resulting in larger deflection, accordingly (Bischoff 2005). Controlling the deflection under service loads becomes critical to meet serviceability requirements and enhance sustainability (Bischoff 2007a).

Despite ongoing experimental research investigating the behavior of FRP prestressed girders, there is a lack of uniformity and consistency in testing procedures, definitions of material characteristics, and results that raises the need for a computational model to analyze the behavior of FRP prestressed girders (Dolan et al. 2001). Kim (2010) investigated the flexural behavior of AFRP prestressed rectangular beams via numerical analyses. Different sectional properties and level of prestressing were studied. It was concluded that the prestressing level typically governs the flexural performance at service state; however the I_g/I_{cr} (gross to cracked moment of inertia) ratio controls the deflection characteristics of the AFRP prestressed members until failure. Although

valuable results have been gained from previous investigations, studies have been mostly limited to rectangular sections or reduced scale beams where the effect of bridge deck in providing a composite section is typically ignored (Pisani 1998, Toutanji and Saafi 1999, Rafi and Nadjai 2009).

New information has been learned based on a computational model recently developed by the authors to gain insight into the flexural performance for the design of full scale girders with a composite bridge deck per AASHTO LRFD. Studying the flexural response of the composite girder in different steps of loading including prestressing load, full dead load of the girder and cast-in-place deck, live load when the deck is hardened (beginning the composite action), and failure load, is required to judge if an AFRP prestressed girder meets the service and strength limit states. The developed computational model using MATLAB software is capable of performing the following: (1) nonlinear fiber elements analysis of a prestressed girder's section with pretensioned tendons to find the stress and strain distributions, (2) moment-curvature analysis taking into account the effect of composite action between the girder and slab once the concrete of the slab is hardened, (3) refined analysis to capture cracking and failure, (4) long-term loss estimation analysis including creep and shrinkage of the concrete as well as relaxation of the tendons, and (5) beam nonlinear analysis to find the load-deflection relationship of every point along the beam until failure.

In this chapter, an AASHTO I-girder (Type I) composite with a bridge deck is designed as a fully-prestressed section based on serviceability requirements and strength demand for two different cases: (1) pretensioned AFRP and (2) pretensioned steel. Then, numerical analysis is performed to determine the stress distribution over the cross section, moment-curvature and load-deflection relationships of the girder, which will be verified by existing experimental test data. In the final analysis, the deflection equation in ACI 440 will be evaluated by numerical results.

7.2 Bridge Girder Prototype

A bridge prototype including prestressed precast AASHTO I-girders (Type I) and cast-in-place (CIP) deck is shown in Fig. 54. Simply-supported girders are spaced 1830 mm on center and span 12.2 m. The girder is designed based on AASHTO LRFD Bridge Design Specifications (2010) for service and strength limit states. The modulus of elasticity of AFRP is considerably less than that of steel, so once the section is cracked, there is a substantial decline in the flexural stiffness of the beam leading to a larger deflection. Therefore, for the sake of controlling the deflection of the beam, the girder should remain uncracked under service load, and hence the girder is designed as a fully prestressed beam. Steel strands and AFRP tendons are assumed to be initially prestressed up to 70% and 60% of their ultimate strength. Material properties are summarized in Table 18. The design vehicle load cases are illustrated in Fig. 54 including the lane load, and truck load (HS20-44) or tandem axle load depending on which one governs the design.

Table 18- Properties of material (MPa)

Girder	Compressive Strength, f_c'	41.4
	Fracture Modulus, f_{cr}	4
Slab	Compressive Strength, f_c'	27.6
	Fracture Modulus, f_{cr}	3.24
AFRP	Ultimate Strength, f_{pu}	1400
	Modulus of Elasticity, E_p	60000
Steel Strand	Ultimate Strength, f_{su}	1863
	Yield Strength, f_y	1677
	Modulus of Elasticity, E_s	193200

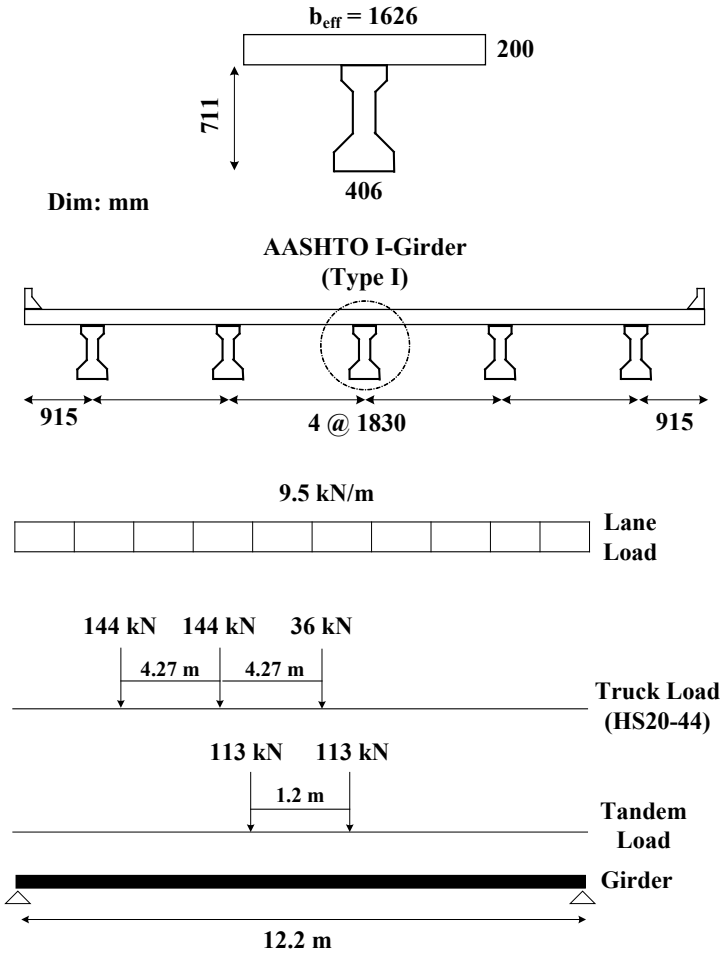

Fig. 54. Bridge prototype and design vehicle load cases

7.2.1 Summary of flexural design of AFRP prestressed girder

The maximum moment due to service load is 810 kNm including 291 kNm due to the total dead load and 560 kNm induced by live load. For the prototype bridge, calculations show that in the case of conventional prestressing steel, twelve 7 wire steel strands with 12.7 mm diameter are required: ten in the bottom flange and two in the top flange. In this case, the area of tensile reinforcement is A_s=1.96 14 mm^2. For the AFRP case, twenty four tendons are required with 10 mm diameter: 22 in the bottom flange and two in the top flange. In this case, the area of tensile reinforcement is A_p =17.8 mm^2.

Similar to the balance ratio, ρ_{bs}, commonly used for steel prestressed beams to ensure ductile behavior, a brittle ratio, ρ_{bp}, is defined for FRP prestressed beams. In this case, $\rho \leq \rho_{bp}$ (under-reinforced) indicates failure by tendon rupture, while $\rho \geq \rho_{bp}$ (over-reinforced) represents concrete compression failure. Although concrete compression failure provides more deformability over the tendon rupture, it is difficult to over-reinforce most of the common prestressed shapes since fitting in too many tendons is impractical (Dolan et al. 2001). A more significant reason for this difficulty, is the effect of the topping deck that considerably raises the balance or brittle ratio. As will be discussed, for the AFRP prestressed girder without topping deck the area of reinforcement corresponding to the brittle ratio is A_{bp} =7.8 mm^2; however, taking into account the effect of composite action gives A_{bp} = 56.5 mm^2. It is clearly seen that if the composite section was to be over-reinforced, approximately 70 AFRP tendons (22×8.75/2.76) would have to be used which is not feasible. Thus, the failure mode is dominated by tendon rupture. The prestressing layout of both girders prestressed with AFRP tendons and steel strands are subsequently illustrated.

7.2.2 Flexural design calculations

Maximum dead load moments induced by each component of the bridge prototype are summarized in Table 19 including the dead load of the girder, slab, barrier, and future wearing. Maximum live load moments, per lane, due to the truck load and lane load are calculated as $M_{L\text{-}Truck}$=623 kNm, and $M_{L\text{-}Lane}$=177 kNm. It should be noted that, for the girder shown in Fig. 54, tandem axle load results in pretty much the same maximum moment as the truck load. The distribution factor for moment is computed as DFM=0.56 based on AASHTO 4.6.2.2.2b-1. Assuming the impact factor as IM=1.33, the maximum live load moment can be computed from the following equation

$$M_L = DFM\left(M_{L-Truck} \times IM + M_{L-Lane}\right) \tag{24}$$

which gives M_L= 560 kNm. According to AASHTO 3.4, the service load for deflection control (D+L) is M_s=858 kNm and the ultimate load for strength design (1.25D+1.75L)

is M_u=1353 kNm. To compute the required number of AFRP tendons, the service load for controlling the tension in prestressed concrete (D+0.8L) is considered as follows

$$f_b = \left(\frac{M_{D-Beam} + M_{D-Slab}}{S_b} \right) + \left(\frac{M_{D-Barrier} + M_{D-Wearing} + 0.8\left(M_{L-Truck} + M_{L-Lane}\right)}{S_{bc}} \right) \quad (25)$$

Table 19- Maximum deal load moments (kNm)

$M_{D\text{-}Beam}$	$M_{D\text{-}Slab}$	$M_{D\text{-}Barrier}$	$M_{D\text{-}Wearing}$
76	152	33	36
$\sum$ =228		$\sum$ = 69	
M_D=297			

Given the section modulus for the bottom fiber of the girder and composite section are S_b=29611 mm^3 and S_{bc}=60517 mm^3, respectively, the tensile normal stress at the bottom fiber of the section is computed as f_b=16.56 MPa. Based on AASHTO 5.9.4.2.2-1, the allowable tensile stress is f_t=3.2 MPa. Therefore, the compressive stress due to prestressing must be f_{bp}=16.56-3.2≈13.4 MPa. This compressive stress can be written as

$$f_{bp} = \frac{P}{A} + \frac{Pe}{S_b} \quad (26)$$

where, the cross sectional area of the girder is A=1781 mm^2. As shown in Fig. 55, the prestressing eccentricity is e=19 mm, so the required prestressing force equals P=1180 kN. AFRP tendons are prestressed up to 60% of their ultimate strength and it can be conservatively assumed that the total loss during the lifetime of the structure is 20%. Thus, the required number of AFRP tendons in the bottom flange is

$$N = \frac{1180000}{78.5 \times 1400 \times 0.6 \times (1 - 0.2)} \approx 22$$

In order to control the stress at transfer (before loss) close to the support, two more prestressed AFRP tendons are used at the top flange. The normal tensile stress at the top fiber can be calculated as

$$f^T = \left(-\frac{22+2}{A} + \frac{22\times e}{S^T} - \frac{2\times e'}{S^T} \right) \times 78.5 \times 1400 \times 0.6 \qquad (27)$$

where positive and negative signs indicate tension and compression, respectively. Substituting the section modulus for the top fiber of the girder, S^T= 24187 mm^3, gives f^T= 0.69 MPa which is less than the allowable tension at transfer, f_{ti}=3.6 MPa based on AASHTO 5.9.4.1.2-1. The reinforcement layout of the prestressed girders is shown in Fig. 56.

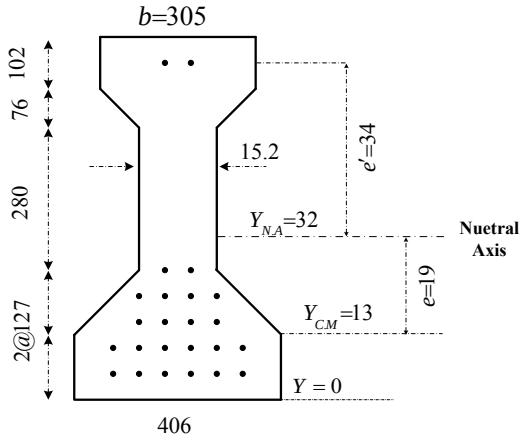

Fig. 55. Dimensions, neutral axis location, and C.M of the tendons for AFRP prestressed girder

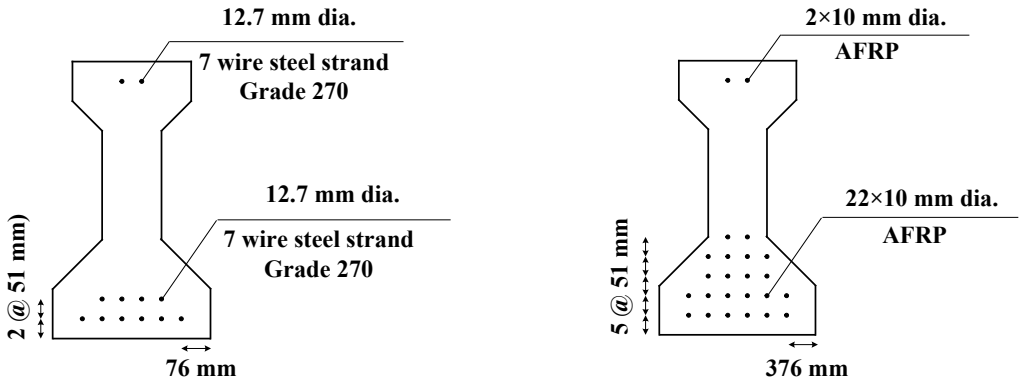

a) conventional steel *b) AFRP*

Fig. 56. Prestressing layout of the AASHTO I girder (Type I)

7.2.3 Effect of topping deck on brittle ratio of the AFRP prestressed girder

Brittle ratio of the AFRP prestressed girder can be calculated using the basic equations of equilibrium and strain compatibility for the girder section. As illustrated in Fig. 57, the depth of the neutral axis can be determined from the strain compatibility equation

$$\frac{c}{d} = \frac{0.003}{0.003 + \varepsilon_f} \tag{28}$$

Assuming 60% prestressing and 5% as loss in prestressing force gives ε_{p0}=0.013 and ε_f=0.01. ε_{p0} is the strain due to prestressing (after loss) and ε_f is what left for flexure. Referring to Fig. 55, d≈58.4 mm, and based on the above equation c= 13.5 mm. The area of reinforcement corresponding to the brittle ratio can be found from the following equilibrium equation

$$C = \left(\varepsilon_{p0} + \varepsilon_f\right) E_p A_{bp} \tag{29}$$

which results in A_{bp} = 7.8 mm^2. Now if the effect of topping deck is taken into account (Fig. 58), d=78.7 mm and c=181.6 mm which means that the neutral axis is within the slab. Given b=b_{eff}, the equilibrium equation gives A_{bp} =56.5 mm^2 which is approximately seven times that of the case without the topping slab. If the area of reinforcement in

AFRP prestressed girder, A_p =17.8 mm^2, is compared to A_{bp} =7.8 mm^2, it might be concluded that the flexural failure is due to the crushing of the concrete. However, accounting for the effect of composite action between the girder and topping deck shows that the reinforcement ratio is about one-third of the actual brittle ratio (2.76/8.75) confirming the tendon rupture as the failure mode. In other words, to change the failure mode from tendon rupture to concrete crushing the area of reinforcement should be tripled meaning that approximately 70 AFRP tendons have to be accommodated in the bottom flange of the girder which is impractical.

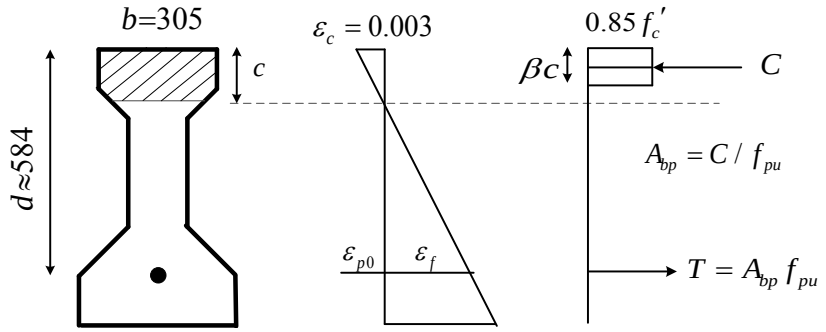

Fig. 57. Balance failure for the AFRP prestressed girder

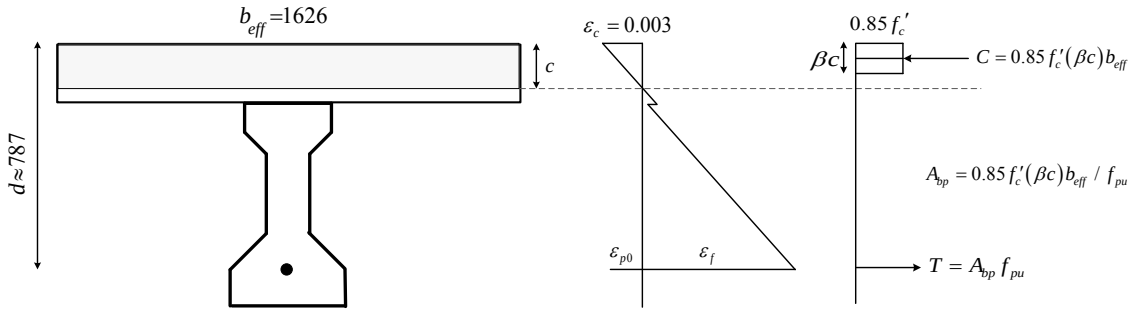

Fig. 58. Balance failure for the composite section of AFRP prestressed girder

7.3 General Moment-Curvature Relationship

Figs. 59(a) and 59(b) show the general moment-curvature relationships for conventional steel and AFRP prestressed AASHTO I-girder composite with bridge deck, respectively. After prestressing, the dead loads of girder and slab tend to reduce and counterbalance the initial camber induced by prestressing, thereby minimizing the effects of creep on long-term deflection. Once the concrete of the slab is hardened, the girder exhibits larger flexural stiffness to bear the live load, as a result of the composite action between girder and slab. This can be seen by an increase in slope of the moment-curvature diagram before cracking. With increasing the load, the section cracks and decompression occurs in the bottom fibers of the section. From a serviceability point of view, before prestressed steel exhibits any inelastic stresses, the girder is in the serviceability region as indicated by ($\emptyset_0$, M_0) in Fig. 59(a). Further increase in load causes the prestressed steel to reach the limit state of yielding. This stage of loading is referred to as the post-serviceability stage. Finally, the girder fails due to concrete crushing at the top fibers of the section ($\rho \leq \rho_{bs}$). However, in the case of prestressed AFRP, since tendons behave linearly up to rupture and the reinforcement ratio is typically less than the brittle ratio ($\rho \leq \rho_{bp}$), tendon rupture occurs before the concrete can induce any considerable inelastic stresses; hence, the AFRP prestressed girder exhibits low deformability, Fig. 59(b). This issue will be further discussed in the subsequent sections.

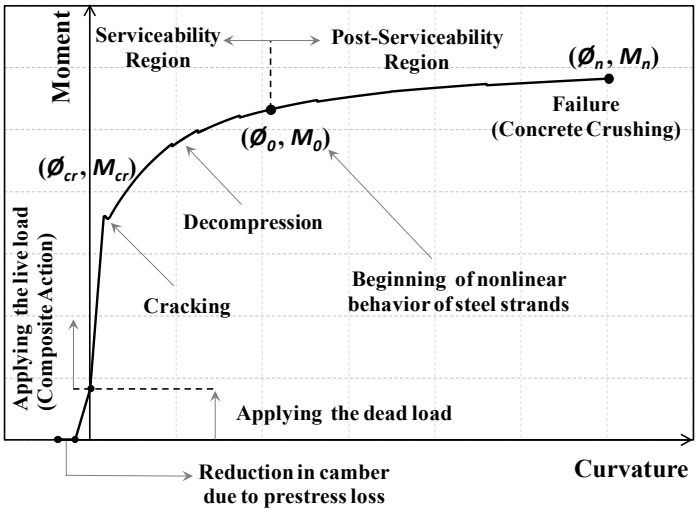

a) steel prestressed girder

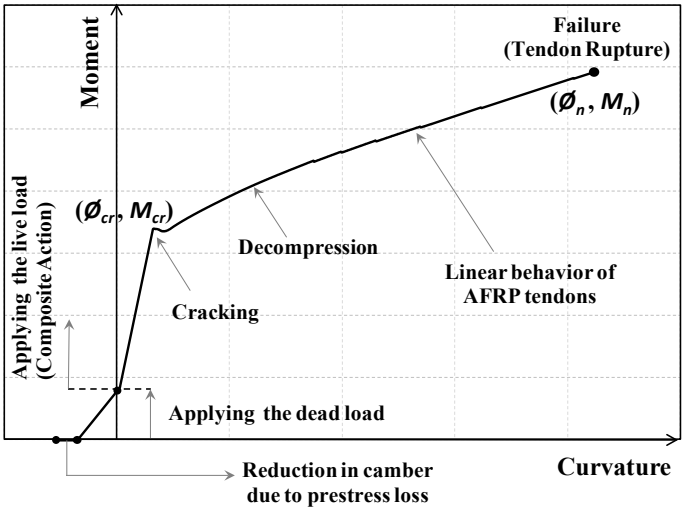

b) AFRP prestressed girder

Fig. 59. General moment-curvature diagram

7.4 Full Computational Model for Numerical Analysis

7.4.1 Computational model development

An extensive computational model to perform refined nonlinear analyses is developed using fiber element method via MATLAB software to study the following: (1) stress distribution over the height of the composite section, (2) moment-curvature relationship, and (3) load-deflection response of the girder up to failure. This model starts the analysis by finding the moment corresponding to the given curvature of the composite section. In general, the load-deformation relationship for a structural member can be written as

$$\begin{bmatrix} P \\ M \end{bmatrix} = \begin{bmatrix} EA & EZ \\ EZ & EI \end{bmatrix} \begin{bmatrix} \varepsilon_0 \\ \phi \end{bmatrix} \tag{30}$$

where P is the applied axial load, M is the applied bending moment, EA is the axial stiffness of the member, EI is the flexural stiffness, EZ is the nonlinear coupling between axial load and bending moment, ε_0 is the strain at a reference point, and ϕ is the curvature of the section. The strain at any fiber element of the section can be found using the following equation given the plain section remains plain after bending

$$\varepsilon(y) = \varepsilon_0 + \phi y \tag{31}$$

where y is the distance of the element from the reference point. ε_0 and ϕ are the first guesses and the strain profile is determined using Eq. (31). Stress-strain behavior of the concrete is defined using the Popovic's equation (1973):

$$f_c = \frac{n\left(\varepsilon_c / \varepsilon_c'\right)}{n - 1 + \left(\varepsilon_c / \varepsilon_c'\right)^{nk}} f_c' \tag{32}$$

where ε'_c is the strain corresponding to f_c', n is a curve-fitting factor, and k is a factor that controls the slopes of the ascending and descending parts of the stress-strain curve. For concrete with f_c'=41.4 MPa, n and k are equal to 2.77 and 1.33, respectively. Formulas for the factors n and k can be found in the reference. Fig. 60(a) shows the assumed behavior for the concrete of the girder based on the Popovic's equation. It is seen that the

stress-strain relationship is almost linear up to 0.7 f_c' which is equal to 29 MPa. Stress-strain behavior for prestressing steel strand is defined using the Menegotto Pinto's formula (1973):

$$f_s = E_s \varepsilon_s \left(Q + \frac{1-Q}{\left(1+\left|\varepsilon_s E_s / f_y\right|^R\right)^{1/R}} \right) \tag{33}$$

Parameters E_s, f_y, Q, and R are determined experimentally. For prestressing steel (Grade 270), these parameters are equal to E_s=193200 MPa, f_y=1656 MPa, Q=0.03, and R=6. Further discussion can be found in the reference. The assumed behavior for prestressing steel strands and AFRP tendons are depicted in Fig. 60(b).

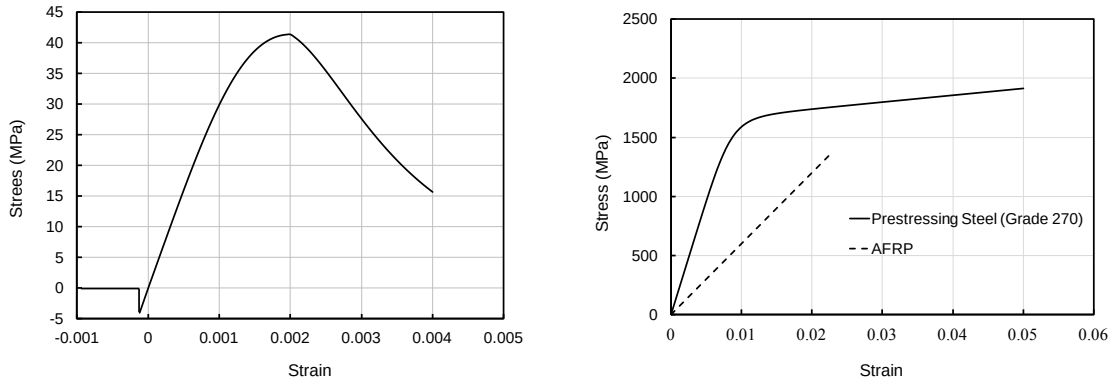

Fig. 60. Stress-strain relationships: (a) concrete (girder); and (b) prestressing steel and AFRP

A linear stress-strain relationship is assumed for AFRP material. Given the stress at each element is found out, P and M can be computed, subsequently. The equilibrium equations ($\sum P = 0$, $\sum M = 0$) are used as a key to find the actual strain profile and curvature. This can be done by an iterative analysis using a differential form of Eq. (30)

$$\begin{bmatrix} dP \\ dM \end{bmatrix} = \begin{bmatrix} \frac{\partial P}{\partial \varepsilon_0} & \frac{\partial P}{\partial \phi} \\ \frac{\partial M}{\partial \varepsilon_0} & \frac{\partial M}{\partial \phi} \end{bmatrix} \begin{bmatrix} d\varepsilon_0 \\ d\phi \end{bmatrix} = [D] \begin{bmatrix} d\varepsilon_0 \\ d\phi \end{bmatrix} \tag{34}$$

Eq. (34) should be solved incrementally which is beneficial in a highly non-linear state of stress. *dP* and *dM* are indeed the errors found when the equilibrium equation is checked. In each increment, given the constant curvature, a tiny change in strain is applied and the partial derivatives $\partial p/\partial \varepsilon_0$ and $\partial M/\partial \varepsilon_0$ are computed. The same procedure, however this time for the constant strain, is followed to find $\partial P / \partial \phi$ and $\partial M / \partial \phi$. Once the matrix *D* is established, the strain and curvature adjustments, $d\varepsilon_0$ and $d\phi$, can be computed and added to the strain and curvature of the previous step to decline the error and enhance the accuracy of the response. This iteration should be done as many times as the error in equilibrium equation is found to be acceptably small. When the moment curvature relationship of the composite section is numerically established, the deflection of the beam under any load configuration can be evaluated using the conjugate beam theory. The fibers over the cross section of the girder are refined to the extent that cracking and failure can be captured with the least error. The accuracy of the program is validated by comparing the numerical results for the steel prestressed girder and its corresponding experimental test data reported by Trejo et al. 2008, Fig. 61(a). This verification shows that the maximum error induced by the computational model at cracking and failure loads are 7% and 5%, respectively, which indicates the high accuracy and acceptability of the numerical analysis.

7.4.2 Moment-curvature analysis of the section

As shown in Fig. 61(b), the cracking moment, 969 kNm, is higher than the moment due to the service load, 858 kNm, confirming that the section is fully prestressed. It is also observed that both prestressed AFRP and steel girders have an ultimate strength of about 1661 kNm which is almost 1.2 times the required strength per AASHTO LRFD Bridge Design Specifications (2010). For prestressed steel, flexural failure is due to concrete crushing at top fibers of the section, where the compressive strain reaches to

0.003. As pointed out earlier, after cracking, decompression occurs in bottom fibers of the section, and subsequently prestressed steel yields due to increase in load. In the post-serviceability region, since ultimate strain of prestressed steel is considerable, 0.05, concrete can exhibit inelastic stresses at top fibers of the section and finally reach its ultimate compressive strain before rupture of the steel strands; hence, significant flexural ductility is provided up to failure. The numerical analysis shows the failure curvature equal to 2.36×10^{-5} 1/mm which is 40 times the cracking curvature. In contrast, the AFRP prestressed girder fails in a more brittle fashion caused by rupture of the tendons farthest from the neutral axis. Since the ultimate strain of the AFRP, 0.023, is much lower than that of steel, rupture of the tendons occurs before the concrete can provide any considerable inelastic stress, and results in less deformability compared to prestressing steel case.

Numerical analysis confirms this, and shows that the failure curvature of the AFRP prestressed girder, 1.1×10^{-5} 1/mm, is almost half of that of steel; however, it can provide sufficient warning before failure as it is 18 times the cracking curvature. Based on experimental test data, the prestress loss at the time of testing the steel prestressed girder was reported as 5%, most of which was due to elastic shortening (Trejo et al. 2008). While additional experimental tests to verify the prestress loss are underway, loss calculations in the computational model were adjusted to result in the same loss in the prestressing force as reported from the experiment for consistency. According to what was shown in Fig. 61, results of moment-curvature analysis are summarized in Table 20.

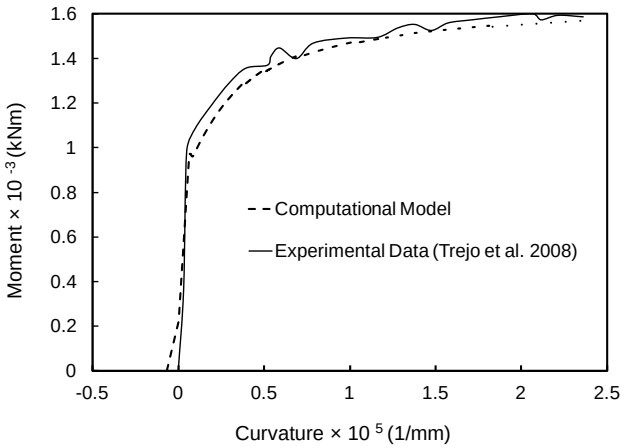

a) verification

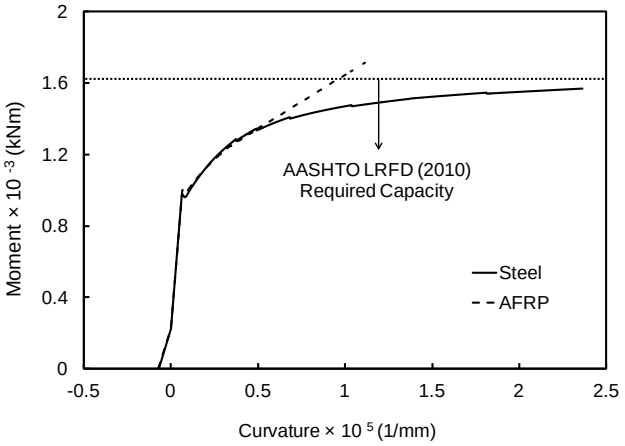

b) comparison of analytical results for steel and AFRP prestressed girder

Fig. 61. Moment-curvature diagram

Table 20- Results of moment-curvature analysis

	Cracking		Yielding		Failure	
	$M_{cr} \times 10^{-3}$ (kNm)	$\phi_{cr} \times 10^{5}$ (1/mm)	$M_0 \times 10^{-3}$ (kNm)	$\phi_0 \times 10^{5}$ (1/mm)	$M_n \times 10^{-3}$ (kNm)	$\phi_n \times 10^{5}$ (1/mm)
Steel	0.98	0.059	1.52	0.85	1.6	2.36
AFRP	1.01	0.062	.....	.....	1.74	1.1

7.4.3 Stress analysis over the cross-section

The computational model produces stress distributions over the entire cross-section from the first stage of prestressing up to failure of the girder to gain a clear insight about flexural behavior of prestressed girders in composite action with the topping slab. As illustrated in Figs. 62 and 63, four steps of analysis were selected to study the stress distribution as follows: prestressing the precast girder, applying the dead load of the girder and slab, applying live load up to cracking, and increasing live load up to failure. It is seen that from the third step where the concrete of the slab is hardened and live load is applied, composite action begins and the slab starts to bear compressive stresses. For the AFRP prestressed girder, induced stresses at prestressing and at service load meet the service limit states according to AASHTO LRFD Bridge Design Specifications (2010), and are similar to that of steel. For both cases, the neutral axis lies within the slab when close to failure; however, for the case of the AFRP prestressed girder the concrete compressive stresses are almost linearly distributed indicating non-ductile flexural behavior of the section as opposed to the steel case, where the concrete slab exhibits inelastic stresses until crushing of the top fiber.

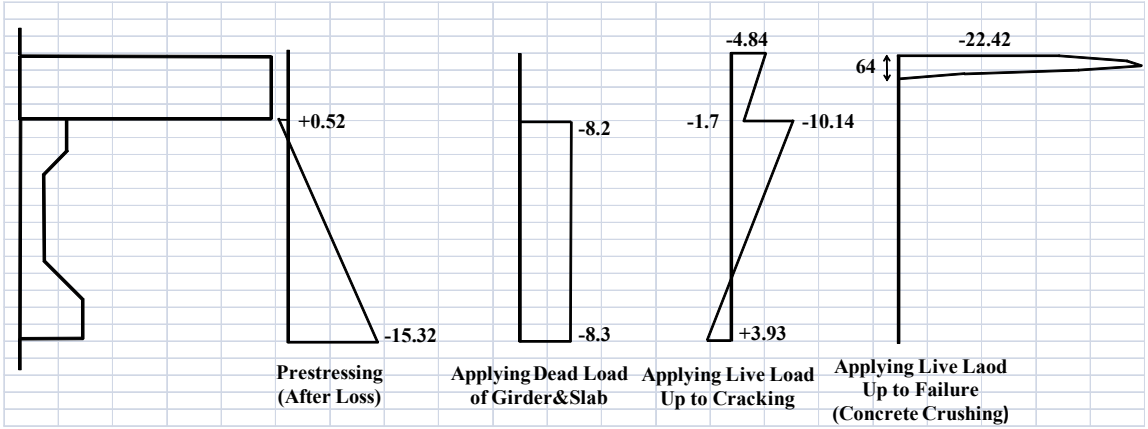

Fig. 62. Stress distribution in different steps of loading, steel prestressed girder (MPa)

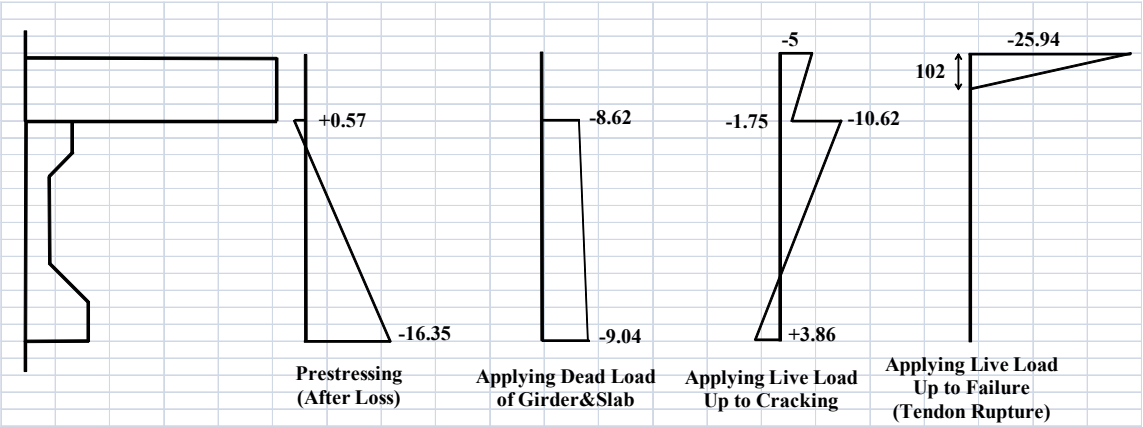

Fig. 63. Stress distribution in different steps of loading, AFRP prestressed girder (MPa)

7.4.4 Load-deflection analysis along the girder

To find the deflection along the girder at different steps of loading, refined nonlinear analysis is performed based on conjugate beam theory. The results for the service load, post-cracking load and failure load are depicted in Figs. 64(a)-64(c). The girder was designed as a fully prestressed section such that under service load it can remain uncracked. Therefore, the deflection of the girder under the service load is the same for either the steel or AFRP prestressed girder. The maximum deflection in this case is 7.1 mm, which is less than the allowable amount defined as the length of the girder divided by 800, equal to 15.2 mm, according to AASHTO LRFD Bridge Design Specifications (2010). Once the load exceeds the cracking load, the deflection of the AFRP prestressed girder is still close to that of steel. However, at failure, the maximum deflection of the steel prestressed girder is larger than that of AFRP because of the considerable ductility provided by yielding of steel strands and compressive inelastic stresses at top fibers of the concrete section. The maximum deflections at failure are about 76.2 mm and 152.4 mm for the AFRP and steel prestressed girder, respectively.

Analytical results for maximum deflection of the girder for both AFRP and steel cases are compared and illustrated in Fig. 61(d). It is clearly seen that the girder prestressed with AFRP has sufficient cracking strength and ultimate strength. Fig. 61(e)

shows the experimental data from Trejo et al. (2008) for midspan deflection of the steel prestressed girder compared to numerical results. The error of the analysis in predicting the maximum deflection at failure is 4%, representing high fidelity of the developed computational model. It should be noted that the M_{max} shown in Figs. 61(a)-61(c) includes the applied live load plus the dead load of the composite section.

7.5 Evaluation of the Deflection Equation of ACI 440

ACI 440.4R recommends the use of the effective moment of inertia, I_e, to calculate the deflection of FRP prestressed concrete beams. In this procedure, I_e is assigned to the entire beam and the maximum deflection is calculated using linear elastic analysis.

$$I_e = \left(\frac{M_{cr}}{M_a}\right)^3 \beta_d I_g + \left[1 - \left(\frac{M_{cr}}{M_a}\right)^3\right] I_{cr} \leq I_g \tag{35}$$

where M_{cr}= cracking moment; M_a = maximum moment in the girder at which the deflection is being computed; I_g= gross moment of inertia; I_{cr}= cracked moment of inertia; and β_d=0.5(E_p/E_s+1) is a factor to soften the effective moment of inertia. E_p and E_s are the modulus of elasticity of FRP tendon and steel, respectively. Fig. 65 shows that the equation underestimates the flexural stiffness of the girder, and hence, overestimates the deflection. The authors believe that the difference is due to the fact that this equation and also other similar formulas which are based on the original equation proposed by Branson (1965) for steel reinforced concrete beams, assume that the flexural behavior after cracking is linear elastic up to yielding of the steel reinforcement (for steel reinforced concrete) or rupture of the tendons (for FRP reinforced concrete). However, for a prestressed girder that is composite with a slab, the flexural behavior after cracking is not quite linear as a result of a gradual decompression at bottom fibers. This gradual decompression provides an additional post-cracking flexural stiffness that reduces the deflection. Furthermore, investigations have shown that the ACI 440.4R equation for predicting the effective moment of inertia is considerably influenced by the I_g/I_{cr} ratio (Kim 2010).

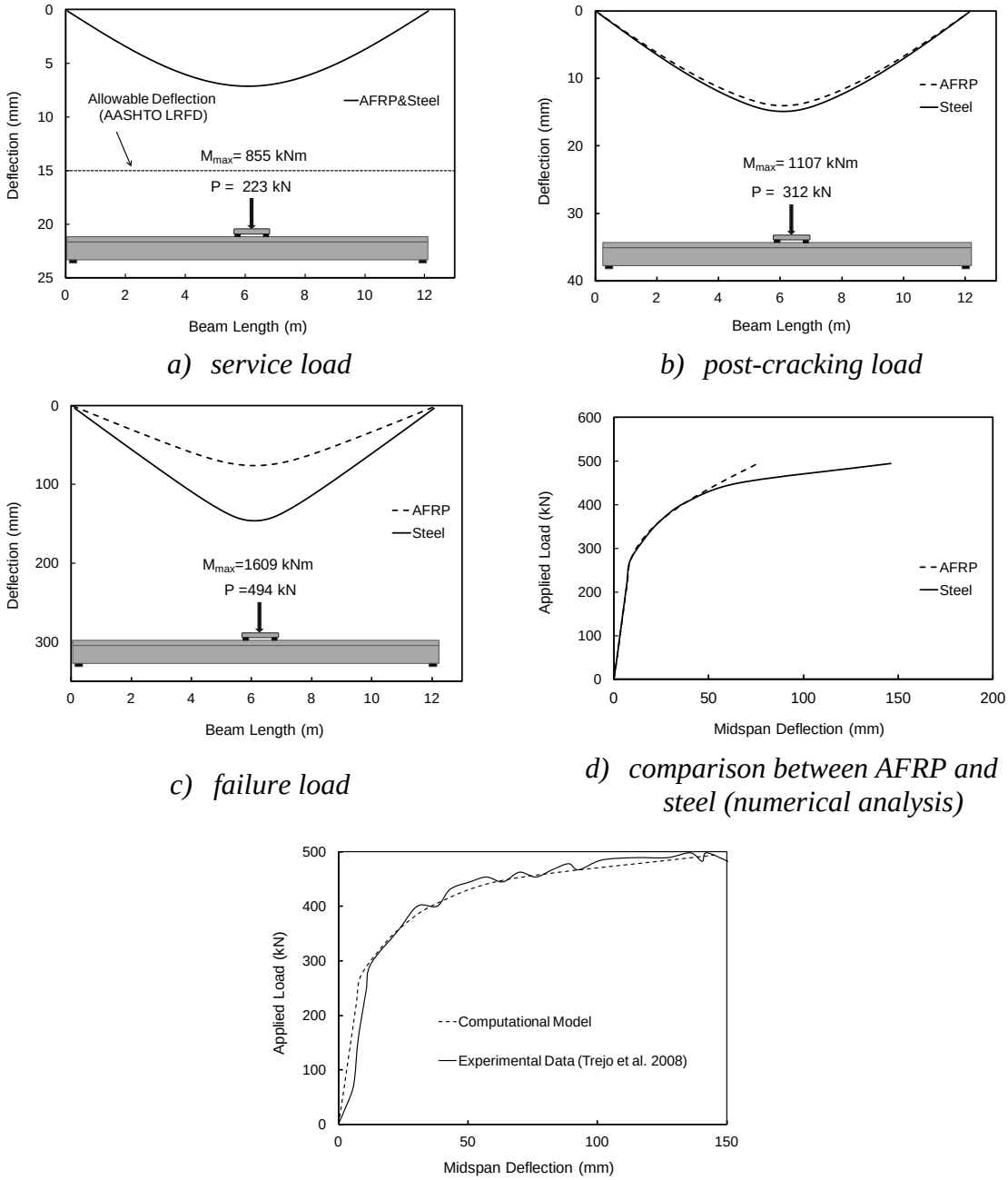

a) service load

b) post-cracking load

c) failure load

d) comparison between AFRP and steel (numerical analysis)

e) analytical and experimental result for the steel prestressed girder

Fig. 64. Deflection of the prestressed girders

One of the main reasons is because the Branson equation was calibrated for steel reinforced concrete beams with the reinforcement ratio around 1.65% which is corresponding to the ratio I_g/I_{cr} of about 2.2 (Bischoff 2005). In spite of many formulas available to predict the deflection of steel and FRP reinforced concrete (Mota et al. 2006), there is still a need for an equation with a high degree of accuracy to predict the deflection of FRP prestressed beams.

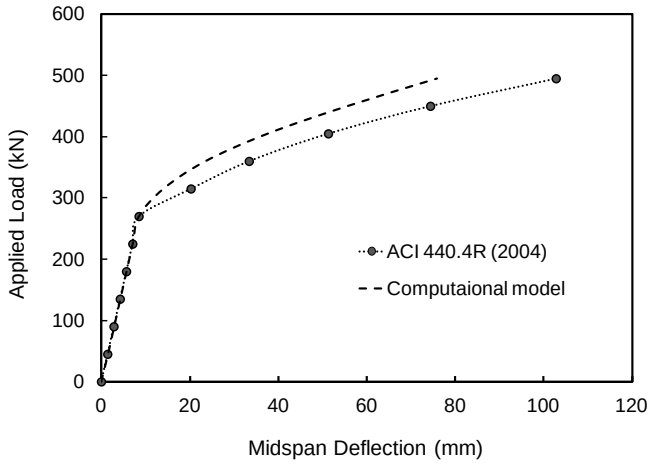

Fig. 65. Evaluation of ACI 440 (2004) equation for AFRP prestressed girder

7.6 Conclusions

AASHTO I-girder (Type I) was designed as a fully-prestressed section conforming to AASHTO LRFD Bridge Design Specification using two different tendons: (1) pretensioned AFRP and (2) pretensioned steel. Then, a fiber element analysis was performed using a computational model developed to study the stress distribution over the cross section, moment-curvature and load-deflection relationships of the girders. Comparison between analytical and experimental data for steel prestressed girder showed maximum error of 5% and 7% in prediction of failure and cracking moments,

respectively, which indicates the reasonably high accuracy of the developed computational model.

Stress and moment-curvature analyses confirmed that the AFRP prestressed girder not only meets service limit states, but also provides sufficient flexural strength. However, in contrast to steel prestressed girder whose failure mode was crushing of the concrete at the top fibers of the section, the failure mode of the AFRP prestressed girder was rupture of the tendons causing less deformability. This is mainly due to the fact that over-reinforcing the composite girder to reach to concrete crushing as the predominant failure mode rather than rupture of the tendons is almost impractical since the brittle ratio of the composite section is considerably large. Although tendon rupture as a failure mode is less desirable, the failure curvature was found 18 times the cracking curvature that can still provide sufficient warning before failure.

Load-deflection analysis of the girders showed that the deflection under service load is almost half of the allowable amount. At failure, deflection of the steel prestressed girder was about twice that of AFRP prestressed girder due to the large ductility provided by yielding of the steel strands and inelastic compressive stresses in concrete. It was also shown that the deflection equation in ACI 440.4R underestimates the post-cracking stiffness of the AFRP prestressed girder, and consequently overestimate the deflection. This matter becomes more crucial when the girder is partially prestressed and deflection under service loads commonly governs the design, and hence there is a need for an equation with a high degree of accuracy to predict the deflection of FRP prestressed beams. This issue will be discussed in Chapters 8 and 9.

Although the area of reinforcement in the AFRP prestressed girder was about 1.5 times that of prestressing steel, the numerical analyses clearly indicated that the AFRP prestressed girder can be successfully designed to meet AASHTO criteria. Although replacing the prestressing steel with AFRP strand helps to overcome corrosion-induced deterioration and enhance the durability of the structure, time-dependent characteristics of AFRP bars such as creep-rupture and fatigue strength should also be incorporated in

design as they affect the serviceability of the structure. Experimental research on creep-rupture behavior of AFRP bars has shown a linear relationship between logarithm of time and creep-rupture strength where the 50-year creep-rupture strength can be approximately extrapolated. The ratio of stress at failure to the ultimate strength of AFRP bars has been found about 0.5 (Taerwe 1995), 0.47 (Yamaguchi et al. 1997), 0.66 (Ando et al. 1997), and 0.6 (Dolan et al. 2001) which almost indicates the range 0.45-0.65. ACI 440.1R (2006) imposes a safety factor of 1/0.6 to the existing experimental data and recommends an allowable sustained stress level equal to 0.3. In this study, the AFRP bars were assumed to be initially prestressed up to 0.6 of their ultimate strength, which results in a sustained stress level equal to 0.48, given a 20% long-term loss in prestressing force. Also, fatigue characteristics of AFRP bars needs to be considered in design as the bridge deck is subjected to dynamic load of vehicles. Research conducted by Odagiri et al. (1997) shows that the maximum stress level needs to be set between 54 to 73% of the ultimate tensile strength. However, ACI 440.1R (2006) uses the same stress limits for fatigue as for creep-rupture. Further experimental research seems to be required regarding the time-dependent characteristics of AFRP bars as well as long-term performance of AFRP prestressed members in order to provide a more reliable and consistent design procedure.

8. RATIONAL MODEL FOR DEFLECTION OF FRP PRESTRESSED CONCRETE BEAMS

8.1 Introduction

Prestressed concrete structures are typically designed to meet stress and deflection serviceability requirements and to satisfy capacity checks to ensure that the structure is safe from collapse under ultimate load (Nawy 2005). Deflections are commonly not of primary concern as designs are typically based on uncracked behavior. Partially prestressed concrete systems are permitted to have limited cracks. However, in prestressed FRP concrete structures, deflection may be of major concern since FRPs have a lower modulus of elasticity than steel, which gives rise to a substantial reduction in the post-cracking flexural stiffness and larger deflection, accordingly. Hence, a dependable and rational evaluation of deflection is necessary to improve the design criteria for FRP structural concrete. For FRP systems, larger crack widths are permitted due to the non-corrosive nature of that material.

One common and easy-to-apply method to compute the deflection is to use the effective moment of inertia, I_e. When the cracking load is exceeded, the flexural stiffness varies along the beam due to the presence of discrete cracks. The effective moment of inertia basically reflects this variation and indicates a gradual transition from uncracked, I_g, to cracked moment of inertia, I_{cr}, as the load increases. In fact, the effective moment of inertia, which is assigned to the entire beam, obviates the need for rigorous analysis to account for the effect of cracking. Branson (1965) presented the equation using the weighted average of I_g and I_{cr} to estimate I_e for steel reinforced concrete:

$$I_e = \left(\frac{M_{cr}}{M}\right)^3 I_g + \left[1 - \left(\frac{M_{cr}}{M}\right)^3\right] I_{cr} \le I_g \tag{36}$$

where M is the maximum moment in a member at which the deflection is being calculated and M_{cr} is the cracking moment. This formula, which is an implicit stiffness

formulation, was calibrated for steel reinforced concrete beams over the range $0.3<I_{cr}/I_g<0.5$ (Washa and Fluck 1952; Branson 1965).

Recent investigations have revealed that the Branson's equation provides a stiff and unconservative response for slabs and beams with lightly reinforced steel or FRP, where the I_{cr}/I_g ratios are not in the range for which Branson's equation was calibrated (Bischoff 2007b, c). Extensive research has been conducted to propose an applicable equation of effective moment of inertia suitable for FRP reinforced concrete beams (Mota et al. 2006). Some researchers may believe that the basic form of the effective moment of inertia should be kept similar to the Branson's equation since it is convenient to use for designers; several researchers have modified Eq. (36) by applying a power larger than 3 (Brown and Bartholomew 1996; Toutanji and Saafi 2000) while others multiplied I_g or I_{cr} or both by a coefficient less than 1 (Benmokrane et al. 1996; ACI 440.1R-03). Another method for deflection analysis involves the calculation of curvatures at specific points along the beam and integrating to compute the deflection (Faza and Gangaro 1992; CSA 2002). In this method the deflection is explicitly expressed in terms of the moment of inertia, which may be more accurate but, not so easy for design office implementation.

Bischoff (2005) has recently proposed an equation incorporating the tension stiffening concept, which provides reasonable predictions for either steel or FRP reinforced concrete. This equation has an implicit flexibility form as it expresses $1/I_e$ as a weighted average of $1/I_g$ and $1/I_{cr}$

$$\frac{1}{I_e}=\left(\frac{M_{cr}}{M}\right)^2\frac{1}{I_g}+\left[1-\left(\frac{M_{cr}}{M}\right)^2\right]\frac{1}{I_{cr}} \tag{37}$$

This equation has a similar basis to Eurocode 2 (1994). It models the tension stiffening fairly accurately and estimates the instantaneous deflection more reliably than Eq. (36) (Bischoff 2005; Gilbert 2007). The majority of the research done on effective moment of inertia is relevant to reinforced concrete, and less attention has been given to the

prestressed concrete beams particularly where the low modulus materials such as FRP is used for prestressing. ACI Committee 440.4R (2004) recommends the use of an effective moment of inertia for prestressed FRP reinforced concrete beams, which is very similar to Branson's equation

$$I_e = \left(\frac{M_{cr}}{M}\right)^3 \beta_d I_g + \left[1 - \left(\frac{M_{cr}}{M}\right)^3\right] I_{cr} \leq I_g \tag{38}$$

where β_d = a factor to soften the effective moment of inertia for a better fit with experimental data and equals

$$\beta_d = 0.5\left[\frac{E_p}{E_s} + 1\right] \tag{39}$$

In which E_p and E_s are elastic modulus of FRP and steel, respectively. In spite of using the reduction factor, β_d, the empirical nature of this equation makes its general applicability uncertain (Gilbert 1999).

This chapter of thesis incorporates a rational model to develop an applicable equation for estimating the effective moment of inertia to predict the deflection of FRP prestressed concrete beams. Instantaneous deflection is only considered and FRP bars are assumed to be pretensioned. The derived equation presented herein is subsequently verified by experimental data and compared with the ACI 440.4R (2004) formula.

8.2 Flexural Behavior

In the case of steel prestressed concrete beams, the moment-curvature relationship of the section becomes nonlinear as the steel yields. Moreover, since the beam commonly fails due to crushing of the concrete, the inelastic compressive stresses in concrete add some ductility to the flexural behavior of the beam. In contrast, experimental and analytical research have revealed that the moment-curvature behavior of FRP prestressed concrete sections is typically a bilinear diagram (Pirayeh Gar et al. 2012 and Dolan et al. 2001), where the slope of the first line represents the uncracked flexural stiffness, EI_g, and the slope of the second line indicates the cracked flexural

stiffness, EI_{cr}. In this case, the failure mode can be governed by rupture of the tendons rather than crushing of the concrete, which prevents the concrete from inducing considerable inelastic stresses. Contrary to the prestressed case, the post-cracking behavior of non-prestressed FRP reinforced concrete sections is a curve whose slope converges to the cracked flexural stiffness. This is due to the significant effect of tension stiffening as a result of the concrete's ability to bear tension between the cracks (Bischoff 2005). Tension stiffening in prestressed concrete beams has been studied in Chapter 10.

Figs. 66(a) and 66(b) show the moment-curvature behavior for prestressed and non-prestressed reinforced concrete beams, respectively. In this figure, specifically, ϕ_0 represents the negative curvature, camber, induced by the eccentric prestressing force. In practice, such a camber will be cancelled out by the dead load. Since only the deflection under live load is sought, the origin of the coordinate system in Fig. 66(a) can be shifted to ϕ_0, without loss of generality.

Under any load level, the curvature can be determined along the beam using the moment-curvature relationship. Now consider a simply-supported FRP concrete beam under four-point loading, where the maximum moment, M, exceeds the cracking moment, M_{cr}, in a length equal to $a+2a'$, where a is the distance between the two loads, and a' is the extension of the cracked zone beyond the constant moment region (Fig. 67).

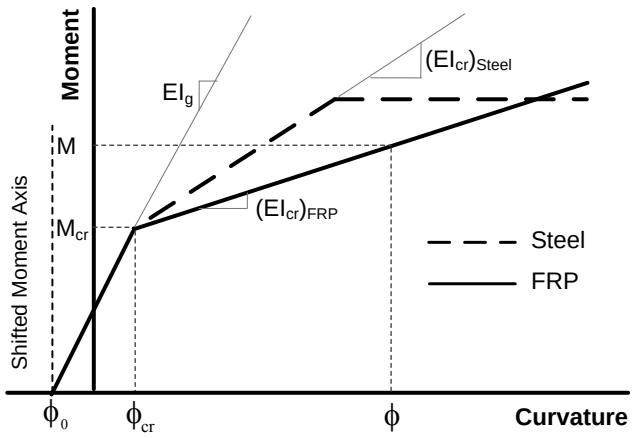

a) prestressed section

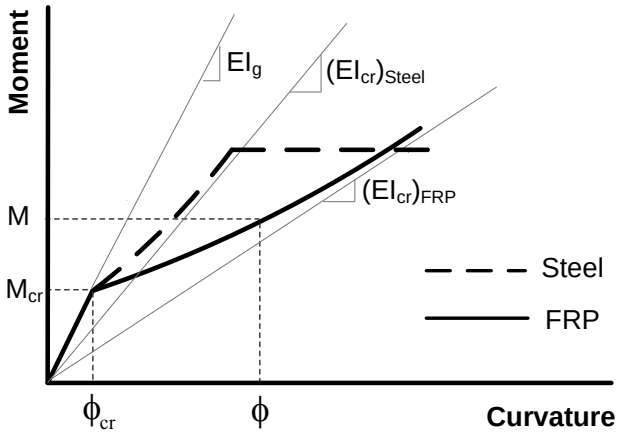

b) non-prestressed section

Fig. 66. Moment-curvature diagram for concrete section

The curvature along the beam can be determined given the moment-curvature relationship of the section under consideration. At the cracked zone, the curvature consists of the elastic, ϕ_g, and inelastic parts, ϕ^*. As a result of prestressing force, the inelastic curvature induced by cracking in the prestressed beam is considerably less than that of its non-prestressed counterpart given the same level of loading. For the prestressed FRP beam, the cracking and post-cracking curvature can be computed using Eq. (40).

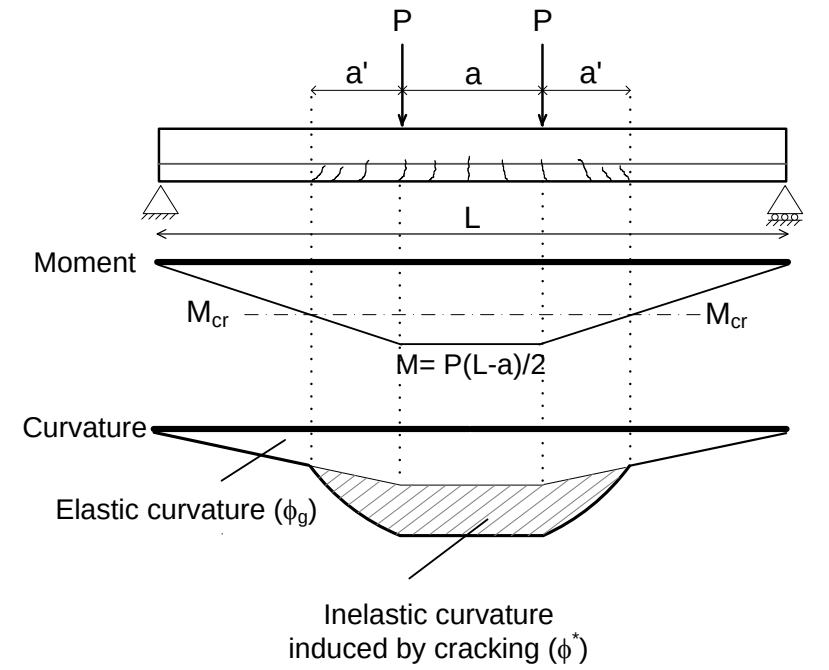

a) non-prestressed

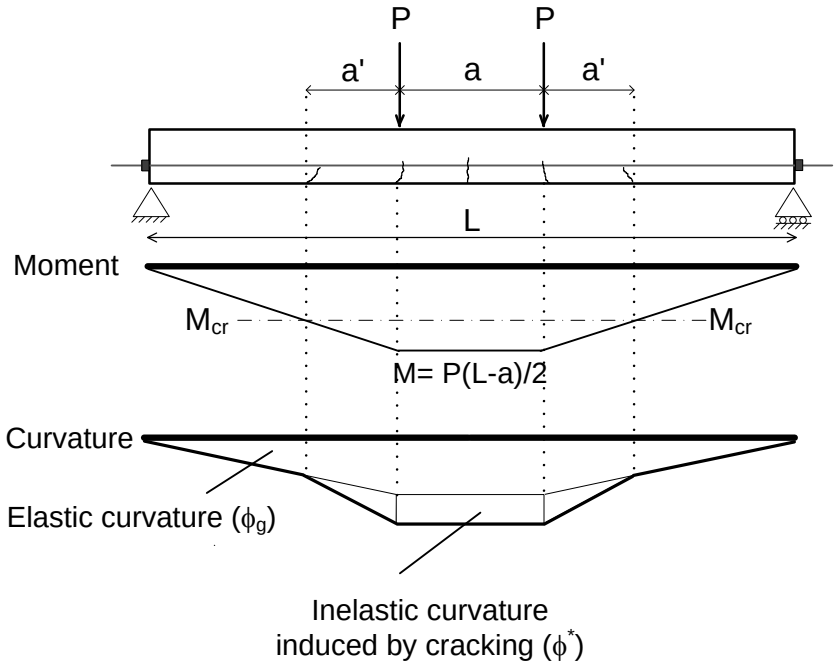

b) prestressed

Fig. 67. Moment and curvature diagrams for FRP concrete beam under four-point loading

$$\phi_{cr} = \frac{M_{cr}}{EI_g} \tag{40}$$

$$\phi = \frac{M_{cr}}{EI_g} + \frac{M - M_{cr}}{EI_{cr}} \tag{41}$$

Fig. 68 shows the curvature diagram for half of the FRP prestressed beam taking the advantage of symmetry. As seen, the curvature diagram can be divided into two parts: 1) elastic curvatures (plain area), and 2) inelastic curvatures (hatched area) induced by cracking. In fact, the maximum deflection at midspan is a contribution of the elastic and inelastic parts of the curvature. It should be noted that the same moment-curvature relationship was assumed for the entire beam meaning that the pretensioned bars have a straight profile.

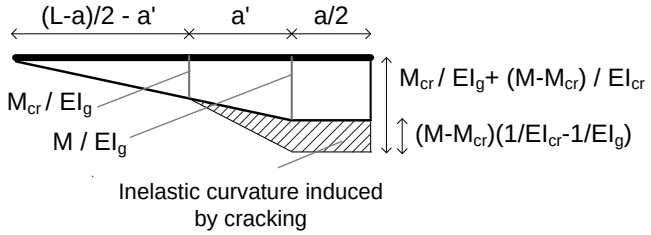

Fig. 68. Curvature diagram for half of the FRP prestressed concrete beam

8.3 Rational Model

The bilinear flexural behavior of FRP prestressed concrete beam can be well resembled with a rheological model of springs which is commonly used to express the plastic deformation in metals (Dowling 1993). As shown in Fig. 69, this model consists of two springs and one frictional slider. The first spring's stiffness represents the uncracked flexural stiffness of the beam, K_g, and the second spring's stiffness represents the flexural stiffness of the inelastic zone of the beam, K^*, due to cracking. The second spring and the slider are in parallel and their resultant is in series with the first spring. As

long as the applied load, M, is less than the cracking load, M_{cr}, the stiffness of the slider is infinity and it acts as a rigid body. Therefore, all the deformation is induced by the first spring, Δ_g, which means that the whole beam is in the elastic field and the flexural stiffness of the beam is equal to K_g. Once the load exceeds the cracking load, the stiffness of the slider becomes zero and it slides while holding a constant amount of load equal to M_{cr}. Consequently, the second spring starts to bear a load equal to the difference of the total and the cracking load, M-M_{cr}. The additional deformation induced by the second spring, Δ^*, corresponds to the inelastic deformation caused by cracking. Therefore, the total deformation of the spring system is equal to the elastic part, Δ_g, caused by the first spring and the inelastic part, Δ^*, induced by the second spring. In this case, the post-cracking stiffness of the beam, K_{cr}, is equal to the resultant stiffness of the two springs in series. The main objective is to find the effective stiffness, K_e, which linearly correlates the load to the total deflection and obviates the need for a rigorous analysis to account for inelastic deflections caused by cracking. This is equivalent to having only one spring with variable stiffness depending on the load level. K_g and K^*, corresponding to the elastic and inelastic parts of the deflection, can be computed using the conjugate beam theory. The post-cracking flexural stiffness of the beam, K_{cr}, can be determined using the following equation

$$\Delta = \frac{M}{K_g} + \frac{(M - M_{cr})}{K^*} = \frac{M_{cr}}{K_g} + \frac{(M - M_{cr})}{K_{cr}} \tag{42}$$

which, after simplification, yields to

$$\frac{1}{K_{cr}} = \frac{1}{K^*} + \frac{1}{K_g} \tag{43}$$

As seen, the post-cracking flexural stiffness of the beam is equal to the resultant stiffness of the two springs in series. Reasonably supposing, K_g is considerably larger than K^*, and it can be well inferred that the post-cracking stiffness of the beam, K_{cr}, is much closer to the stiffness of the second spring, K^*. This implies that the maximum deflection is mostly governed by the inelastic curvatures developed in cracked part of the beam.

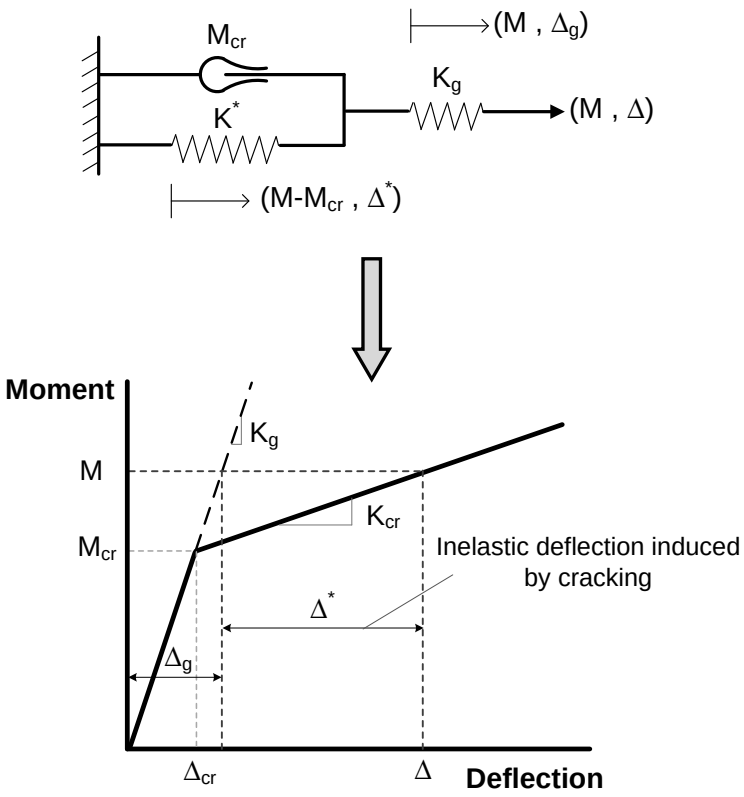

Fig. 69. Rheological model of springs to resemble the moment deflection behavior

The elastic deflection, Δ_g, or the deformation induced by the first spring is written as

$$\Delta_g = \frac{M}{K_g} \tag{44}$$

where, K_q can be found via conjugate beam theory as stated

$$K_g = \frac{12EI_g}{{L_g}^2} \tag{45}$$

and L_g is computed using the following equation

$${L_g}^2 = L^2(1-\beta)^2 F(\beta) \tag{46}$$

in which $\beta=a/L$ and $F(\beta)$ is defined as below

$$F(\beta) = 1 + \frac{3\beta}{1-\beta} + \frac{3}{2}\left(\frac{\beta}{1-\beta}\right)^2 \tag{47}$$

Likewise, the inelastic deflection, Δ^*, or the deformation induced by the second spring can be expressed as

$$\Delta^* = \frac{M - M_{cr}}{K^*} \tag{48}$$

and K^* is similarly calculated as

$$K^* = \frac{12EI^*}{L^{*2}} \tag{49}$$

where L^* equals to

$$L^{*2} = L^2\left[\frac{3}{2} + (1-\beta)^2\left(2F(\beta) + 0.5\frac{M_{cr}}{M} - \left(\frac{M_{cr}}{M}\right)^2\right)\right] \tag{50}$$

and I^* is

$$\frac{1}{I^*} = \frac{1}{I_{cr}} - \frac{1}{I_g} \tag{51}$$

The equivalent flexural stiffness of the beam, K_e, can be found if the total deflection, Δ, is equalized to the summation of the elastic, Δ_g, and inelastic, Δ^*, deflections

$$\frac{M}{K_g} + \frac{(M - M_{cr})}{K^*} = \frac{M}{K_e} \tag{52}$$

where K_e equals to

$$K_e = \frac{12EI_e}{{L_g}^2} \tag{53}$$

and I_e, so called the effective moment of inertia, can be assigned to the entire beam's section. Substituting Eqs. (45)-(47), (49)-(51), and (53) into Eq. (52) gives $1/I_e$ in terms of $1/I_g$ and $1/I_{cr}$

$$\frac{1}{I_e} = \left[\left(1 + \frac{1}{2F(\beta)}\right)\left(\frac{M_{cr}}{M}\right) - \frac{1}{2F(\beta)}\left(\frac{M_{cr}}{M}\right)^3\right]\frac{1}{I_g} + \left[1 - \left(1 + \frac{1}{2F(\beta)}\right)\left(\frac{M_{cr}}{M}\right) + \frac{1}{2F(\beta)}\left(\frac{M_{cr}}{M}\right)^3\right]\frac{1}{I_{cr}} \tag{54}$$

For further simplification, the following assumption is made

$$G(\beta) = \frac{1}{2F(\beta)} \tag{55}$$

where β varies from 0 to 1 theoretically; however in practice, the variation range can be deemed between 0 and 0.3. As illustrated in Fig. 70, the function *G(β)* can be well estimated with *0.5-β* in the aforementioned range for *β*. The effective moment of inertia can now be rewritten as

$$\frac{1}{I_e} = \lambda \frac{1}{I_g} + (1-\lambda)\frac{1}{I_{cr}} \tag{56}$$

$$\lambda = [1+G(\beta)]\left(\frac{M_{cr}}{M}\right) - G(\beta)\left(\frac{M_{cr}}{M}\right)^3 \tag{57}$$

$$G(\beta) \cong 0.5-\beta \qquad\qquad 0 \le \beta \le 0.3 \tag{58}$$

This equation can also be used for FRP prestressed one-way slabs; however, to account for the initial tension that unavoidably occurs due to drying shrinkage and thermal deformation, M_{cr} should be appropriately decreased (Gilbert 2007). Eurocode 2 (1992) and BS 8110 (1985) account for such a reduction in the cracking moment.

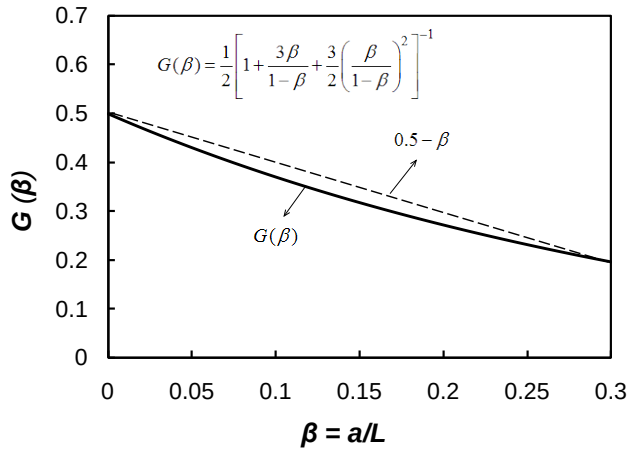

Fig. 70. Variation of G(β) versus the practical range for β

8.4 Verification with Experimental Data

Eight specimens tested by other researchers were selected with different specimen geometries, FRP types, and I_{cr}/I_g ratios to verify the proposed equation, Eq. (56). Specifications of these specimens are presented in Table 21, where ρ_t represents the total reinforcement ratio, β_d is indicative of FRP elastic modulus compared to that of steel, Eq. (4), $G(\beta)$ is defined per Eq. (58), and I_{cr}/I_g denotes the post-cracking to uncracked flexural stiffness of the section. All selected specimens were prestressed using pretensioned FRP tendons with a straight profile. Fig. 71 presents the comparison between experimental data, proposed equation, and ACI 440.4R formula, Eq. (3). Experimental values for cracking moment, M_{cr}, and code values for modulus of elasticity of concrete, E_c, are used in this comparison.

It is seen that for all specimens, the proposed equation matches well with the experimental data, thereby confirming its high fidelity. ACI 440.4R equation estimates the deflection reasonably only for some of the specimens. For instance, predictions of ACI 440.4R equation for specimens B9-4F and B12-4F tested by Dolan et al. (2001) and the specimen tested by Sen et al. (1998) are very similar to the experimental results and the proposed equation as well. However, for other specimens the deflection at midspan is significantly different with ACI 440.4R predictions.

For example, the ACI 440.4R equation overestimates the deflection of the specimen tested by Abdelrahmaan et al. (1995), and underestimates the deflections of the specimen B9-2F tested by Dolan et al. (2001) and the specimens tested by Lees et.al (1999). It is also seen that for the specimen tested by Stoll et al. (2000), ACI 440.4R estimates the deflection well after cracking; however when the load exceeds approximately 1.5 times the cracking load, it begins to overestimate the deflection but still acceptable. The experimental results of the prestressed strip specimen tested by the authors and discussed in Chapter 5, is compared with the proposed equation and ACI 440.4R as shown in Fig. 71(i). Since the I_{cr}/I_g ratio is very low, 0.014, the ACI 440.4R equation underestimates the deflection significantly.

Table 21- Selected experimental specimens for verification

Researcher	Specimen Geometry	FRP Type	ρ_t	β_d	$G(\beta)$	I_{cr}/I_g
Author	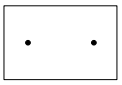 200 × 305	AFRP (Arapree)	0.0026	0.67	0.25	0.014
Lees et al. (1999)	 200×100	AFRP (Spiral)	0.0012	0.635	0.167	0.02
Lees et al. (1999)	 200×100	AFRP (Braided)	0.0016	0.67	0.167	0.03
Dolan et al. (2000)	 229 × 152 Designation: B9-2F	CFRP (Strawman)	0.0028	0.87	0.33	0.06
Dolan et al. (2000)	 305 × 152 Designation: B12-4F	CFRP (Strawman)	0.0042	0.87	0.33	0.08
Dolan et al. (2000)	 229×152 Designation: B9-4F	CFRP (Strawman)	0.0056	0.87	0.33	0.085
Sen et al. (1998)	 150×114	AFRP (Arapree)	0.0036	0.812	0.35	0.085
Stoll et al. (2000)	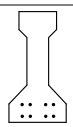 AASHTO I-Beam Type II	CFRP (Leadline)	0.0027	0.867	0.287	0.09
Abdelrahman et al. (1995)	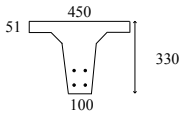	CFRP (Leadline)	0.0031	0.87	0.327	0.12

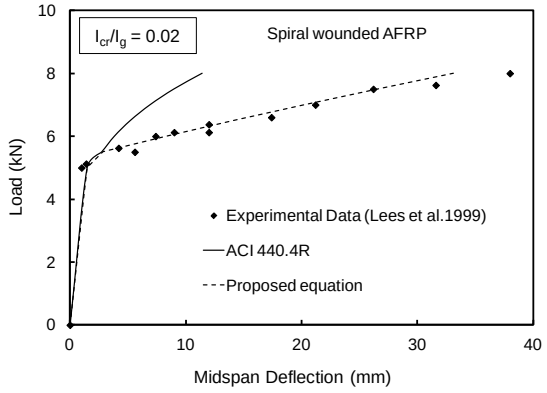

a) I_{cr}/I_g=0.02

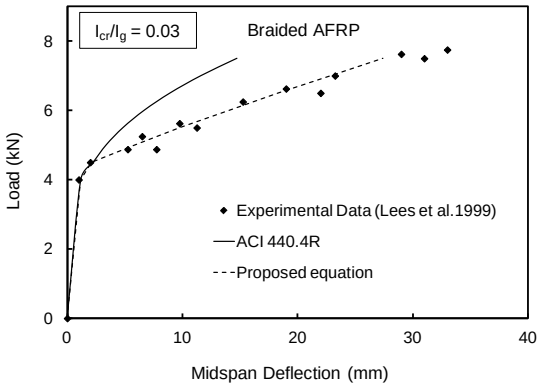

b) I_{cr}/I_g=0.03

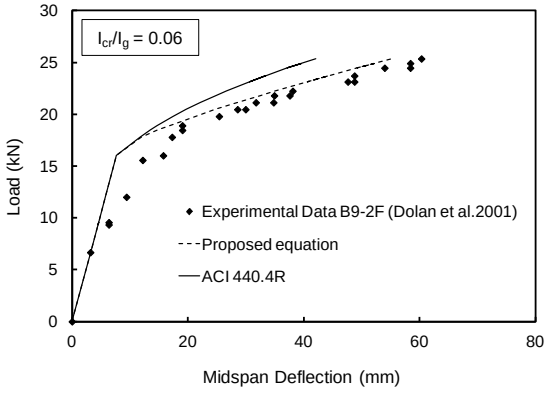

c) I_{cr}/I_g=0.06

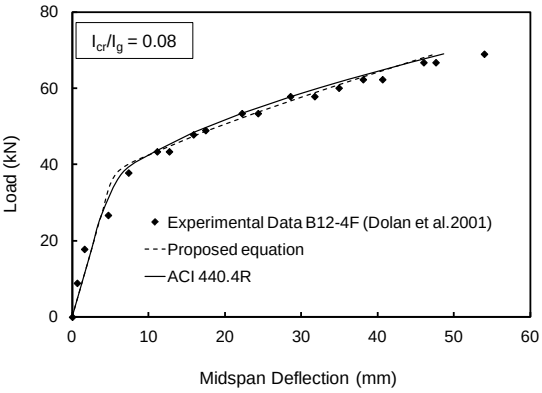

d) I_{cr}/I_g=0.08

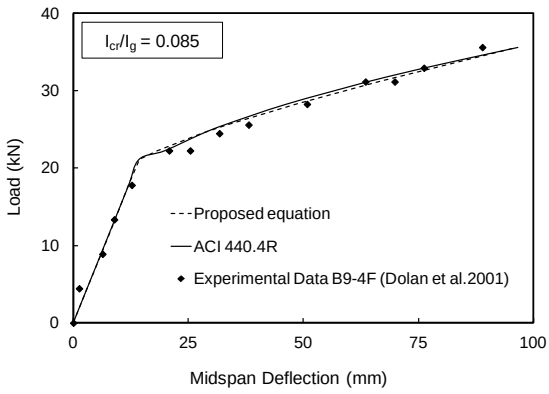

e) I_{cr}/I_g=0.085

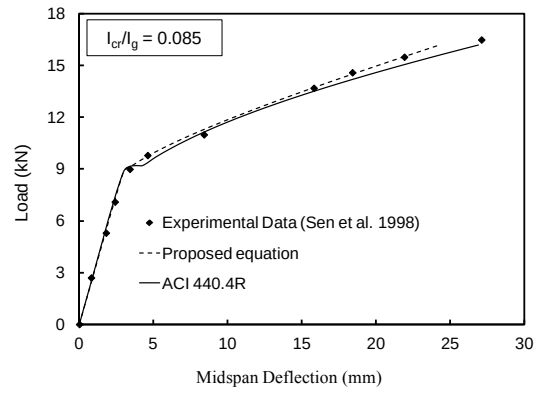

f) I_{cr}/I_g=0.085

Fig. 71. Verification of load deflection response

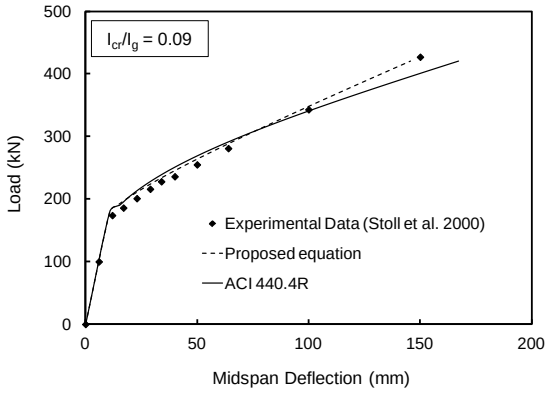

g) I_{cr}/I_g=0.09

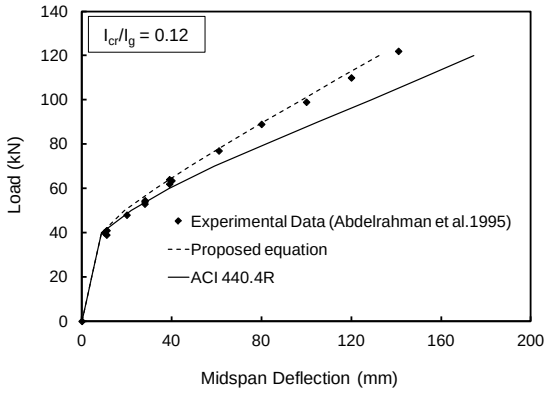

h) I_{cr}/I_g=0.12

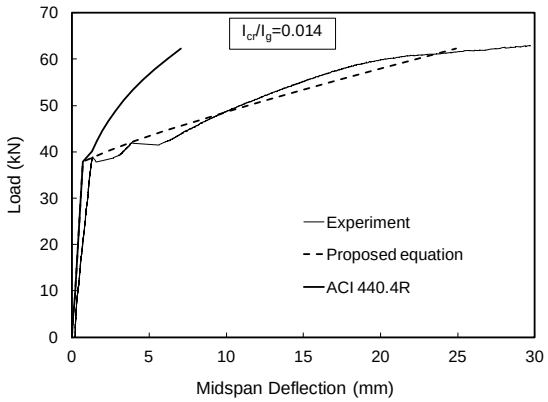

i) I_{cr}/I_g=0.014

Fig. 72. Verification of load deflection response (cont'd)

8.5 Discussion

The observations obtained from comparison between experimental data, the proposed equation, and ACI 440.4R equation raises the question "why the proposed equation provides fairly accurate predictions, but ACI 440.4R estimates the deflection reasonably only for some of the specimens?" In other words, what parameter is affecting the accuracy of ACI 440.4R deflection equation? Research done by Bischoff (2005, 2007a, b, c) regarding deflection evaluation of non-prestressed FRP reinforced concrete beams has well revealed the limitations that Branson's empirically derived equation

suffers from. In these studies, it has been shown that the Branson's equation which was calibrated for steel reinforced concrete beams results in responses which are too stiff for FRP case, and hence the deflection is often under-predicted. The dependence of the Branson's equation to the I_g/I_{cr} ratio was realized as the main reason, and it was clarified that for non-prestressed FRP reinforced concrete beams whose the I_{cr}/I_g ratio is typically greater than 0.2, this equation underestimates the deflection. The acceptable predictions can be achieved when the I_{cr}/I_g ratio is between 0.33 and 0.5, which is suitable for steel reinforced concrete beams. Since ACI 440.4R equation is based on the Branson's original equation, the ratio of I_{cr}/I_g is thought to be a parameter which is affecting the accuracy of this deflection equation.

To study the effect of I_{cr}/I_g ratio on effective moment of inertia, I_e is calculated using the proposed equation as well as ACI 440.4R equation for different values of I_{cr}/I_g ratio. For the sake of consistency between all the responses and without loss of generality, $G(\beta)$ and β_d are assumed to be equal to 0.33 and 0.87, respectively. Fig. 72 illustrates the responses, where the vertical axis represents I_e normalized to I_{cr}, and the horizontal axis indicates the moment normalized to the cracking moment. Since the proposed equation proved to be well matched with the experimental data, it is used as a criterion to evaluate the effective moment of inertia predicted by ACI 440.4R. It is observed from Fig. 72 that for low I_{cr}/I_g ratios, less than 0.08, ACI 440.4R overestimates I_e particularly in the serviceability domain. That is why for the specimens tested by Lees et al. (1999), where the I_{cr}/I_g is low, ACI 440 under-predicts the deflection, Figs. 71(a) and 72(a). On the other hand, for I_{cr}/I_g ratios between 0.08 and 0.1, it is seen that both the proposed equation and ACI 440.4R equation give rise to very close responses. This well justifies why these two equations predict fairly similar deflections for specimens B9-4F and B12-4F tested by Dolan et al. (2001), and Sen et al. (1998). However, for I_{cr}/I_g ratios larger than 0.1, ACI 440.4R begins to underestimate the I_e which leads to over-predicting the deflection, accordingly. The experimental result from the test conducted by Abdelrahmaan et al. (1995) confirms this, Fig. 71(h), and shows that as the load goes beyond the cracking load, the deflection estimated by ACI 440.4R becomes

larger than the experimental results. Referring to the test conducted by Stoll et al. (2000), where the I_{cr}/I_g ratio is 0.09, Fig. 71(g), ACI 440.4R equation estimates the deflection well after the cracking; however, when the load exceeds approximately 1.5 times the cracking load, it begins to overestimate the deflection. This indicates that as the I_{cr}/I_g ratio becomes close to 0.1, the ACI 440.4R formula tends to overestimate the deflection.

This can be better understood by Figs. 72(e) and 72(f), where the effective moment of inertia has been calculated for $I_{cr}/I_g = 0.09$ and 0.1, respectively. It is seen that for the I_{cr}/I_g ratio close to 0.1, when the load exceeds approximately 1.5 times the cracking load, ACI 440.4R begins to under-predict the effective moment of inertia, which subsequently leads to overestimating the deflection. The same concept, however conversely, is true when $I_{cr}/I_g < 0.08$, in the sense that I_e is overestimated by ACI 440.4R and the deflection is under-predicted. Figs. 72(a) and 72(b) clearly confirm this conclusion.

The susceptibility of the ACI 440.4R equation particularly to the low I_{cr}/I_g ratios lies in the fact that this equation uses a directly weighted average of the gross and cracked moment of inertia for a certain load level. This is analogous to two parallel springs whose stiffness is proportional to I_g and I_{cr} depending on the load level. In this case the resultant stiffness is governed by the stiffer spring (I_g). However, Eq. (56) takes a weighted average of the inverse gross and cracked moment of inertia for a certain load level, which is analogous to two series springs and implies that the resultant stiffness is governed by the flexible spring (I_{cr}). As shown in Eq. (52), the maximum deflection of the beam is a summation of the deflection induced by the elastic and inelastic curvatures. Therefore, in reality the maximum deflection, and not the effective moment of inertia, is a weighted average of the elastic and inelastic deflections. Since the deflection is inversely proportional to the moment of inertia, the inverse of the effective moment of inertia is the weighted average of the inverse of I_g and I_{cr} indeed, Eq. (56).

To elaborate this substantial difference, the effective moment of inertia predicted by ACI440.4R and Eq. (56) has been illustrated in Figs. 73(a) and 73(b). Without loss of the generality, the function $G(\beta)$ is deemed as equal to 0.33 and the coefficient β_d is

taken equal to 1 (Branson's equation), and I_{cr}/I_g=0.08. It is observed that I_g has the most weight in I_e predicted by ACI440.4R when 1< M/M_{cr}< 2.25 and beyond this load range the weight of I_{cr} becomes more pronounced. This generally shows that I_e is mostly governed by I_g particularly in serviceability region. In contrast, in Eq. (56), I_{cr} has the most weight in I_e and I_g is only influential in very early stages of cracking (1< M/M_{cr}< 1.2). This makes a physical sense as the proposed rheological model showed that the post-cracking stiffness of the beam (K_{cr}) is largely dominated by the stiffness of the cracked zone (K^*) rather than the uncracked stiffness of the beam (K_g).

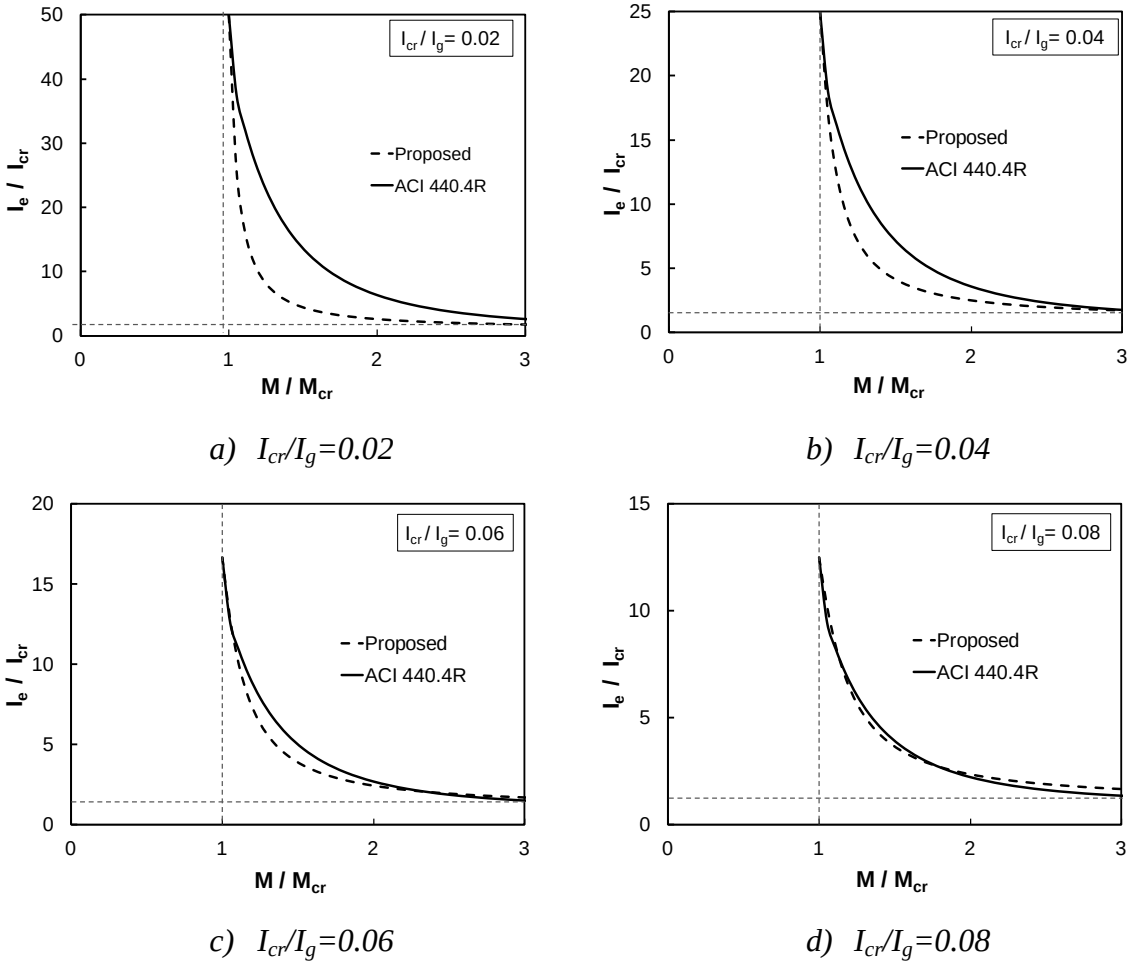

a) I_{cr}/I_g=0.02

b) I_{cr}/I_g=0.04

c) I_{cr}/I_g=0.06

d) I_{cr}/I_g=0.08

Fig. 73. Effective moment of inertia for different I_{cr}/I_g ratios

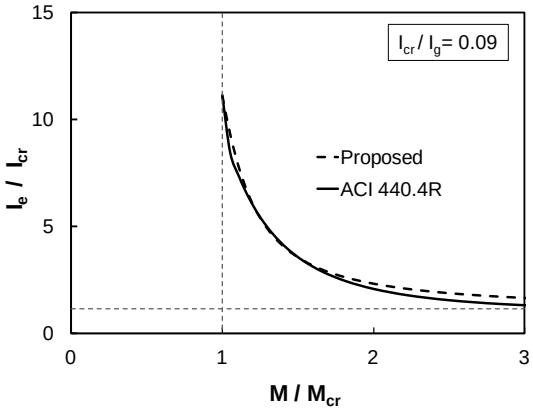

e) I_{cr}/I_g=0.09

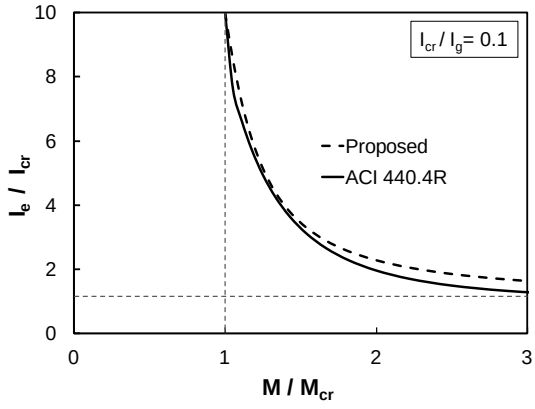

f) I_{cr}/I_g=0.1

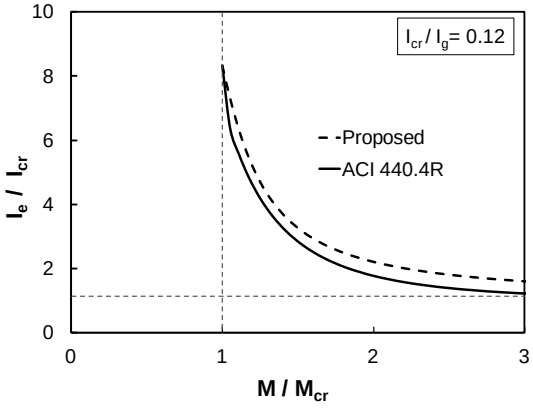

g) I_{cr}/I_g=0.12

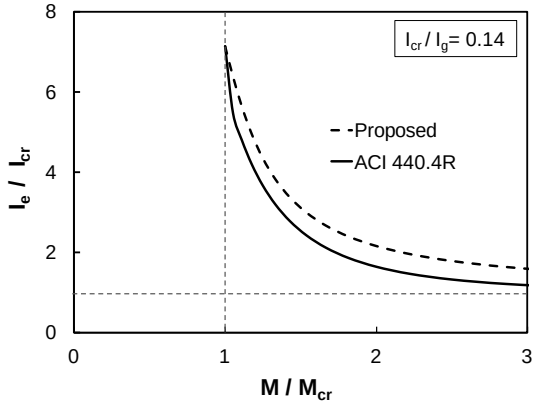

h) I_{cr}/I_g=0.14

Fig. 74. Effective moment of inertia for different I_{cr}/I_g ratios (cont'd)

8.6 Sensitivity Analysis

To further clarify the susceptibility of the ACI 440.4R equation to low Icr/Ig ratios, the predicted Ie is depicted versus the ratio I_{cr}/I_g for various load levels, Figs. 74 and 75. It is seen that for low ratios of I_{cr}/I_g, ACI 440.4R gives the responses which are significantly stiffer than what Eq. (56) shows. Moreover, in practical range of I_{cr}/I_g for prestressed FRP reinforced concrete beams (between 0.02 and 0.1) the proposed equation shows that as the load level raises and the beam section becomes fully cracked, I_e/I_{cr} does not perceptibly change as the I_{cr}/I_g ratio varies, however, the I_e/I_{cr} predicted by ACI 440.4R equation shows considerable variations particularly for low I_{cr}/I_g ratios.

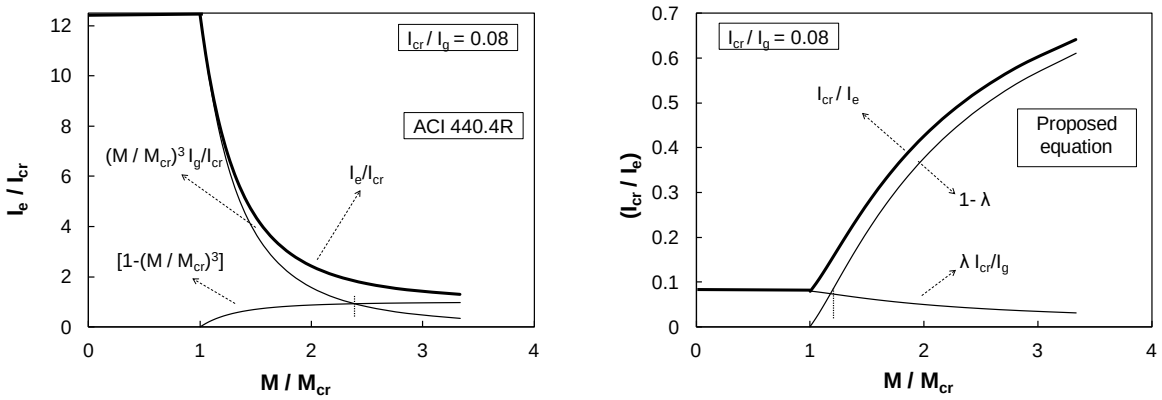

a) ACI 440.4R *b) proposed equation*

Fig. 75. Effective moment of inertia for different M/M_{cr} ratios

Fig. 10 well confirms this result and shows that the ACI 400.4R equation is vulnerable to low I_{cr}/I_g ratios and the predictions change drastically with decreasing the I_{cr}/I_g ratio. To make a direct comparison of the predicted effective moment of inertia, the ratio of the ACI 440.4R prediction to that of Eq. (56) is depicted versus the load level.

Fig. 76 shows that in serviceability domain, for low I_{cr}/I_g ratios the responses predicted by ACI 440.4R are much stiffer than that of Eq. (56). For instance, ACI 440.4R assesses the effective moment of inertia three times the actual amount when I_{cr}/I_g = 0.02 which results in a deflection far less than the actual amount as was observed in Fig. 72(a) and 72(b). The results also show that the vulnerability of ACI 440.4R to high I_{cr}/I_g ratios is not as much pronounced as seen for the low I_{cr}/I_g ratios, but nonetheless, still affecting the design.

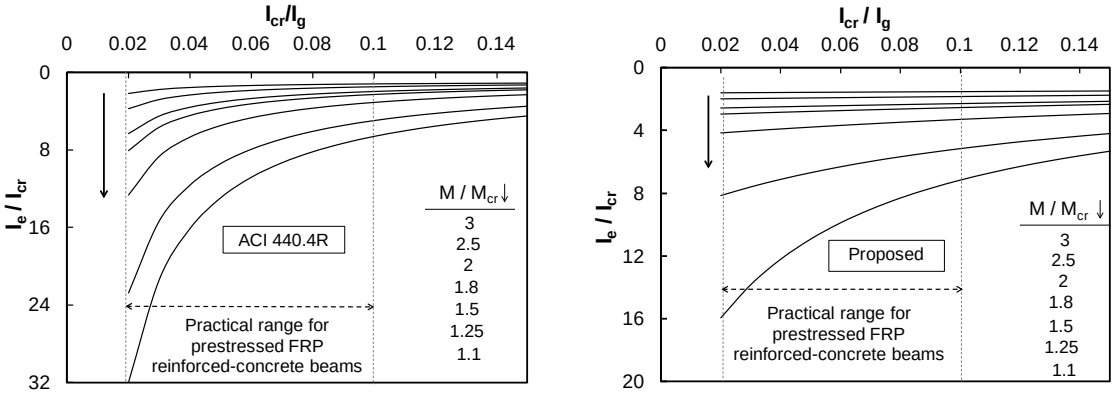

a) ACI 440.4R *b) proposed equation*

Fig. 76. Variation of effective moment of inertia versus I_{cr}/I_g ratio

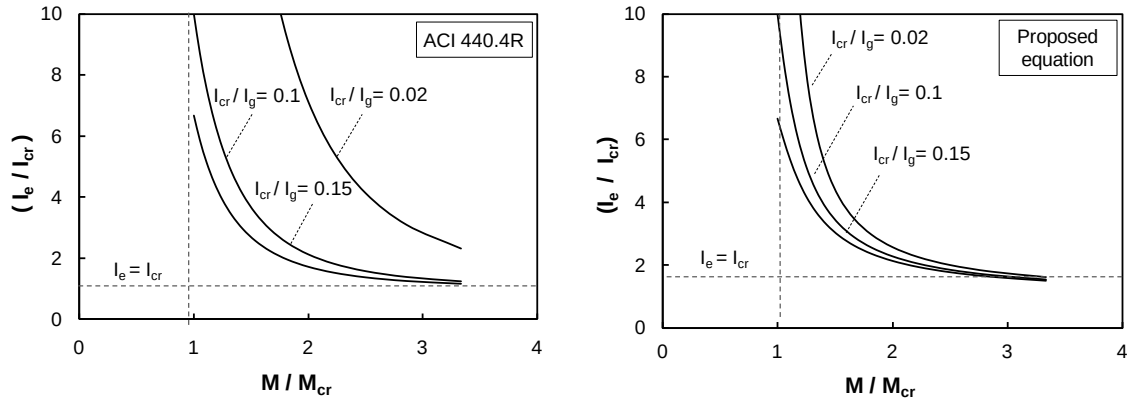

a) ACI 440.4R *b) proposed equation*

Fig. 77. Effect of I_{cr}/I_g ratio on effective moment of inertia

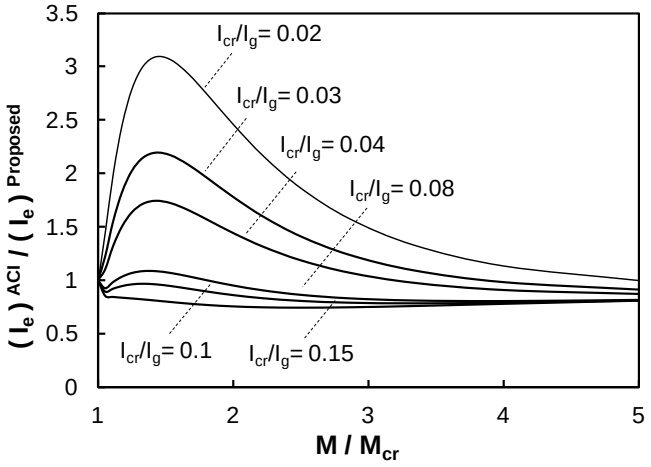

Fig. 78. Sensitivity of the effective moment of inertia predicted by ACI 440.4R to I_{cr}/I_g ratio

8.7 Conclusions

The moment-curvature characteristic of FRP reinforced concrete beams was studied and a rational model resembled by a rheological system of springs was introduced to better understand the flexural behavior of FRP prestressed concrete beam. Based on this, an applicable equation for effective moment of inertia, I_e, was derived. This equation, Eq. (56), estimates $1/I_e$ using a gradual transition from $1/I_g$ to $1/I_{cr}$ depending on the load configuration and load level. Load configuration is reflected by the function $G(\beta)$ which is equal to 0.5 for three-point loading, 0.5-β for four-point loading, and approximately 0.2 for uniformly distributed load. Also, M_{cr}/M ratio reflects the effect of load level. For verification, eight experimental specimens tested by other researchers were selected with different geometries, FRP types, and I_{cr}/I_g ratios. It was observed that the developed equation is in good agreement with experimental data; however, the ACI 440.4R equation provided reasonable predictions only for some of the specimens. Further studies revealed that the ACI 440.4R equation overestimates I_e when $I_{cr}/I_g < 0.08$ which results in under-predicted deflections and underestimates I_e when $I_{cr}/I_g>0.1$ which gives rise to over-predicted deflections.

Vulnerability of ACI 440.4R equation to high I_{cr}/I_g ratios is not as much pronounced as seen for the low I_{cr}/I_g ratios, nonetheless affects the design and leads to conservative deflections. The rational model developed and the comparison with the experimental data are quite conclusive in showing that the substantial problem of ACI 440.4R equation is using the weighted average of stiffness to find the effective moment of inertia, I_e, which physically implies two parallel springs. In this case I_e is mostly governed by the stiffer spring, I_g, in the sense that the deflections are often under-predicted. However, as deflection is inversely proportional to stiffness, the weighted average of flexibility, *1/I*, should be used to find the effective moment of inertia, I_e, which physically represents two springs in series. In this case I_e is mostly governed by softer spring, I_{cr}. The authors believe that modification of Branson's equation by multiplying a reduction factor or using a power larger than three is not an appropriate way, as the basis of this equation is empirical and not rational.

9. RATIONAL MODEL FOR DEFLECTION OF FRP REINFORCED CONCRETE BEAMS

9.1 Introduction

Steel reinforced concrete beams are commonly designed for strength and then checked for serviceability. In contrast, in FRP reinforced concrete beams, serviceability related to deflection and not strength typically governs the design because of the low modulus of elasticity of FRPs compared to steel. Therefore, accurate prediction of the maximum deflection becomes more crucial in design process. However, due to inherent corrosion resistivity of FRPs, controlling the crack width is not as critical as the deflection, and hence larger crack widths are typically allowed.

Deflection equations are commonly categorized in two different groups: 1) cross-sectional model and 2) block model. In the block model, the deflection of the flexural member is evaluated using the member block between two consecutive cracks. This is done by writing the equilibrium and compatibility equations in all blocks given the constitutive laws of the material and a rational bond-slip behavior, which results in a set of differential equations for deflection. The cross-sectional model, however, is more common and assumes that plane section remains plane after pure bending and there is a perfect bond between the concrete and reinforcement. In contrast to the cross-sectional model that generally tends to overestimate the deflection, the block model computes the deflection more accurately, but it is not convenient to use for engineers, and hence not suitable for design office implementation (Aiello and Ombres 2000).

As discussed in Chapter 8, one common and easy-to-apply method within the cross-sectional model to find the maximum deflection is to use the effective moment of inertia, I_e, of the beam proposed by Branson (1965). When a reinforced concrete beam cracks, the moment of inertia of the beam's section at the cracked zone changes from the gross moment of inertia, I_g, to the cracked moment of inertia, I_{cr}, and hence the flexural stiffness varies along the beam. This stiffness variation is basically reflected by

assigning I_e to the entire beam, which obviates the need for rigorous analysis to find the maximum deflection. Branson (1965) proposed an equation, where I_e is formulated as a gradual transition from I_g to I_{cr}

$$I_e = \left(\frac{M_{cr}}{M}\right)^3 I_g + \left[1 - \left(\frac{M_{cr}}{M}\right)^3\right] I_{cr} \leq I_g \tag{59}$$

in which M is the maximum moment in a member at which the deflection is being calculated and M_{cr} is the cracking moment. This semi-empirical equation was calibrated for steel reinforced concrete beams most of which had a reinforcement ratio about 1.65% which approximately corresponds to $2< I_g/I_{cr} <3$ (Washa and Fluck 1952; Branson 1965). However, this equation is not suitable for FRP RC beams where typically $5< I_g/I_{cr} <25$ and it leads to very stiff responses that substantially underestimates the deflection (Nawy and Neuwerth 1977; Yost et al. 2003; Bischoff 2005; Bischoff and Scanlon 2007). Poor bond strength and excessive cracking in FRP RC members which lead to loss in tension stiffening were first thought to be the main reasons of this problem (ACI Committee 440.1R 2006).

Three different methodologies are seen among all the proposed deflection equations for FRP RC beams (Mota et al. 2006). One method is a direct modification to Branson's equation for the sake of keeping the basic form of this equation unchanged as it is convenient to use for engineers. For instance, some researchers have used a power larger than three in Eq. (59) to let I_e converge to I_{cr} quicker than the cubic form and result in softer responses (Brown and Bartholomew 1996; Toutanji and Saafi 2000). Some other researchers multiplied I_g or I_{cr} or both by a coefficient less than 1 in an attempt to add some flexibility to the responses (Benmokrane et al. 1996; Yost 2003; ACI committee 440 2006). Recent studies (Bischoff 2003, 2005) have revealed that the problem with Branson's equation is not attributed to loss in tension stiffening or poor bond strength. In fact, Branson's equation doesn't model tension stiffening correctly since it is based on the weighted average of stiffness, *EI*, rather than flexibility, *1/EI*, and hence it is very susceptible to I_{cr}/I_g ratio. Consequently, any modified version of Branson's equation still

caries this rational problem. The second method is using a simplified moment curvature diagram and applying the virtual work method to find the deflection in an explicit form (Faza and GangaRao 1992; Razaqpur et al. 2000; Rasheed et al. 2004; CSA 2002). Although this method has a rational basis, tension stiffening effect will not be correctly reflected given the simplified moment-curvature response. Also the final equation is not as easy to use as the Branson's equation is. In the third method, the actual moment curvature response where the tension stiffening is taken into account is employed to determine the I_e (Fig. 77).

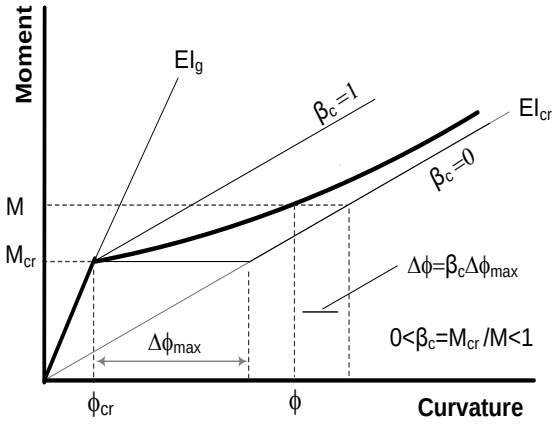

Fig. 79. Typical moment-curvature diagram for FRP RC beams

In this figure $\beta_c = 0$, $\beta_c = 1$, and $\beta_c = M_{cr}/M$ indicate no tension stiffening, full tension stiffening, and actual response, respectively. Also, ϕ_{cr} and ϕ are the curvatures corresponding to cracking and post-cracking moments, M_{cr} and M, respectively. If zero tension stiffening is assumed, then the actual curvature at cracking and post-cracking loads will be raised by $\Delta\phi_{\max}$ and $\Delta\phi$, respectively. The tension stiffening factor for curvature, β_c, is defined as $\Delta\phi/\Delta\phi_{\max}$ ratio. $\Delta\phi_{\max}$ can be written as

$$\Delta\phi_{\max} = \frac{M_{cr}}{E_c I_{cr}} - \frac{M_{cr}}{E_c I_g} = \frac{M_{cr}}{E_c I_{cr}}\left(1 - \frac{I_{cr}}{I_g}\right) \tag{60}$$

therefore, ϕ can be determined given $\Delta\phi = \beta_c \Delta\phi_{\max}$

$$\phi = \frac{M}{E_c I_{cr}} - \Delta\phi = \frac{M}{E_c I_{cr}} - \beta_c \Delta\phi_{\max} = \frac{M}{E_c I_{cr}} \left[1 - \beta_c \frac{M_{cr}}{M} \left(1 - \frac{I_{cr}}{I_g} \right) \right] \tag{61}$$

given $E_c I_e = M / \phi$, the effective moment of inertia can be expressed as

$$I_e = \frac{I_{cr}}{1 - \beta_c (M_{cr} / M)(1 - I_{cr} / I_g)} \tag{62}$$

Tension stiffening factor is typically assumed to be $\beta_c = M_{cr} / M$ (Murashev et al. 1971; CEB-FIP 1990), and hence Eq. (62) can be simplified and rearrange in the following form (Bischoff 2007)

$$\frac{1}{I_e} = \left(\frac{M_{cr}}{M} \right)^2 \frac{1}{I_g} + \left(1 - \left(\frac{M_{cr}}{M} \right)^2 \right) \frac{1}{I_{cr}} \tag{63}$$

The curvature at the critical section is found from $\phi = M / E_c I_e$, and the maximum deflection is computed from $\delta_m = kL^2 M / E_c I_e$ where coefficient k depends on loading and support conditions. Although using Eq. (63) to find the maximum deflection results in reasonable predictions (Gilbert 2007); assuming the same moment of inertia for the critical section as for the entire beam is not physically true. In other words, the effective moment of inertia at the critical section has been assigned to the entire beam to find the deflection which will clearly result in over-prediction due to ignoring the uncracked parts of the beam. Evidently, this error will be more pronounced for beams with low I_{cr}/I_g ratio. In fact, to find the actual effective moment of inertia it is required to integrate the curvature along the beam. This point has recently been noticed by Bischoff and Gross (2011), and an integration-based expression for effective moment of inertia, I'_e, has been represented in the following form

$$\frac{1}{I'_e} = \gamma \left(\frac{M_{cr}}{M} \right)^2 \frac{1}{I_g} + \left(1 - \gamma \left(\frac{M_{cr}}{M} \right)^2 \right) \frac{1}{I_{cr}} \tag{64}$$

Depending upon the loading type and the boundary conditions, γ can be found from separate formulae that have been presented in Bischoff and Gross (2011) in a tabular form. They have found that I'_e in Eq. (64) gives a stiffer response that improves prediction of deflection compared to I_e in Eq. (63), particularly for beams with low I_{cr}/I_g

ratios. Although Eq. (64) is considered as an improvement, there is no doubt on the fact that the accuracy of any integration-based expression for effective moment of inertia is greatly influenced by the assumed distribution of the curvature along the beam. For instance, assuming a larger tension stiffening factor, β_c, results in less curvature and less deflection, accordingly. Studying the distribution of the curvature along the beam and its effect on I_e seems to be an issue that has not been well investigated yet. In addition to a rational assumption for curvature distribution, the final form of the equation should also be kept as simple as possible for engineering design purposes. In this chapter, two rational and easy-to-use equations are derived for I_e based on different assumptions for curvature distribution in very slender and slender FRP reinforced concrete beams and the verification with experimental data is presented as well. The experimental results of the non-prestressed FRP strip, presented in Chapter 5, are again discussed herein to compare with the deflection equations derived.

9.2 Cracking Pattern

In order to rationally predict the maximum deflection, the curvature distribution along the beam should be first determined. Therefore an appropriate moment-curvature relationship where the tension stiffening is correctly taken into account should be employed. Tension stiffening is the ability of the concrete to bear tension between cracks in the sense that the larger crack spacing is a sign of higher contribution of the concrete in tension and larger tension stiffening, accordingly. This can be well seen in slabs where the reinforcement ratio is considerably less than beams or in FRP RC members where the modulus of elasticity is substantially less than that of conventional steel. Fig. 78 shows the general cracking pattern for very slender ($L_s/d>7$) and slender ($3<L_s/d<7$) beams under four-point loading (Park and Paulay 1975), where L_s/d is the shear span-to-depth ratio. As seen, the cracking pattern in shear span of slender beam is clearly different with very slender beam due to presence of shear diagonal cracks.

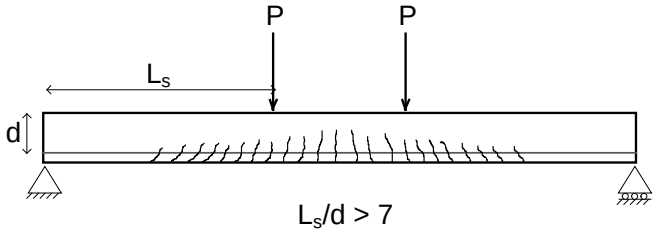

a) very slender beam

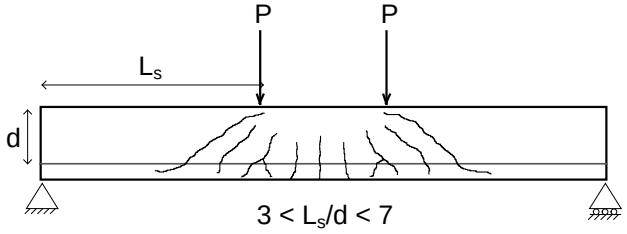

b) slender beam

Fig. 80. Cracking Pattern with different shear span-to-depth ratio

Experimental and analytical studies have confirmed that at shear span of slender beams the crack spacing is typically larger than that of constant moment span (Leonhardt 1965; Yang et al. 2003) implying that the tension stiffening factor is expected to be larger in this region. This point should be considered when assuming the moment-curvature relationship of the cross section along the beam as it affects the accuracy of the deflection prediction.

9.3 Effective Moment of Inertia

9.3.1 Very slender beam ($L_s/d > 7$)

As shown in Fig. 79, consider a very slender FRP RC beam under four-point loading. The maximum moment, M, exceeds the cracking moment, M_{cr}, in a length equal to $a+2a'$, where a is the distance between the two loads, and a' is the extension of the cracked zone beyond the constant moment span which is typically named transition zone.

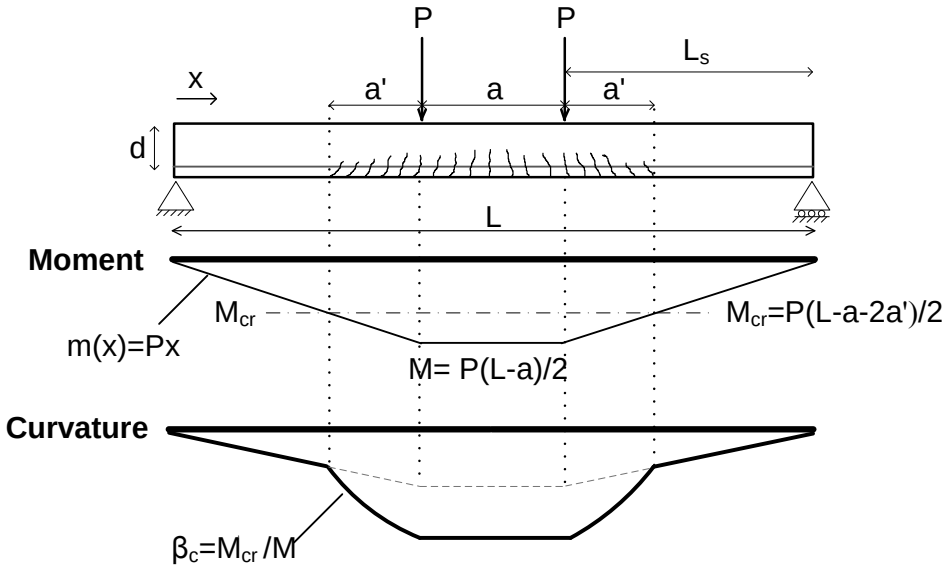

Fig. 81. Curvature distribution for very slender simply supported beam (under four point loading)

In this case, the curvature distribution along the beam can be reasonably assumed based on the moment-curvature behavior shown in Fig. 77 with tension stiffening factor $\beta_c = M_{cr}/M$ as the flexure governs the overall behavior of the beam. For the sake of simplicity and taking the advantage of symmetry, only half of the beam is considered in deflection computations. Curvature distribution has been quantitatively illustrated in Fig. 80 where lines 1 and 3 represent the lower bound or full tension stiffening, and the upper bound or zero tension stiffening, respectively. Line 2 indicates the assumed actual distribution based on which the effective moment of inertia is going to be specified. To find the maximum deflection at midspan, conjugate beam theory is applied where the curvature is treated as load, and the induced moment with respect to the left support in the conjugate beam, indicates the maximum deflection in the actual beam. The maximum deflection can be written as

$$\Delta = \frac{1}{3}\left(\frac{(L-a)}{2}-a'\right)^2 \frac{M_{cr}}{EI_g} + \frac{a}{2}\left(\frac{L}{2}-\frac{a}{4}\right)\left(\frac{\beta_c M_{cr}}{EI_g}+\frac{M-\beta_c M_{cr}}{EI_{cr}}\right) + \int_{\frac{L-a}{2}-a'}^{\frac{L-a}{2}} x\phi(x)dx \qquad (65)$$

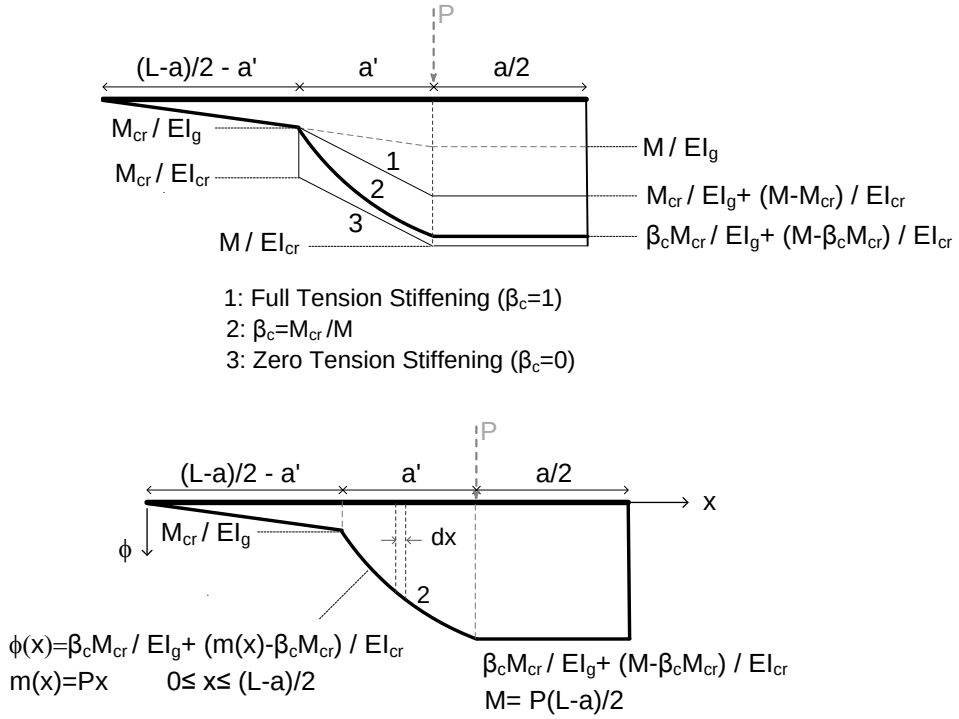

Fig. 82. Curvature distribution for different tension stiffening responses

where the curvature equation in transition zone, *a'*, is

$$\phi(x)=\frac{\beta_c M_{cr}}{EI_g}+\frac{m(x)-\beta_c M_{cr}}{EI_{cr}} \quad \text{and} \quad m(x)=Px \quad 0\le x\le \frac{L-a}{2} \tag{66}$$

from the bending moment diagram, *a'* can be related to *a* using

$$a'=\frac{L-a}{2}\left(1-\frac{M_{cr}}{M}\right) \tag{67}$$

substituting Eqs. (66) and (67) in Eq. (65) and assuming $\beta_c = M_{cr}/M$, gives the maximum deflection in the following form

$$\Delta=\frac{M_{cr}}{EI_g}\frac{(L-a)^2}{12}\left[\frac{M_{cr}}{M}(2+f(\beta))-2\left(\frac{M_{cr}}{M}\right)^2\right]+\frac{M-M_{cr}}{EI_{cr}}\frac{(L-a)^2}{12}\left[f(\beta)+\frac{M_{cr}}{M}f(\beta)-2\left(\frac{M_{cr}}{M}\right)^2\right] \tag{68}$$

where $\beta = a/L$ and $f(\beta)$ is defined as

$$f(\beta) = \frac{3}{2}\left(\frac{\beta}{1-\beta}\right)^2 + 3\left(\frac{\beta}{1-\beta}\right) + 1 \tag{69}$$

now if I_e is assigned to the entire beam given the linear behavior, the maximum deflection then can be readily computed as

$$\Delta_e = \frac{M}{EI_e}\frac{(L-a)^2}{12} f(\beta) \tag{70}$$

equalizing Eqs. (68) and (70) results in an expression for I_e in terms of I_g and I_{cr}

$$\frac{1}{I_e} = \frac{1}{I_g}\left[\left(\frac{2}{f(\beta)}+1\right)\left(\frac{M_{cr}}{M}\right)^2 - \frac{2}{f(\beta)}\left(\frac{M_{cr}}{M}\right)^3\right] + \frac{1}{I_{cr}}\left[1-\left(\frac{2}{f(\beta)}+1\right)\left(\frac{M_{cr}}{M}\right)^2 + \frac{2}{f(\beta)}\left(\frac{M_{cr}}{M}\right)^3\right] \tag{71}$$

Similar to what was presented in Chapter 8, the following assumption is made for the sake of further simplification

$$G(\beta) = \frac{1}{2f(\beta)} \tag{72}$$

where β varies from 0 to 1 from theoretical standpoint; however in practice, the variation range can be deemed between 0 indicating three-point loading, and 0.3 which approximately represents the uniformly distributed load. As illustrated in Fig. 81, *G(β)* can be well estimated with 0.5-β in the aforementioned range for β. With substituting Eq. (72) in (71), I_e can be rewritten as

$$\frac{1}{I_e} = \lambda\frac{1}{I_g} + (1-\lambda)\frac{1}{I_{cr}} \tag{73}$$

$$\lambda = [1+4G(\beta)]\left(\frac{M_{cr}}{M}\right)^2 - 4G(\beta)\left(\frac{M_{cr}}{M}\right)^3 \tag{74}$$

$$G(\beta) \cong 0.5-\beta \qquad\qquad 0 \le \beta = a/L \le 0.3 \tag{75}$$

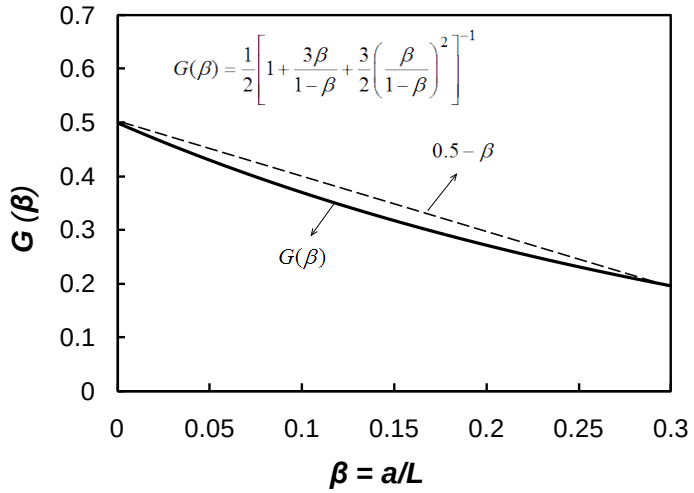

Fig. 83. Variation of *G(β)* versus the practical range for β

It should be noted that Eq. (73) results in the same prediction as Eq. (64) adopted by Bischoff and Gross (2011); however, the derived equation has a simpler form that can be used for either four-point loading, $\beta = a/L$, or three-point loading, $\beta = 0$. It can also be conservatively used for uniformly distributed load, $\beta = 1/3$. If this analysis is repeated for full and zero tension stiffening shown by line 1 and 3, respectively, in Fig. 62, the coefficient λ corresponding to the lower and upper bound for deflection is obtained as shown in Table 22.

9.3.2 Slender beam ($3<L_s/d<7$) — Experimental study of curvature distribution

As discussed, for slender beams where the shear span-to-depth ratio is between 3 and 7, the compound shear-flexural cracks with larger spacing form in the transition zone (the zone with length *a'* in Fig. 79) that raises the effect of tension stiffening in this region. Therefore, it seems to be more rational to assume a larger tension stiffening factor for transition zone in shear span compared to constant moment span. For further investigation, the experimental results of the AFRP RC strip, discussed in Chapter 5, is studied herein to better understand the distribution of the curvature along the beam. The experimental specimen, test set up, and failure mode are illustrated in Fig. 82. String

pots (STP) were hooked up to the beam to record the deflection at every 150 mm. Strain gages (STG) were mounted on AFRP bars to record the strain at the middle of the AFRP bars. The load was monotonically increased until failure of the beam. Figs. 83 and 84 show the moment diagram, curvature distribution, and deflection profile of the beam at post-cracking regions. It can be observed that the curvature at constant moment region is close to Eq. (63) adopted by Bischoff (2005) where the tension stiffening factor is deemed to be $\beta_c = M_{cr} / M$. However, at the transition zone of the shear span, as already discussed, the curvature tends to follow the bilinear distribution (lower bound) implying the tension stiffening factor close to $\beta_c = 1$. It is seen from the experiment that the deflection profile of the beam is generally between the Bischoff's original equation and the bilinear model.

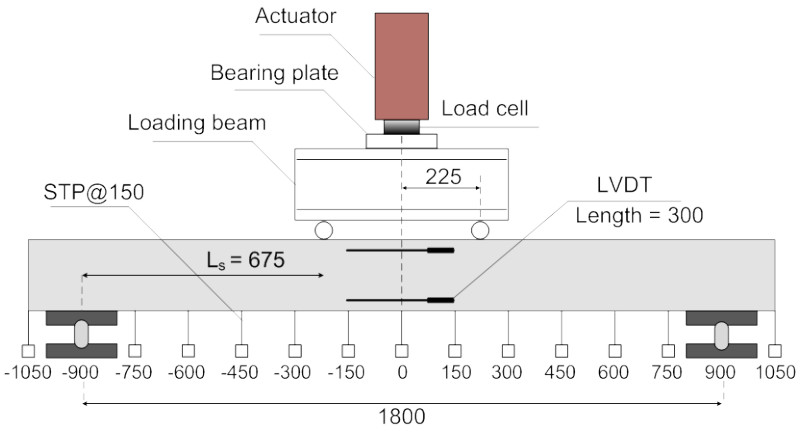

a) test setup

b) shear diagonal cracks in shear span

Fig. 84. AFRP reinforced concrete strip test

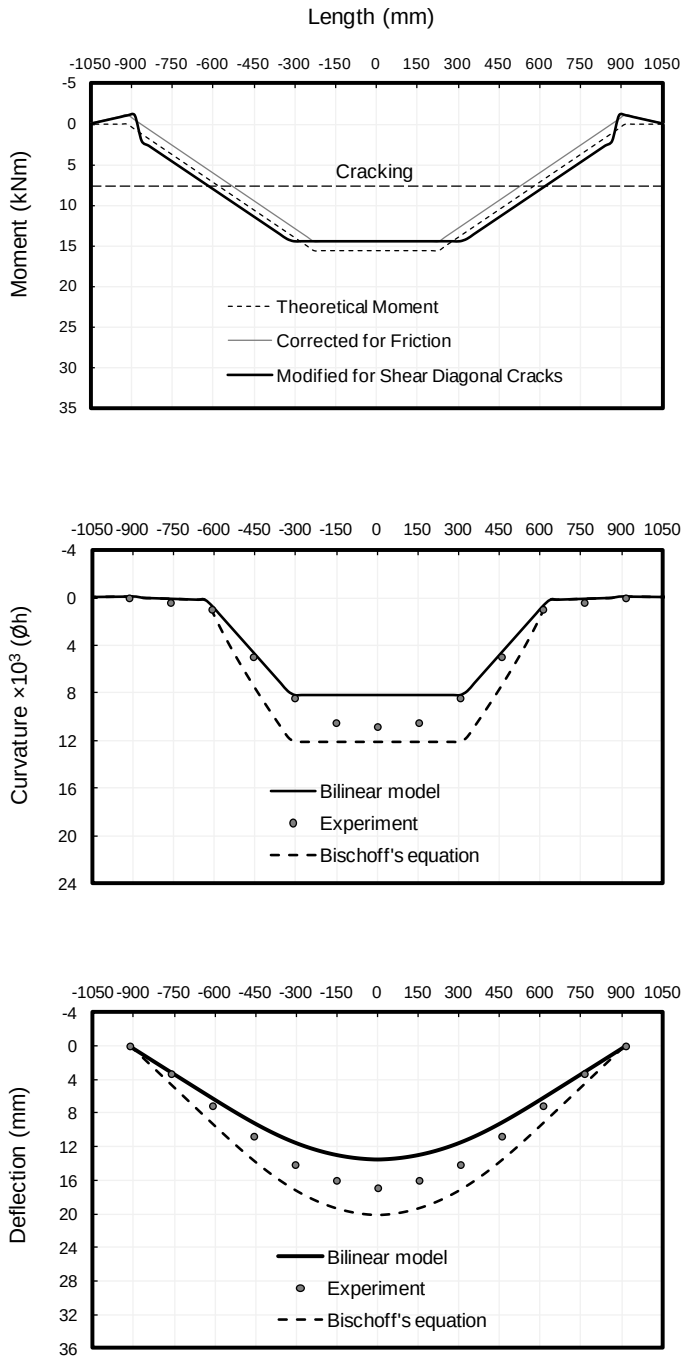

Fig. 85. Moment, curvature, and deflection along the beam at P=45 kN

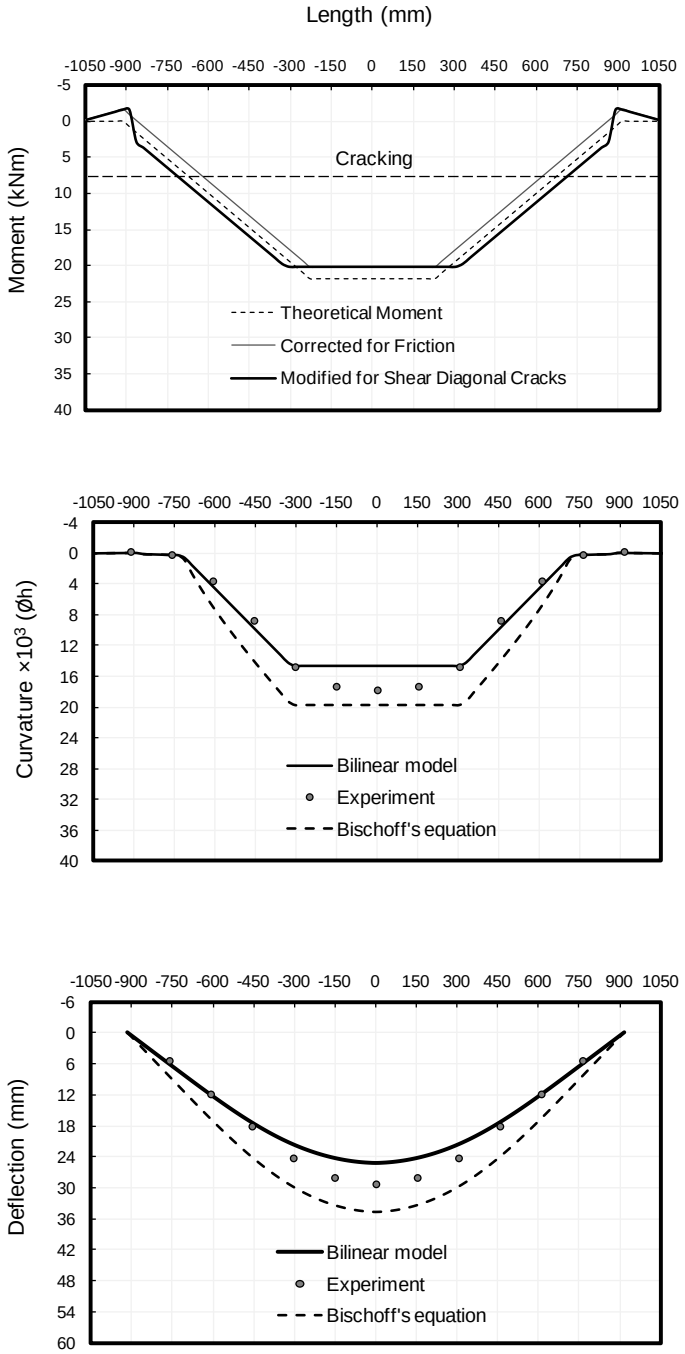

Fig. 86. Moment, curvature, and deflection along the beam at P=63 kN

Therefore, a better estimate of effective moment of inertia might be achieved by supposing $\beta_c = 1$ for the transition zone in shear span, and $\beta_c = M_{cr} / M$ for the constant moment span. Repeating the analysis done for very slender beam, however with this updated curvature distribution, results in the following equation for slender beams

$$\lambda = 3G(\beta)\left(\frac{M_{cr}}{M}\right) + [1 - 2G(\beta)]\left(\frac{M_{cr}}{M}\right)^2 - G(\beta)\left(\frac{M_{cr}}{M}\right)^3 \qquad (76)$$

Table 22 provides the summary of the equations for effective moment of inertia with different curvature distribution assumptions. $G(\beta)$ is a function that reflects the effect of loading configuration. It should be noted that the maximum deflection of a cantilever beam can be computed from a simply supported beam taking the advantage of symmetry. The derived equations can also be used for one-way slabs; however the reduction in cracking moment due to drying shrinkage and thermal deformations should be accounted, accordingly (Eurocode 2 1992 and BS 8110 1985).

Table 22- Coefficient λ for different curvature distribution

<table>
<tr><td></td><td colspan="2">λ</td></tr>
<tr><td>Upper bound
(Zero tension stiffening)</td><td colspan="2">$\lambda = 2G(\beta)\left(\frac{M_{cr}}{M}\right)^3$</td></tr>
<tr><td>Lower bound
(Full tension stiffening)</td><td colspan="2">$\lambda = [1 + G(\beta)]\left(\frac{M_{cr}}{M}\right) - G(\beta)\left(\frac{M_{cr}}{M}\right)^3$</td></tr>
<tr><td>Very slender beams
($L_s/d > 7$)</td><td colspan="2">$\lambda = [1 + 4G(\beta)]\left(\frac{M_{cr}}{M}\right)^2 - 4G(\beta)\left(\frac{M_{cr}}{M}\right)^3$</td></tr>
<tr><td>Slender beams ($3 < L_s/d < 7$)</td><td colspan="2">$\lambda = 3G(\beta)\left(\frac{M_{cr}}{M}\right) + [1 - 2G(\beta)]\left(\frac{M_{cr}}{M}\right)^2 - G(\beta)\left(\frac{M_{cr}}{M}\right)^3$</td></tr>
<tr><td colspan="3">$\frac{1}{I_e} = \lambda\frac{1}{I_g} + (1-\lambda)\frac{1}{I_{cr}} \qquad G(\beta) \cong 0.5 - \beta$</td></tr>
<tr><td>Four-point loading:
$\beta = a / L$</td><td>Three-point loading:
$\beta = a / L$</td><td>Uniform loading:
$\beta \cong 1/3$</td></tr>
</table>

Moment-curvature analysis using the computational model, developed in Chapter 7, shows that the tension stiffening assumption of $\beta_c = M_{cr} / M$ gives rise to reasonable predictions of curvature at midspan, as shown in Fig. 85. However, Bischoff's original deflection equation which uses the above tension stiffening factor overestimates the maximum deflection since it assumes the same I_e for the critical section as for the entire beam.

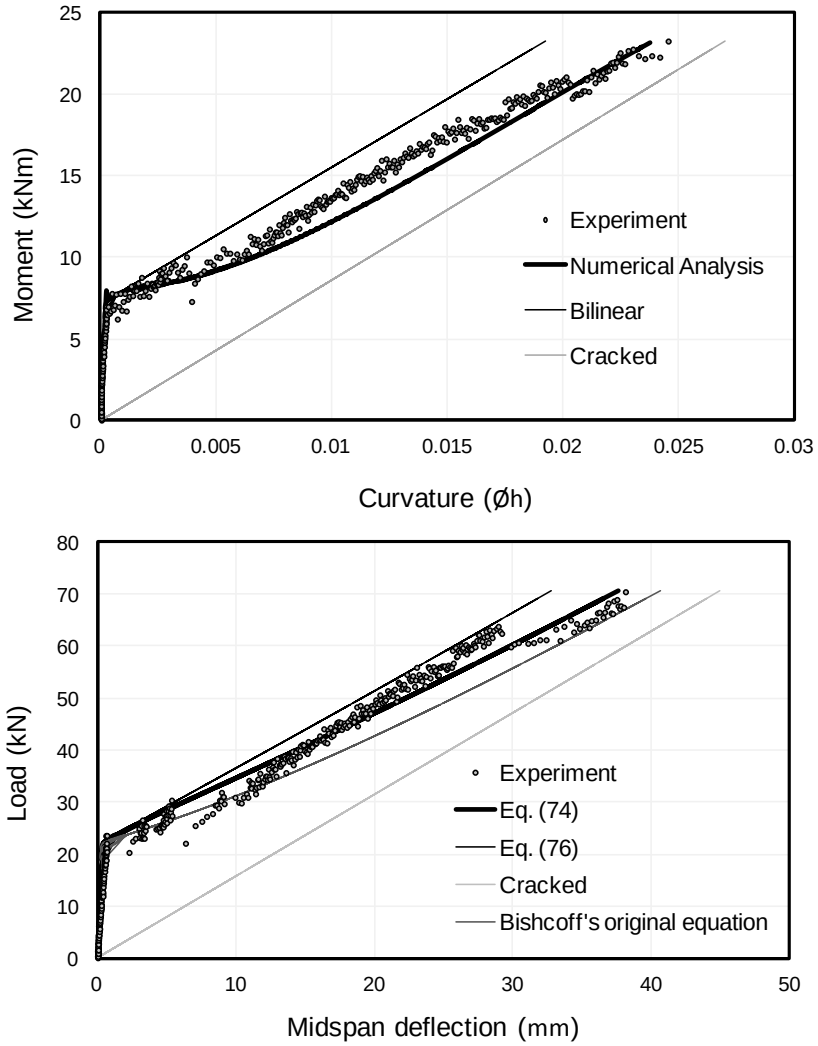

Fig. 87. Moment-curvature and load-deflection diagrams at midspan

Fig. 85 shows that Eq. (76) provides a reasonable prediction of maximum deflection particularly at post-cracking stages, Eq. (74) seems to have an acceptable accuracy though. This is first attributed to the fact that Eq. (76) is based on integration of the curvature along the beam and hence providing a more rational estimate of flexural stiffness. Secondly, the larger tension stiffening factor has been assumed for transition zone in the shear span which slightly provides stiffer responses than Eq. (74). Although Bischoff's original equation provides conservative predictions of deflection, assuming a realistic distribution of the curvature along the beam can considerably improve the accuracy of the predictions.

9.4 Verification

Different experimental tests including different shear span-to-depth ratio were selected to verify the predictions of the derived equations. In this comparison Bischoff's original equation, Eq. (63), the proposed equation for very slender beams, Eq. (74), and the proposed equation for slender beams, Eq. (76) are considered. It should be noted that Eq. (74) has the same basis as Bischoff and Gross' equation, Eq. (64). Experimental values for cracking moment, M_{cr}, and code values for the modulus of elasticity of concrete, E_c, are used in this comparison. All beams were simply-supported under four-point loading. More information about specimens can be found in the references. As illustrated in Fig. 66, comparison shows that Bischoff's original equation overestimates the deflection as already expected; however, Eqs. (74) and (76) provide more accurate predictions. For slender beams the results are more close to Eq. (76) which accounts for larger tension stiffening in transition zone of the shear span. For the sake of clarity in diagrams, the lower bound of deflection, $\beta = 1$, has not been shown in these graphs. It should be noted that the derived equations are viable in serviceability domain where the compressive stresses in concrete are mostly in the elastic range. With increasing the load and getting close to failure, inelastic stresses develop and result in less flexural stiffness and more deflection, accordingly.

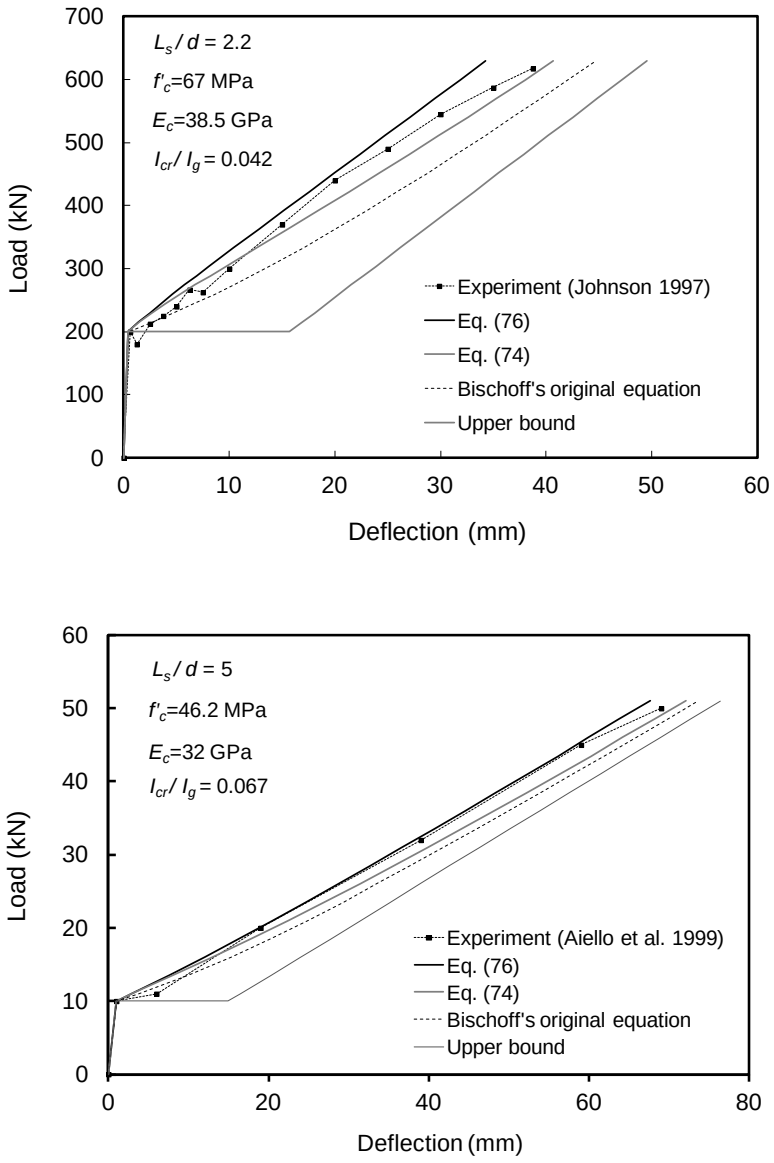

Fig. 88. Experimental verification of deflection equations (slender beam)

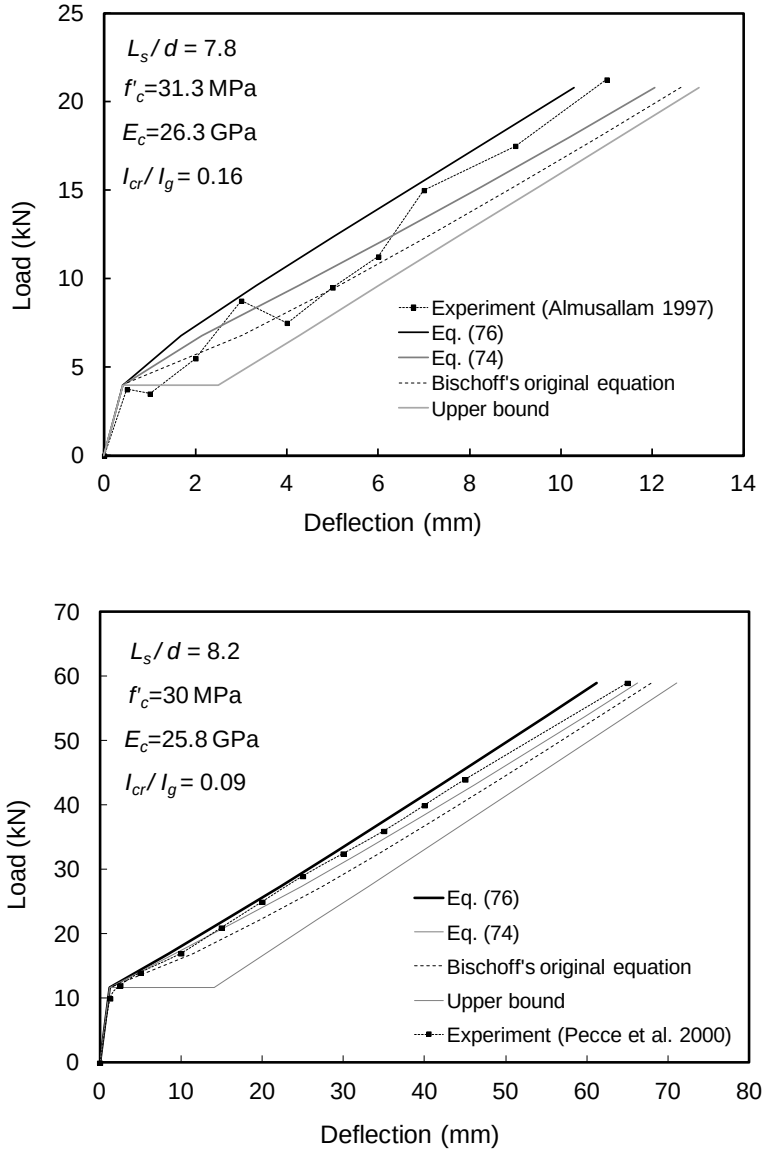

Fig. 89. Experimental verification of deflection equations (very slender beam)

9.5 Conclusions

Different distributions of the curvature along the beam and its influence on effective moment of inertia of FRP RC beams were discussed. For very slender beams (L_s >7) where the flexure typically governs the behavior of the beam, a common moment-

curvature relationship with tension stiffening factor equals to $\beta_c = M_{cr} / M$ was used to find the curvature distribution. Based on integration of the curvature along the beam, Eq. (74) was derived for I_e which is convenient-to-apply and can be used for either three-point, four-point, or uniformly distributed loadings adjusted by function *G(β)*. This equation basically yields to the same result as Eq. (64) adopted by Bischoff and Gross (2011). An alternative equation was derived for slender beams ($3<L_s<7$) based on assuming larger tension stiffening at transition zone of the shear span, Eq. (76). In slender beams, compound shear-flexural cracks commonly governs the behavior of the beam and shear diagonal cracks typically form in shear span with larger crack spacing compared to flexural cracks at constant moment region, thereby the tension stiffening factor is expected to be larger than the conventional value, $\beta_c = M_{cr} / M$. To further investigate this presumption, the AFRP reinforced concrete strip presented in Chapter 5 as a slender beam was selected and the curvature distribution was studied. The results showed that the curvature of the beam at transition zone in shear span is more close to the bilinear model, $\beta_c = 1$, however converging to the conventional value, $\beta_c = M_{cr} / M$, at the constant moment region. This is in good agreement with the assumption made in deriving Eq. (76).

For better verification of the derived equations, four experimental tests including beams with different L_s/d ratios were selected from other researchers' experimental studies. The results showed that Bischoff's original equation generally overestimates the deflection. The overestimation seems to be more pronounced for slender beams. This is first attributed to assigning the effective moment of inertia at critical section to the entire beam instead of integration-based calculation. Secondly, curvature distribution in slender beams is not necessary the same as for very slender beams due to the effect of shear diagonal cracks. Both Eq. (74) and (76) proved to provide deflection predictions with an acceptable accuracy; however Eq. (76) seems to be a better choice for slender beams with slightly stiffer responses. Further research is still required to study the distribution of the curvature in cracked regions where shear diagonal cracks tend to disturb the region and affect the tension stiffening characteristics of the concrete.

10. TENSION STIFFENING IN PRESTRESSED CONCERETE BEAMS USING MOMENT-CURVATURE RELATIONSHIP*

10.1 Introduction

Tension stiffening phenomenon plays a vital role in serviceability of non-prestressed reinforced concrete (RC) beams as it enhances the post-cracking flexural stiffness leading to a smaller deflection, accordingly. However, the authors' findings indicate that in contrast to RC sections, the effect of tension stiffening is negligible for fully prestressed concrete sections. Herein, a closed form equation of moment-curvature for prestressed concrete sections under service load is presented, where the tensile strength of the concrete is taken into account. This equation is verified by experimental test data and numerical analysis, thereby proving the negligible effect of tension stiffening on fully prestressed concrete sections.

Tension stiffening is the ability of concrete to carry tension between cracks in reinforced concrete members, and it controls the deformation particularly in the serviceability stage (Bischoff 2003). The general moment-curvature diagram for non-prestressed concrete sections is shown in Fig. 88, where ϕ_{cr} is the curvature at which first cracking occurs corresponding to the moment, M_{cr}. Likewise, ϕ_n is the curvature in the post-cracking stage induced by the moment, M_n. If theoretically no tension stiffening occurs, there will be an increase in the curvature at cracking and post-cracking loads denoted by $\Delta\phi_{cr}$ and $\Delta\phi_n$, respectively. In other words, beyond the cracking moment, tension stiffening gives rise to a reduction in curvature, $\Delta\phi_n$, and an increase in flexural stiffness, accordingly. The larger the $\Delta\phi_{cr}$, the more pronounced the contribution of the concrete, $\Delta\phi_n$, to carry tension in the post-cracking stage since $\Delta\phi_n$

* Reprinted with permission from "Tension Stiffening in Prestressed Concrete Beams Using Moment-Curvature Relationship" by Shobeir Pirayeh Gar, Monique Head, Stefan Hurlebaus, 2012, *ASCE Journal of Structural Engineerin*,Volume 138, Number 8, Page 1075-1078, Copyright 2012 by *ASCE Jouranl of Structural Engineering.*

is directly proportional to $\Delta\phi_{cr}$ with a factor, β_c, to account for tension stiffening (Bischoff 2005). Therefore, finding $\Delta\phi_{cr}$ in the theoretical moment-curvature relationship can indicate to what extent tension stiffening is going to be effective in the post-cracking stage. Although tension stiffening in RC members has been investigated by many researchers (Fields and Bischoff 2004, Scott and Beeby 2005, Gilbert 2007), less attention has been paid to studying this phenomenon in prestressed beams. Some researchers studied prestressed concrete prisms under direct tension, not flexure, and concluded that the prestressing force enhances the tension stiffening effect (Collins and Mitchel 2001, Davoudi et al. 2008). Gilbert and Mickleborough (1990) noted that for most practical prestressed members, tension stiffening is not very significant and deflection can be reasonably estimated by ignoring it. However, no more explanation was provided to support this. This chapter of thesis is intended to clarify this matter by deriving a closed form equation for the moment-curvature relationship.

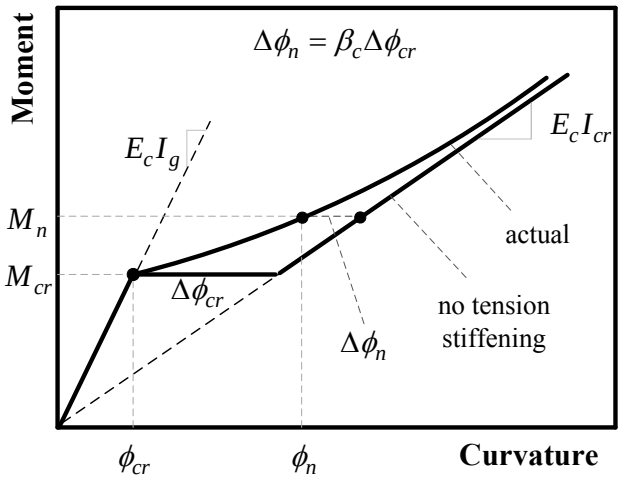

Fig. 90. Effect of tension stiffening on flexural behavior of non-prestressed concrete sections

10.2 Closed-Form Equation of Moment-Curvature for Prestressed Concrete Sections

To find the theoretical moment-curvature equation of prestressed concrete sections, a cracked prestressed concrete section is considered under service load given the linear elastic behavior of the concrete and reinforcement (Fig. 89). Compatibility equations of strain over the height of the section can be expressed as

$$\varepsilon_c = \phi c \tag{77}$$

$$\varepsilon_p = \phi(d - c) \tag{78}$$

$$\varepsilon_{cr} = \phi z \tag{79}$$

where ε_c, ε_p, and ε_{cr} are the flexural induced strains corresponding to the top of the section, at prestressed tendons, and at crack tip, respectively. The following variables are defined in Eqs. (77) through (79): ϕ is the curvature, c indicates the neutral axis depth, d represents the location of the tendons, and z is the depth of the tensile portion of the concrete as shown in Fig. 89. ε_{cr} can be related to the curvature at which first cracking occurs, ϕ_{cr}, using the following equations

$$\varepsilon_{cr} = \phi_{cr}(h - c_{cr}) \tag{80}$$

$$c_{cr} = \beta h \tag{81}$$

where c_{cr} is the neutral axis depth right before cracking, h is the height of the section, and β is a constant coefficient that can be computed using Eq. (87). The coefficient α, which represents the level of prestressing, is defined based on Eq. (82), where ε_0 denotes the effective prestressing strain in tendons and ε_{cr} indicates the cracking strain of concrete

$$\alpha = \frac{\varepsilon_0}{\varepsilon_{cr}} \tag{82}$$

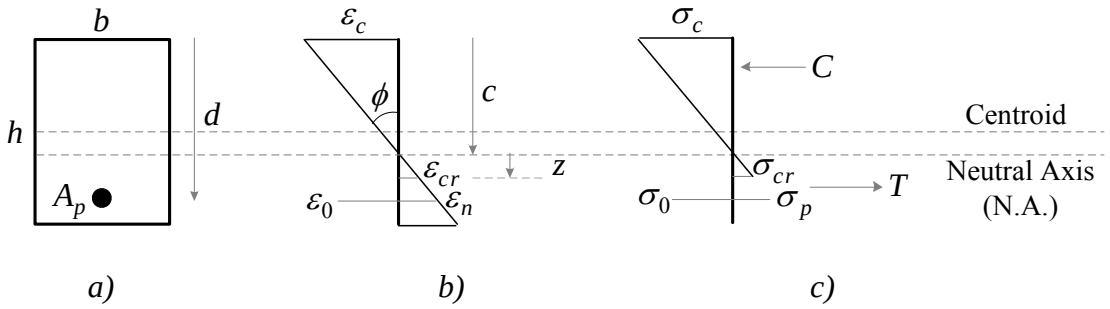

Fig. 91. Cracked section under service load; a) prestressed section, b) strain profile, and c) stress profile

The equilibrium equations can be stated as

$$T = C \tag{83}$$

$$\sum M_{N.A.} = 0 \tag{84}$$

where T and C are the tensile and compressive resultant forces, respectively, and $M_{N.A.}$ is the moment with respect to the neutral axis. Substituting Eqs. (77) through (82) in Eq. (83) gives the location of the neutral axis as follows

$$\left(\frac{c}{h}\right)^2 + 2n_p\rho_t\left(\frac{c}{h}\right) - \left[(1-\beta)^2\left(\frac{\phi_{cr}}{\phi}\right)^2 + 2n_p\rho_t\alpha(1-\beta)\left(\frac{\phi_{cr}}{\phi}\right) + 2n_p\rho_t\frac{d}{h}\right] = 0 \tag{85}$$

where n_p is the ratio of the modulus of elasticity of the prestressed tendons to that of concrete and ρ_t is the ratio of the tendons' cross sectional area, A_p, to the total area of the section. Likewise, substituting Eqs. (77) through (82) in Eq. (84) gives the moment-curvature equation

$$\frac{M}{E_c I_g \phi_{cr}} = 4\left(\frac{c}{h}\right)^3\left(\frac{\phi}{\phi_{cr}}\right) + 6\left(\frac{c}{h}\right)^2\left[2n_p\rho_t\left(\frac{\phi}{\phi_{cr}}\right)\right]$$
$$-12\left(\frac{c}{h}\right)\left[2n_p\rho_t\frac{d}{h}\left(\frac{\phi}{\phi_{cr}}\right) + n_p\rho_t\alpha\left(1-\beta\right)\right]$$
$$+12\left[\frac{1}{3}\left(1-\beta\right)^3\left(\frac{\phi_{cr}}{\phi}\right)^2 + n_p\rho_t\left(\frac{d}{h}\right)^2\left(\frac{\phi}{\phi_{cr}}\right) + n_p\rho_t\alpha\frac{d}{h}\left(1-\beta\right)\right] \quad (86)$$

where E_c is the modulus of elasticity of concrete and I_g is the gross moment of inertia of the section. Solving Eq. (85) for cracking stage where, $c = c_{cr} = \beta h$ and $\phi = \phi_{cr}$, gives the coefficient β as a function of section geometry, reinforcement ratio, modular ratio, and prestressing level

$$\beta = \frac{0.5 + n_p\rho_t\left(\alpha + d/h\right)}{1 + n_p\rho_t\left(\alpha + 1\right)} \quad (87)$$

In order to verify Eq. (86), the result of an experiment conducted by Dolan et al. (2001), and the result of a computational model developed by the authors are compared. The chosen prestressed concrete beams are designated as B9-2F, B9-4F, and B12-4F. Further details can be found in Dolan et al. (2001). Fig. 90 shows that Eq. (86) matches well with the results of the experimental test and numerical analysis. It should be noted that the origin of the coordinate was shifted to the negative curvature induced by the prestressing force for the sake of consistency with the reported experimental results. The parameters used in Eq. (86) corresponding to each specimen are summarized in Table 23.

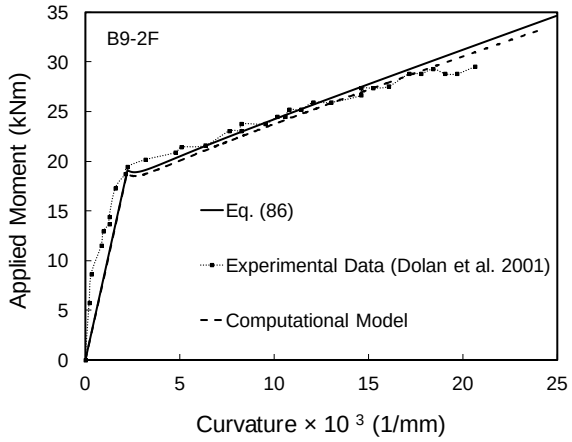

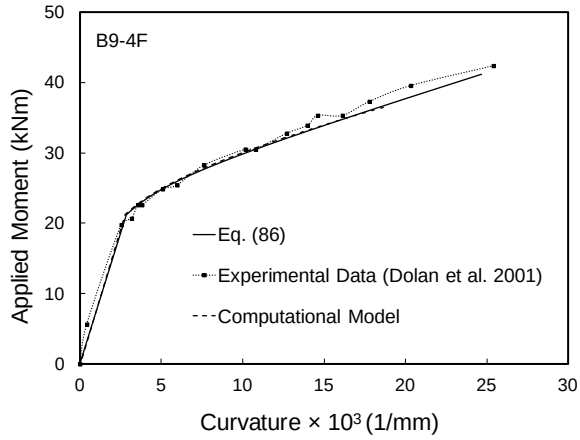

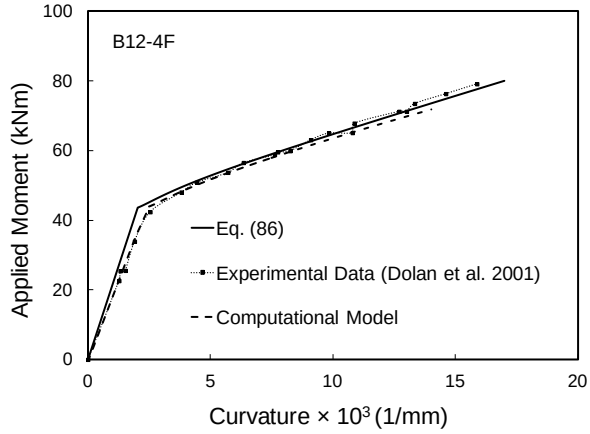

Fig. 92. Moment-curvature diagram of specimens B9-2F, B9-4F, and B12-4F

Table 23- The parameters used in Eq. (86) for each specimen

Specimen	Prestressing level (%)	n_p	ρ_t	d/h	α	β
B9-2F	60	4.2	0.0028	0.833	60.8	0.712
B9-4F	58	4.63	0.0056	0.66	59.26	0.802
B12-4F	57	4.63	0.0042	0.75	58.23	0.767

10.3 Tension Stiffening in Prestressed Concrete Sections

The effective prestressing force applied in B9-2F specimen is 60% of the tensile capacity of the tendons, which provides a fully prestressed section. If this prestressing force decreases, the coefficient α in Eq. (82) decreases and the moment-curvature behavior changes based on Eq. (86). As shown in Fig. 91, the prestressing ratio is decreased to 40% (α = 40.5), 20% (α = 20.25), and 0% (α = 0) and the moment-curvature relationship is extracted from Eq. (86). It can be observed that decreasing prestressing force causes $\Delta\phi_{cr}$ to be more pronounced which can be quantified in terms of a Cracking Index, *CI*, defined as $\Delta\phi_{cr} / \phi_{cr}$ and measured for different amounts of prestressing. This ratio is equal to 11.5, 6, 2.5, and 0.8 for 0%, 20%, 40 %, and 60% prestressing ratio, respectively. As discussed earlier, the larger the $\Delta\phi_{cr}$ or *CI*, the more pronounced the contribution of the concrete, $\Delta\phi_n$ in Fig. 88, to carry tension in the post-cracking stage and hence the enhanced the effect of tension stiffening. Therefore, for the non-prestressed concrete section the effect of tension stiffening is large and considerable; however, as the prestressing force is increased, this effect becomes insignificant and hence negligible for the fully prestressed concrete section.

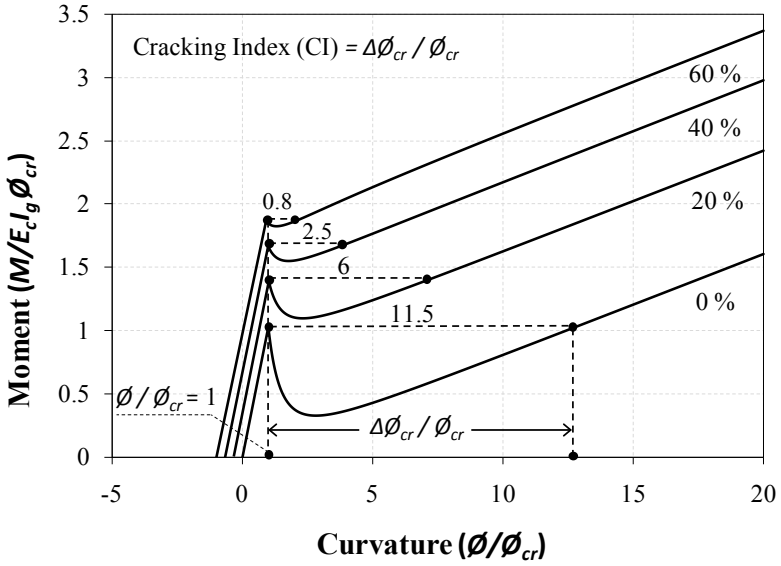

Fig. 93. Normalized theoretical moment-curvature diagram for different prestressing ratios

There are two reasons why the prestressing force causes a decline in raise of the curvature and drop of the moment at cracking. The first reason is related to the depth of the neutral axis. Fig. 92 illustrates the variation of the neutral axis depth for specimen B9-2F right after cracking using Eq. (85). It can be inferred that the neutral axis depth is larger when the concrete section is prestressed, thereby the smaller portion of the section is cracked, and this prevents large raise of the curvature at cracking. The second reason lies in the fact that the eccentricity of the prestressing force grows as the neutral axis shifts up gradually, which induces an additional moment compensating for the loss of the flexural resistance caused by cracking. The moment induced by prestressing force with respect to the neutral axis, M_p, can be found if the expressions having coefficient α, are extracted from Eq. (86)

$$\frac{M_p}{E_c I_g \phi_{cr}} = 12 n_p \rho_t \alpha \left(1-\beta\right)\left(\frac{d}{h}-\frac{c}{h}\right) \tag{88}$$

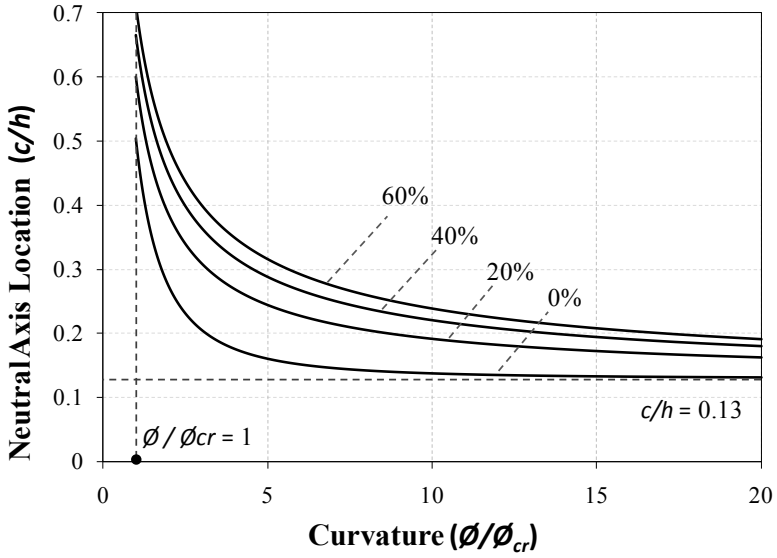

Fig. 94. Variation of the neutral axis location versus curvature for different prestressing ratios

M_p at cracking, M_p^{cr}, can be readily calculated from Eq. (88) given $c/h=\beta$. Subtracting M_p^{cr} from M_p gives the additional prestressing moment, ΔM_p due to growth in eccentricity of the prestressing force

$$\frac{\Delta M_p}{E_c I_g \phi_{cr}} = 12 n_p \rho_t \alpha \left(1-\beta\right)\left(\beta - \frac{c}{h}\right) \tag{89}$$

For a specific level of prestressing, all the parameters in Eq. (89) are constant during the loading except c/h and it can be clearly deduced that with further cracking and decreasing the depth of the neutral axis, ΔM_p increases and to some extent compensates for the loss of the flexural resistance caused by cracking, depending on the level of prestressing (Fig. 93).

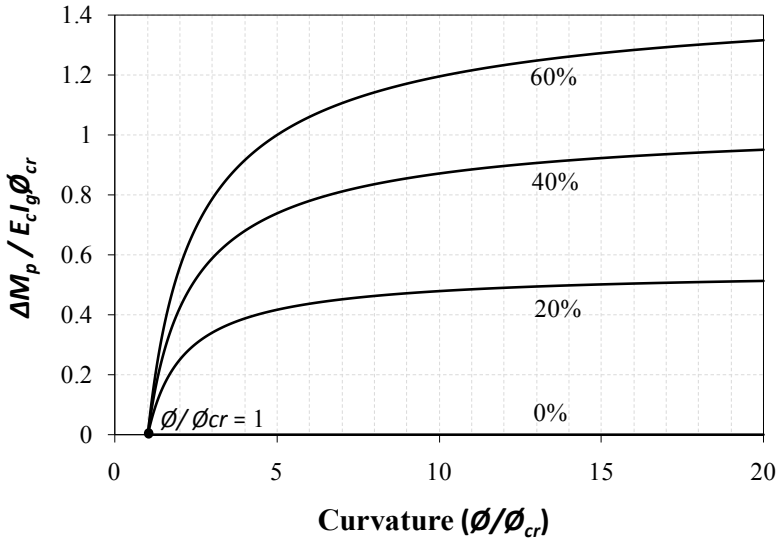

Fig. 95. Additional moment due to growth in the prestressing force eccentricity (specimen B9-2F)

10.4 Conclusions

A closed form equation for moment-curvature relationship of prestressed concrete sections under service load was presented and verified by experimental test data and numerical analysis. Neutral axis depth and growth of the prestressing force eccentricity were found to be the reasons causing a different post-cracking flexural behavior of prestressed concrete sections such that the results of this study clearly showed that in fully prestressed concrete sections, the effect of tension stiffening is negligible and it barely affects the flexural performance of the beam in serviceability stage. However, as the prestressing force declines, the effect of tension stiffening becomes more pronounced.

11. CONCLUSIONS

11.1 Summary of the Major Results

1) A comprehensive experimental and analytical study was conducted to validate the structural applicability of an AFRP concrete bridge deck system. The experimental tests on uniaxial characteristics of ARAPREE bars showed the following dependable values: modulus of elasticity E=69 GPa, strain capacity ε_u=0.02, and the tensile strength f_u=1380 MPa. The load capacity of the conventional anchorage system was evaluated about 67% of the bar strength; however, with no capability to sustain the prestressing load for a short-period of time. A new prestressing system was developed which is capable of prestressing the ARAPREE bars up to 85% and sustaining the load without any significant loss or local failure at the anchorage.

2) Long-term relaxation tests showed that the relaxation loss for 50-60% initial prestressing is ranged between 6-10% during 1000 hours. In case of prestressing steel strand, the relaxation loss for 70-80% initial prestressing is typically ranged between 8-12%. There seems to be a similarity between the relaxation characteristics of ARAPREE bars and prestressing steel. Long-term creep tests showed 4% increase in strain during 1000 hours for 50% initial prestressing. For 60% initial prestressing, 6.5% increase in strain was measured during 550 hours for one of the specimens. Short-term creep tests showed that any initial prestressing above 85% results in rupture between 2 or 3 hours.

3) Experimental test of the full-scale bridge deck slab confirmed a satisfactory structural performance of the bridge deck slab where the strength and serviceability criteria were met. The average failure load of the interior spans and overhangs were found 3.8 and 1.3 times the maximum factored load specified by AASHTO LRFD (2010), respectively. The deflection of the interior span at

service load level was found about 1 mm which is 40% of the allowable amount specified by AASHTO LRFD (2010).

4) The failure mechanism of the bridge deck slab was mostly governed by flexure, particularly at the overhang. However, at interior spans the failure mechanism was somewhat influenced by the punching shear due to the restrained edges. The failure mechanism could be recognized by the cracking pattern on top and bottom surface of the slab and the curvature distribution in both *x* and *y* directions. The failure mechanism of the interior spans was recognized as a compound shear-flexural failure. However, at overhang flexure mostly governed the mechanism. It was found that the load configuration affects the failure mechanism. For example, since the truck axle transfers the load in a more distributed fashion over the single wheel load, the failure mechanism is more influenced by flexure than shear. This was clearly seen when comparing the load cases 2 and 5 at the overhang, or load cases 1 and 7 at the interior span.

5) The shear capacity of the panel-to-panel seam, 1 MPa, seemed to be sufficient as no local or premature failure was observed and the flexural cracks were mostly transferred from the panel under the load to the adjacent panel. Furthermore, no major cracking or local failure was observed at the composite shear pockets and full composite action between the slab and the support beams was achieved.

6) The strip specimens representing the non-prestressed and prestressed directions of the bridge deck slab as well as the panel-to-panel seam were tested to investigate their structural capacity. The non-prestressed strip specimen failed due to concrete crushing in a shear-flexural manner with no evidence of tendon rupture. The ultimate strength M_u=77 kNm/m and the curvature capacity $(\emptyset h)_u$=0.024 were found at failure. Prestressed strip specimen failed due to rupture of the AFRP bars while crushing the concrete was already commenced. The ultimate strength M_u=69 kNm/m and the curvature capacity $(\emptyset h)_u$=0.02 were found at failure. Shear test of the seam strip showed an acceptable shear strength

per ACI 318. The joint failed due to crushing of the diagonal concrete strut and the shear capacity was found equal to 41 kN (1 MPa). However, flexural test confirmed the negligible flexural strength of the panel-to-panel seam. The results of the strip specimens were directly used for failure load analysis of the bridge deck slab.

7) The considerable deformability observed in testing the slab as well as the strip specimens, similar to the ductility in steel reinforced members, raised the question if a plastic method of analysis can be employed for failure load analysis. Hence, yield line concept, commonly used for steel reinforced concrete slabs, was modified where the yield moment was substituted with an equivalent plastic moment to account for the deformability of the AFRP concrete section despite the non-ductile behavior of the AFRP bars. The average error of analysis for all load cases was found about 2% showing the excellent accuracy of the modified yield line theory. The general cracking pattern at interior span and overhang resembled an elliptical and trapezoidal shape, respectively.

8) An extensive computational model was developed to numerically analyze an AFRP prestressed concrete girder in composite action with bridge deck. Comparison between analytical and experimental data for steel prestressed girder, for the sake of verification, showed maximum error of 5% and 7% in prediction of failure and cracking moments, respectively, which indicates the high accuracy of the developed computational model. Stress and moment-curvature analyses confirmed that the AFRP prestressed girder not only meets service limit states, but also provides sufficient flexural strength. However, in contrast to steel prestressed girder whose failure mode was crushing of the concrete at the top fibers of the section, the failure mode of the AFRP prestressed girder was rupture of the tendons causing less deformability. This is mainly due to the fact that over-reinforcing the composite girder for the sake of having concrete crushing as a failure mode, rather than ruptures of the tendons, is almost

impractical since the brittle ratio of the composite section is considerably large. Although tendon rupture as a failure mode is less desirable, the failure curvature was found 18 times the cracking curvature that can still provide sufficient warning before failure. Load-deflection analysis of the girders showed that the deflection under service load is almost half of the allowable amount. At failure, deflection of the steel prestressed girder was about twice that of AFRP prestressed girder due to the large ductility provided by yielding of the steel strands and inelastic compressive stresses in concrete.

9) Rational equations for effective moment of inertia were developed to estimate the maximum deflection of either FRP reinforced or prestressed concrete beams. The equations have an implicit flexibility form as opposed to empirical deflection equation of ACI 440 with an implicit stiffness form. Verification with experimental data confirmed an acceptable accuracy of the developed equations while the ACI equation showed a considerable susceptibility to I_{cr}/I_g ratio. Substituting the typical design values ($I_{cr}/I_g \approx 0.1$ and $M_{cr}/M \approx 0.5$) in the rational deflection equations developed in this thesis, $I_e = 0.15 I_g$ and $I_e = 0.1 I_g$ can be used in design for AFRP prestressed and reinforced concrete beams, respectively.

10) Tension stiffening phenomenon, which plays a governing role in design of FRP reinforced concrete beams, was studied to analyze the prestressing effect. A closed-form equation for moment-curvature response was derived under service load for FRP prestressed concrete beams which revealed that as the prestressing ratio increases the effect of tension stiffening becomes less dominating.

11.2 Design and Construction Recommendations

1) For design of concrete beams and slabs, the following dependable values for ARAPREE bars with 10 mm diameter are recommended: modulus of elasticity E=69 GPa, strain capacity ε_u=0.02, and the tensile strength f_u=1380 MPa.

2) Based on the creep test, the initial prestressing ratio is recommended to be between 50 to 60%, and the long-term relaxation loss for this ratio ranges between 6-10%.

3) The prestressing setup developed in this research can be used as a reliable and applicable system for off-site precast plant. The anchorage system at the dead and live ends includes steel pipes with 457 mm length, 48 mm diameter, and 5 mm wall thickness filled with the expansive and quick setting Shep Rock grout. At the live end, the hydraulic central hole jack is placed between two pipes where the front pipe is utilized for pulling the bar and the rear pipe is used to lock the prestressing system. The pipes should be fully filled with grout to avoid excessive slippage of the bar and loss in prestressing force or premature failure at the anchorage once the grout has hardened. The grout should be consistent and flowable; very thick or thin grout should be avoided. Also, it is better to have two holes at opposite ends on the pipe's upper surface and inject the grout through the first hole until the grout level is flush with the second hole. This ensures that there is no air bubble entrapped inside the pipe. Gently tapping the pipe when pouring the grout can help for a better settlement of the grout. The full grip of the bar inside the pipe can be reached after 3 hours. Using a plastic stopper with a central hole at each end of the pipe helps to hold the bar at the center of the pipe and avoid rubbing against the pipe's edges and also prevents leakage of the grout.

4) For design of full-depth precast prestressed panels, nine shear pockets, each measuring 254 × 178 mm, were found sufficient to reach full composite action between the slab and support beams. The gross area of each precast panel was

13.4 m^2. The number of shear pockets required should be adjusted based on the size of the precast panels and induced shear demand. Using two high strength bolts, with 25 mm diameter, inside each composite pocket is sufficient as a shear connector.

5) To avoid any possible damage to prestressed bars, the prestressing is suggested to be the last action before pouring the concrete. In this case, walking on the reinforcement grid before or during concreting should be avoided. To prevent possible long-term prestressing losses at anchorage, the time gap between prestressing and concreting is suggested no to exceed 72 hours. Vibration of the concrete was found non-dangerous to the prestressed bars. To ease the construction, the prestressed and non-prestressed bars are better not to pass through the shear pockets. To fill the haunch, the high performance Sika grout with water to powder ratio ranged between 0.18 to 0.2 is recommended. The optimal ratio should be found with both consistency and flowability tests.

6) Prestressing the precast panels in transverse direction helps to increase the cracking strength and stiffness of the bridge deck slab perpendicular to the traffic direction where the flexural demand is considerably high. It also helps to minimize cracking close to the shear pockets and lessen the intrusion of chemicals. Although the prestressed bars were placed at the center of the section, they can be used in two layers at top and bottom of the section to better distribute the prestressing force and increase the deformability of the slab. The net compressive stress applied to the slab section in transverse direction, due to prestressing, was about 2 MPa. Based on the span length and flexural demand, the required compressive force should be adjusted, accordingly. The reinforcement ration in prestressed direction was 0.0032.

7) The non-prestressed bars in longitudinal direction were bent in a U shape where the legs formed the top and bottom layers of the reinforcement. The bent part of the bar is placed right at the seam to provide a better connectivity between the

panels and increase the capacity of the shear key. As the joint is under considerable shear demand, it is better to fill it with structural concrete rather than grout. In this case, the maximum aggregate size should be carefully chosen as the distance between the bars at panel-to-panel seam is half of the distance between longitudinal bars of each panel. The total reinforcement ratio, top and bottom layers, in non-prestressed direction was 0.0056.

8) Modified yield line theory is a valid and convenient-to-apply method to perform the failure load analysis of the slab, suitable for design office implementation. However, reasonable evaluation of the equivalent plastic moment along the yield line is critical. For instance, at overhang the transfer length of the prestressed bars or development length of the non-prestressed bars should be accounted in calculations. Furthermore, the flexural or shear contribution of the panel-to-panel seam must be realistically evaluated. The theoretical failure shape that resembles an elliptical cracking pattern at interior span and trapezoidal cracking pattern at overhang seems to be a reasonable assumption for failure load analysis of the bridge deck slab. At overhang, compound flexural failure of the panel under the load and shear failure at the seam should be checked as a possible governing failure mode.

9) The existing punching shear equations significantly underestimate the load capacity of the interior span since the failure mode is more governed by flexure. In fact, the actual failure mode of the interior span is a compound shear-flexural failure. Since the contribution of flexure is very considerable, the modified yield line theory gives rise to much more accurate results compared to punching shear equations.

10) To find the actual failure mode of the AFRP prestressed girder, the effect of topping deck should be taken into account. In this case the failure mode is often governed by tendon rupture since the brittle ratio of the composite section is very high. Therefore, the safety factor for strength reduction needs to be accordingly

selected. It should be noted in design that, the top reinforcement of the girder is under tension at the ultimate limit state since the neutral axis lies within the deck slab.

11) To control the deflection under service load, it is better to design the AFRP concrete girder as a fully prestressed beam in that the girder remains uncracked under service load. In this case, the effect of tension stiffening is negligible. If using ARAPRRE bars to prestress the girder, the reinforcement ratio is recommended not to be less than 1.5 times that of the steel case.

12) The rational equations for effective moment of inertia, developed in this research, are recommended for computing the maximum deflection of FRP RC or PRC beams. The current deflection equations in design codes, like ACI 440.4R 2004, are typically based on the empirically derived Branson's equation which was originally calibrated for steel reinforced concrete beams. These equations, which have an implicit stiffness format, are very susceptible to low I_{cr}/I_g ratios, the typical case of FRP concrete beams, and underestimate the maximum deflection.

11.3 Future Work

1) The major concern with the use of AFRP bars is the effect of aging on their mechanical properties, so called the durability of AFRP bars. Although AFRP bars have high strength and non-corrosive nature, moisture softens the structure of the aramid fibers over the time and results in increased creep (Trejo et al. 2000). Research by Chen (2007) showed that aramid fibers are susceptible to moisture absorption. Also, sodium hydroxide and hydrochloric acid cause a significant accelerated hydrolysis of aramid fibers. However, Soroushian et al (2002) conducted extensive accelerated aging tests on aramid fibers, Technora type, and reported that the AFRP bars exhibited desirable durability characteristics. It seems that further investigation is required to explore the durability of the AFRP bars (Ceroni 2006). Furthermore, large deterioration of flexural strength of aramid/epoxy laminates occurs in a saturated state at

elevated temperature (Chen 2007). Experimental studies by Wang et al. (2003) on CFRP and GFRP bars showed that the strength of the bars reduces at elevated temperature. However, they did not study AFRP bars. Therefore, fire resistance of AFRP reinforced concrete structures is still a concern that needs to be more studied.

2) Cost justification of using AFRP bars is based on the fact that the higher initial cost of material is going to be offset by ease in installation and construction as well as obviating the need for future rehabilitation due to corrosion-induced deterioration. However, life-cycle cost analysis for short span bridges done by Nystrom et al. (2003) showed that replacing steel with AFRP increases the overall construction cost. Therefore, a comprehensive life-cycle cost analysis is required to clarify this matter.

3) As the rate of loading affects the behavior of the composite material, hence, the response of the structure under impact may not be as predictable as under the monotonically increased load. Testing the mechanical characteristics of the AFRP bars under high loading rate can be interesting and useful to study the impact resistance of the reinforced member.

4) Long-term performance of AFRP concrete bridge deck system needs to be experimentally evaluated in aggressive weather conditions. Change in the crack width and deflection of the deck slab, which depend on the modulus of elasticity of AFRP bars should be continuously monitored to provide a realistic evaluation of serviceability of the structure.

5) A practical prestressing operation for post-tensioning the AFRP bars seems to be required if the precast panels are to be longitudinally or transversely post-tensioned. In this case, long steel pipes filled with expansive grout used for pretensioning may not be a good option for anchorage as they occupy a considerable space. The sustainability of the anchorage system should be carefully evaluated for a long period of time according to the codes of practice.

6) To complete the experimental evaluation of the AFRP concrete bridge deck system, a full-scale 12 m AASHTO I-girder prestressed with AFRP bars in composite action with bridge deck, which was numerically analyzed in Chapter 7, needs to be experimentally evaluated. The results of the girder test along with the results of the current research can form a solid instructive guideline for analysis and design of the superstructure of AFRP concrete bridge.

7) An experimental study of a bridge deck system consisting of SIP bottom panels prestressed with AFRP bars and CIP top panels reinforced with AFRP bars can be studied as an alternative to full-depth precast panels. Comparison can clarify the advantages and disadvantages of each system.

8) Using prestressed AFRP bars in concrete beams increases the strength and stiffness; however, the deformability of the section typically reduces since less strain in AFRP bars is left for flexure. Therefore, using a combination of prestressed and non-prestressed AFRP bars to reinforce the section can exhibit an optimal structural behavior where the required strength and stiffness is provided by prestressed bars and deformability of the section mainly originates from non-prestressed bars. It seems that such combined systems have not been well noticed yet and further research is required.

9) The results of this study are valid only for ARAPREE bars. In case of using CFRP bars which typically have a higher modulus of elasticity over AFRP bars, an experimental investigation is required to study the structural performance of the bridge deck system. The considerable deformability observed in this study, may not be achievable by using the CFRP bars due to their high modulus of elasticity that raises the likelihood of punching shear at interior span of the deck and lessen the contribution of flexure. Further research is required to clarify this point.

10) The structural connections reinforced with AFRP bars must be experimentally investigated to specify their load capacity. The satisfactory reinforcement detail in panel-to-panel seam, girder-to-deck and pier-to-foundation connections are the examples that can be studied further in detail.

REFERENCES

AASHTO, 2010, "LRFD Bridge Design Specifications," American Association of State Highway and Transportation Officials, Washington D.C.

Abdelrahmaan, A. A.; Tadros, G.; and Rizkalla, H. S., 1995, "Test Model for the First Canadian Smart Highway Bridge," *ACI Structural Journal*, 92(4): 451-458.

ACI Committee 440.4R, 2004, "Prestressing Concrete Structures with FRP Tendons."

ACI Committee 318, 2008, "Building Code Requirements for Structural Concrete and Commentary."

ACI Committee 440.1R, 2006, "Guide for the Design and Construction of Structural Concrete Reinforced with FRP Bars."

Ahmad, S. H; Zia, P.; Yu, T. J; and Xie, Y., 1993, "Punching Shear Tests of Slabs Reinforced with 3-D Carbon Fiber Fabric", Concrete International, 16 (6): 36-41.

Aiello, M. A.; and Ombres, L., 2000, "Load-Deflection Analysis of FRP Reinforced Concrete Flexural Members," *Journal of Composites for Constructions*, ASCE, 4(4): 164-173.

Ando, N.; Matsukawa, H.; Hattori, A.; and Mashima, A., 1997, "Experimental Studies on the Long-Term Tensile Properties of FRP Tendons," *Proceedings of the Third International Symposium on Non-Metallic (FRP) reinforcement for Concrete Structures (FRPRCS-3)*, V. 2, Japan Concrete Institute, Tokyo, Japan, pp. 203-210.

ASTM (American Society for Testing and Materials), 2008, D638: "Standard Test Method for Tensile Properties of Plastics," A416: "Standard Specification for Steel Strand, Uncoated Seven-Wire for Prestressed Concrete," C939: "Standard Test Method for Flow of Grout for Preplaced-Aggregate Concrete," C230/C230M: "Standard Test Method for Flow Table for Use in Tests of Hydraulic Cement."

Benmokrane, B.; El-Salakawy, E.; Desgagne, G.; and Lackey, T., 2004, "FRP Bars For Bridges," *Concrete International*, 26(8): 84-90.

Benmokrane, B.; Rahman, H.; Mukhopadhyaya, R.; Masmoudi, R.; Zhang, B.; Lord, I.; and Tadros, G., 2001, "Fiber-Optic Sensors Monitor FR-Reinforced Bridge," *Concrete International*, 23(6): 33-38.

Benmokrane, B.; Salakawy, E. El.; Cherrak, Z.; and Wiseman, A., 2004, "Fiber Reinforced Polymer Composite Bars for the Structural Concrete Slabs of a Public Works and Government Services Canada Parking Garage," *Canadian Journal of Civil Engineering*, Vol. 31, pp. 732-748.

Benmokrane, B.; Chaallal, O.; and Masmoudi, R., 1996, "Flexural response of concrete beams reinforced with FRP reinforcing bars," *ACI Structural Journal*, 91(2): 46-55.

Bischoff, P.H., 2003, "Tension Stiffening and Cracking of Steel Fiber-Reinforced Concrete," *ASCE Journal of Materials in Civil Engineering*, 15(2): 174-182.

Bischoff, P.H., 2005, "Reevaluation of Deflection Prediction for Concrete Beams Reinforced with Steel and Fiber Reinforced Polymer Bars," *Journal of Structural Engineering*, ASCE, 131(5): 752-766.

Bischoff, P.H., 2007a, "Rational Model for Calculating Deflection of Reinforced Concrete Beams and Slabs," *Canadian Journal of Civil Engineering*, Vol. 34, pp. 992-1002.

Bischoff, P.H., 2007b, "Deflection Calculation of FRP Reinforced Concrete Beams Based on Modifications to the Exisiting Branson Equation," *Journal of Composites for Construction*, 11(1): 4-14.

Bischoff, P.H., 2007c, "Effective Moment of Inertia for Calculating Deflections of Concrete Members Containing Steel Reinforcement and Fiber-Reinforced Polymer Reinforcement," *ACI Structural Journal*, 104(1): 68-75.

Bischoff, P. H.; and Gross, S. P., 2011, "Equivalent Moment of Inertia Based on Integration of Curvature," *Journal of composite for construction*, ASCE, 15(3): 263-273.

Bischoff, P. H.; and Paixao, R. , 2004, "Tension Stiffening and Cracking of Concrete Reinforced with Glass Fiber Reinforced Polymer (GFRP) Bars," *Canadian Journal of Civil Engineering*, 31(4): 579-588.

Bischoff, P. H.; and Scanlon, A., 2007, "Effective Moment of Inertia for Calculating Deflections of Concrete Members Containing Steel Reinforcement and FRP Reinforcement," *ACI Structural Journal*, 104(1): 68-75.

Branson, D.E., 1965, "Instantaneous and Time-Dependent Deflections of Simple and Continuous Reinforced Beams," Alabama Highway Department, Bureau of Public Roads, Montgomery, Ala, HPR Rep. No.7, Part 1.

British Standard Institution (BS), 1985, "Structural Use of Concrete, Part 2, Code of Practice for Special Circumstances," BS8110: Part2: 1985, British Standard, London, England.

Brown, V. L.; and Bartholomew, C. L., 1996, "Long-Term Deflections of GFRP-Reinforced Concrete Beams," Proc., ICCI, Tucson, Ariz., pp. 389-400.

Canadian Standards Association (CSA), 2002, "Design and Construction of Building Components with Fibre-Reinforced Polymers," CSA Standard S806-02, Rexdale, Ontario, Canada.

CEB-FIP, 1990, Model Code for Concrete Structures. Comité Euro-International du Béton (CEB) – Fédération Internationale de la Précontrainte, Thomas Telford Ltd., London, UK.

Ceroni, F.; Cosenza, E.; Gaetano, M.; and Pecce, M.; 2006, "Durability Issues of FRP Rebars in Reinforced Concrete Members," *Cement & Concrete Composites*, Vol. 28, 857-868.

Chen, Y., 2007, "Accelerated Aging Tests and Long-Term Prediction Models for Durability of FRP Bars in Concrete," PhD Dissertation, West Virginia University, College of Engineering and Mineral Resources.

Collins, M.P.; and Mitchel, D., 2001, "Prestressed Concrete Structures," 1st Ed., Prentice Hall, New Jersey.

Davoudi, S.; Vogel, H.; Svecova, D.; and Gheorghiu, C., 2008, "CFRP Prestressed High-Strength Concrete Prisms Subjected to Direct Tension," *Journal of Composites for Construction*, ASCE, 12(6): 588-595.

Dolan, C. W., 1990, "Developments in Non-Metallic Prestressing Bars", *PCI Journal*, Precast/Prestressed Concrete Institute, Chicago, 35(5): 80.

Dolan, C. W., 1991, "Kevlar Reinforced Prestressing for Bridge Decks", *Third Bridge Conference, Transportation Research Board*, Washington, D.C., p. 68.

Dolan, C. W.; and Burke, C. R., 1996, "Flexural Strength and Design of FRP Prestressed Beams", Proceedings of the Second International Conference on Advanced Composite Materials in Bridges and Structures (ACMBS2), Montreal, Quebec, Canada, Aug., pp. 383-390.

Dolan, C.W.; Nanni, A.; Hamilton, H.R.; and Bakis, C.E., 2001, "Design Recommendations for Concrete Structures Prestressed with FRP Tendons," FHWA, V. III: FRP Prestressing for Highway Bridges, Cont. DTFH61-96-C-00019.

Dowling, N., 1993, "Mechanical Behavior of Materials," Prentice – Hall, New Jersey.

Dulude, C.; Ahmed, E.; Gamal, S. El; and Benmokrane, B., 2010, "Testing of Large-Scale Two-Way Concrete Slabs Reinforced with GFRP Bars", *CICE 2010- The 5th International Conference on FRP Composite in Civil Engineering.*

Ehsani, M. R.; Saadatmanesh, H.; and Nelson, C. T, 1997, "Transfer and Flexural Bond Performance of Aramid and Carbon FRP Bars", *PCI Journal*, 42(1): 76-86.

European Committee for Standardization (CEN), 1992, "Eurocode 2: Design of Concrete Structures Part 1-1: General Rules for Buildings," DD ENV 1992-1-1, European Prestandard, Brussels, Belgium.

El-Ghandour, A. W.; Pilaoutas, K.; and Waldron, P., 2003, "Punching Shear Behavior of Fiber Reinforced Polymer Reinforced Concrete Flat Slabs: Experimental Study," *Journal of Composites for Construction*, ASCE, 7(3): 258-265.

Faza, S. S.; and GangaRao, H. V. S., 1992, "Pre- and Post-Cracking Deflection Behavior of Concrete Beams Reinforced with Fibre-Reinforced Plastic Rebars," Proc., Advanced Composite Materials in Bridges and Structures, Canadian Society for Civil Engineering, Sherbrook, Que., Canada, pp. 151-160.

Fields, K.; and Bischoff, P.H., 2004, "Tension Stiffening and Cracking of High-Strength Reinforced Concrete Tension Members," *ACI Structural Journal*, 101(4): 447-456.

Gamal, S. El.; Salakawy E. El; and Benmokrane B., 2005, "Behavior of Concrete Bridge Deck Slabs Reinforced with Fiber-Reinforced Polymer Bars Under Concentrated Loads," *ACI Structural Journal*, Technical Paper, title no. 102-S74, pp. 727-735.

Gamal, S. El.; Salakawy, E. El.; and Benmokrane B., 2007, "Influence of Reinforcement on the Behavior of Concrete Bridge Deck Slabs Reinforced with FRP Bars," *Journal of Composites for Construction*, ASCE, 11(5): 449-458.

Gerritse, A.; and Werner, J., 1991, "Arapree, a Non-metallic Bar—Performance and Design Requirements", *Advanced Composite Materials in Civil Engineering Structures*, Proceedings of the Specialty Conference, ASCE, Las Vegas, February, pp. 143-154.

Gilbert, R. I., 1999, "Deflection Calculation for Reinforced Concrete Structures-Why We Sometimes Get It Wrong," *ACI Structural Journal*, 96(6): 1027-1033.

Gilbert, R. I., 2007, "Tension Stiffening in Lightly Reinforced Concrete Slabs," *Journal of Structural Engineering*, ASCE, 133(6): 899-903.

Gilbert, R. I; and Mickleborough, N. C., 1990, "Design of Prestressed Concrete," 1st Ed., Unwin Hyman Ltd, London.

Hassan, T.; Abdelrahman, A.; Tadros, G.; and Rizkalla, S., 2000, "Fibre Reinforced Polymer Reinforcing Bars for Bridge Decks," *Canadian Journal of Civil Engineering*, Vol. 27, pp. 839-849.

Hastak, M.; Halpin, D.W.; and Hong, T., 2004, "Constructability, Maintainability, and Operability of Fiber Reinforced Polymer (FRP) Bridge Deck Panels", *DOT Final Report (FHWA/IN/JTRP-2004/15).*

Holden, T.; Restrepo, J.; and Mander, J. B., 2003, "Seismic Performance of Precast Reinforced and Prestressed Concrete Walls," *Journal of Structural Engineering*, ASCE, 129(3): 286–296.

Issa, M.; Idriss, A.; Kaspar, I.; and Khayyat, S., 1995, "Full-Depth Precast Prestressed Concrete Bridge Deck Panels," *PCI Journal*, 40(1): 74-85.

Issa, M. A.; Yousif, A. A.; and Issa, M. A., 2000, "Experimental Behavior of Full-Depth Precast Concrete Panels for Bridge Rehabilitation," *ACI Structural Journal*, Technical Paper, Title no. 97-S43, pp. 397-407.

JSCE, 1997, "Recommendation for Design and Construction of Concrete Structures Using Continuous Fiber Reinforcing Materials," Concrete Engineering Series No. 23, pp. 325.

Kim, Y. J., 2010, "Flexural Response of Concrete Beams Prestressed with AFRP Tendons: Numerical Investigation," *Journal of Composites for Construction*, 14(6): 647-658.

Lees, M. J.; and Burgoyne, J. C., 1999, "Experimental Study of Influence of Bond on Flexural Behavior Concrete Beams Pretensioned with Aramid Fiber Reinforced Plastics," *ACI Structural Journal*, 96(3): 377-385.

Lee, J. H.; Yoon, Y. S.; and Mitchell, D., 2009, "Improving Punching Shear Behavior of Glass Fiber-Reinforced Polymer Reinforced Slabs", ACI Structural Journal, 106(4): 427-434.

Leonhardt, F.; and Walther, R., 1965, "Welded Wire Mesh as Stirup Reinforcement–Shear Tests of T-Beams and Anchorage Tests," (in German) Bautechnik, Vol. 42, No. 10, October, English Translation by W. Dilger.

Lu, Z., 1998, "Flexural Performance of Fiber Reinforced Polymer Prestressing Bars," M.S. Thesis, The Pennsylvania State University, University Park, PA.

Mander, T. J., 2009, "Structural Performance of a Full Scale Precast Concrete Bridge Deck System," MS thesis, Texas A&M Univ., College Station, TX.

Mander, J. B.; Bracci, J. M.; Hurlebaus, S.; Grasley, Z.; Karthik, M. M.; Liu, S. H.; and Scott, R. M., 2011, "Structural Assessment of D Region Affected By Premature Concrete Deterioration," Technical Report, No. FHWA/TX-12/0-5997-1.

Mander, T. J.; Henley, M. D.; Scott, R. M.; Head, M. H.; and Mander, J. B., 2010, "Experimental Performance of Full-Depth Precast, Prestressed Concrete Overhang, Bridge Deck Panels," *Journal of Bridge Engineering*, ASCE, 15(5): 503-510.

Mander, T. J.; Mander, J. B.; and Head, M. H., 2011a, "Modified Yield Line Theory for Full-Depth Precast Concrete Bridge Deck Overhang Panels", Journal of Bridge Engineering, ASCE, 16(1): 12-20.

Mander, T. J.; Mander, J. B.; and Head, M. H., 2011b, "Compound Shear-Flexural Capacity of Reinforced Concrete-Topped Precast Prestressed Bridge Decks", Journal of Bridge Engineering, ASCE, 16(1): 4-11.

Matthys, S.; De Schutter, G.; and Taerwe, L., 1996, "Influence of Transverse Thermal Expansion of FRP Reinforcement on the Critical Concrete Cover", Advanced Composite Materials and Structures, Montreal, pp. 665-72.

Matthys, S.; and Taerwe, L., 2000, "Concrete Slabs Reinforced with FRP Grids. II: Punching Resistance," *Journal of Composites for Construction*, ASCE, 4(3): 154-161.

McKay, K. S.; and Erki, M. A., 1993, "Flexural Behavior of Concrete Beams Pretensioned with Aramid Fiber Reinforced Plastic Tendons," *Canadian Journal Civil Engineering*, 20(4): 688-695.

Medina, J. C., 2011, "Structural Performance of a Full Scale Precast Concrete Bridge Deck System," MS thesis, Texas A&M Univ., College Station, TX.

Menegotto, M.; and Pinto, P., 1973, "Method of Analysis for Cyclically Loaded Reinforced Concrete Plane Frames Including Changes in Geometry and Non-Elastic Behavior of Elements Under Combined Normal Force and Bending," IABSE Symposium on the Resistance and Ultimate Deformability of Structures Acted on by Well-defined Repeated Loads, Lisbon, 1973.

Mota, C.; Alminar, S.; and Svecova, D., 2006, "Critical Review of Deflection Formulas for FRP-RC Members," *Journal of Composites for Construction*, 10(3): 183-194.

Mukae, K.; Kamagai, S.; Nakai, H.; and Asai, H., 1993, "Characticistics of Aramid FRP Rods," International Symposium on FRP Reinforcement for Concrete Structures, ACI SP 138.

Murashev, V. I.; Sigalov, E. E.; and Baikov, V. N., 1971, "Design of Reinforced Concrete Structures," second edition, translation of Zhelezobetonnye Konstruktsii, MIR Publishers, Moscow, 596 pp.

Naaman, A.; Tan, K.; Jeong, S.; and Alkhairi, F., 1993, "Partially Prestressed Beams with Carbon Fiber Composite Strands Preliminary Tests Evaluation", *Fiber-Reinforcement-Plastic Reinforcement of Concrete Structures Proceedings of the ACI International Symposium*, March, pp. 441-464.

Naaman, A. E., 2004, "Prestressed Concrete Analysis and Desingn: Fundamentals," 2nd Edition, Michigan, USA.

Nanni, A.; and Tanigaki, M., 1992, "Pretensioned Prestressed Concrete Members with Bonded Fiber Reinforced Plastic Bars: Development and Flexural Bond Length (Static)", *ACI Structural Journal*, 89(4): 433-441.

Nanni, A.; Utsunomiya, T.; Yonekura, H.; and Tanigaki, M., 1992, "Transmission of Prestressing Force to Concrete by Bonded Fiber Reinforced Plastic Tendons", *ACI Structural Journal*, 89(3): 335-344.

Nawy, E. G., 2005, "Prestressed Concrete: A Fundamental Approach," Fifth Edition, Pearson Prentice Hall, New Jersey.

Nawy, E. G.; and Neuwerth, G.E., 1977, "Fiber Glass Reinforced Concrete Slabs and Beams," *Journal of Structural Engineering*, ASCE, Vol. 103, pp. 421-440.

NCHRP (National Cooperative Highway Research Program), 2006, "Manual on service life of corrosion-damaged reinforced concrete bridge superstructure elements," Transportation Research Board, Washington, D.C.

Nielsen, M. P., 1999, "Limit Analysis and Concrete Plasticity", 2nd Edition, Wiley, New York.

NIH (National Institute of Health), 2004, http://www.nih.gov/

Nystrom, H. E.; Watkins, S. E.; Nanni, A.; and Murray, S., 2003, "Financial Viability of Fiber-Reinforced Polymer (FRP) Bridges," ASCE, *Journal of Management in Engineering*, 10(1): 2-8.

Odagiri, T.; Matsumoto, K.; and Nakai H., 1997, "Fatigue and Relaxation Characteristics of Continuous Aramid Fiber Reinforced Plastic Rods," *Proceedings of the Third International Symposium on Non-Metallic (FRP) Reinforcement for Concrete Structures (FRPRCS-3)*, V. 2, Japan Concrete Institute, Tokyo, Japan, pp. 227-234.

Ospina, C. E.; Alexander, S. D. B.; and Cheng, J. J. R., 2003, "Punching of Two-Way Concrete Slabs with Fiber-Reinforced Polymer Reinforcing Bars or Grids," *ACI Structural Journal*, 100(5): 589-598.

Park, R.; and Gamble, W. L., 2000, Reinforced Concrete Slabs, 2nd Edition, Wiley, New York.

Park, R.; and Paulay, T., 1975, "Reinforced Concrete Structures," John Wiley & Sons, New York.

Pirayeh Gar, S.; Head, M.; and Hurlebaus, S., 2012, "Discussion on Tension Stiffening in Prestressed Concrete Beams Using Moment-Curvature Relationship," *Journal of Structural Engineering*, ASCE, Vol. 138, No. 8, pp. 1075-1078.

Pisani, M.A., 1998, "A Numerical Survey on the Behavior of Beams Pre-stressed with FRP Cables," *Construction and Building Materials*, V. 12, pp. 221-232.

Popovics, S., 1973, "Numerical Approach to the Complete Stress-Strain Relation for Concrete," *Cement and Concrete Res*., 3(5): 583-599.

Rafi, M.M.; and Najdai, A., 2009, "Evaluation of ACI 440 Deflection Model for Fiber-Reinforced Polymer Reinforced Concrete Beams and Suggested Modification," *ACI Structural Journal*, 106(6): 762-771.

Rahman, A. H.; Kingsley, C. Y.; and Kobayashi, K., 2000, "Service and Ultimate Load Behavior of Bridge Deck Reinforcement with Carbon FRP Grid," *Journal of Composites for Construction*, ASCE, 4(1): 16-23.

Rasheed, H. A.; Nayal, R.; and Melhem, H., 2004, "Response Prediction of Concrete Beams Reinforced with FRP Bars," *Composite Structures*, 65(2): 193-204.

Rashid, M. A.; Mansur, M. A.; and Paramasivam, P., 2005, "Behavior of Aramid Fiber-Reinforced Polymer Reinforced High Strength Concrete Beams Under Bending", *Journal of Composites for Construction*, pp. 117-127.

Razaqpur, A. G.; Svecova, D.; and Cheung, M. S., 2000, "Rational Method for Calculating Deflection of Fiber-Reinforced Polymer Reinforced Beams," *ACI Structural Journal*, 97(1): 175-185.

Razaqpur, A. G., 2009, Private communications.

Rizkalla, S.; and Tadros, G., 1994, "First Smart Bridge in Canada," *Concrete International*, 16(6): 42-44.

Saadatmanesh, H.; and Tannous, F. E., 1999, "Relaxation, Creep, and Fatigue Behavior of Carbon Fiber-reinforced Plastic Tendons," *ACI Materials Journal*, 96(2): 143-153.

Salakawy, E. F. El; and Benmokrane, B., 2004a, "Serviceability of Concrete Bridge Deck Slabs Reinforced with Fiber-Reinforced Polymer composite Bars," *ACI Structural Journal*, Technical Paper, Title no. 101-S72, pp. 727-736.

Salakawy, E. F. El; and Benmokrane, B., 2004b, "Concrete Bridge Deck Slabs Reinforced With FRP Composite Bars: Magog Bridge," *Emirate Journal for Engineering Research*, 9(2): 21-27.

Scott, R.H.; and Beeby, A.W., 2005, "Long-Term Tension Stiffening in Concrete," *ACI Structural Journal*, 102(1): 31-39.

Sen, R.; Shahawy, M.; Rosas, J.; and Sukumar, S., 1998, "Durability of Aramid Pretensioned Elements In a Marine Environment," *ACI Structural Journal*, 95(5): 578-587.

Shahawy, M.A.; and Beitelman, T., 1995, "Static flexural response of members pretensioned with multiple layered aramid fiber bars", *Journal of Composites Part B: Engineering*, pp. 253-261.

Soroushian, P.; Ravanbakhsh, S.; and Nagi, M. A., 2002, "Laboratory Evaluation and Field Application of Concrete Reinforcement with Aramid Fiber-Reinforced Polymer Bars," ACI, *Material Journal*, 99(6): 584-590.

Stoll, F.; Saliba, E. J.; and Casper, E. L., 2000, "Experimental Study of CFRP-Prestressed High-Strength Concrete Bridge Beams," *Composite Structures*, Vol. 49, pp. 191-200.

Taerwe, L., 1995, "Non-Metalic (FRP) Reinforcement for Concrete Structures," London, UK.

Tang, B.; and Podolny, W., 1998, "A successful beginning for fiber reinforced polymer (FRP) composite materials in bridge applications", *FHWA Proc., Int. Conf. on Corrosion and Rehabilitation of Reinforced Concrete Structures.*

Toutanji, H.; and Saafi, M., 1999, "Performance of Concrete Beams Prestressed With Aramid Fiber-Reinforced Polymer Tendons," Composite Structures, V. 44, pp. 63-70.

Toutanji, H. A.; and Saafi, M., 2000, "Flexural Behavior of Concrete Beams Reinforced with Glass Fiber-Reinforced Polymer (GFRP) Bars," *ACI Structural Journal*, 97(5): 712-719.

Trejo, D.; Aguiniga, C.; Buth, E.; Yuan, R.; James, R. W.; and Keating, P., 2000, "FRP Reinforcing Bars in Bridge Decks: State-of-the-Art Review," Texas Transportation Institute (TTI) Research Report 1520-2.

Trejo, D.; Hueste, M.B.; Kim, Y.H.; and Atahan, H., 2008, "Characterization of Self-Consolidating Concrete for Design of Precast, Prestressed Bridge Girders," Texas Transportation Institute. Rep. No. FHWA/TX-09/0-5134-2.

Wang, Y.C.; Wong, P.M.H.; and Kodur, V.; 2003, "Mechanical Properties of Fiber Reinforced Polymer Reinforcing Bars at Elevated Temperatures;" *NRCC-46121*.

Washa, G. W.; and Fluck, P. G., 1952, "Effect of compressive reinforcement on the plastic flow of reinforced concrete beams," *ACI Structural Journal*, 49(2): 89-108.

Yamaguchi, T.; Kato, Y.; Nishimura, T.; and Uomoto, T., 1997, "Creep Rupture of FRP Rods Made of Aramid, Carbon and Glass Fibers," Proceedings of the Third International Symposium on Non-Metallic (FRP) Reinforcement for Concrete Structures (FRPRCS-3), V. 2., Japan Concrete Institute, Tokyo, Japan, pp. 179-186.

Yang, Z. J.; Chen, J. F.; and Proverbs, D., 2003, "Finite Element Modeling of Concrete Cover Separation Failure in FRP Plated RC Beams," Construction and Building Materials, 17 (2003) 3-13.

Yost, J. R.; Gross, S. P.; and Dinehart, D. W., 2003, "Effective Moment of Inertia for Glass Fiber-Reinforced Polymer-Reinforced Concrete Beams," *ACI Structural Journal*, 100(6): 732–739.

Zou, P. X. W., 2003, "Flexural Behavior and Deformability of Fiber Reinforced Polymer Prestressed Concrete Beams," *Journal of Composites for Construction*, ASCE, 7(4): 275-284.